UNIVERSITY OF SOUTHAMPTON

FACULTY OF ENGINEERING, SCIENCE & MATHEMATICS

Institute of Sound and Vibration Research

Dynamic Analysis and Active Control of Lattice Structures

Paulo José Paupitz Gonçalves

A thesis submitted in partial fulfilment of the requirements for Doctor of Philosophy by instructional course.

October 2007

UNIVERSITY OF SOUTHAMPTON

ABSTRACT

FACULTY OF ENGINEERING, SCIENCE & MATHEMATICS

INSTITUTE OF SOUND AND VIBRATION RESEARCH

Doctor of Philosophy

DYNAMIC ANALYSIS AND ACTIVE CONTROL OF LATTICE STRUCTURES

by Paulo José Paupitz Gonçalves

This thesis presents an investigation of the factors controlling the performance of two forms of active vibration control applied to lattice structures, such as those used for space applications. The structure considered is based on a lattice structure assembled by NASA in 1984. It consists of a satellite boom with 93 aluminium members connected rigidly through 33 spherical joints. The structure has two distinct forms of motion which are categorized in terms of short and long wavelength modes. The short wavelength modes occurs when the length of the individual members is a multiple of half wavelength of bending waves. The second category, named long wavelength modes occur when the length of the whole structure is a multiple of half wavelength of waves propagating by longitudinal motion in the structure. Simple expressions are derived to identify the factors that control the frequency bands where short and long wavelength modes occur. It is possible to alter the dynamic behaviour of the system by changing some of the factors in these expressions and thus study the active and passive control of vibration in a variety of such structures. The two strategies of active control considered in the thesis are feedforward control and integral force feedback control. Feedforward control usually requires deterministic forms of disturbance sources while feedback control can be applied to random disturbances. It has been found that short wavelength modes can reduce the performance in the feedback control strategy, while the results of feedforward control are not affected so much. To support this analysis, the energy dissipation and power flow mechanisms in the structure are studied. The results in this thesis are based on numerical simulations and experimental tests which have been used to validate the mathematical model of the structure.

Contents

List of Tables

List of Figures

Declaration of Authorship

I, Paulo J. Paupitz Gonçalves, declare that the thesis entitled Dynamics Analysis and Active Vibration Control of Lattice Structures and the work presented in it are my own. I confirm that

- This work was done wholly while in candidature for a research degree at this University;
- where any part of this thesis has previously been submitted for a degree or any other qualification at this University or any other institution, this has been clearly stated;
- where I have consulted the published work of others, this is always clearly attributed;
- where I have quoted from the work of others, the source is always given. With the exception of such quotations, this thesis is entirely my own work;
- I have acknowledged all main sources of help;
- where the thesis is based on work done by myself jointly with others, I have made clear exactly what was done by others and what I have contributed myself.
- part of this work have been published in conference proceedings and journal paper as described in the text.

_____

Paulo José Paupitz Gonçalves

_____

Date

Abbreviations

ACCESS	Assembly Concept for Construction of Erectable Space Structures
COFS	Control of Flexible Structures
DOF	Degree of Freedom
DPS	Distributed Parameter Systems
EVA	Extra Vehicular Activity
FRF	Frequency Response Function
IFF	Integral Force Feedback
ISAS	(Japanese) Institute of Space and Astronautical Science
ISVR	Institute of Sound and Vibration Research
LW	Long Wavelength
LWM	Long Wavelength Mode
NASA	National Aeronautics and Space Administration
SW	Short Wavelength
SWM	Short Wavelength Mode

List of Symbols

General

a, A	Scalar variables
$\mathbf{a}$	Vectors
$\mathbf{A}$	Matrices
$\mathbf{A}^T$	Transpose of $\mathbf{A}$
$\mathbf{A}^{-1}$	Inverse of $\mathbf{A}$
$\mathbf{A}^H$	Hermitian form of $\mathbf{A}$
$\|\mathbf{A}\|$	Modulus of $\mathbf{A}$
$\mathbf{I}_{n\times m}$	Indentity Matrix, $n \times m$
$\mathbf{0}_{n\times m}$	Zero Matrix, $n \times m$
j	Imaginary number, $\sqrt{-1}$

Structural Analysis

$\mathbf{B}$	Boolean matrix
$\mathbf{b}$	Boolean vector
$\mathbf{D}$	Dynamic Stiffness Matrix [N/m]
$\mathbf{K}$	Finite Element Stiffness Matrix [N/m]
$\mathbf{M}$	Finite Element Mass Matrix [kg]
$\mathbf{R}$	Receptance Matrix [m/N]
$\mathbf{T}$	Coordinate Transformation Matrix
Ψ	Transmission Matrix
$()_{\mathrm{C}}$	Subscript - Equivalent Continuous Property
C_s	Shear force correction factor for a continuous model
E	Young's Modulus [N/m]
f	Force [N]
$()^H$	Super-script, Hermitian operator
I	Second Moment of Area [m^4]
I_o	Polar Second Moment of Area [m^4]
J_o	Torsional Constant [m^4]
k	Wavenumber [m^{-1}]
l	Length [m]
q	displacement [m]
$()_{L,B,D}$	Subscripts - Longitudinal, Batten and Diagonal members, respectively
m	Number of bays of the structure

n_j	Number of joints of the structure
n_m	Number of member of the structure
P,p	Power [Watts]
p(diss)	Power dissipated [Watts]
p(in)	Power input [Watts]
S	Cross Section Area [m^2]
v	velocity [m/s]
β	Ratio between first SW natural frequency and a LW natural frequency
ϕ_n	n^{th} Mode Shape
ρ	Density [kg/m^3]
μ	$(I/l^B S)/(I/l^B S)_{\text{nominal}}$
ω	Angular Frequency [rad/s]
ω_n	n^{th} Natural Frequency [rad/s]
$\boldsymbol{\psi}$	State Variables of the Transmission Matrix

Control Theory

$\mathbf{B}$	Boolean matrix
f_c	Control force [N]
f_d	Disturbance force [N]
$\mathbf{H}_{ff}$	Feedforward controller
$\mathbf{H}_{fb}$	Feedback controller
$\mathbf{H}_{\text{iff}}$	Integral force feedback controller
J	Cost Function
n_c	Number of control sources
n_d	Number of disturbance sources
v_m	Velocities of the monitored dofs [m/s]
v_s	Velocities of the sensed dofs [m/s]
Y_{md}	Mobility relating the disturbance forces with the dofs m [m/Ns]
Y_{md}	Mobility relating the control forces with the dofs m [m/Ns]
ω	Angular Frequency [rad/s]

Chapter One

Introduction

1.1 The vibration problem in space structures

Large deployable structures, which can be launched in a packaged condition and expanded in space, have been necessary since the beginning of space exploration. An increasing number of space systems are being developed for telecommunication, weather monitoring and earth and space sciences. The Japanese *Institute of Space and Astronautical Science* (ISAS), has predicted that Japanese satellites will be launched at the rate of one per year [1], for example. In order to reduce spacecraft launch costs, space structures should be assembled using slender components made of light materials such as aluminium or graphite/epoxy composites [2]. These components tend to be flexible compared to those used for civil engineering applications. The flexibility of these components and the associated low values of structural damping (typically ~ 0.5 percent critical) are in contrast to the requirements for space applications and have shown to be a challenge for engineers and scientists [3, 4]. The absence of air is also another cause of the problems, because surrounding fluid can have a great influence on the damping of light structures. Future space missions involving optical interferometers and space telescopes may make use of large space structures of the order of 100 metres across [5, 6] and in some cases these structures may reach the order of kilometres across, as discussed in reference [7]. The requirements for vibration levels in such structures would, however, be on the scale of micro and nano-vibrations [8, 9, 10, 11, 12]. The *National Aeronautics and Space Administration* (NASA) has developed the program for *Control of Flexible Structures* (COFS) [13] concerning the interaction of flight control, structure and gimbal systems. According to Balas [14], some of the challenges for the design of such systems are because they are *distributed parameter systems* (DPS) and consequently infinite dimensional in theory, with very large dimensions in practice. These systems have many low frequency resonances which often appear closely spaced. Moreover, performing experimental tests for large spacecraft prior to launch is quite limited. There are various sources of disturbance in the space environment. A struc-

ture in the hard vacuum of space is subject to non-uniform temperature distribution due to the different heat transfer modes. A typical structure in orbit has significant temperature gradients in different parts. Thermal shock excitation can occur to the system in orbit (every about 90 minutes in some cases), due to the path through the Earth's shadow. This can be seen in the example shown in figure 1.1 for the point error of the Hubble telescope extracted from reference [15]. Also the position of the structure in space creates the conditions for the system to have high temperature gradients, making some parts of the system deform more than others [16].

Reaction wheels, or momentum wheels, are equipment used to give attitude control to spacecrafts. These devices are used on many satellites to hold them steady or move the pointing direction from one place to another. They increase the pointing precision and reliability of a spacecraft, and may also reduce the mass fraction needed for fuel. Momentum wheels are usually implemented as special electric motors. Both spin-up and braking are controlled electronically by computer. Since the momentum wheel is a small fraction of the spacecraft's total mass, easily-measurable changes in its speed provide very precise changes in angle. It therefore permits very precise changes in a spacecraft's attitude. For this reason, momentum wheels are often used to aim spacecraft with cameras or telescopes. Vibration from these devices is often generated by the bearings, although shafts are also never totally balanced. These factors can cause disturbances with the frequency of rotation and its harmonics. Digital tape recorders have also been suggested as sources of tonal disturbances. Infrared sensors, vital to remote sensing, often require cooling before useful signal-to-noise ratios can be achieved. This is due to the thermal generation of current in semiconductor devices (detectors) even when there is no incident radiation (signal). To solve the problem, mechanical coolers are used, which involves thermodynamic cycles, and consequently use some sort of compressor which, is a well known source of disturbance. In summary the sources of vibration in a space structure can be regarded as being composed of harmonic disturbance from rotating equipment and random disturbances from other sources. An example of a typical disturbance spectrum that which a spacecraft is subjected is shown in figure 1.2, where this figure has been extracted from reference [17]. The vibration can be controlled using a number of techniques, both passive and

active, although the performance of an active control system will depend in the type of disturbance.

1.2 Introduction to lattice structures

In the literature, the terms *Truss* and *Frame* are both used to describe lattice structures and come from the field of static analysis. These terms refers to two- or three-dimensional structures composed of one-dimensional elements. A one dimensional-element is long and thin, so that all its properties can be reasonably defined by a single axial coordinate. The members of a lattice structure meet at joints. Joints can be either pinned or rigid. At a pinned joint, members can rotate freely with respect to one another (this configuration can be very difficult to achieve in practice for three-dimensional lattice structures) [18]. At a rigid joint, members are connected in such a way that no member can rotate freely with respect to the joint and in this case moments are transmitted from one member to one another due to joint rotation. Various terms are found in the literature to describe the one-dimensional elements of lattice structures, such as bar, strut, rod and beam. For planar lattice structures, three variables are necessary to represent the motion of a point in the system while for space lattice structures six variables are required to represent the motion of one point.

Lattice structures have attracted the attention of engineers for many years. The first applications of these structures can be found in the field of civil engineering. One of the earliest publications describing the use of lattice structures is *The Four Books of Architecture* published in 1570 by A. Palladio [19]. The American Society of Civil Engineers [20, 21] has published an extensive survey on the theme prior to 1975. In the aerospace engineering field, lattice structures are employed in applications such as solar energy panels, solar sails, large astronomical telescopes, communication antennae and space station structures. These structures should have a minimum weight and lattice structures have an easy way of packing, deployment and construction in space. Most developments of large space structures was conducted in the nineteen eighties [22]. During the mid 1980's, NASA developed the *Assembly Concept for Construction of Erectable Space Structures*(ACCESS) program [23]. It was the first experiment to study orbital construction in *Extra Vehicular Activity* (EVA) . This program gave an

idea of how space construction would be conducted in future.

1.2.1 The structure studied in this thesis

The structure studied in this thesis is based on a scaled version of the satellite boom deployed and assembled in space by NASA during the program ACCESS (Assembly Concept for Construction of Erectable Space Structures). This structure was already available in the Dynamics Group Laboratory in the Institute of Sound and Vibration (ISVR) from previous work [24, 25, 26]. It is a tetrahedral lattice structure with 93 members connected by 33 joints connected rigidly to the members, and is shown in figure 1.3. A schematic figure with the joint numbering scheme and a coordinated reference system (xyz) is shown in figure 1.4. Some authors [27, 28] have categorized such type of structure as a *Single Bay-Single Laced Beam* lattice structure. The system has 10 equal spaced bays and has approximate scale of 1.0/2.7 compared to the full-size ACCESS structure. The total length of the laboratory structure is 4.5 metres. Other differences are the cross section of the structural members, which in the ACCESS structure has a hollow cross section and in the structure considered in this work has a solid cross section. Beam members are made of aluminium with Young's modulus of 6.897×10^{10} N/m^2, density of 2.684×10^3 kg/m^3 and diameter of 0.00635 m and each joint has mass of 0.022 kg. The joint coordinates are given in table 1.1. The members defining a bay are called Longitudinals (or Longerons), Battens and Diagonals and they are identified in figure 1.5. Figure 1.6 shows the views from different perspectives for one of the structure bays. All the analysis in this thesis is based on the assumption of linearity of the system.

1.3 Introduction to the dynamic behaviour of lattice structures

Lattice structures have a special dynamic property: the coexistence of very different short and long wavelength modes of vibration [29]. These modes are controlled by different mechanisms and they occur in lattice structures almost "independently". The *Long Wavelength Modes* (LWM) occur when the length of the structure is a multiple

of half wavelength of the waves propagating longitudinally in the whole structure. This mode shape is characterized by longitudinal compression and extension of the individual members. In most cases LWM can be compared to the mode shape of equivalent continuous systems, such as a beam or a plate. For this reason, a technique called *Continuum Modelling* of lattice structures [30] has been used to predict natural frequencies and mode shapes in the long wavelength regime. An example of a LWM for the structure considered in this thesis is shown in figure 1.7. In this example the LWM can be compared to the bending mode shape of a continuous beam.

The other form of behaviour exhibited by lattice structures are the *Short Wavelength Modes* (SWM). The SWM is generally dominated by bending of the individual structural members. They occur when the length of a structural member is a multiple half wavelength of bending waves propagating in the individual members. An example of a SWM is given in figure 1.8, showing the bending of some structure members.

Because lattice structures are assembled using many similar coupled subsystems, many SWM may occur in a narrow frequency band. Manufacturing imperfections and small non-linearities (joint backlash, member buckling, joint friction, etc), can, however, cause the natural frequencies to change from one member to the others, increasing the number of natural frequencies and causing a phenomenon called mode localization, where the motion is confined in a few regions of the system [31, 32, 33, 34]. SWM can be beneficial in terms of vibration, if they work as absorbers, as discussed in reference [29], or they may be undesirable if they interfere with an active control strategy, for example. In many mechanical systems, SWMs occur only in mid and high frequencies, lattice structures, however, may exhibit this behaviour in frequencies even lower than the LWMs, if they are composed of long slender elements. The mathematical tools used to analyse mechanical systems, such as modal analysis, are based on the assumptions that the structure is dominated by a few, well spaced, modes. Conventional modal analysis can only be used up to the high frequency acoustic limit, when the spacing between modes becomes comparable with their bandwidth, as discussed by von Flotow [35]. The term acoustic limit is used here in reference to von Flotow work, but it is dificult to define a boundary between structural dynamics and structural acoustics, indeed, one might even insist that the former includes the later. This limit can be

different for different structures, for an aicraft a resoanable division my by a few tens of Hz, for large space structures a few Hz. Another way to understand the dynamics of regular lattice structures is through periodic structures theory. A periodic structure is a system with repeating units, consisting of identical substructures, or cells. This type of structure exhibits dynamic characteristics that makes it act as a mechanical filter for wave propagation. This means that waves can propagate along the structure within certain frequency bands, called *Pass Bands* and the wave propagation is blocked within other frequencies bands called *Stop Bands*. The theory of periodic structures was initially developed for solid sate applications [36] and extended, in the early seventies, to the design of mechanical structures [37, 38]. Since then, the theory has been extensively applied to various types of structures, such as spring-mass systems [39], periodic beams [40] and space structures [41]. Assembling a structure with periodic units can have advantages, as the system becomes easy to construct and assemble. One disadvantage of a periodic structure, however, is that it can transmit vibration very efficiently at certain frequencies [42].

1.4 The active vibration control in space lattice structures

Some desirable characteristics of vibration in the space structures are

- rapid decay of transient disturbances
- desired frequency spectrum and mode shapes, so that natural frequencies of the system are not coincident with the usual working frequencies of rotating equipment, for example.
- adaptability to passive and active control

It is known, however, that space structures and the materials used for their construction do not have all these desirable characteristics. To reduce the addition of mass usually inherent to passive vibration control approaches, active vibration control is often considered to reduce vibration levels. However, as discussed by von Flotow [29] concerning the equipment for active control, "*If all equipment used in the experiment is included, it is doubtful if an experiment has been performed in which the control system weight is*

less than the structure!". Nevertheless, flight hardware tends to be less massive than laboratory equipment. Moreover, active control is not used as a substitute for passive control, but is used as a complementary technique. This has also been discussed by Preumont [10], who describes the application of a large interferometer system that required an active control system as well as passive damping treatment applied to the structure.

Active control makes use of sensors, actuators and a signal processing unit in order to reduce vibration levels in selected positions in the system. Piezoelectric transducers are often used as feedback or reference sensors and as actuators to transform mechanical energy into electrical energy and *vice versa*. The sensors usually measure point-wise variables which may be more or less sensitive to excitations at various points. When controlling vibration in a distributed system, every point in the structure is related to every other point dynamically. Although the vibration levels in the vicinity of the sensors are reduced by the control action, vibration in other areas on the structure could be adversely affected as discussed in reference [43].

An ideal actuator/sensor for vibration suppression (in terms of space applications) would be electrically powered, with high efficiency, would have low mass and would have a high bandwidth. The high bandwidth is important so that the roll-off characteristics of the closed loop system can be designed regardless of the dynamics of the actuator/sensor.

In active lattice structures, members (or part of them) are usually replaced by piezoelectric actuators, which then become active members. These piezo-actuators act in the structure applying two forces in parallel to the axis of the members but with opposite directions. References [10, 44, 45] are examples of applications of piezo-actuators to control vibration in lattice structures. Reference [46] discusses the power requirements for use of piezoelectric actuators is space structures and reference [47] presents a review of the recent advances on the optimization of actuators for smart structures. Other types of actuators have also been used to control vibration in structures; shape memory alloy has been used to control low frequency vibration in a lattice structure [48] and piezoelectric actuators have been used to control vibration in a lattice structure by means of tendons [49]. Electromagnetic actuators have tended not to be used in space

structures because generally only small displacements are required that can be generated piezoelectrically with less weight. More recent work on active control of vibration in space structures can be found in references such as [50, 51, 52, 53]. In terms of general control strategies, two active control frameworks have been proposed, feedforward and feedback. The use of the feedforward control strategy has been discussed for noise control applications in [54] and for vibration control [55]. Reference [25] is an example of an application of feedforward to control vibration in a lattice structure.

Feedback control strategies have been more widely applied in the active control of vibration, perhaps because feedforward control strategies require a reference signal correlated to the disturbance and the feedback control strategy does not. The feedback control strategy is discussed in many books, for example [56, 57]. In the vibration control area, references [10] and [58] discuss various control strategies and aspects of the integration of system and sensors/actuators. The differences between feedforward and feedback control strategies are illustrated in the block diagrams of figures 1.9 and 1.10. The variable to be controlled in these block diagrams is a vector of velocities $\mathbf{v}_m$. In both cases, the systems are subjected to the vector of disturbance forces $\mathbf{f}_d$. The mobility matrix $\mathbf{Y}_{md}$ relates the vector of velocities $\mathbf{v}_m$ to the vector of disturbance forces $\mathbf{f}_d$ and $\mathbf{Y}_{mc}$ is a matrix of mobilities relating the vector of control forces $\mathbf{f}_c$ to the vector of velocities $\mathbf{v}_m$. The control forces are determinate by the matrices of controllers gains $\mathbf{H}_{ff}$ and $\mathbf{H}_{fb}$. In the case of feedforward control, $\mathbf{H}_{ff}$ is driven by a reference signal correlated to the disturbance force, while for the feedback controller, $\mathbf{H}_{fb}$ is driven by the vector of controlled velocities $\mathbf{v}_m$. These control strategies are further discussed in chapter 4 and 5.

1.4.1 Objective function for vibration control

Often in applications of active vibration control it is common to use quadratic cost functions, based on the square of a quantity such as acceleration or velocity. The formulation of sensible cost functions for similar applications has been discussed in references [24] and [59]. In this thesis, the objective function is defined as the sum of the linear squared velocities of the joints 31, 32 and 33 of the lattice structure showed in figure 1.4. This objective function, or Cost Function J, is proportional to the kinetic

energy at these joints and it is calculated from

$$J(\omega) = \mathbf{v}_m^H(\omega)\mathbf{v}_m(\omega) \tag{1.1}$$

where, ω is the angular frequency. $\mathbf{v}_m^H(\omega)$ is the Hermitian form of the vector $\mathbf{v}_m(\omega)$ (conjugate transpose). Suppressing the symbol ω for simplicity, the vector $\mathbf{v}_m$ is defined by

$$\mathbf{v}_m = \begin{bmatrix} v_x^{31} & v_y^{31} & v_z^{31} & v_x^{32} & v_y^{32} & v_z^{32} & v_x^{33} & v_y^{33} & v_z^{33} \end{bmatrix}^T \tag{1.2}$$

where, v_x^{31} is, for example, the velocity of joint 31 in the x direction. T is the transpose of the vector. For a general control strategy, the performance of the controller can be measured by considering the change in the cost function. The attenuation for a certain control is defined in decibels as

$$\text{Attenuation [dB]} = 10\log_{10}\frac{J(\omega)}{J_c(\omega)} \tag{1.3}$$

where J_c is the cost function when active control is applied to the system and $J(\omega)$ is the cost function without control.

1.5 Objectives and Contributions

The objectives of the thesis are:

1. To develop simple expressions to indicate the frequency regions where short and long wavelength modes occur in lattice structures;
2. The application of feedforward and feedback control strategies for the reducing of vibration in space lattice structures and comparison of these strategies.
3. To demonstrate the influence of active control in two different regimes of vibration present in lattice structures (short and long wavelength modes).
4. To investigate, using power analysis, the way in which energy flows and is dissipated in lattice structures, including the influence of active control.

Contributions to the established literature have been made in each of these areas. Parts of this work have been presented in references [60, 61, 62, 63].

1.6 Summary of the thesis

The thesis is divided into six chapters. This first chapter is an introduction and motivation to the work. The second chapter is a review of the methods used to model lattice structures. Particular attention is given into the structure considered in this thesis. The dynamic stiffness method, using exact solutions of wave equations and the finite element method, is then used to obtain a model, which is compared to the results of experimental tests. In chapter 3, the detailed dynamics of the lattice structure is considered, including analysis of energy through a study of power flow and power dissipation in the structural members. The chapter also presents an analysis of short and long wavelength mode shapes, developing simple expressions to explain the behaviour and its influence in the dynamics of the structure. In chapter 4, the performance of a feedforward control strategy is investigated. The cases of one, two and three actuators are considered. Power analysis is used to determine the physical effects of this type of control strategy. The performance of such active controller is studied for the different regimes of vibration (short and long wavelength modes). Chapter 5 considers an implementation of the feedback control strategy. Only the decentralized case is considered, using integral force feedback. The performance of the controller for the different dynamic regimes is also discussed (short and long wavelength modes). Power analysis is used to aid understanding of the dynamics of feedback control. The last chapter is a summary of the thesis including a list of conclusions with suggestions for future work.

Joint Number	**Coordinates**		
	x	y	z
1	0	0	0
2	0	$\sqrt{3}L/2$	$L/2$
3	0	0	L
4	L	0	0
5	L	$\sqrt{3}L/2$	$L/2$
6	L	0	L
7	$2L$	0	0
8	$2L$	$\sqrt{3}L/2$	$L/2$
9	$2L$	0	L
10	$3L$	0	0
11	$3L$	$\sqrt{3}L/2$	$L/2$
12	$3L$	0	L
13	$4L$	0	0
14	$4L$	$\sqrt{3}L/2$	$L/2$
15	$4L$	0	L
16	$5L$	0	0
17	$5L$	$\sqrt{3}L/2$	$L/2$
18	$5L$	0	L
19	$6L$	0	0
20	$6L$	$\sqrt{3}L/2$	$L/2$
21	$6L$	0	L
22	$7L$	0	0
23	$7L$	$\sqrt{3}L/2$	$L/2$
24	$7L$	0	L
25	$8L$	0	0
26	$8L$	$\sqrt{3}L/2$	$L/2$
27	$8L$	0	L
28	$9L$	0	0
29	$9L$	$\sqrt{3}L/2$	$L/2$
30	$9L$	0	L
31	$10L$	0	0
32	$10L$	$\sqrt{3}L/2$	$L/2$
33	$10L$	0	L

Table 1.1: The coordinates of the lattice structure joints considered in this work where $L = 0.45$ metres is the length of one bay.

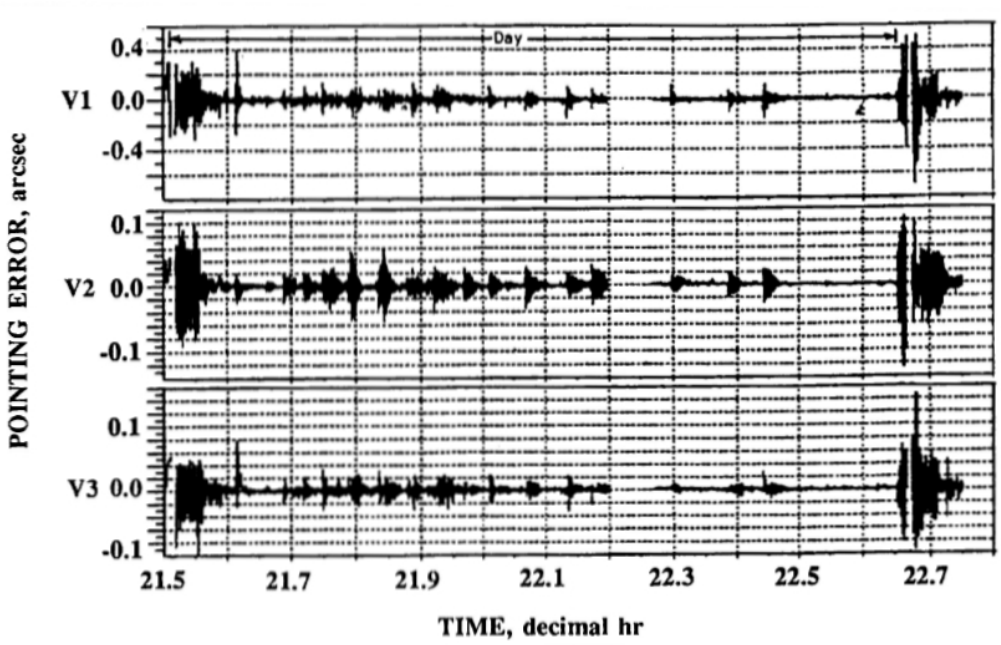

Figure 1.1: Orbital day disturbance profile of the Hubble Space Telescope Pointing System. Figure has been extracted from Foster et al. [15].

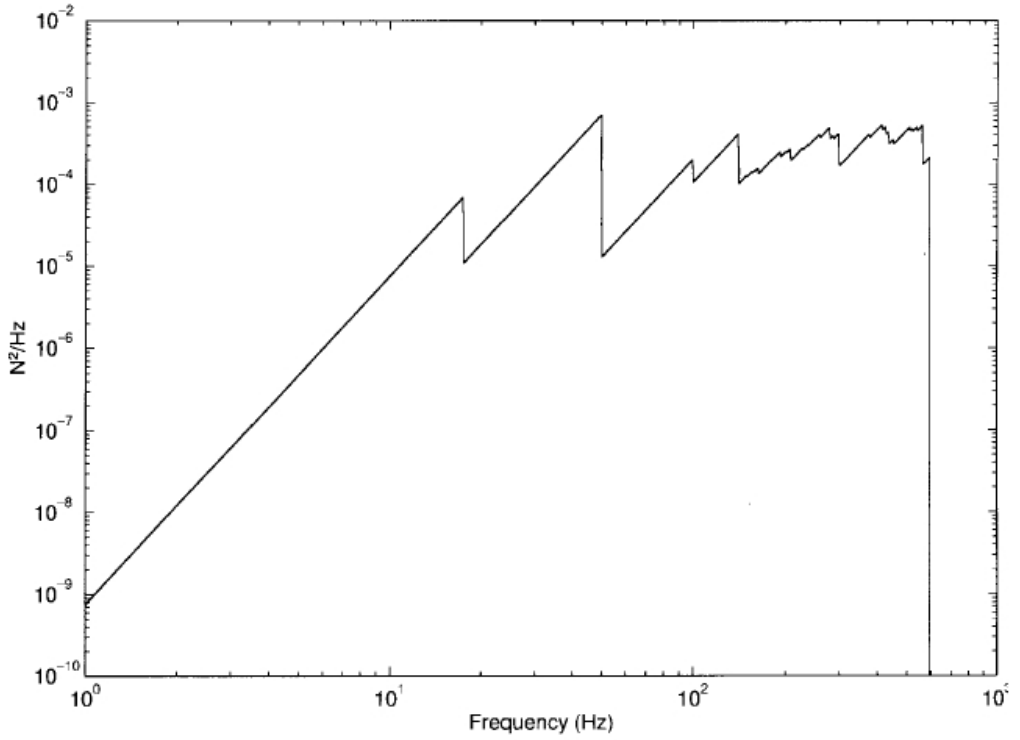

Figure 1.2: Stochastic reaction wheel axial-force disturbance power spectral density assuming a uniform random variable wheel speed over the interval (0, 3000) r/min. Figure has been extracted from Neat et al. [17].

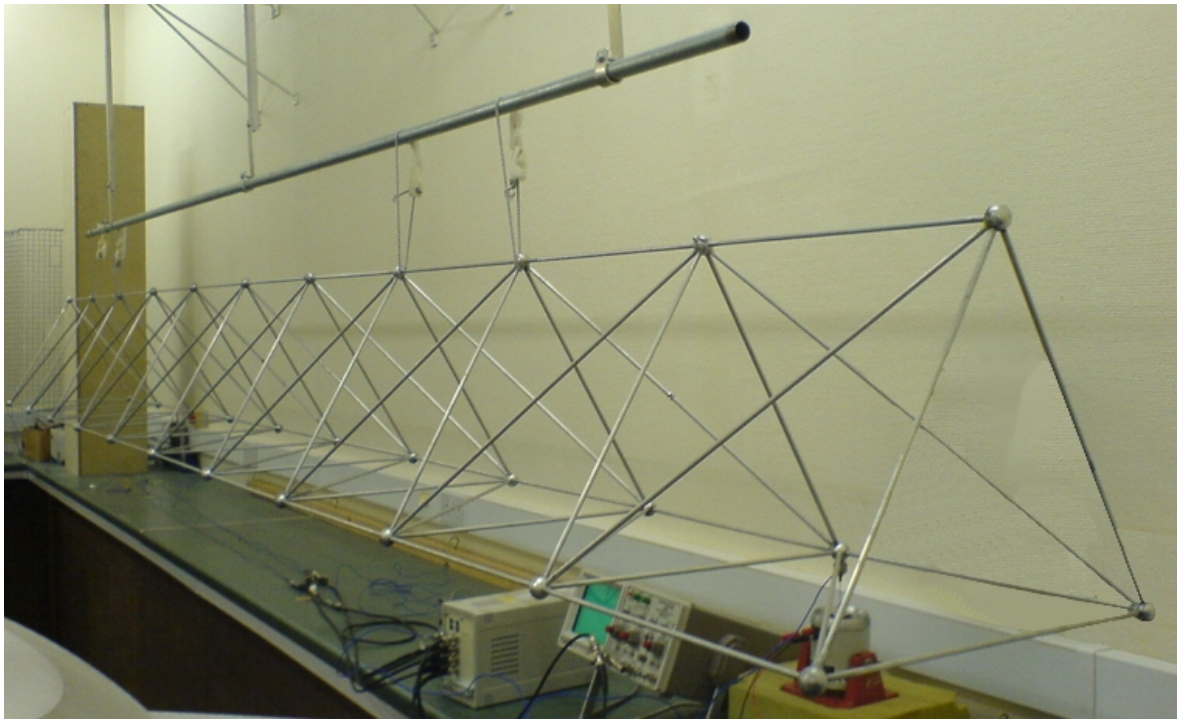

Figure 1.3: A photograph of the lattice structure available at the Dynamics Group Laboratory in the Institute of Sound and Vibration Research.

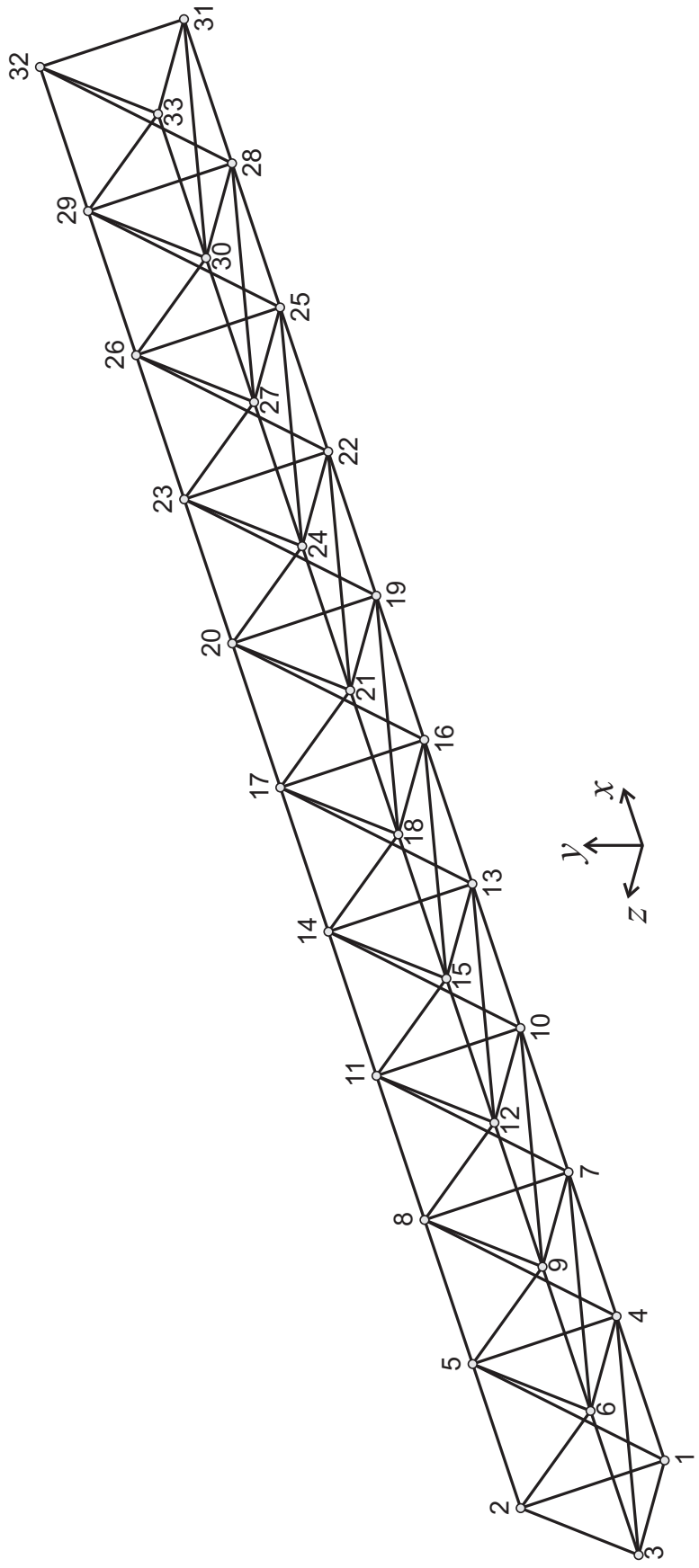

Figure 1.4: The lattice structure considered in this thesis with 93 members and 33 joints with respective numbering scheme oriented in a global coordinate system (xyz).

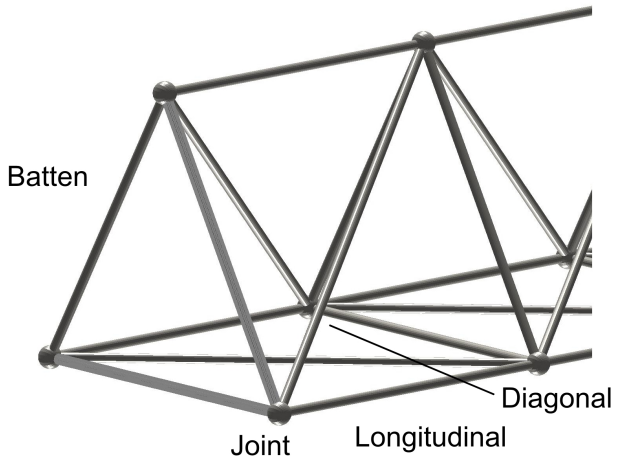

Figure 1.5: A bay of the lattice structure defining the three types of members, longitudinal, batten and diagonal.

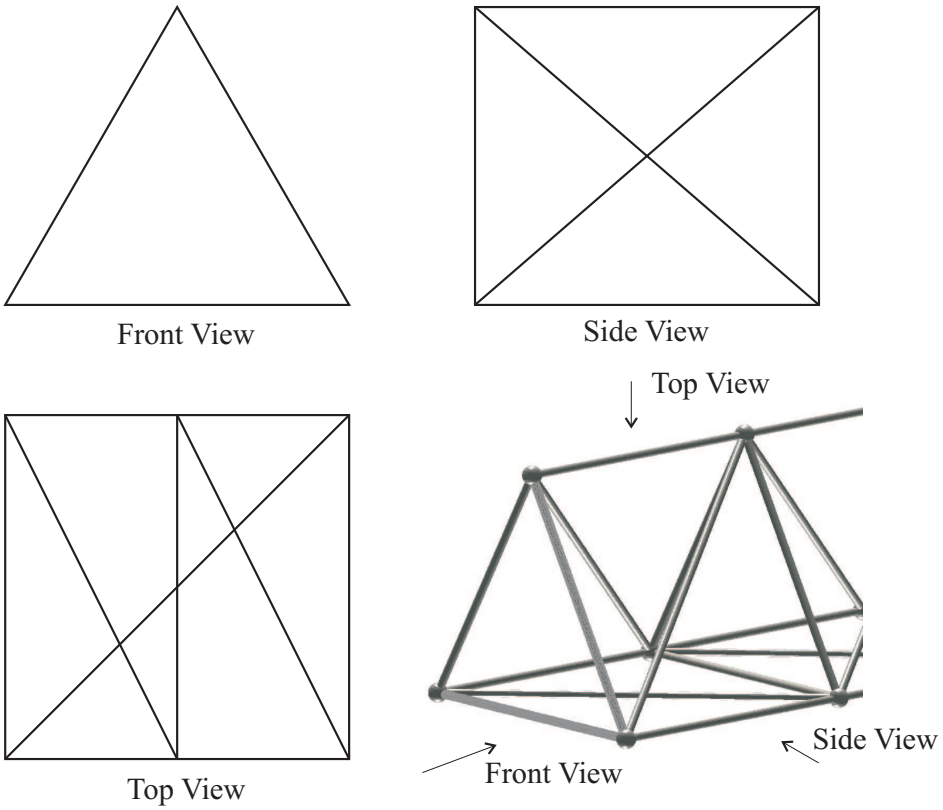

Figure 1.6: The various views of one of the lattice structure bays.

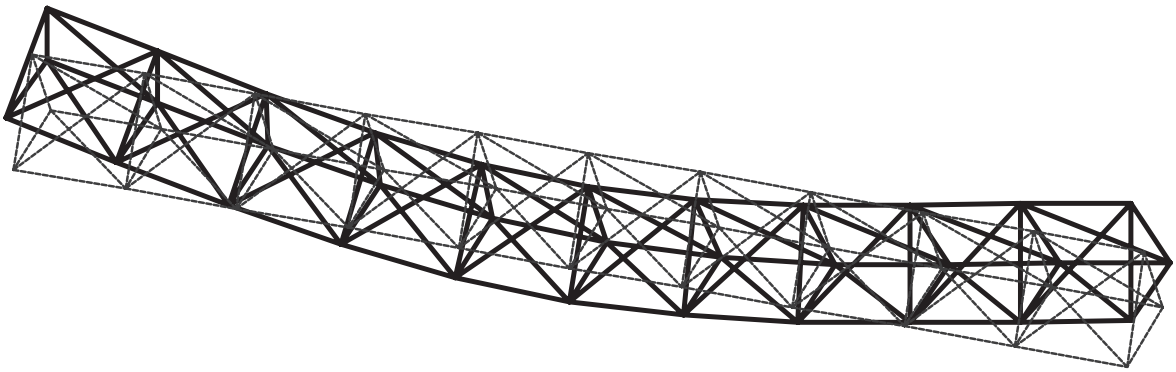

Figure 1.7: An example of a long wavelength mode for the structure considered in this thesis.

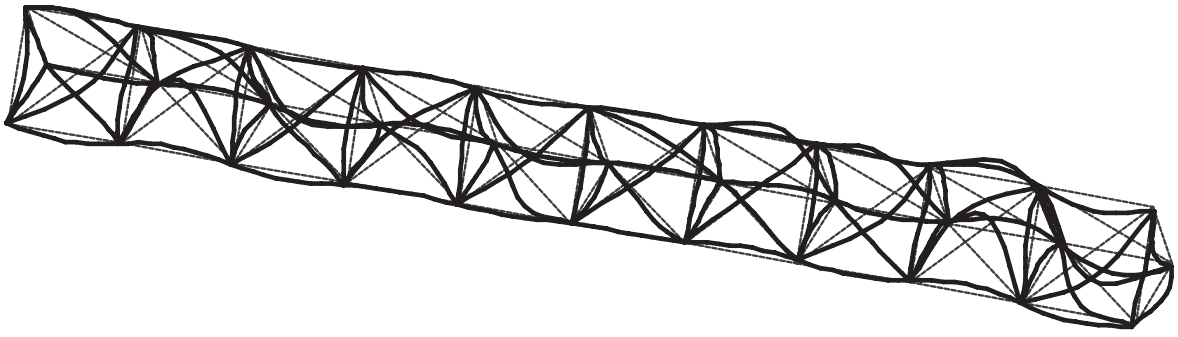

Figure 1.8: An example of a short wavelength mode for the structure considered in this thesis.

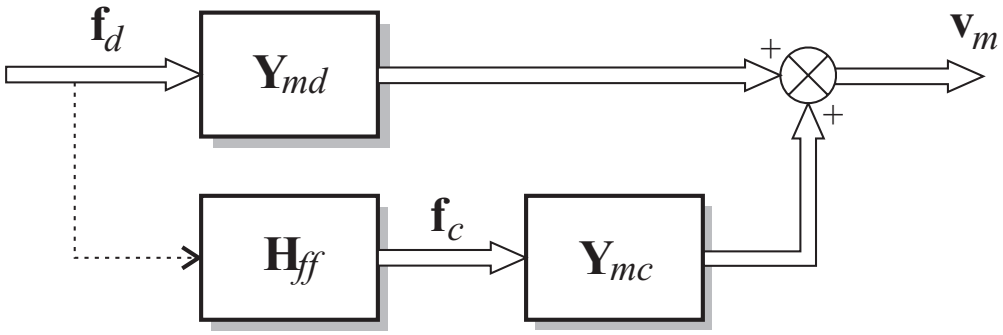

Figure 1.9: Block diagram showing the elements of a feedforward control system.

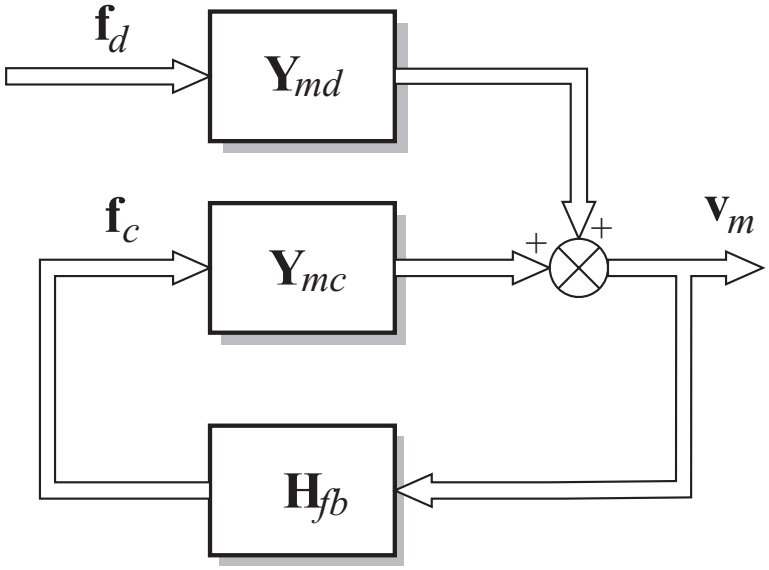

Figure 1.10: Block diagram showing the elements of a feedback control system.

Chapter Two

Modelling of lattice structures

2.1 introduction

In this chapter methods of modelling the dynamics of the lattice structure described in chapter 1 are discussed. One of the approaches, called the direct method [64], is described in detail. The model of the structure is used to predict the cost function, defined in chapter 1 and other dynamic characteristics, such as power flow and mechanisms of energy dissipation. The model is also used in the investigation of active vibration control discussed in chapters 4 and 5.

2.2 Introduction to modelling of lattice structures

The analysis of lattice structures is based on the dynamics of its members which are one dimensional distributed parameter elements. A lattice member can have four different types of motion; longitudinal, torsion and bending in two orthogonal planes. In this work, Euler-Bernoulli beam theory is used to analyse the lattice members. This assumes that the thickness of the beam is smaller than 2π times the wavelength of a bending wave at the highest frequency of interest [65]. The analysis of Euler-Bernoulli beams is presented in a complete and comprehensive text by Bishop and Johnson [66]. For the cases where Euler-Bernoulli theory is not applicable, Timoshenko beam theory should be used [67, 68, 69].

In the literature, the terms *Truss* and *Frame* are frequently used to describe lattice structures composed of one-dimensional elements. Each one-dimensional element is long and thin, so that all of its properties can be reasonably defined by a single axial coordinate. The term *truss* is used for lattice structures with pinned joints where forces are applied only at these joints, therefore the members of a truss submitted to static loads react only with forces that are axial. In this situation, the members of a truss are modelled as linear "springs" that can move only in the longitudinal direction.

For dynamic analysis, modelling a structure using a "truss-like" element, is only possible if the bending motion of the members can be neglected in the frequency range

of analysis. If members do undergo flexural motion, bending motion is transmitted from one member to one another by the joints due to the shear forces acting at these joints (considering dynamic excitation). If bending of structural members is neglected and members are modelled assuming only the dynamics associated with longitudinal motion, the model of the whole structure will have only mode shapes due to the longitudinal compression/extension of its members. In this thesis, this type of mode is termed a *Long Wavelength Mode* (LWM).

The term *frame* is often used to refer to a lattice structure where the members are connected rigidly at the joints. The members of a frame structure can support different types of load which can be applied at joints or at a position in the member. Because joints are rigid, moments can be transferred from one member to one another through the joints. Therefore members of a frame structure are modelled considering bending, torsion and longitudinal dynamics of the structural members.

It is possible for a bending natural frequency of a member to be present in the frequency range of interest causing, what is called in this thesis a *Short Wavelength Mode* (SWM), which occurs when the length of one or more structural members is a multiple of half wavelength of waves that propagate by bending in the structural members.

For the structure considered in this work, bending and torsion of structural members should be included in the model as the joints are considered to be rigid. Lattice structures modelled using a complete beam model for its members (motion in all directions) may or may not have SWM. The presence of short wavelength modes depends upon the frequency range, the cross section of the lattice members, the lattice structure geometry and its length. This is discussed in chapter 3.

2.2.1 Methods for modelling lattice structures

Most modelling methods for lattice structures consider them as a system of discrete elements, taking into account only the responses in certain positions of the structure, usually at the joints. These positions represent the motion of the continuous system by a finite number of *degrees-of-freedom* (DOFs). Each DOF is a variable which can be the joint displacement, velocity or acceleration (either linear or angular). For computational purposes, these variables are written in vector form, and it is clear that a

large number of DOFs increases the computational cost of analysis for a system. In the same way, variables representing the internal and external forces at these DOFs can be written in vector form. Because the system is continuous, each of these vectors of forces and displacements are related to every other variable in a coupled way due to the system continuity. In dynamic analysis, the objective of a mathematical modelling procedure is to obtain functions that relate these forces to every other DOF dynamically and vice-versa. The methods used to obtain these functions, involve physical assumptions that start with the governing equations for a structural member. The governing equations are transformed to the frequency domain by assuming harmonic motion, and all time dependencies disappear, giving equations that depend only on the frequency and on the position along the beam. The functions in the frequency domain relating forces and displacements are known as the beam dynamic stiffness. Once these functions are known, the overall system dynamic stiffness is obtained by applying the conditions of compatibility for each member (making the displacement and force vectors to be coincident with a global coordinate system) and by considering the equilibrium condition for each system joint (where the sum of internal and external forces for each joint is a null vector). This condition comes from the assumption that the system is linear.

The most usual method for modelling lattice structures is the direct method. The direct method make uses of the dynamic stiffness of members that can be calculated directly from the beam wave equations as described by [70, 71, 72], from the series expansion form (modal approach) [66, 72]. The traditional expressions found in these books are, however, numerically unstable for the higher order modes usually necessary in the calculation of the dynamic stiffness over the frequency range of interest. Numerical stable forms for calculating higher order mode shapes have been developed by Gonçalves et al. [63]. Dynamic stiffness can also be calculated by means of approximation using the finite element method [73, 74]. The procedure for calculating the overall dynamic stiffness for a structure in this method is very attractive in terms of computational implementation, since the equilibrium condition is achieved by simply summing the individual dynamic stiffness matrices of the members.

Another method for calculating the response of a lattice structure model is the recep-

tance method. The receptance method is very similar to the dynamic stiffness method, in the sense that the member receptances are the inverse of the member dynamic stiffnesses and they can be calculated similarly by the solutions of wave equations [66] or by a series expansion form [66, 75, 76]. Although the computational implementation of the receptance method for a simply structure can be easy, it becomes quite involved for complex structures. The difference between the receptance and the dynamic stiffness method is that the final result of the receptance method is not a receptance matrix, but a set of equations describing the internal forces acting at the ends of each member. An advantage of the receptance method is that intermediate information can be found prior to solving all equations of the system in the set, and it would thus be possible to calculate the internal forces in a few regions, without having to solve all the other equations.

For structures with some sort of periodicity, such as lattice structures with many similar bays, it is also possible to take advantage of the transfer matrix approach [77, 78]. In this method, only a cell defining the system periodicity is modelled by the dynamic stiffness or receptance method. The cell dynamic stiffness or receptance matrix is then transformed to another representation, called the transfer matrix. The transfer matrix relates a vector defined by the forces and displacements in the left hand side of the cell to the forces and displacements of the right hand side. The properties of the transfer matrix for periodic lattice structures have been studied in [41] and are briefly discussed in the appendix H. The eigenvalues of the transfer matrix can give information about the characteristic waves propagating from one cell to another. Using the transfer matrix, the responses at the end of the structure to excitations at the other end of the structure are found by simple multiplication of the transfer matrix of each cell. Information on internal degrees of freedom are, however, not available directly.

Another method of modelling lattice structures is the continuous modelling approach. A continuum model for a lattice structure is an approach for rapid extraction of the system natural frequencies and mode shapes. The idea is to achieve a model by approximation of the geometry and material properties to that of a continuum system such as a beam or a plate; hence the continuum method is not an unique approach.

It is also possible to consider non deterministic methods, such as statistical energy

analysis. This method is the most recent technique for modelling mechanical systems. It uses gross quantities to describe the system responses in terms of mean values. The method is applicable for high frequencies where there is high modal density [79].

2.2.2 The methods described in this chapter

In this chapter the direct method, which is used in the remainder of the thesis, is described in more detail using three different models for the structural members. In the first, a complete beam model (longitudinal, torsional and bending motion) is considered and the dynamic stiffness matrices of the members are obtained using the exact solutions of the beam wave equations. The second model considered also uses a complete beam model, however, the dynamic stiffness matrices of the members are given in terms of mass and stiffness matrices, approximated by *finite element method* (FEM). In terms of computational implementation, the model which uses the exact solutions of the wave equations is more attractive, since each structural member is modelled as one element. To achieve similar results using the *finite element* (FE) element it is necessary to divide each member into various elements. The beam model calculated from the solutions of the wave equations is sometimes called a spectral element [80] and it is used in this work for the predictions of power flow and simulations involving the active control of vibration. The FE element which assumes the three different motions for a beam in space is usually called a beam element and it is used in this work with the purpose of extracting the system mode shapes and natural frequencies of the lattice. The lattice structure model developed using the beam finite element is obtained by using the commercial FE package ANSYS. The third model considered for the structural members is also obtained from FE mass and stiffness matrices, both bending and torsion of the structural members have been neglected by considering only the longitudinal motion. This assumption leads to a model that has only LWMs, while the complete beam model approach leads to lattice structure models that can have SWMs associated with bending of the structural members.

To complement this last approach, the continuum modelling method is described for the lattice structure considered in this work. The results at the end of this chapter show that the continuum modelling approach is capable of giving results, such as natural

frequencies and mode shapes which are similar to the FE model that considers only longitudinal motion of the structural members. This method is used in chapter 3 to determine the frequencies where LWMs occur.

2.3 The dynamics of lattice members

In this section, the dynamics of a single lattice member is considered. The structural members can undergo different types of motion; longitudinal, torsional and bending. Independent longitudinal, torsional and bending waves in two perpendicular planes can exist in a lattice member. These waves can be excited simultaneously, and to represent the motion 6 variables are necessary. It is convenient to describe the motion of the lattice member by the displacements at its ends, since these positions are generally connected to other subsystems.

2.3.1 The governing differential equations

The motion of a beam can be represented by a set of four partial differential equations governing axial and torsional vibrations and bending given, respectively, by [66, 70, 72]

$$ES\frac{\partial^2 q_1(x)}{\partial x^2} - \rho S\frac{\partial^2 q_1(x,t)}{\partial t^2} = -f_1(x,t) \tag{2.1}$$

$$G\frac{\partial^2 q_4(x)}{\partial x^2} - \rho\frac{\partial^2 q_4(x,t)}{\partial t^2} = -M_4(x,t) \tag{2.2}$$

$$EI\frac{\partial^4 q_i(x)}{\partial x^4} + \rho S\frac{\partial^2 q_i(x,t)}{\partial t^2} = f_i(x,t) \tag{2.3}$$

where q_1 and q_4 are, respectively, the axial displacement and the twist of the beam over the line orthogonal to the beam cross section with respective external loads f_1 (force per unit length) and M_4 (Moment per unit length), q_i with $i = 2$ or $i = 3$ are the lateral displacements of the beam in the two principal planes which are coupled to the rotations q_6 and q_5, respectively. f_i can be a force or a moment per unit length. The variables E, G, ρ are the Young's modulus, shear modulus, and density, respectively. S and I are the cross sectional area and second moment of area, respectively; x and t

are the position along beam length and the time, respectively. Equations 2.1 and 2.2 are second order partial differential equations describing axial and torsional motion, respectively; equation 2.3 is a fourth order partial differential equation describing the motion of the beam in bending using Euler-Bernoulli theory [66]. Assuming time harmonic motion of the form $q(x,t) = Q(x)e^{j\omega t}$, the solution for equations 2.1 and 2.2 can each be written in terms of propagating waves as

$$Q(x) = A_r e^{-jkx} + A_l e^{jkx} \tag{2.4}$$

where Q is a complex variable that can be the displacement for the case of equation 2.1 or a rotation for the case of equation 2.2. The variables A_r and A_l are amplitudes of waves propagating to the right and left, respectively. k is the wavenumber that is defined as $k_l = \omega(\rho/E)^{1/2}$ for longitudinal vibration and $k_t = \omega(\rho/G)^{1/2}$ for torsional vibration (in beams with circular cross section area) or $k_t = \omega(\rho I_o/GJ_o)^{1/2}$ for beams with generic cross section, where I_o is the polar second moment of area and J_o is the torsional constant. For a fixed end, $Q = 0$, and for a free end $Q' = 0$ (where $Q' = \partial Q/\partial x$). The solution of equation 2.3 is given by

$$Q(x) = B_r e^{-kx} + A_r e^{-jkx} + B_l e^{kx} + A_l e^{jkx} \tag{2.5}$$

where B_r is an evanescent wave decaying to the right, B_l is an evanescent wave decaying to the left, A_r is a wave propagating to the right and A_l is a wave propagating to the left; k now is the flexural wavenumber and is given by $k_b = \omega^{1/2}(\rho S/EI)^{1/4}$. The dynamic stiffness or receptances for a beam can be calculated by applying appropriate boundary conditions to equations 2.4 and 2.5. When connecting beams in a lattice structure, in order to find the dynamic stiffness of the whole structure, it is the *free-free* boundary condition which is necessary. For the most common boundary conditions, according to [66] these expressions can be written as

$$\left.\begin{aligned} Q = 0 \text{ and } \frac{\partial Q}{\partial x} = 0 \quad &\text{at a clamped end} \\ Q = 0 \text{ and } \frac{\partial^2 Q}{\partial x^2} = 0 \quad &\text{at a pinned end} \\ \frac{\partial Q}{\partial x} = 0 \text{ and } \frac{\partial^3 Q}{\partial x^3} = 0 \quad &\text{at a sliding end} \\ \frac{\partial^2 Q}{\partial x^2} = 0 \text{ and } \frac{\partial^3 Q}{\partial x^3} = 0 \quad &\text{at a free end} \end{aligned}\right\} \tag{2.6}$$

The dynamics stiffness and receptances can be calculated from the solutions of the wave equations or by means of a series expansion, known as the modal approach. The derivation of the dynamic stiffness matrix of a single lattice member is given in appendix A.

2.3.2 *Dynamics stiffness, displacement and force vectors for a single lattice member*

In order to determine the dynamic response of lattice members a numbering scheme for the displacements of a beam in space with ends **0** and **1** is shown figure 2.1. The displacements at beam ends **0** and **1** are represented, respectively by

$$\bar{\mathbf{q}}(\mathbf{0}) = \begin{bmatrix} q_1 & q_2 & q_3 & q_4 & q_5 & q_6 \end{bmatrix}^T \tag{2.7}$$

$$\bar{\mathbf{q}}(\mathbf{1}) = \begin{bmatrix} q_7 & q_8 & q_9 & q_{10} & q_{11} & q_{12} \end{bmatrix}^T \tag{2.8}$$

where the super-script T denotes the transpose of a vector. The bar symbol over the vectors indicate a local coordinate reference system. The displacements with subscripts $\{1, 2, 3, 7, 8, 9\}$ are linear displacements and $\{4, 5, 6, 10, 11, 12\}$ are angular displacements. Similarly, the forces and moments acting at these positions, as shown in figure 2.2, have a similar numbering scheme represented as

$$\bar{\mathbf{f}}(\mathbf{0}) = \begin{bmatrix} f_1 & f_2 & f_3 & M_4 & M_5 & M_6 \end{bmatrix}^T \tag{2.9}$$

$$\bar{\mathbf{f}}(\mathbf{1}) = \begin{bmatrix} f_7 & f_8 & f_9 & M_{10} & M_{11} & M_{12} \end{bmatrix}^T \tag{2.10}$$

where the forces with subscripts $\{1, 2, 3, 7, 8, 9\}$ are for forces acting in the direction shown and the subscripts $\{4, 5, 6, 10, 11, 12\}$ refer to moments. The displacement and force vectors defining the motion at the ends are given by

$$\bar{\mathbf{q}} = \begin{bmatrix} \bar{\mathbf{q}}^T(\mathbf{0}) & \bar{\mathbf{q}}^T(\mathbf{1}) \end{bmatrix}^T, \bar{\mathbf{f}} = \begin{bmatrix} \bar{\mathbf{f}}^T(\mathbf{0}) & \bar{\mathbf{f}}^T(\mathbf{1}) \end{bmatrix}^T \tag{2.11}$$

The motion in axis 1 and 4 are independent from any other axis, while axis {2 and 6} and {3 and 5} have coupled motion due to bending. The displacements and forces can be related in the frequency domain by a dynamic stiffness matrix $\overline{\mathbf{D}}$ as

$$\bar{\mathbf{f}} = \overline{\mathbf{D}}\bar{\mathbf{q}} \tag{2.12}$$

This relation can also be written in terms of sub-matrices as

$$\begin{bmatrix} \bar{\mathbf{f}}(\mathbf{0}) \\ \bar{\mathbf{f}}(\mathbf{1}) \end{bmatrix} = \begin{bmatrix} \overline{\mathbf{D}}(\mathbf{0},\mathbf{0}) & \overline{\mathbf{D}}(\mathbf{0},\mathbf{1}) \\ \overline{\mathbf{D}}(\mathbf{1},\mathbf{0}) & \overline{\mathbf{D}}(\mathbf{1},\mathbf{1}) \end{bmatrix} \begin{bmatrix} \bar{\mathbf{q}}(\mathbf{0}) \\ \bar{\mathbf{q}}(\mathbf{1}) \end{bmatrix} \tag{2.13}$$

In equation 2.13 the reciprocity condition applies: $\overline{\mathbf{D}}(\mathbf{0},\mathbf{1}) = \overline{\mathbf{D}}(\mathbf{1},\mathbf{0})^T$. The elements of the dynamic stiffness matrix are calculated from the beam equation of motion given in appendix A.

2.4 The dynamic stiffness method

The dynamic stiffness method is adopted from the direct stiffness method in static analysis where the system displacements are based on the degrees of freedom of each joint of the lattice structure. The displacements and forces at the system joints are written in vector form and they are related by the system dynamic stiffness matrix as

$$\mathbf{f}(\omega) = \mathbf{D}(\omega)\,\mathbf{q}(\omega) \tag{2.14}$$

where $\mathbf{q}$, $\mathbf{f}$ and $\mathbf{D}$ are, respectively, the displacement vector, force vector and dynamic stiffness matrix. Considering bending, torsion and axial deformation of the members, the dynamic stiffness matrix for a structure in space has dimension $6n_j \times 6n_j$ and the displacements and force vectors dimension $6n_j \times 1$, where n_j is the number of

joints of the structure. The term ω is the angular frequency which has been dropped in subsequent formulation for simplicity. The formulation of the dynamic stiffness matrix, involves the application of two conditions:

1. *Compatibility condition.* The dynamic stiffness of the structural members are written in terms of global coordinates using a coordinate transformation matrix.

2. *Equilibrium condition.* Dynamic stiffness global matrix is calculated by considering that the sum of forces at a generic joint is a null vector.

To achieve the compatibility condition, the vector of displacements for a certain member given in local coordinates needs to be mapped into a global reference system by means of coordinate transformation. Considering that the vector of displacements for the n-th member in local coordinates can be written in terms of global coordinates by means of a transformation matrix $\mathbf{T}_n$ as

$$\bar{\mathbf{q}}_n = \mathbf{T}_n \mathbf{q}_n \tag{2.15}$$

where the vector $\bar{\mathbf{q}}_n$ is in local coordinates and the vector $\mathbf{q}_n$ is in global coordinates. Similarly, the vector of forces can be related in both coordinated by also using $\mathbf{T}_n$ as

$$\bar{\mathbf{f}}_n = \mathbf{T}_n \mathbf{f}_n \tag{2.16}$$

The coordinate transformation matrix is calculated from the position of the ends of the members given in global coordinates. The transformation matrix is orthogonal [71, 73, 81], which means that $\mathbf{T}^{-1} = \mathbf{T}^T$. Details of the derivation of the matrix are given in appendix B. The dynamic stiffness of the beam in local coordinates can be represented in global coordinates using equations 2.15 and 2.16 as

$$\mathbf{f}_n = \mathbf{T}_n^{-1} \bar{\mathbf{D}}_n \mathbf{T}_n \mathbf{q}_n \tag{2.17}$$

The term $\mathbf{T}_n^{-1} \bar{\mathbf{D}}_n \mathbf{T}_n$ can be written as $\mathbf{D}_n$ and it can be seen as the dynamic stiffness of the member n in global coordinates. After aligning all members' forces and displacements, the dynamic stiffness matrix is calculated by assuming that the sum of force

vectors at a particular joint is a null vector. In terms of computation, it can be done by using a Boolean matrix $\mathbf{B}_n$. The Boolean matrix makes the displacements and forces of a member match to the displacements and forces of the structural joints where the member is connected. The elements of the Boolean matrix are zero or one, such that when the h-th element of $\mathbf{q}_n$ is coincident with the k-th element of $\mathbf{q}$, then $\mathbf{B}_n^{hk} = 1$, otherwise it is zero. $\mathbf{B}$ has dimension $12 \times 6n_j$. After this operation, the terms of the fundamental matrix remain unchanged, but their relative positions are altered as follows

$$\tilde{\mathbf{D}}_n = \mathbf{B}_n^T \mathbf{D}_n \mathbf{B}_n \tag{2.18}$$

By considering that the total energy in the system is the sum of the energies in the individual members, and considering the conditions of equilibrium, the global dynamic stiffness matrix can be defined by

$$\mathbf{D} = \sum_{n}^{n_m} \tilde{\mathbf{D}}_n \tag{2.19}$$

where n_m is the number of members in the structure.

2.4.1 *Effect of joint masses*

Considering that the joints between members are spherical with mass m and they have small diameters, it is possible to neglect the energy related to the joint rotation and the equation of motion for a single joint can be written as

$$f_i = m\ddot{q}_i \tag{2.20}$$

where, i =1, 2 or 3 are the directions of the linear axis. Equation 2.20 can be written in the frequency domain to give the dynamic stiffness for a joint mass m_j as

$$\mathbf{D}_{\mathrm{j}} = -\omega^2 m_{\mathrm{j}} \begin{bmatrix} \mathbf{I}_{3\times3} & \mathbf{0}_{3\times3} \\ \mathbf{0}_{3\times3} & \mathbf{0}_{3\times3} \end{bmatrix} \tag{2.21}$$

where, $\mathbf{I}_{3\times3}$ and $\mathbf{0}_{3\times3}$ are the identity and zero matrices of order 3. Using a similar procedure to the Boolean transformation of equation of equation 2.18, the dynamic

stiffness for the joint mass is found by summing the dynamic stiffness of each joint as

$$\mathbf{D}_{\text{joints}} = \sum_{\text{j}}^{n_j} \mathbf{D}_{\text{j}} \tag{2.22}$$

and the dynamic stiffness of the structure, including the joint masses is found by adding the joint dynamic stiffness $\mathbf{D}_{\text{joints}}$ to the dynamic stiffness of the structure.

2.4.2 Displacements due to external loads

The displacements due to an external load configuration can be calculated by

$$\mathbf{q} = \mathbf{D}^{-1}\mathbf{f}^e \tag{2.23}$$

where $\mathbf{q}$ contains the displacements of the joints due to the external loads $\mathbf{f}^e$ applied to the joints. The evaluation of this equation can be done by inversion of the matrix $\mathbf{D}$ or by using any method to solve a set of linear equations such as Gauss-elimination.

2.4.3 The internal forces

The reaction forces acting at the end of each member due to some external applied force are calculated using the displacements in equation 2.23 after transforming them to local coordinates as

$$\bar{\mathbf{f}}_n^r = \mathbf{D}_n\mathbf{T}_n\mathbf{B}_n\mathbf{q} = \mathbf{D}_n\mathbf{T}_n\mathbf{B}_n\mathbf{D}^{-1}\mathbf{f}^e \tag{2.24}$$

The vector $\bar{\mathbf{f}}_n^r$ can be divided in two sub-vectors $\bar{\mathbf{f}}_n^r = [\bar{\mathbf{f}}_n^T(\mathbf{0}) \;\; \bar{\mathbf{f}}_n^T(\mathbf{1})]^T$ which contains the internal forces at the joints $\mathbf{0}$ and $\mathbf{1}$ of the member. For a particular joint the sum of the internal forces in global coordinates should be a null vector as long as joint masses are not considered in the model. For the case where joint masses are considered, the sum of forces at a particular joint should be equal to the product $-$(joint mass $\times$ joint acceleration) in each linear axis. In what follows, the internal forces for a member are used to find the power flow through joints in the structure.

2.5 Introduction to power analysis in lattice structures

This section aims the analysis of power flow and power dissipation in the lattice structure, is a procedure similar to the work described in reference [70]. Power is the rate at which work is performed. The SI unit of power is Watts [W]. Power is usually seen as an energy flow, which is equivalent to the rate of change of energy in a system. It can be defined by [82]

$$P = \frac{dW}{dt} = \frac{dE}{dt} \tag{2.25}$$

where, W is the work and E is the energy. In mechanical systems, power can be defined in the frequency domain as

$$P(\omega) = \frac{1}{2}\mathrm{Re}\left\{F(\omega) \cdot V^*(\omega)\right\} \tag{2.26}$$

where, F is the complex amplitude of the force and V^* is the conjugate of the complex amplitude of the velocity. Details of the calculation of equation 2.26 are given in appendix D. The power in a lattice structure is exchange at the joints. The net power exchange at a particular joint is zero. The power is calculated from the internal forces and the velocities at the member end as

$$\bar{\mathbf{p}}_n = \frac{1}{2}\mathrm{Re}\left\{\bar{\mathbf{f}}_n^r \times \dot{\bar{\mathbf{q}}}^*\right\} \tag{2.27}$$

where the symbol "$\times$" means multiplication of element by element of the vectors. The frequency dependency has been dropped for simplicity. The bar over the vectors in equation 2.27 means that the vectors of power, force and velocity are in local coordinates and it has been dropped in subsequent formulation for simplicity, but it should be clear that the variables are given in the local coordinates. The power vector can be subdivided as $\mathbf{p}_n = [\mathbf{p}_n^T(\mathbf{0}) \;\; \mathbf{p}_n^T(\mathbf{1})]^T$, where $\mathbf{p}_n(\mathbf{0})$ and $\mathbf{p}_n(\mathbf{1})$ are the vectors of power flowing at beam ends $\mathbf{0}$ and $\mathbf{1}$ in local coordinates, respectively. Using a numbering scheme as in equations 2.7 and 2.8, the power at the ends of the beam can be written

as

$$\mathbf{p}_n(\mathbf{0}) = \begin{bmatrix} p_1 & p_2 & p_3 & p_4 & p_5 & p_6 \end{bmatrix}^T \tag{2.28}$$

$$\mathbf{p}_n(\mathbf{1}) = \begin{bmatrix} p_7 & p_8 & p_9 & p_{10} & p_{11} & p_{12} \end{bmatrix}^T \tag{2.29}$$

The total power flow at the ends of the beam is found by the sum of its components as

$$\begin{aligned} p_n(\mathbf{0}) &= p_1 + p_2 + p_3 + p_4 + p_5 + p_6 \\ p_n(\mathbf{1}) &= p_7 + p_8 + p_9 + p_{10} + p_{11} + p_{12} \end{aligned} \tag{2.30}$$

If the average power at an end of the beam is positive, it means that power is input into the beam at that end, if the power is negative it means that power is output from the beam at that end. By conservation of energy, the sum of energies input, output and dissipated by a system should be zero

$$p_n(\mathbf{0}) + p_n(\mathbf{1}) + p_n(\text{diss}) = 0 \tag{2.31}$$

where, $p_n(\text{diss})$ is the average power dissipated in the n-th member of the structure and by the balance of energy, it is given by $p_n(\text{diss}) = -(p_n(\mathbf{0}) + p_n(\mathbf{1}))$. The total power dissipated in the structure is the sum of the power dissipated in each member given by

$$P_{\text{structure}}(\text{diss}) = \sum_{\text{n}}^{n_m} p_n(\text{diss}) \tag{2.32}$$

By conservation of energy, the sum of the total power input into the structure and the total power dissipated should be zero

$$P_{\text{structure}}(\text{in}) + P_{\text{structure}}(\text{diss}) = 0 \tag{2.33}$$

2.5.1 The mechanisms of power flow and power dissipation

Using the terms of equation 2.30 it is possible to categorize the power flow and the power dissipated in a beam by considering its different mechanisms; longitudinal, torsion and bending. For a particular member they are defined in table 2.1

2.6 The finite element method

The finite element method has been widely used with the advent of high performance computers that make possible the solution of the governing differential equations describing the motion of dynamic systems. Reference [83] gives a detailed introduction about the evolution of the finite element method. Some authors refer to as the first publication about the finite element method an article published in 1960 by Ray Clough [84]. The major advances in the FE method came during the 1960's and 1970's. In the structural engineering area, references [73, 74, 85] are examples. In this section, two types of finite element are discussed. The first is known as the beam element and it considers longitudinal motion, torsional motion and bending for each structural member. The second element is known as a truss or rod element and in this case, bending and torsional motion are neglected. In both cases, the stiffness and mass matrices define the system equation of motion for an undamped mechanical system given by

$$\mathbf{M}\ddot{\mathbf{q}} + \mathbf{K}\mathbf{q} = \mathbf{f} \tag{2.34}$$

where, $\mathbf{K}$ and $\mathbf{M}$ are the mass and stiffness matrices, respectively. For harmonic motion, equation 2.34 can be written in the frequency domain as $(\mathbf{K} - \omega^2\mathbf{M})\,\mathbf{q} = \mathbf{f}$. In the case of the beam element, the matrices have dimension 12×12 and for the truss element they have dimension 6×6. These matrices are readily available in many finite element method text books such as [73, 85] and are given in appendix C. For the undamped structure, the natural frequencies and mode shapes for a system can be found by solving the eigenvalue problem

$$\left(\mathbf{K} - \omega_i^2\mathbf{M}\right)\phi_i = 0 \tag{2.35}$$

where ω_i is a natural frequency and ϕ_i is its corresponding mode shape. The structural response can be either found by inversion of the system dynamic stiffness as

$$\mathbf{q} = \left(\mathbf{K} - \omega^2\mathbf{M}\right)^{-1}\mathbf{f} \tag{2.36}$$

or by the summation over the orthogonal modes of the system as

$$\mathbf{q} = \sum_{i=1}^{i=k} \frac{\phi_i \phi_i^T}{\mu_i \left(\omega_i^2 - \omega^2 + 2j\xi_i\omega_i\omega\right)} \mathbf{f} \tag{2.37}$$

where, k is the number of modes, ξ_i is the modal damping ratio, μ_i is the modal mass. The orthogonal relationship gives

$$\Phi^T \mathbf{M} \Phi = diag(\mu_i) \tag{2.38}$$

$$\Phi^T \mathbf{K} \Phi = diag(\mu_i \omega_i^2) \tag{2.39}$$

2.7 Continuum modelling of lattice structures

Continuum modelling is an approach that is used to reduce computational cost when modelling large lattice structures. The approach is useful to model structures with repeating elements, such as structures with many similar cells, where it is possible to extract information such as natural frequencies and mode shapes. The idea is to develop a model by approximation of the geometry and material properties to that of a continuous system, hence the continuum method can result in different expressions for the same system and as discussed in reference [86] it can be categorised in the following way

1. Relating force or deformation characteristics of a repeating cell of a lattice model to those of the continuum model;
2. Converting finite difference equations from the discrete field method into approximate differential equations;
3. Using energy equivalence between lattice and continuum models;
4. Averaging the contribution of each unidirectional structural element to the overall structural stiffness;
5. Conducting static or experimental analysis of a repeating cell to measure its structural properties.

For the structure considered in this work, it is possible to extract the system natural frequencies and mode shapes using an equivalent continuum model of an Euler-Bernoulli

beam. The concept is shown in figure 2.3 where the overall properties of the lattice structures are represented by the properties of a beam. Let l_L, l_B and l_D be the length of longitudinal, batten and diagonal members, respectively, where these members have been categorized in chapter 1. The total length of the continuous beam model is ml_L, where m is the number of bays in the structure. Considering the free-free boundary condition, the equivalent natural frequencies for the system under bending, axial motion and torsion are given, respectively, by [27]

$$(\omega_i)_{\mathrm{C}} = \left(\frac{(EI)_{\mathrm{C}}}{(\rho S)_{\mathrm{C}}}\right)^{1/2} k_i^2 \text{ ,for bending motion} \tag{2.40}$$

$$(\omega_i)_{\mathrm{C}} = \frac{i\pi}{ml_L}\left(\frac{(ES)_{\mathrm{C}}}{(\rho S)_{\mathrm{C}}}\right)^{1/2} \text{, for longitudinal motion} \tag{2.41}$$

$$(\omega_i)_{\mathrm{C}} = \frac{i\pi}{ml_L}\left(\frac{(GJ)_{\mathrm{C}}}{(\rho I_o)_{\mathrm{C}}}\right)^{1/2} \text{, for torsional motion} \tag{2.42}$$

where the sub-script C refers to the equivalent continuous property, hence, $(EI)_{\mathrm{C}}$, $(ES)_{\mathrm{C}}$ and $(GJ)_{\mathrm{C}}$ are, respectively, the equivalent continuous bending stiffness, longitudinal stiffness and torsional stiffness of the whole structure. Similarly, the equivalent inertia terms are $(\rho S)_{\mathrm{C}}$ for bending and longitudinal vibration and $(\rho I_o)_{\mathrm{C}}$ for torsional vibration, the term i is the mode number. Considering the total mass of one bay in the structure as the sum of masses of the bay members [27] $(3[\rho_L S_L l_L + \rho_B S_B l_B + \rho_D S_D l_D])$, the equivalent mass distribution is easily found by dividing it by the bay length (l_L) to give

$$(\rho S)_{\mathrm{C}} = 3\left(\rho_L S_L + \frac{l_B}{l_L}\rho_B S_B + \frac{l_D}{l_L}\rho_D S_D\right) \tag{2.43}$$

For a homogeneous structure, all members have the same material properties, and the density of the members is represented by ρ. If it is considered that all members have the same cross sectional area S, then equation 2.43 simplifies to

$$(\rho S)_{\mathrm{C}} = 3\rho S\left(1 + \frac{l_B}{l_L} + \frac{l_D}{l_L}\right) \tag{2.44}$$

For the lattice structure considered in this work, the length of its members are related by $l_L = l_B = l_D/\sqrt{2}$ and equation 2.44 reduces to

$$(\rho S)_{\mathrm{C}} = 3\rho S\left(2+\sqrt{2}\right) \tag{2.45}$$

For torsional vibration, the term $(\rho I_o)_{\mathrm{C}}$ can not be calculated by a similar simple procedure. The value for $(\rho I_o)_{\mathrm{C}}$ has been calculated in reference [27] and is given by

$$(\rho I_o)_{\mathrm{C}} = l_B^2\left(\rho_L S_L + \frac{1}{2}\frac{l_B}{l_L}\rho_B S_B + \frac{1}{2}\frac{l_D}{l_L}\rho_D S_D\right) \tag{2.46}$$

which can be simplified for the structure considered in this work ($\rho = \rho_L = \rho_B = \rho_D$, $S = S_L = S_B = S_D$ and $l_L = l_B = l_D/\sqrt{2}$) to

$$(\rho I_o)_{\mathrm{C}} = l_B^2 \rho S \frac{(3+\sqrt{2})}{2} \tag{2.47}$$

2.7.1 *Equivalent bending stiffness*

In this section, an expression for the equivalent bending stiffness of the lattice structure is calculated by summing the contribution of each structural member. Considering figure 2.4 showing the cross section of one of the lattice structure bays, where the areas S_1, S_2 and S_3 are the cross sectional areas of the longitudinal members. The line defining the neutral axis ZZ is placed in position $\frac{1}{3}h$ from the base of the triangle as given in reference [87]. The contribution of one of the longitudinal members to the second moment of area I_{ZZ} can be calculated by

$$I = I_{cg} + \delta^2 S \tag{2.48}$$

where I_{cg} is the second moment of area with respect to an axis parallel to ZZ and passing through the centroid of the shape (coincides with the neutral axis); S is the cross sectional area and δ is the distance between the neutral axis of the structure to the centroidal axis of the member. For a circular cross section, it is given by

$$I_{cg} = \frac{\pi d^4}{64} \tag{2.49}$$

where, d is the diameter of the longitudinal member. Assuming that the cross sectional areas S_1, S_2 and S_3 are equal to S and using equations 2.48 and 2.49, the contribution of the longitudinal members to the second moment of area of the structure can be written as

$$I_{ZZ,\text{Longitudinals}} = 3I_{cg} + \delta_1^2 S + \delta_2^2 S + \delta_3^2 S \tag{2.50}$$

where, $\delta_1 = \frac{2}{3}h$ can be written in terms of the length of the members using a trigonometric relationship to give $\delta_1 = \frac{\sqrt{3}}{3}l_B$. Similarly, $\delta_2 = \delta_3 = \frac{\sqrt{3}}{6}l_B$. Equation 2.50 can then be written as

$$I_{ZZ,\text{Longitudinals}} = 3\frac{\pi d^4}{64} + \frac{l_B^2 S}{2} \tag{2.51}$$

which can be re-formulated to give

$$I_{ZZ,\text{Longitudinals}} = \frac{S}{2}\left(\frac{3d^2}{8} + l_B^2\right) \tag{2.52}$$

For the structure considered in this thesis, $3\frac{d^2}{8} << l_B^2$, so the second moment of area can be written as

$$I_{ZZ,\text{Longitudinals}} \approx \frac{l_B^2 S}{2} \tag{2.53}$$

Equation 2.53 does not take into account the contribution of the diagonal members defined by the areas S_4, S_5 and S_6. The area S_5 has fixed position δ from the structure neutral axis ZZ, however, the areas S_4 and S_6 have a varying distance δ along the bay of the structure. In figure 2.4, two positions of these areas are shown for the bay cross sections CS′ and CS″ as an example. Also, the angle of the areas in the axis XX orthogonal to the two axes YY and ZZ should be considered. Using the relationship $l_L = l_B = l_D/\sqrt{2}$, this angle is given by $\pi/4$ rad. The contribution of the diagonal members to the second moment of area of the structure can then be written as

$$I_{ZZ,\text{Diagonals}} = \sin\frac{\pi}{4}\left(3\frac{\pi d^4}{64} + \frac{3}{36}l_B^2 S + \delta_4^2 S_4 + \delta_6^2 S_6\right) \tag{2.54}$$

where, δ_4 and δ_6 vary along the cross section of the structure. Figure 2.5 shows the variation of the second moment of area of the diagonal members $I_{ZZ,\text{Diagonals}}$ compared to the second moment of area of the longitudinal members. In this figure, it is possible to see that by the middle of each bay, the contribution of the diagonal members to the second moment of area of the structure is minimum being about 20% of the value of the contribution of the longitudinal members. The values of the second moment of area in this region controls the stiffness of the bay (the members should deform in regions with less resistance to the stress). For simplicity, in this thesis, the bending stiffness of the bay is considered to be only the contribution of the longitudinal members and it is defined as

$$(EI)_{\text{C}} = \frac{E_L l_B^2 S_L}{2} \tag{2.55}$$

The value of the equivalent bending stiffness for the axis YY can be found by similar procedure. The bending stiffness over the axis YY is similar to the expression given in equation 2.55. This equation is equal to the expressions found in the reference [27] which use an energy method to calculate the stiffness of different structures and also in reference [28] which uses the finite difference method. According to reference [88], the expression given in equation 2.55 needs to be modified to take into account the effect of shear forces as

$$(EI)_{\text{C}} = \frac{(EI)^*_{\text{C}}}{(1 + C_s/m^2)} \tag{2.56}$$

where, m is the number of bays of the lattice structure, $(EI)^*_{\text{C}}$ is given by equation 2.55 and C_s depends on the mode shape, and the bay geometry given by [89]

$$C_s = \frac{\pi^2 i^2 S_L}{3 l_L^3} \left(\frac{l_D^3}{S_D} + \frac{l_B^3}{S_B} \right) \tag{2.57}$$

Equation 2.57 can be simplified by making the approximation $S = S_L = S_B = S_D$ and $l_L = l_B = l_D/\sqrt{2}$. It becomes

$$C_s = \frac{\pi^2 i^2 (1 + 2\sqrt{2})}{3} \tag{2.58}$$

In the following sections, the expressions for the equivalent longitudinal and torsional stiffness are given. These expressions were extracted from reference [28], where the first equation given in each section is the form found in this reference and the second equation is a simplified expression using $S = S_L = S_B = S_D$, $E = E_L = E_B = E_D$ and $l_L = l_B = l_D/\sqrt{2}$.

2.7.2 Equivalent longitudinal stiffness

- The expression given in reference [28] is

$$(ES)_{\mathrm{C}} = 3E_L S_L \tag{2.59}$$

- which can be simplified for the lattice structure considered in this thesis, to give

$$(ES)_{\mathrm{C}} = 3ES \tag{2.60}$$

2.7.3 Equivalent torsional stiffness

- The expression given in reference [28] is

$$(GJ)_{\mathrm{C}} = \frac{l_B^4 l_L}{4\left(\frac{l_L^3}{E_L S_L} + \frac{l_B^3}{E_B S_B} + \frac{l_D^3}{E_D S_D}\right)} \tag{2.61}$$

- which can be simplified for the lattice structure considered in this thesis, to give

$$(GJ)_{\mathrm{C}} = \frac{l_B^2 ES}{(8 + 8\sqrt{2})} \tag{2.62}$$

The natural frequencies for torsion and axial deformation of the lattice structures can be found by similar procedures and are given in references [27, 28] for various types of lattice structures. For the structure considered here, they are presented in table 2.2. The formulation given in this table is used in chapter 3 to derive expressions defining the frequencies where long wavelength mode shapes occur.

2.8 Numerical simulations

The numerical results obtained by using the different methods discussed in this chapter are presented in this section. The simulations were performed using the following values for the structural members.

- Young's modulus, $E = 6.898 \times 10^{10}$ N/m^2
- density, $\rho = 2.684 \times 10^3$ kg
- Poisson's ratio, $\upsilon = 0.33$
- shear modulus, $G = E/2(1+\upsilon) = 2.593 \times 10^{10}$ N/m^2
- structural damping, $\eta = 0.005$, (using complex Young's modulus, $E(1+j\eta)$)
- diameter of members, $d = d_L = d_B = d_D = 0.00635$ m
- length of members , $l_L = l_B = 0.45$ m, $l_D = 0.6364$ m
- joints masses, $\mathrm{J_{mass}} = 0.022$ kg

2.8.1 Dynamic stiffness method numerical results

Using a complete beam model (considering bending, torsion and longitudinal displacements) and the dynamic stiffness method of section 2.4, mobility *frequency response functions* (FRFs) were obtained by applying a harmonic force of 1 N at joint 4, in the y direction (as shown in figure 1.4 of chapter 1) in the frequency range 20 Hz - 1 kHz, using 1 Hz of frequency resolution. The displacements at joints 31, 32 and 33 in the x, y and z directions were calculated and differentiated in the frequency domain to obtain the mobility FRFs. The magnitudes of these mobilities are shown in figure 2.6. The cost function, defined in chapter 1, is calculated by $J = \mathbf{v}_m^H \mathbf{v}_m$, where the vector $\mathbf{v}_m$ contains these mobilities. The cost function as a function of frequency is presented in figure 2.7. Most of the resonance peaks shown in figures 2.6 and 2.7 are related to short wavelength modes due to the bending of lattice members. This short wavelength modal behaviour is shown in figure 2.8, where some examples of modes associated with the bending of lattice members are given. These mode shapes were obtained using the

finite element package ANSYS with the three-dimensional beam element (defined in the software as *beam4* element). Each structural member was divided into 12 finite elements. The results show that, at low frequencies, before any long wavelength modes occur, many short wavelength modes have occurred. The mode count graph also shows that this system has a high modal density in this frequency band. The implication of such high a modal density in the dynamics and control of a lattice structure is discussed in chapter 3, 4 and 5.

2.8.2 Finite element method numerical results

Considering the longitudinal motion and neglecting bending and torsion of the structure members, a numerical model was obtained by the approach described in a previous section. Similar to the results obtained using the complete beam model, a cost function for the system, comprising the sum of the squared absolute linear velocities at joints 31, 32 and 33 in direction x, y and z have been calculated for a harmonic force of 1 N applied at joint 4 in the y direction. The resulting cost function is compared with the results of the dynamic stiffness method in figure 2.9. The model obtained using the truss finite element (torsion and bending of structural members is neglected) does not contain any resonance peaks associated with the bending of the lattice members and all the peaks in the cost function are associated with longitudinal extension and compression of the structural members. The interesting result of this comparison is that, both models have similar mean values for the cost function when it is averaged over the frequency range 0 - 1 kHz. To complement this information, the mode count in the frequency range 0 - 1 kHz is plotted in figure 2.10. The number of natural modes in this frequency range was also obtained by the software ANSYS using a method called subspace iteration [71]. Figure 2.11 shows the first six mode shapes obtained by finite element method with only longitudinal motion.

2.8.3 Continuum modelling numerical results

Table 2.3 shows the natural frequencies of a equivalent beam model calculated using the expression given in table 2.2 for the first 10 natural modes. These results are

compared to the natural frequencies obtained by the finite element method using the ratio ω_C/ω_{FEM} in figure 2.12, where ω_C is the natural frequency of the continuous model and ω_{FEM} is the natural frequency of the equivalent mode shape calculated by the finite element method. The results show reasonable agreement between the two methods.

2.9 Experimental work

Experimental tests were conducted in the lattice structure described in the introduction in order to validate the mathematical model obtained by the dynamic stiffness method. The experimental rig consists of a lattice structure of 93 aluminium members and 33 aluminium spherical joints of mass 0.022 kg. This structure was already available in the laboratory of the Dynamics Group of the Institute of Sound and Vibration Research and it is the same used in the work by M. Moshrefi-Torbati, [25]. A picture of the experimental rig is shown in figure 2.13. To simulate the free-free boundary condition, the structure was suspended using elastic wires. The suspension apparatus with the structure has natural frequencies below 4 Hz. The system was excited with an electromagnetic shaker mounted on foam rubber. The system was excited with white noise in a frequency band of 0 - 1 kHz. Acceleration at joints 4, 31, 32 and 33 were measured using PCB-Model 352A24 ICP accelerometers (with nominal sensitivity of 10^{-3} V/m/s^2). The mass of the accelerometers is about 0.8 grams which has not been taken into account in the modelling of the system. The input force was measured using a PCB-Model 208C01 ICP force sensor (with nominal sensitivity about 100 mV/N). Using a frequency analyser model HP35650, the transducers signals were recorded and acceleration FRFs (frequency response functions) were calculated with a resolution of 0.25 Hz. Hanning windows were used in the calculation of the FRFs. The FRFs were smoothed by averaging the data 10 times using no time overlapping. A diagram showing the experimental setup is shown in figure 2.14

2.10 Experimental results

By integrating acceleration frequency response functions obtained in the experimental work, it was possible to calculate the transfer mobilities for joints 31, 32 and 33 in

directions x, y and z due to a primary force of 1 N applied at joint 4 in the y direction. The magnitudes of these transfer functions, the phase and the measurement coherence are given in appendix E. Using these transfer mobilities, an experimental cost function was obtained and is plotted, together with the theoretical results obtained by the dynamic stiffness method using the complete beam model, in figure 2.15. It can be seen that there is good agreement between the theoretical and experimental results. Similarly the power input into the structure has been calculated by the dynamic stiffness method and from the experimental data. The power due to the harmonic force of 1 N applied at joint 4 in the y direction is calculated by

$$\frac{P_{\text{in}}}{|f_{4,y}|^2} = \frac{\text{Re}\left\{v_{4,y}\right\}}{2} \tag{2.63}$$

where, $v_{4,y}$ is the velocity of joint 4 in the y direction. The comparison between the theoretical and experimental results are given in figure 2.16, again showing a good agreement between the theoretical and experimental results. The dip in the measured power at about 450 HZ is thought to be due to error in the calculation of the real part of $v_{4,y}$, which is largely reactive at these frequencies.

2.11 Concluding remarks

In this chapter, various methods of modelling lattice structures have been presented, which includes the dynamic stiffness, finite element and continuum modelling methods. Different dynamic behaviour can be obtained using different models for the structural elements. These different models are used in chapter 3 to predict the mechanisms of power flow and energy distribution in a lattice structure with different dynamic regimes. Experimental results proved the accuracy of the model obtained by the dynamic stiffness method using a complete model for the structural members. This model is used in chapters 4 and 5 in order to predict the results of active control.

	End **0**	End **1**	Power Dissipated
Total	$\sum_{k=1}^{6} p_k$	$\sum_{k=7}^{12} p_k$	$-(\mathrm{P}(\mathbf{0}) + \mathrm{P}(\mathbf{1}))$
Longitudinal	p_1	p_7	$-(p_1 + p_7)$
Torsional	p_4	p_{10}	$-(p_4 + p_{10})$
Bending	$(p_2 + p_3 + p_5 + p_6)$	$(p_8 + p_9 + p_{11} + p_{12})$	$-(\mathrm{P}_{bend}(\mathbf{0}) + \mathrm{P}_{bend}(\mathbf{1}))$

Table 2.1: Power Flow in ends **0** and **1**; Power dissipated

	Equivalent Stiffness	Mass Distribution	Natural frequency
Bending	$\frac{El_B^2 S}{2(1 + C_s/m^2)}$	$3\rho S\left(2+\sqrt{2}\right)$	$\frac{l_B}{(12+6\sqrt{2})^{1/2}}\left(\frac{E}{\rho}\right)^{1/2}\frac{mk_i^2}{(m^2+C_s)^{1/2}}$
Longitudinal	$3ES_L$	$3\rho S\left(2+\sqrt{2}\right)$	$\frac{i\pi}{(2+\sqrt{2})^{1/2}ml_L}\left(\frac{E}{\rho}\right)^{1/2}$
Torsion	$\frac{El_B^2 S}{2+2\sqrt{2}}$	$l_B^2\rho S\frac{(3+\sqrt{2})}{2}$	$\frac{i\pi}{2(5+4\sqrt{2})^{1/2}ml_L}\left(\frac{E}{\rho}\right)^{1/2}$

Table 2.2: Equivalent mass, equivalent stiffness and natural frequencies for a equivalent continuous system

Mode shape	Natural frequency [Hz]
1^{st} Bending - y	83.5
1^{st} Bending - z	83.5
1^{st} Torsion	86.3
2^{nd} Torsion	172.6
2^{nd} Bending - y	199.2
2^{nd} Bending - z	199.2
3^{rd} Torsion	258.8
1^{st} Longitudinal	304.8
3^{rd} Bending - y	327.7
3^{rd} Bending - z	327.7

Table 2.3: Natural frequencies of a continuum model

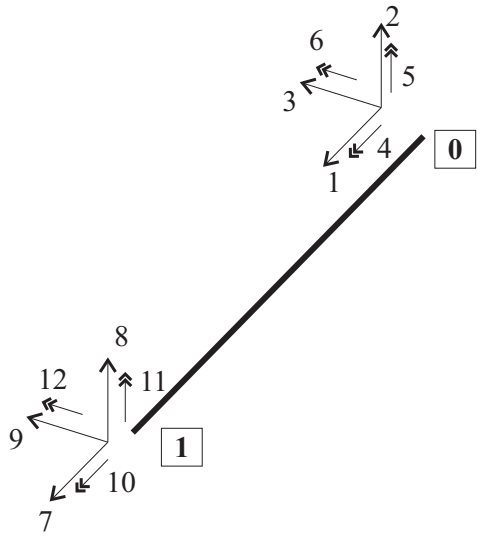

Figure 2.1: Local coordinate system for a beam, with ends **0** and **1** and respective degrees of freedom numbering scheme

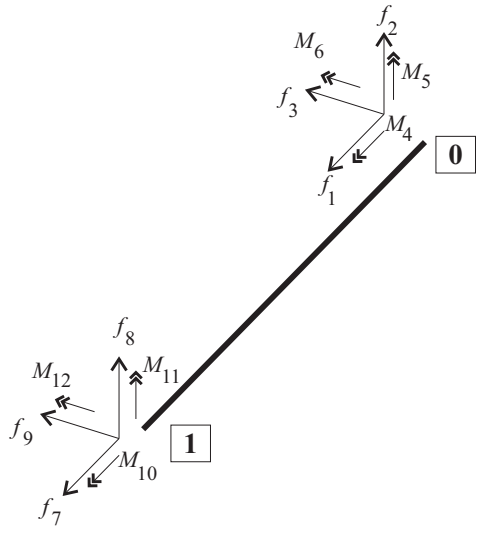

Figure 2.2: Force numbering scheme for a beam in local coordinates with ends **0** and **1**.

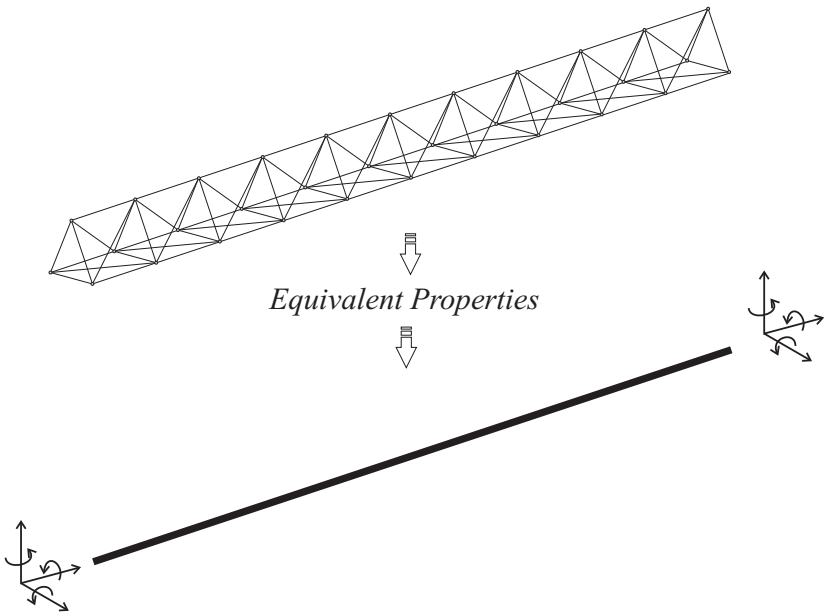

Figure 2.3: Equivalent continuum modelling for a satellite boom

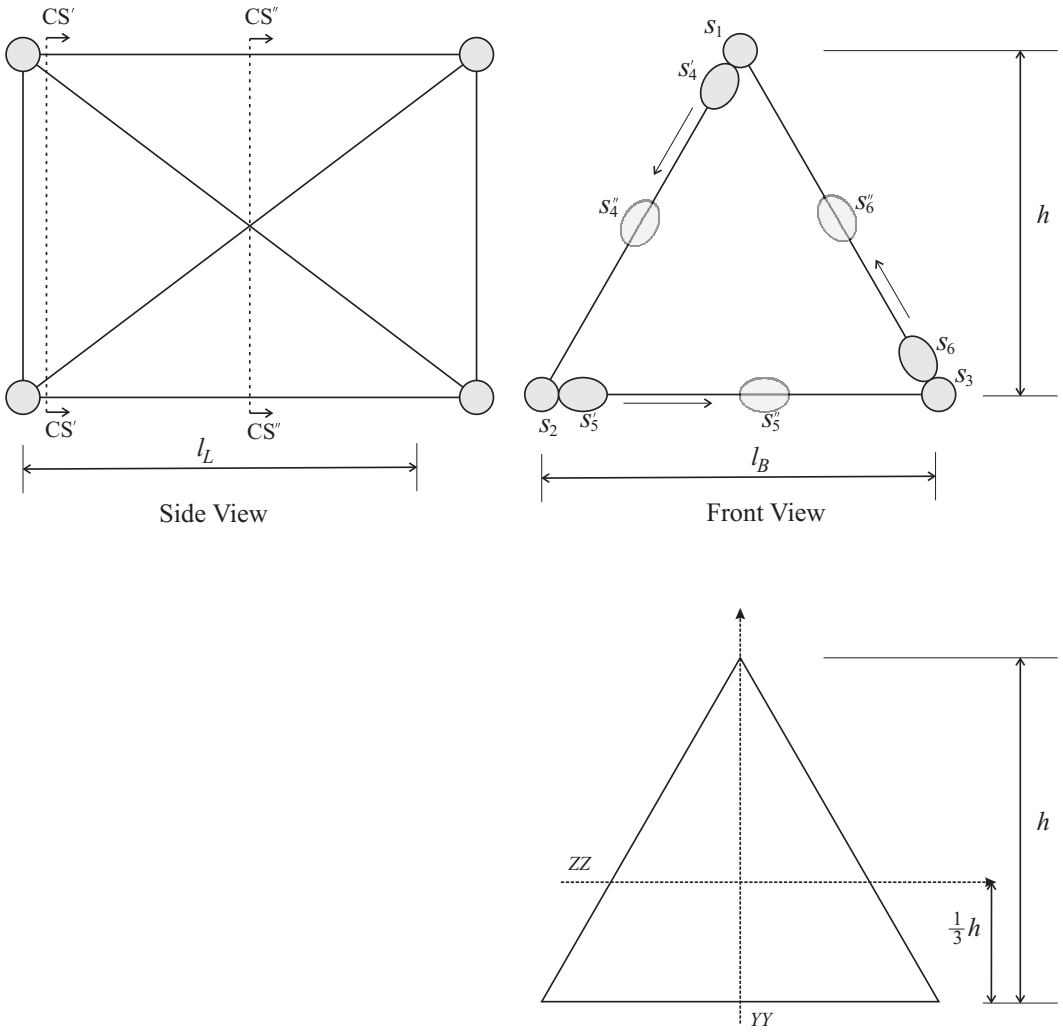

Figure 2.4: The views of bay of the lattice and the bay cross section.

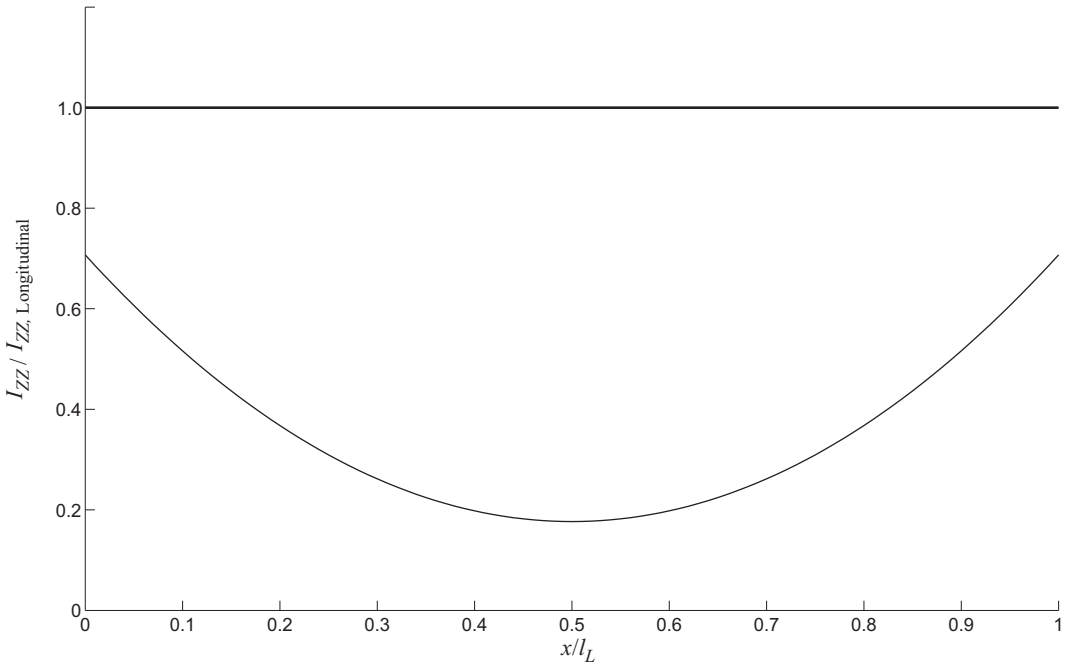

Figure 2.5: The contribution to the second moment of area of the longitudinal members (thick line) and the contribution to the second moment of area of the diagonal members (thin line) according to the position in the structure bay. Values of the second moment of area are normalised in respect to $I_{zz,\mathrm{Longitudinal}}$

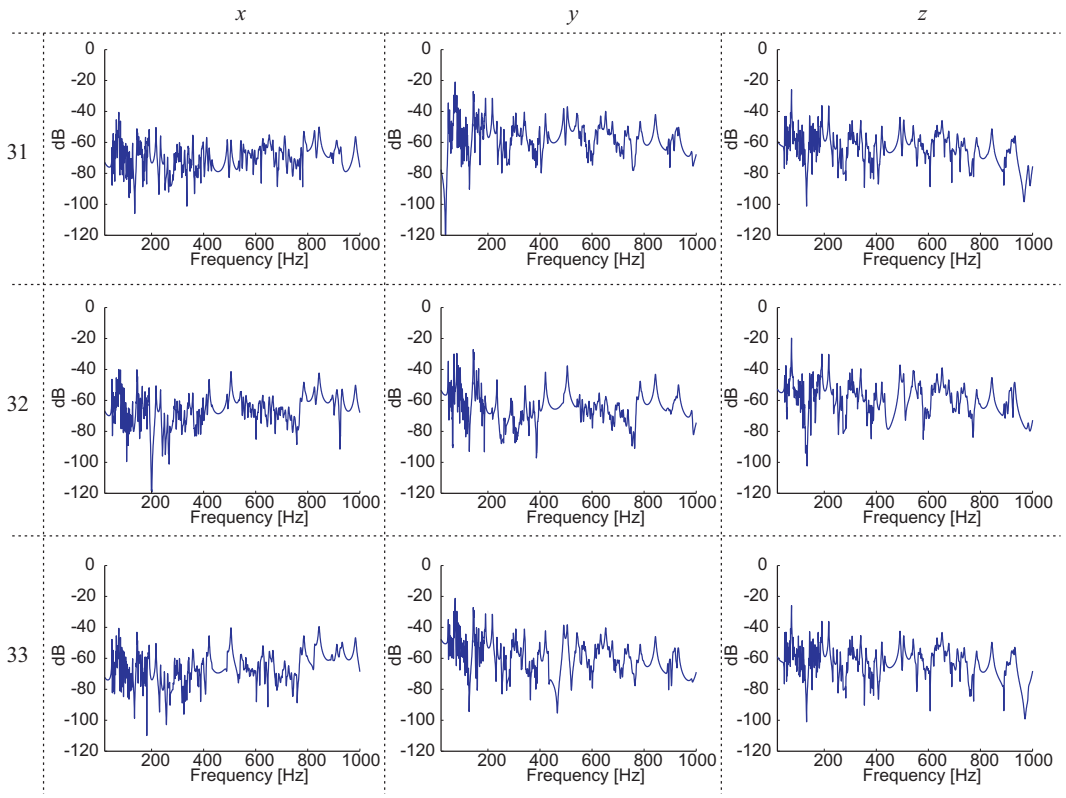

Figure 2.6: Magnitude of the mobilities at joints 31, 32 and 33 in directions x, y and z due to harmonic force of 1 N applied at joint 4 in y direction - dB ref. 1 m/Ns. (Numerical results)

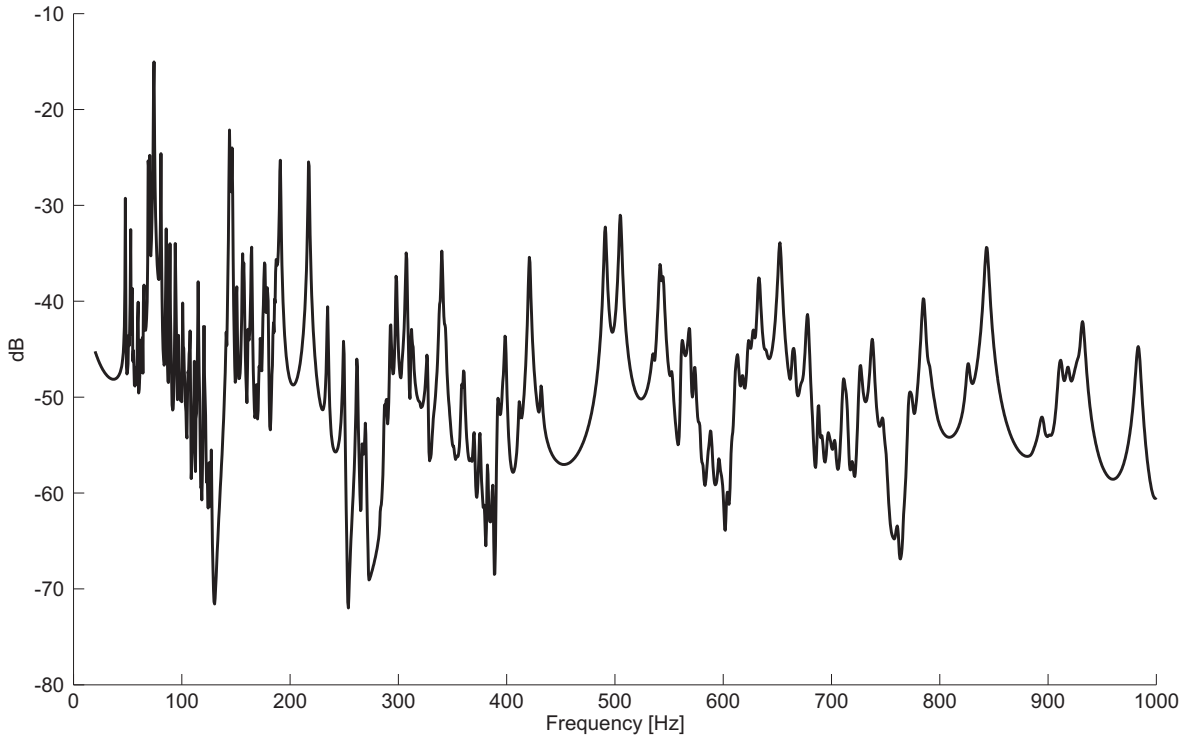

Figure 2.7: Cost function calculated using the dynamic stiffness method from the sum of the squared magnitude of velocities at joints 31, 32 and 33 in direction x, y, and z due to harmonic force of 1 N applied at joint 4, y direction - dB ref. 1 (m^2/Ns^2). (Numerical result).

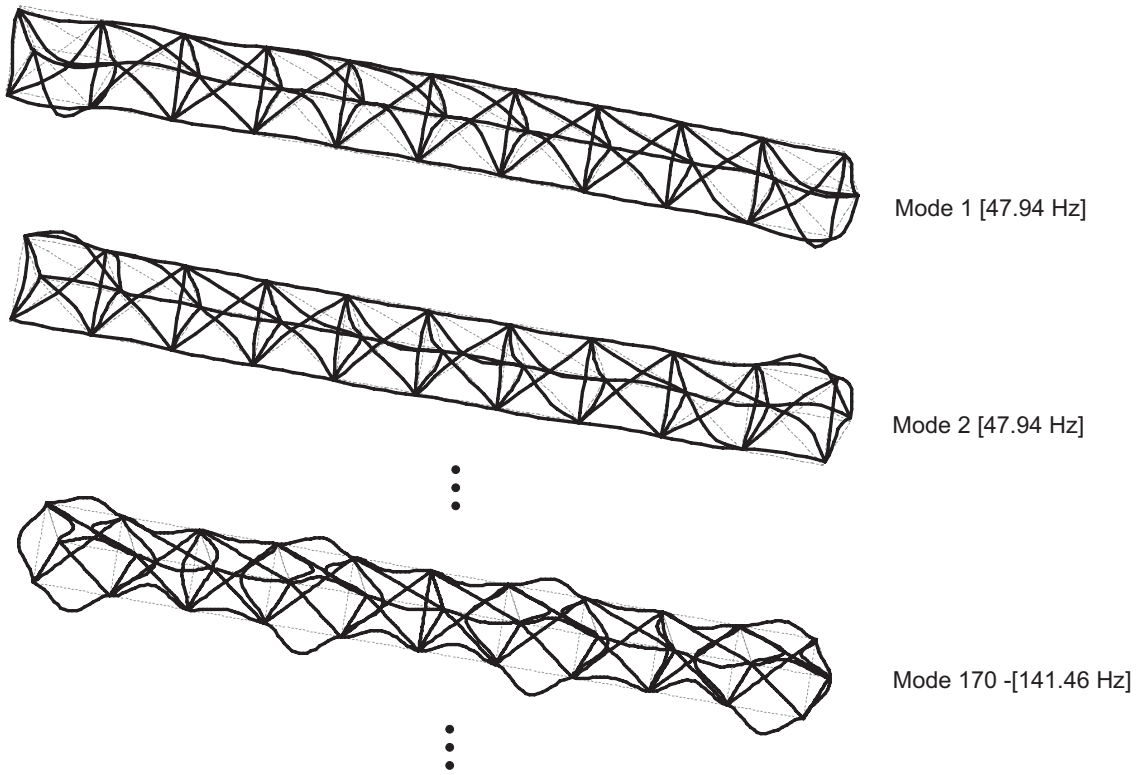

Figure 2.8: Examples of the mode shapes for the lattice structure using a complete beam model obtained by finite element method.

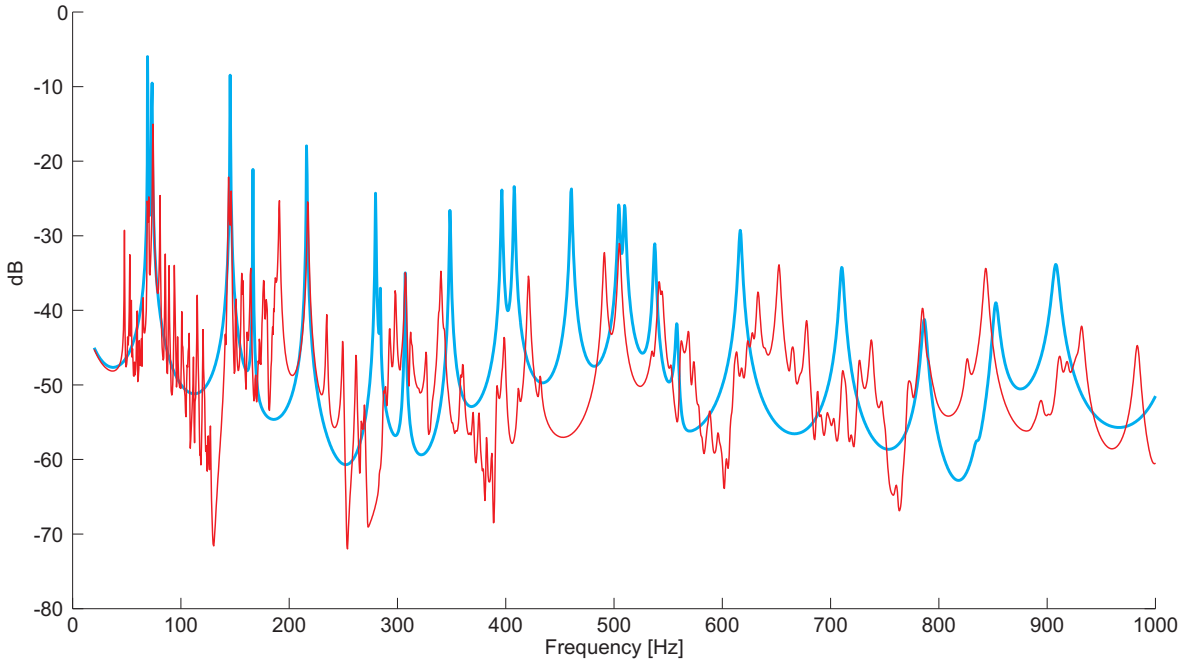

Figure 2.9: Comparison between the cost functions calculated using the complete beam model (thin line) and the finite element method considering only longitudinal motion of the structural members (thick line) due to harmonic excitation of 1 N applied in joint 4, y direction - dB ref. 1 m^2/Ns^2

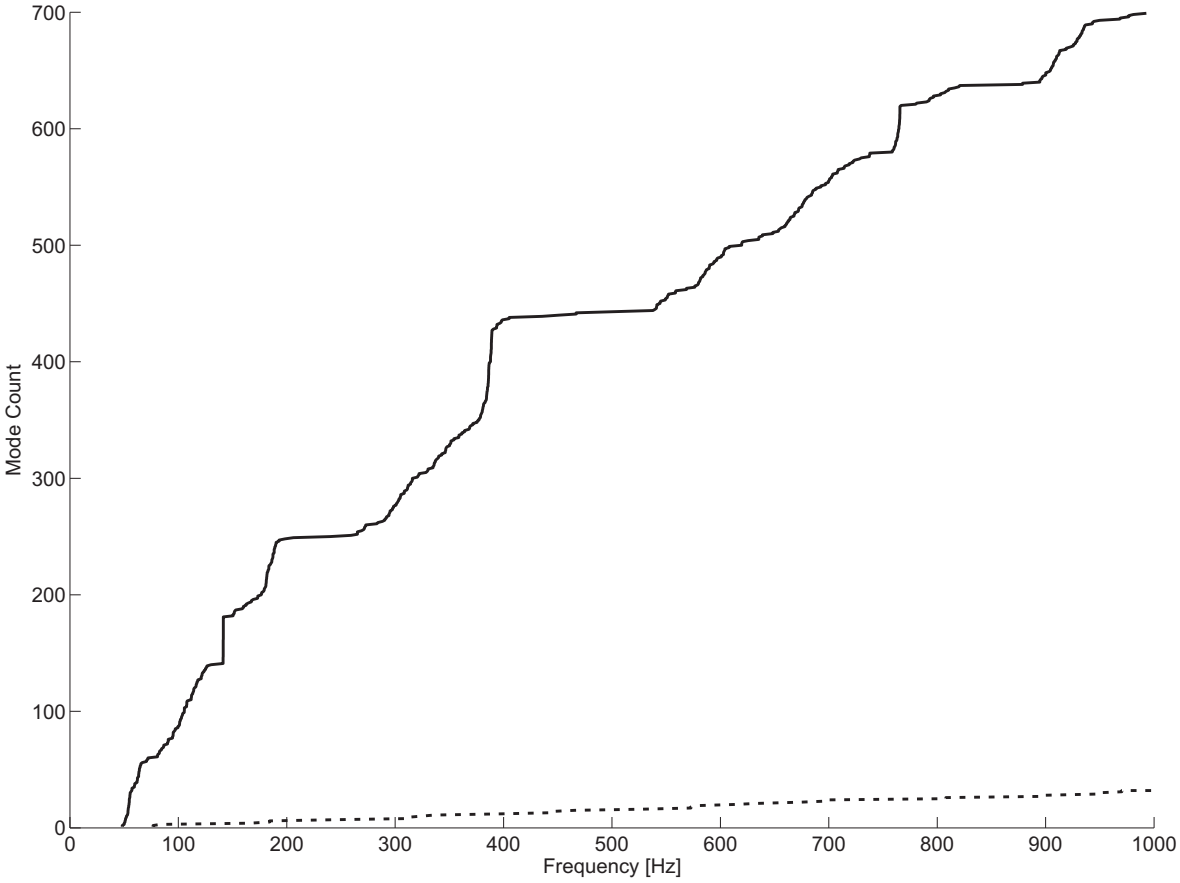

Figure 2.10: Mode count for the lattice structure in the frequency range 0 - 1 kHz. The thick line is for the lattice structure considering the complete member model (bending, longitudinal and torsional motion) and the dashed line if for the lattice structure considering only the longitudinal motion of the structural members. The results were obtained using the finite element software ANSYS.

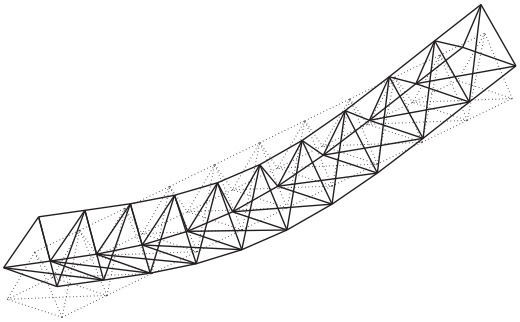

Bending - 76.7 Hz

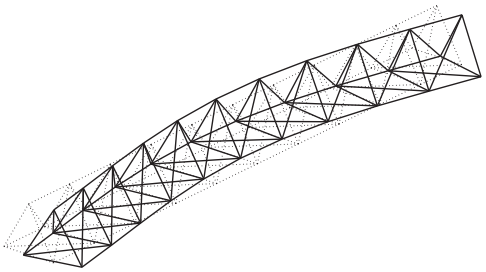

Bending - 76.7 Hz

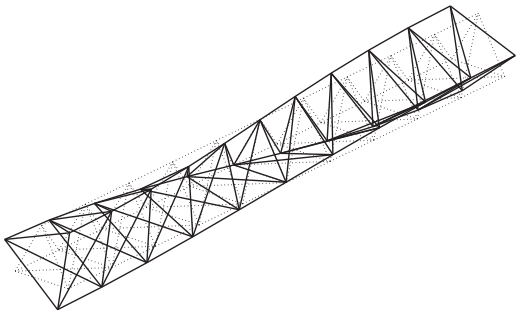

Torsion - 83.45 Hz

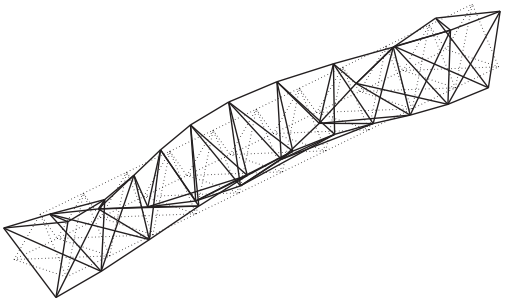

Torsion - 165.9 Hz

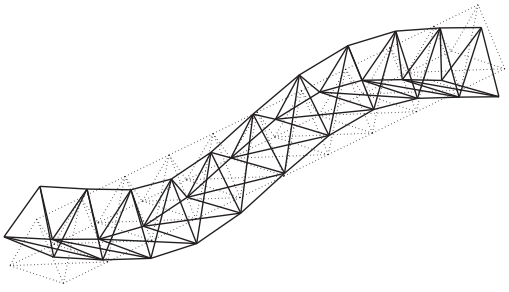

Bending - 184.3 Hz

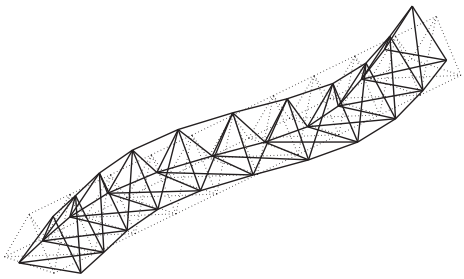

Bending - 184.3 Hz

Figure 2.11: Mode shapes and natural frequencies of the lattice structures obtained by the finite element method and considering only longitudinal deformation of the structure members.

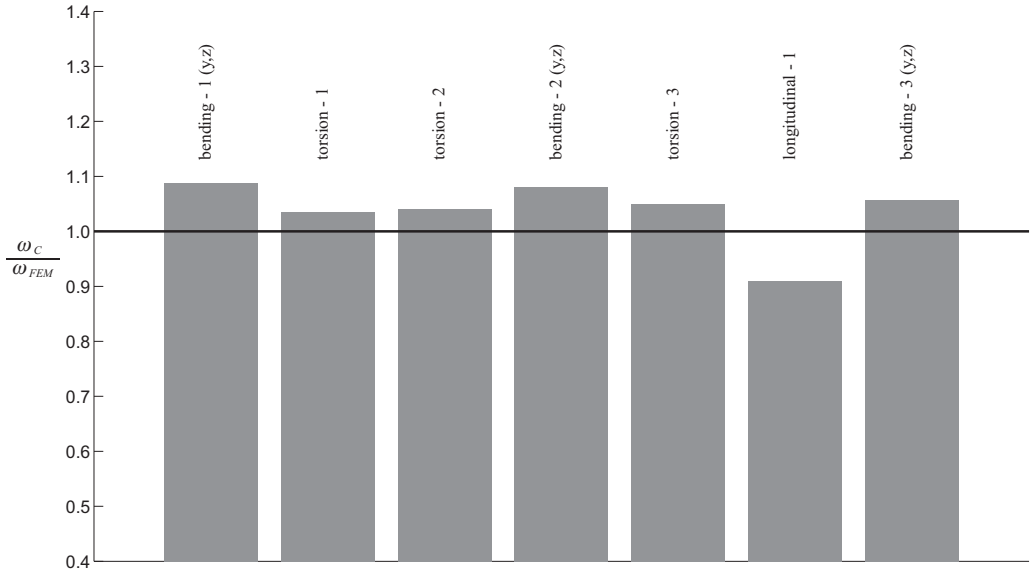

Figure 2.12: Differences in the natural frequencies between equivalent continuum model and finite element method (FEM).

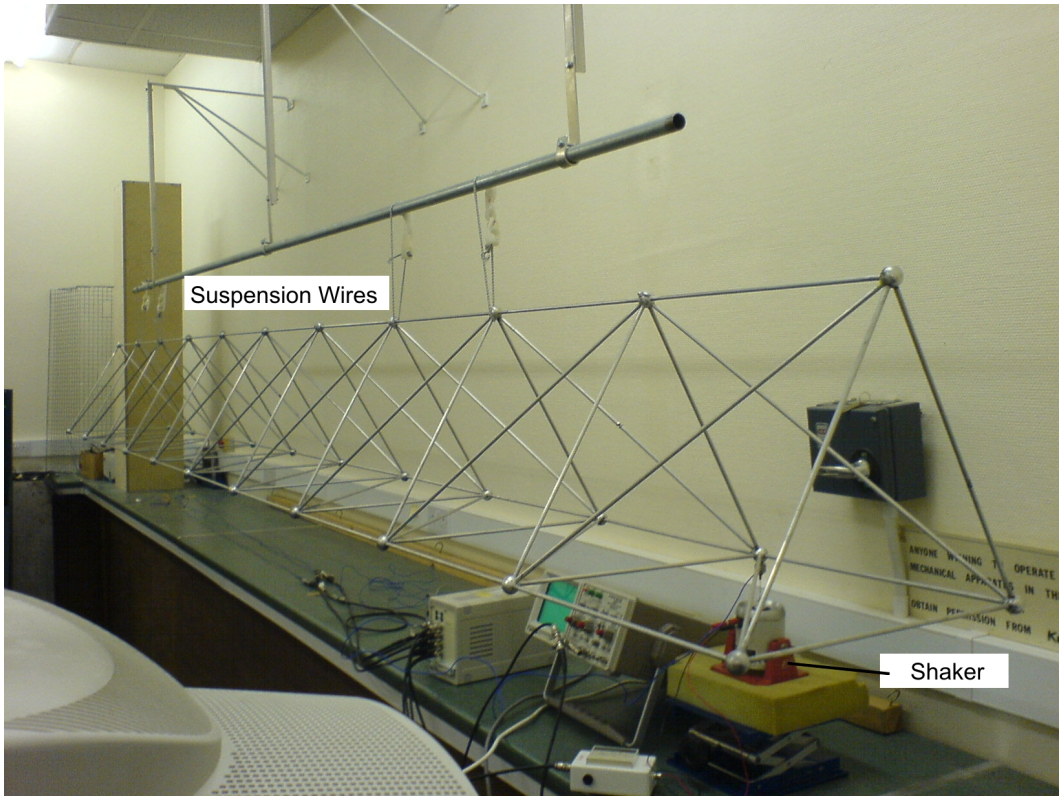

Figure 2.13: Lattice structure experimental rig. Structure is suspended by elastic wires with electromagnetic shaker attached to joint 4.

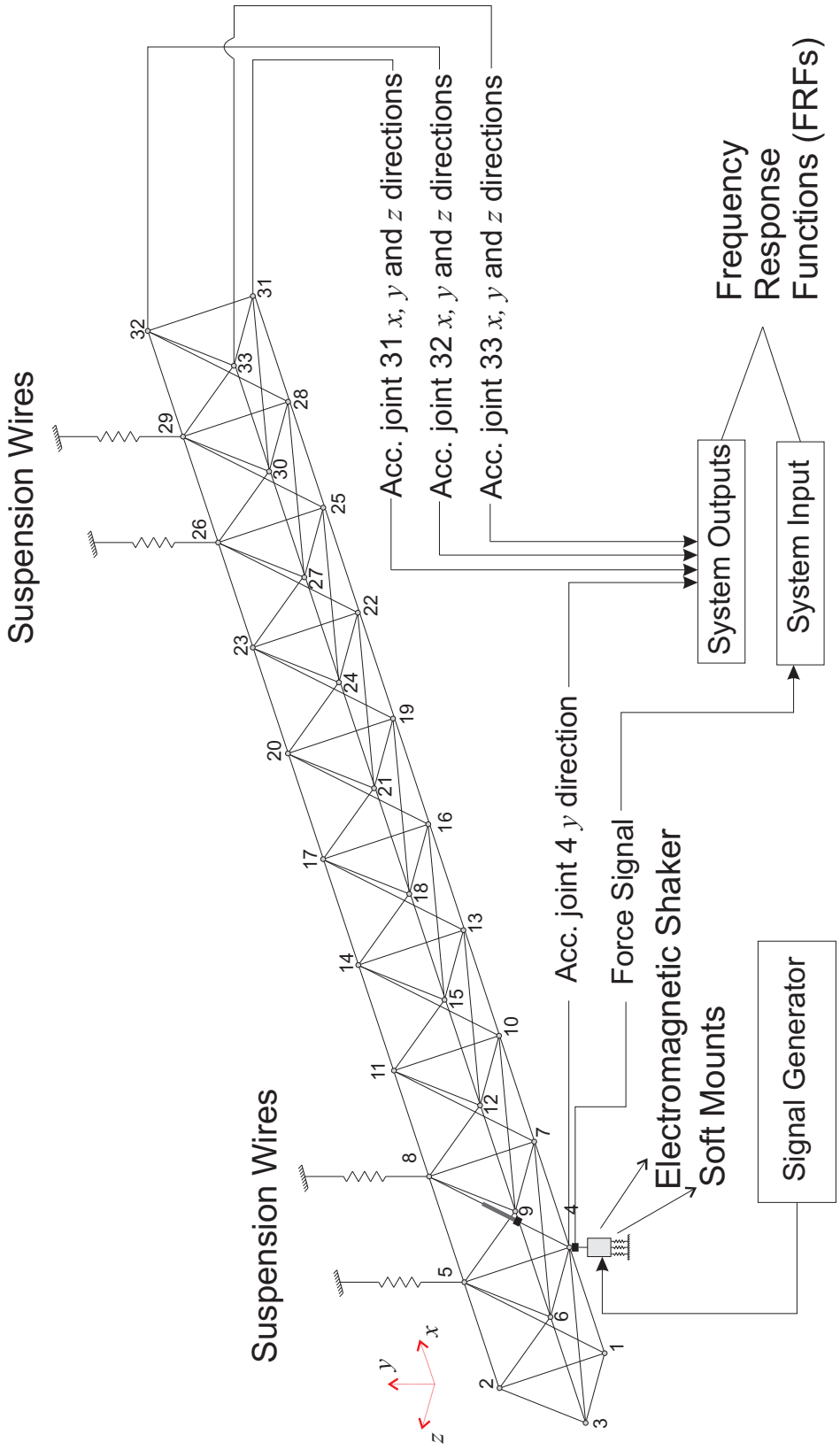

Figure 2.14: Scheme of the Frequency Response Measurement Experiment

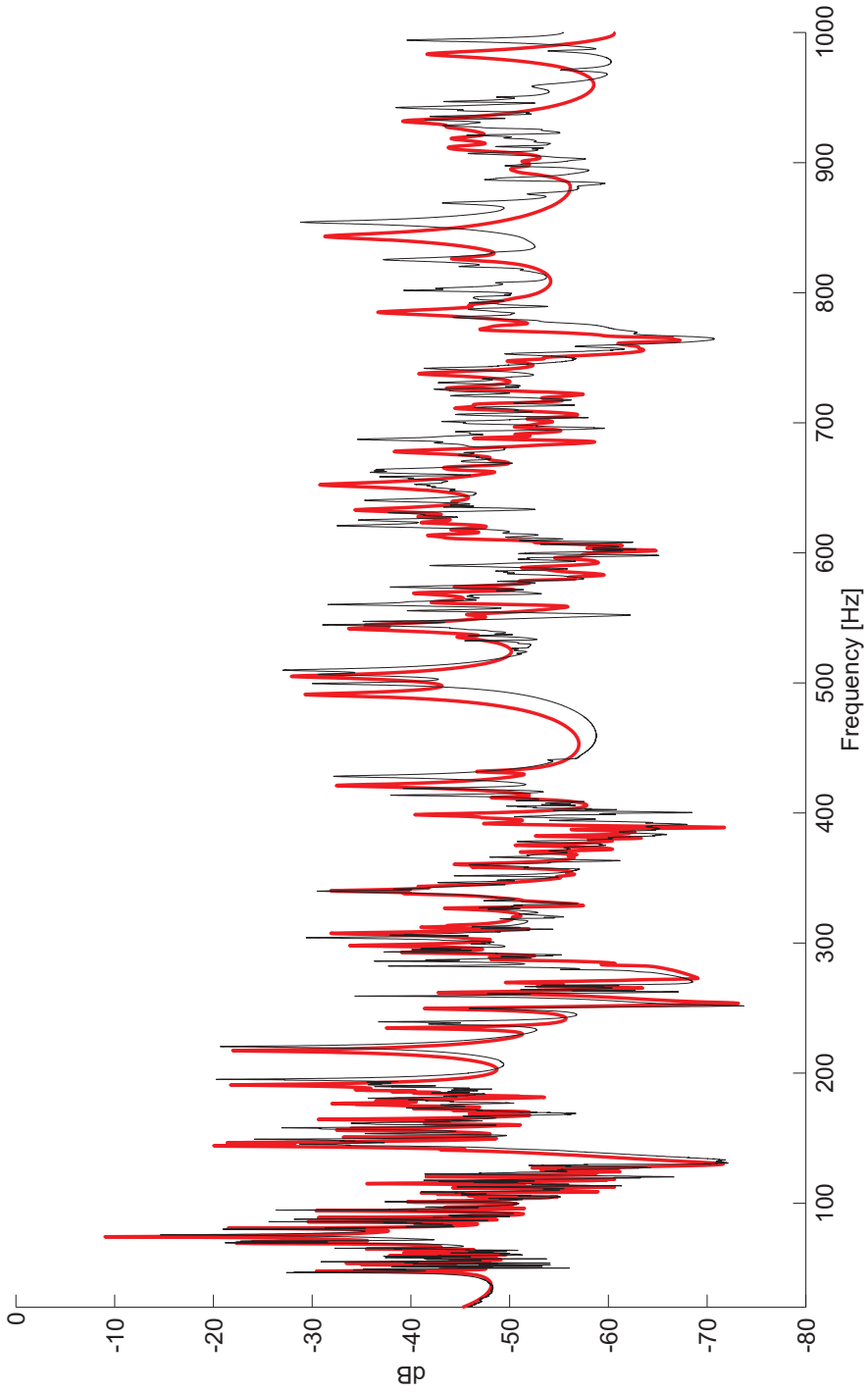

Figure 2.15: Cost Function given by equation 1.1. Thick line is the theoretical. Thin line is the experimental. dB ref. 1 m^2/N^2s^2

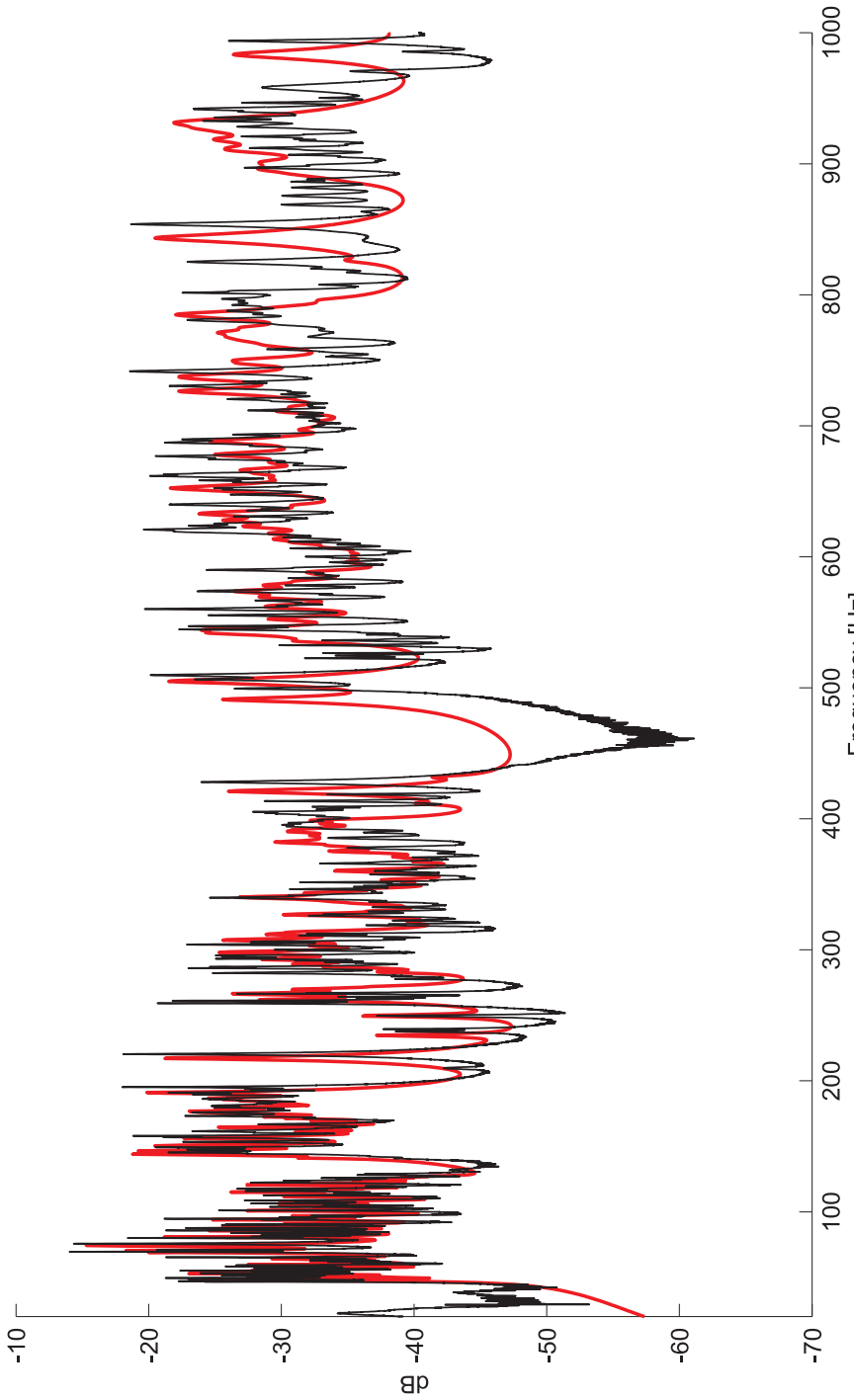

Figure 2.16: Input power. Thick line is the theoretical. Thin line is the experimental. dB ref. 1 W/N^2

Chapter Three

Dynamic analysis of lattice structures

3.1 Introduction

This chapter discusses the dynamic analysis of lattice structures where the interaction of short/long wavelength modes is considered. The aim of this chapter is to develop expressions relating the first short wavelength (SW) natural frequency with a long wavelength (LW) natural frequency. With these expressions it is possible to determine whether SWMs are present or not in a given frequency region. These expressions are used to identify the geometric parameters of the structure which control the frequency range were SW and LW modes occur. By changing some of these parameters, power flow and mechanisms of energy dissipation are analysed by numerical simulations. These results are used in chapters 4 and 5, in order to help determine the physical mechanisms of the different active control approaches applied to the structure considered in the thesis.

3.2 Dynamics of lattice structures

As discussed in chapters 1 and 2, the type of short wavelength modes considered in this thesis consists of bending of the structural members, while the long wavelength modes are assumed to occur due to longitudinal extension/compression of the members. The short wavelength behaviour of lattice structures has long attracted the attention of researchers, specifically in the area of mode localization. A significant contribution, explaining the localization phenomena in the area of solid-state physics, was published by Anderson in 1958 [31] and for this reason it is known as the *Anderson Localization* phenomenon. (The work of Anderson and Mott on localization and its application to solid-state physics was cited in their Nobel Prize of 1977 [90]). Later, mode localization has been studied in the field of structural dynamics and most of the literature in this area can be found in the survey paper of Ibrahim [91]. In structural dynamics, mode localization can either be beneficial, if for instance, short wavelength modes work like passive vibration absorbers, or they may not be beneficial, in terms of component

fatigue, since when localization occurs, stresses remain localized in regions near to the disturbance. This problem of localised fatigue has been discussed for the case of rotor blades in references [92, 93]. Undesirable consequences can also be expected in the performance and stability of active control systems. This topic is discussed in chapters 4 and 5 of this thesis.

Mode localization occurs in structures made up of weakly coupled components, where their equation of motion have closely spaced eigenvalues (similar natural frequencies), as in the case of nearly periodic lattice structures. Such systems have high sensitivity to small irregularities. The effect of disorder on mode localization is considered in references [33, 94, 95].

In most of the references concerning the topic of mode localization, the example of a coupled pendula system is used to explain the phenomenon; such a system is shown in figure 3.2. This system has N identical pendula all weakly coupled with their neighbours, with all the coupling springs being identical. Removing the coupling from all members, would results in all the pendula vibrating at the same natural frequency independently (since all pendula are identical). When a small coupling between each pendulum is allowed, the natural frequency of the pendula will be split in a cluster of frequencies all near to the resonance frequency of the pendula [96]. The vibration modes associated with these natural frequencies are given in reference [97], where it is stated that these modes are *extended* (all pendula move with approximately equal amplitudes) throughout the whole structure. If some changes are made in one of the pendula, such as changing the mass so that it has slightly different natural frequency, the mode will change. In this case, the mode is now localized around the individual pendulum and the coupling between pendula is not strong enough to produce *extended* modes in which all pendula contribute with more or less similar amplitudes. In this thesis, perturbation in the properties of the structural members are not considered, although understanding mode localization is important to explain some of the short wavelength behaviour observed in the structure.

To understand the influence of short and long wavelength behaviour, a ratio relating the first short wavelength natural frequency to a long wavelength natural frequency is defined. This involves the expression for the natural frequencies of Euler-Bernoulli

beams and an expression representing the approximate natural frequency of an equivalent continuum model. Using this ratio, simple expressions are derived using the lattice properties and geometric parameters to determine if short wavelength natural frequencies occur before or after a certain long wavelength natural frequency. This ratio is important as it can indicate if a model of a particular lattice structure should take into account bending of the structural members. If short wavelength modes occur only at high frequencies, a more simplified model can be used that considers only longitudinal motion of the members. This ratio can also be used to predict whether certain active control strategies can be implemented in a frequency range, as discussed in chapters 4 and 5. In the second part of this chapter the characteristics of power flow and energy dissipation are discussed, considering the different dynamic regimes of the lattice structure. This type of analysis has been considered in the work described in reference [70] where the influence of a passive vibration absorber is used to attenuate vibration in a grill-like structure. In reference [76] power was also used to investigate energy dissipation for different geometric configurations of a two-dimensional lattice structure.

3.3 The dynamics of short wavelength modes

The short wavelength modes (SWM) considered in this thesis involves only the bending of the structural members. As members are assumed to be long and thin, Euler-Bernoulli beam theory is used to obtain the expressions for the natural frequencies of the members. For any of the structural members, the bending natural frequency is given by [66]

$$\omega_i = \left(\frac{EI}{\rho S}\right)^{1/2} \frac{k_i^2 l^2}{l^2} \tag{3.1}$$

where, EI is the bending stiffness, ρS is the mass per unit length, l is the length of the member, k is the wavenumber and i is the mode number. In text books, the values for the wavenumber are given in the form $k_i l$, because for the i-th mode, $k_i l$ is a constant value for any length of beam. From equation 3.1 it can be seen that the natural frequency of the members is inversely proportinal to the square of the member

length. This means that longer structural members have lower fundamental natural frequency (assuming members with identical cross sections and material properties). For the three categories of structural members in the lattice structure considered in this thesis (as identified in figure 1.5) equation 3.1 is written as

$$\omega_{i,L} = \left(\frac{E_L I_L}{\rho_L S_L}\right)^{1/2} \frac{k_i^2 l_L^2}{l_L^2}, \text{ for longitudinal members} \tag{3.2}$$

$$\omega_{i,B} = \left(\frac{E_B I_B}{\rho_B S_B}\right)^{1/2} \frac{k_i^2 l_B^2}{l_B^2}, \text{ for batten members} \tag{3.3}$$

$$\omega_{i,D} = \left(\frac{E_D I_D}{\rho_D S_D}\right)^{1/2} \frac{k_i^2 l_D^2}{l_D^2}, \text{ for diagonal members} \tag{3.4}$$

where, the subscripts L, B and D refer to the longitudinal, batten and diagonal members, respectively. If the properties of the members and cross sectional areas are identical, then

$$EI = E_L I_L = E_B I_B = E_D I_D \tag{3.5}$$

$$\rho S = \rho_L S_L = \rho_B S_B = \rho_D S_D \tag{3.6}$$

using also the relationship $l_L = l_B = L_D/\sqrt{2}$, it is possible to relate the natural frequencies of the structural members as

$$\omega_{i,L} = \frac{(k_i l_L)^2}{(k_i l_B)^2}\omega_{i,B} = 2\frac{(k_i l_L)^2}{(k_i l_D)^2}\omega_{i,D} \tag{3.7}$$

In equation 3.7, for any of the types of structural members, the product (wavenumber $\times$ length) is constant for the *i-th* mode. For the most common boundary conditions; clamped, free, pinned and sliding, the value of $k_i l$ can be found in text books, such as [66, 63]. For other boundary conditions, the value of $k_i l$ is not known. If the boundary conditions of all the members are the same (as in the case of pin jointed structures) it would be possible to simplify the relationship of equation 3.7 to

$$\omega_{i,L} \approx \omega_{i,B} \approx 2\omega_{i,D} \tag{3.8}$$

if it is assumed that members have the same geometric and material properties, and $l_L = l_B = l_D/\sqrt{2}$. This shows that the system has two categories of natural frequencies. One associated with the longitudinal and batten members and other associated with the diagonal members. Because the boundary conditions of the members are not identical, these categories are actually groups of natural frequencies occurring in a small frequency range (clusters). These clusters of natural frequencies are similar to the behaviour described in the coupled pendula example. However, in this analysis, variation of the members' properties is not considered, but some mode localization behaviour can occur due to the different boundary conditions of the structural members. In the pendula example described previously, the system is considered to be infinite so that the ends of the system have no influence on the dynamic response, while the structure considered in this thesis is of finite extension. The members which are at the ends of the structure are more influenced by these conditions when compared to the members in the middle of the structure. This leads to a similar, but not identical form of mode localization of those in the pendula example. A short wavelength mode that is localized in the structure can be seen in figure 3.3, where larger displacements are concentrated in the bays at the ends of the structure; while in the figure 3.4 the vibration behaviour is similar in many members in the structure.

3.3.1 Numerical analysis of SWM

Using the nominal properties of the lattice structure considered in this thesis (shown below), numerical simulations were performed in order to identify the short wavelength behaviour of the structure.

- $EI = 5.5044$ Nm^2
- $\rho S = 0.0850$ kg/m
- $l_L = l_B = L_D/\sqrt{2}$ ($l_L = 0.45$ m)

Substituting these values into equation 3.1 and using the values of $k_1 l = \pi$ for pinned-pinned (p-p) beams and $k_1 l = 4.73004$ for clamped-clamped (c-c) beams [66], the diagonal members have p-p and c-c natural frequencies of 31.2 Hz and 70.7 Hz, respec-

tively. For the other members (longitudinal and batten) these frequencies are 62.4 Hz and 141.4 Hz, respectively. The values of natural frequencies for p-p and c-c boundary conditions, roughly indicate frequency regions where the lattice structure have several and indistinct group of member modes (clusters). These groups of modes repeat for each natural frequency of the structural members (every time that the length of the structural member is a multiple of the product $k_i l$). Some of the natural frequencies for the pinned-pinned and clamped-clamped boundary conditions were calculated using the system nominal properties and are shown in table 3.1 for the (longitudinal and batten) members and for the diagonal members where the natural frequency values are given in Hertz. Using some of the natural frequencies of table 3.1, frequency regions were plotted in figure 3.1 using rectangles identified as D or L, respectively diagonal members and longitudinal/batten members. The left hand side of these rectangles represents the p-p natural frequencies of the members. The right hand side of the rectangles represent the c-c natural frequencies of the members. For example, the rectangle D_1, has left hand side at frequency 31.2 Hz and right hand side at frequency 70.7 Hz, which corresponds to the first fundamental natural frequencies of a p-p and c-c diagonal member, respectively. Rectangle L_1, has left hand side at frequency 62.4 Hz and right hand side at frequency 141.5 Hz, which corresponds to the first fundamental natural frequencies of a p-p and c-c longitudinal (or batten) member. The rectangle number D_2 represent the second fundamental natural frequency for the diagonal members, and so on. In the same figure, the natural frequencies of the structure were calculated by the finite element method, using the commercial software ANSYS. In this analysis members were divided in 20 elements each. The finite element used was the three-dimensional elastic beam, that has six degrees of freedom per each node. The natural frequencies are plotted in the frequency range 0 - 1 kHz and are represented by the thin vertical lines. It can be seen that the rectangles (1, ..., 8) roughly bound the various clusters of natural frequencies. For example, rectangle 1, bounds all the natural frequencies associated to the first bending mode of the diagonal members. These results have been used to determine an approximate expression for the first SW natural frequency. Assuming that this first natural frequency is bounded by first p-p and c-c natural frequencies of a diagonal member, it is reasonable to use an average for these

two boundary conditions given by

$$\omega_1 = \frac{\omega_{\text{p-p}} + \omega_{\text{c-c}}}{2} = \left(\frac{EI}{\rho S}\right)^{1/2} \frac{k_{\text{p-p}}^2 + k_{\text{c-c}}^2}{2} \tag{3.9}$$

where, equation 3.9 was obtained empirically. In the expression for the approximate value for the first short wavelength natural frequency for the structure considered in this thesis is 51 Hz which is not much different from the value calculated from a model obtained by dynamic stiffness method (48.3 Hz) and the value obtained by the experimental test (48 Hz) given in chapter 2. The average product wavenumber × length can then be expressed for the first mode as

$$\frac{(\overline{kl})^2}{l^2} = \frac{(kl)_{\text{p-p}}^2 + (kl)_{\text{c-c}}^2}{2l^2} \approx \frac{16.12}{l^2} \tag{3.10}$$

where $(kl)_{\text{p-p}} = \pi$ and $(kl)_{\text{c-c}} = 4.73004$. The value $(kl)^2 = 16.12$ is used in other sections of this chapter.

3.4 The dynamics of long wavelength modes

The results of figure 3.1 and also the plot of mode count as a function of frequency in figure 2.10 (chapter 2) show that the lattice structure has several short wavelength modes in the frequency range 0 - 1 kHz ($\sim$ 700 modes). Identifying a long wavelength mode in these circumstances can be quite difficult. This is because it is necessary to perform a numerical modal analysis and search among many short wavelength modes. If short wavelength modes occur at frequencies closed to the frequencies of a long wavelength mode, there is a high possibility that the dynamic interaction between SWM/LWM will result in a hybrid mode, as shown in 3.5 (where this mode is a combination of a long wavelength torsional mode with bending of the structural members). Alternatively a LWM may vanish due to the destructive interference caused by the SWM. For these reasons, there will only be a pure LWM if SWMs do not interact with them at frequencies close to the LWM natural frequency. The approach used to calculate these "hypothetical" LW natural frequencies, is to use the equivalent continuum model described in chapter 2 (the word hypothetical is used because it is not certain that there exists pure LW modes). The natural frequencies for the equivalent continuum model

for the lattice structure are given in the table 2.2 of chapter 2 and repeated here for convenience

$$(\omega_i)_{\mathrm{C}} = \frac{l_B}{(12+6\sqrt{2})^{1/2}(1+C_s/m^2)^{1/2}} \left(\frac{E}{\rho}\right)^{1/2} (k_i)_{\mathrm{C}}^2 \text{ , for bending motion} \tag{3.11}$$

$$(\omega_i)_{\mathrm{C}} = \frac{i\pi}{ml_L(2+\sqrt{2})^{1/2}} \left(\frac{E}{\rho}\right)^{1/2} \text{ , for longitudinal motion} \tag{3.12}$$

$$(\omega_i)_{\mathrm{C}} = \frac{i\pi}{2ml_L(5+4\sqrt{2})^{1/2}} \left(\frac{E}{\rho}\right)^{1/2} \text{ , for torsional motion} \tag{3.13}$$

Using equations 3.11-3.13 the long wavelength natural frequencies are plotted in figure 3.6. In this figure the longer and thicker vertical lines represent the long wavelength natural frequencies and the thin and short vertical lines are the natural frequencies of the lattice structure calculated using the finite element method as shown in figure 3.1. It can be seen in figure 3.6 shows that most of the LWMs are overlapped by the SWMs, what can result in destructive interference of the LWM as discussed above. An important result from figure 3.6 is that SWMs occur at lower frequencies than the first LWM for this lattice structure.

3.5 *Relating short and long wavelength modes*

The objective of this section is to determine the conditions for which SW natural frequencies occur before or after a certain *i-th* LW natural frequency. The *i-th* LW natural frequency can be a bending, torsion or a longitudinal LWM. Consider the ratio β_i of two natural frequencies, the first SW natural frequency $(\omega_1)_D$ (which is assumed to occur in the diagonal members, hence the subscript D) and the *i-th* LW natural frequency $(\omega_i)_{\mathrm{C}}$ given by

$$\beta_i = \frac{(\omega_1)_D}{(\omega_i)_{\mathrm{C}}} \tag{3.14}$$

The ratio β_i is illustrated in figure 3.7, where it can be seen for values of $\beta_i > 1$, the first SWM occurs at frequencies greater than that of the *i-th* LWM, for values of $\beta_i = 1$,

the first SWM occurs at the same frequency as the LWM and for values of $\beta_i < 1$, the first SWM occurs at frequencies smaller than the LWM. Using the expression for the natural frequency of the SWM for a diagonal member given in equation 3.4

$$\omega_D = \left(\frac{EI}{\rho S}\right)^{1/2} \frac{((k_1)_D l_D)^2}{2l_L^2} \tag{3.15}$$

where, $(k_1)_D$ is the wavenumber for the fundamental natural frequency of a diagonal member. Moreover, $l_L = l_B = l_D/\sqrt{2}$ has been assumed to give the factor 2 in the denominator of equation 3.15. The term $(\omega_i)_{\mathrm{C}}$ can be either one of the expressions of equations 3.11-3.13. The ratio β_i is investigated for these expressions in the following sections.

3.5.1 The ratio for the i-th bending LW natural frequency

Combining equations 3.11, 3.14 and 3.15 the ratio β_i for the *i-th* LW bending mode is determined to be

$$\beta_i = \left[\left(\frac{EI}{\rho S}\right)^{1/2} (k_1)_D^2\right] \left[\frac{(12+6\sqrt{2})^{1/2}(1+C_s/m^2)^{1/2}}{l_B (k_i)_{\mathrm{C}}^2} \left(\frac{\rho}{E}\right)^{1/2}\right] \tag{3.16}$$

where the terms inside the left hand bracket correspond to $(\omega_1)_D$ and the terms in the right hand bracket corresponds to $1/(\omega_i)_C$. As a first step in the simplification of equation 3.16 it is possible to cancel out the material properties E and ρ to give

$$\beta_i = \left(\frac{I}{S}\right)^{1/2} \frac{(12+6\sqrt{2})^{1/2}(1+C_s/m^2)^{1/2}}{l_B} \frac{(k_1)_D^2}{(k_i)_{\mathrm{C}}^2} \tag{3.17}$$

The ratio of wavenumber on the far right of equation 3.17 can be re-written as

$$\frac{(k_1)_D^2}{(k_i)_{\mathrm{C}}^2} = \frac{((k_1)_D l_D)^2}{2l_L^2} \frac{(ml_L)^2}{((k_i)_{\mathrm{C}} ml_L)^2} = \frac{((k_1)_D l_D)^2}{((k_i)_{\mathrm{C}} ml_L)^2} \frac{m^2}{2} \tag{3.18}$$

where the relationship $l_D = \sqrt{2} l_L$ is used and $((k_1)_D l_D)$ is not known due to the boundary condition of the structural members. For simplicity, the value of $((k_1)_D l_D)$ used is that found from the average between the p-p and c-c values for the first natural frequency discussed previously in this chapter. This value is given by $(\overline{(k_1)_D l_D})^2 \approx 16.12$. The term $(1+C_s/m^2)^{1/2}$ is also modified to

$$\left(1+\frac{C_s}{m^2}\right)^{1/2}=\frac{(m^2+C_s)^{1/2}}{m} \tag{3.19}$$

Equation 3.17 can then be written as

$$\beta_i=\frac{m}{l_B}\left(\frac{I}{S}\right)^{1/2}\frac{\left(12+6\sqrt{2}\right)^{1/2}}{2}\left(m^2+C_s\right)^{1/2}\frac{\left(\overline{(k_1)_D l_D}\right)^2}{\left((k_i)_C m l_L\right)^2} \tag{3.20}$$

Equation 3.20 can be divided into three terms, the first term $\frac{m}{l_B}\left(\frac{I}{S}\right)^{1/2}$ consists of the dimensional properties of the structure; the term $(12+6\sqrt{2})^{1/2}(\overline{(k_1)_D l_D})^2/2$, is constant and also introduces some numerical uncertainties in the value of β_i, due to the estimation of the term $(\overline{(k_1)_D l_D})$. The last term $(m^2+C_s)^{1/2}/((k_i)_C m l_L)^2$ depends upon the mode shape number i. For the free-free boundary condition of the lattice structure, the values of $((k_i)_C m l_L)$ for the *i-th* mode are given in reference [66] as

i	1	2	3	4	5	6, 7, ...
$(k_i)_C m l_L$	4.73004	7.85320	10.9956	14.1372	17.2788	$(2i+1)\pi/2$

The shear correction factor C_s also depends upon the mode shape, and for this structure it is given by [88]

$$C_s=i^2\pi^2\frac{\left(1+2\sqrt{2}\right)}{3} \tag{3.21}$$

The interest now is to determine the condition for SWMs to occur before the *i-th* LWM. This can be done by setting $\beta_i>1$, so using equation 3.20 this inequality can be written as

$$\left(\frac{I}{S}\right)^{1/2}\frac{1}{l_B}>\frac{2}{m(m^2+C_s)^{1/2}(12+6\sqrt{2})^{1/2}}\frac{((k_i)_C m l_L)^2}{(\overline{(k_1)_D l_D})^2} \tag{3.22}$$

The term $(I/S)^{1/2}$ relates the second moment of area with the cross section area of the members. For solid circular cross sections $(I/S)^{1/2}=d/4$, where d is the diameter of the cross section. For hollow circular cross sections, $(I/S)^{1/2}=\sqrt{d_2^2+d_1^2}/4$, where d_2 and d_1 are the external and internal cross section diameters, respectively. It is then possible to write equation 3.22 as

$$\frac{\Delta}{l_B} > \frac{8}{m(m^2+C_s)^{1/2}(12+6\sqrt{2})^{1/2}} \frac{((k_i)_C m l_L)^2}{(\overline{k_D l_D})^2} \tag{3.23}$$

where, $\Delta = d$ for members with solid cross sections and $\Delta = \sqrt{d_2^2 + d_1^2}$ for members with hollow cross sections. If equation 3.23 is now inverted to give

$$\frac{l_B}{\Delta} < \frac{m(m^2+C_s)^{1/2}(12+6\sqrt{2})^{1/2}}{8} \frac{(\overline{(k_1)_D l_D})^2}{((k_i)_C m l_L)^2} \tag{3.24}$$

where the term l_B/Δ can be defined as the slenderness ratio. If equation 3.24 is numerically simplified, using the values of $((k_i)_C m l_L)$ given in reference [66] for the first four mode shapes, and making $(\overline{(k_1)_D l_D})^2 = 16.12$, the slenderness ratio for the first four long wavelength bending natural frequencies are given in table 3.2. The values of the slenderness ratio are plotted in figure 3.8 as a function of the number of bays in the lattice structure for the first four long wavelength bending modes of the structure.

3.5.2 The ratio for the i-th longitudinal LW natural frequency

In a similar way to the expressions developed in the previous section, the ratio β_i is calculated for the *i-th* longitudinal LWM. Combining equations 3.12, 3.14 and 3.15 the ratio β_i is defined for the *i-th* LW longitudinal mode as

$$\beta_i = \left[\left(\frac{EI}{\rho S}\right)^{1/2} k_D^2\right] \left[\frac{m l_L (2+\sqrt{2})^{1/2}}{i\pi} \left(\frac{\rho}{E}\right)^{1/2}\right] \tag{3.25}$$

where, the terms in the left brackets correspond to the short wavelength natural frequency $(\omega_1)_D$ of a diagonal member. By cancelling out the material properties and setting $(k_1)_D^2 = (\overline{(k_1)_D l_D})^2/2l_B^2$, where $(\overline{(k_1)_D l_D})$ is once again the estimated value given in the previous section. Equation 3.25 is then simplified to

$$\beta_i = \left(\frac{I}{S}\right)^{1/2} \frac{m l_L (2+\sqrt{2})^{1/2}}{2i\pi} \frac{(\overline{(k_1)_D l_D})^2}{2l_B^2} \tag{3.26}$$

Equation 3.26 can also be divided in three distinct terms, as

$$\beta_i = \left[\left(\frac{I}{S}\right)^{1/2} \frac{m}{l_B}\right] \left[\frac{(2+\sqrt{2})^{1/2}(\overline{(k_1)_D l_D})^2}{2\pi}\right] \frac{1}{i} \tag{3.27}$$

where the term in the left hand bracket consists of geometrical parameters, the middle term inside the brackets is a constant value and may introduce errors in the expression due to the estimation of $(\overline{(k_1)_D l_D})$. The last term is the inverse of the mode number. By assuming values of $\beta_i > 1$, equation 3.27 is written as

$$\left(\frac{I}{S}\right)^{1/2} \frac{1}{l_B} > \frac{2i\pi}{m(2+\sqrt{2})^{1/2}(\overline{(k_1)_D l_D})^2} \tag{3.28}$$

and equation 3.28 can be inverted to give the expression in terms of the slenderness ratio l_B/Δ

$$\frac{l_B}{\Delta} < \frac{m(2+\sqrt{2})^{1/2}(\overline{(k_1)_D l_D})^2}{8i\pi} \tag{3.29}$$

where, Δ is defined previously. If 3.29 is numerically simplified, the slenderness ratio for the first four long wavelength bending natural frequencies are given in table 3.4. These values for the slenderness ratio are plotted in the figure 3.9 as a function of the number of bays in the lattice structure for the first four long wavelength longitudinal modes of the structure. The dashed line corresponds to the Euler-Bernoulli beam theory limit for the first bending mode shape as discussed in reference [63].

3.5.3 The ratio for the i-th torsional LW natural frequency

The ratio β_i can be found in a similar way to the expressions in the last section for the longitudinal LWM. Comparing the two expressions for the long wavelength natural frequency $(\omega_i)_C$ for longitudinal and torsional motion (equations 3.12 and 3.13), the only differences are the terms $(2+\sqrt{2})^{1/2}$ and $2(5+4\sqrt{2})^{1/2}$. Thus, the ratio β_i for the *i-th* torsional LW natural frequency is given by

$$\beta_i = \left[\left(\frac{I}{S}\right)^{1/2} \frac{m}{l_L}\right] \left[\frac{2(5+4\sqrt{2})^{1/2}(\overline{(k_1)_D l_D})^2}{2\pi}\right] \frac{1}{i} \tag{3.30}$$

and the slenderness ratio for the long wavelength torsional motion of the system is given by

$$\frac{l_B}{\Delta} < \frac{m(5+4\sqrt{2})^{1/2}(\overline{(k_1)_D l_D})^2}{4i\pi} \tag{3.31}$$

If 3.31 is numerically simplified, the slenderness ratio for the first four long wavelength bending natural frequencies are given in table 3.3. These values for the slenderness ratio are plotted in figure 3.10 as a function of the number of bays in the lattice structure. The slenderness ratio is plotted for the first four long wavelength longitudinal modes of the structure. The dashed line represents the Euler-Bernoulli beam theory limit for the first beam mode.

Figure 3.11 shows the slenderness ratio for the first LWMs for bending, torsion and longitudinal motion of the lattice structure as a function of the number of bays in the structure. The nominal slenderness ratio for the structural members is also identified. Clearly for the 10 bay structure considered in this thesis, the right hand side of equation 3.24 is less than l_B/Δ for all i, so that β_i is less than one. This result is also in accordance to the results of figure 3.6 where the SWM occur first then the LWM.

3.6 Factors controlling the SW and LWMs

In the expressions for the ratio β_i as in equation 3.20, it can be seen that the ratio β_i depends upon two terms; the mode shape number of the LWM and the geometric properties of the structure. These geometric properties are the length of the batten (or longitudinal members), the variable defining the cross sectional area Δ, and the number of bays, m. It is clear that modifying the number of bays of the structure will have a large influence on the LW natural frequencies as they change with the inverse of the number of bays in the structure. Changing the number of bays in the structure influences the SW natural frequencies slightly, because the boundary conditions of the members are slightly modified. This has been discussed in the introduction to this chapter, where the ends of the structure may have an effect on the boundary conditions of the structural members. Changing the parameter Δ, which is related to the cross section of the members, influences only the SW natural frequencies. This can be seen in equations 3.11-3.13, where these expressions have no dependency on the cross section of the members. The other parameter influencing the *slenderness ratio* is the length of the members. By changing the length of batten members, for instance, both SWM and LWM can be affected (note, the relationship $l_L = l_B = l_D/\sqrt{2}$ is assumed). Because in most cases, the length of the structure is a fixed parameter, modifying the

number of bays in the structure is only possible by changing the length of the structural members. The parameter Δ, however, can be used for tailoring the spectrum of SWM. It is usually possible to change the stiffness to weight ratio by changing a solid circular cross section to a hollow circular cross section. The parameter Δ changes from d to $\sqrt{d_2^2 + d_1^2}$. The practical result of this modification is the possibility to increase the bending stiffness of the members without addition of weight, if the area of the solid and hollow circular cross sections remain equal (a change in the volume of the members is, however, inevitable).

To demonstrate the influence of these parameters on the dynamics of the structure, numerical simulation are presented. In figure 3.12, the natural frequencies of the structure are represented by the dots in the frequency range 0 - 1 kHz. These natural frequencies were calculated by the finite element method using the three-dimensional *beam* element available in the commercial software ANSYS dividing the structural members into 20 element each. These natural frequencies were calculated for different values of the non-dimensional ratio $(I/l_B^2 S)$ and are shown as normalized values by the nominal ratio $(I/l_B^2 S) = 1.2445 \times 10^{-5}$. It can be seen that as the ratio $(I/l_B^2 S)$ increases, some of the dots representing the natural frequencies are shifted in a fashion proportional to the square root of this ratio (as $\beta \propto (I/l_B^2 S)^{1/2}$), in this case, mainly the SW natural frequencies are changed. The LW natural frequencies, however, remain nearly unchanged. Some differences in the LW natural frequencies are expected when SWM occur at frequencies close to the LWMs. The shifting effect of the SWM can also influence the structural responses to disturbance forces. This is demonstrated for the cost function considered in this work, for a disturbance force applied at joint 4, in the y direction. The sum of squared linear velocities at joints 31, 32 and 33 was calculated for different values of the ratio $(I/l_B^2 S)$ using the dynamic stiffness method. The sum of these cost functions over the frequency range 20 Hz - 1 kHz (with 1 Hz frequency resolution) are plotted in figure 3.13 as a function of the ratio $(I/l_B^2 S)$ where the values are given in dB. As can be seen in the results of figure 3.13, the sum of the cost function varies by up to 3.5 dB, for the values of $(I/l_B^2 S)/(I/l_B^2 S)_{\text{nominal}}$ varying between 1 and 25. The conclusion is that although the structural response can be quite different when SWM are shifted in frequency, the overall level of the structure response

for this frequency range (20 Hz - 1 kHz) does not change by very much.

3.7 The analysis of power in the lattice structure

In this section the mechanisms of energy dissipation and power flow in the structural members are considered. The results are used in the following chapters to help determine the physical mechanisms of the two forms of active control considered in this thesis; feedforward and feedback control. This is done using the expression for power flow given in appendix D, and the method described in the chapter 2, where the power at any position in the structure is calculated by

$$p(\omega) = \frac{1}{2}\mathrm{Re}\left\{F(\omega)V^*(\omega)\right\} \tag{3.32}$$

where $p(\omega)$ is the power at circular frequency ω and F and V are the internal force and the velocity. The symbol $()^*$ denotes the complex conjugate. Dropping the angular frequency symbol ω for simplicity, the power flowing at ends **0** and **1** of the *n-th* structural member is given in terms of vectors by

$$\mathbf{p}_n(\mathbf{0}) = \frac{1}{2}\mathrm{Re}\left\{\mathbf{f}_n(\mathbf{0}) \times \mathbf{v}_n^*(\mathbf{0})\right\}, \mathbf{p}_n(\mathbf{1}) = \frac{1}{2}\mathrm{Re}\left\{\mathbf{f}_n(\mathbf{1}) \times \mathbf{v}_n^*(\mathbf{1})\right\} \tag{3.33}$$

where the symbol $\times$ means the multiplication of element by element of the vectors $\mathbf{f}$ and $\mathbf{v}$. The power dissipated in the *n-th* member is found by the principle of conservation of energy as

$$\mathbf{p}_n(\mathrm{diss}) = -(\mathbf{p}_n(\mathbf{0}) + \mathbf{p}_n(\mathbf{1})) \tag{3.34}$$

where for a passive member, the vector $\mathbf{p}_n(\mathrm{diss})$ has only negative elements. In an expanded form it can be written as

$$\mathbf{p}_n^T(\mathrm{diss}) = \left[\begin{array}{cccccc} p_{\mathrm{long}}(\mathrm{diss}) & p_{\mathrm{bend},y}(\mathrm{diss}) & p_{\mathrm{bend},z}(\mathrm{diss}) & p_{\mathrm{tors}}(\mathrm{diss}) & p_{\mathrm{bend},\theta y}(\mathrm{diss}) & p_{\mathrm{bend},\theta z}(\mathrm{diss}) \end{array}\right] \tag{3.35}$$

where $p_{\mathrm{long}}(\mathrm{diss})$ is the power dissipated by the longitudinal motion of the member, $p_{\mathrm{tors}}(\mathrm{diss})$ is the power dissipated by the torsional motion of the members and $p_{\mathrm{bend}}(\mathrm{diss})$

is the power dissipated by bending motion of the members which can occur in two planes (due to the product of shear force × linear velocity and bending moment × angular velocity). If these elements are summed, the result is the total power dissipated in the *n-th* structural member $p_n(\text{diss})$. If the dissipated power in all structural members are summed, by the principle of conservation of energy, the result should be equal (in magnitude) to the power input into the system as

$$p(\text{in}) = \sum_n |p_n(\text{diss})| \tag{3.36}$$

Using the model obtained by the dynamic stiffness method described in the chapter 2, and by applying a harmonic force with magnitude 1 N at joint 4, in the y direction, the power input and the total power dissipated calculated by equation 3.36 are plotted in figure 3.14 in the frequency range 20 Hz - 1 kHz. The same results are also plotted in the figure 3.15 given in dB (where the power dissipated has been plotted as $-p(\text{diss})$ to fit into the dB scale). The results in these two figures show that the two methods for calculating the power dissipation in the members is consistent, as the results agree well. Considering also the results of figure 2.16, where the input power calculated numerically by the dynamic stiffness method has been compared with experimental results, leads to the conclusion that this methodology can predict the mechanisms of energy dissipation and power flow in the structure with a reasonably degree of confidence. Using equation 3.35, it is also possible to categorise the mechanisms of power dissipation into three types; the power dissipated by longitudinal, torsional and bending motion. The first two are the first and the fourth elements of the vector in equation 3.35, while the power dissipated by bending is given by

$$p_{\text{bend}}(\text{diss}) = p_{\text{bend},y}(\text{diss}) + p_{\text{bend},z}(\text{diss}) + p_{\text{bend},\theta y}(\text{diss}) + p_{\text{bend},\theta z}(\text{diss}) \tag{3.37}$$

If these three categories are normalized by the total power dissipated, it is possible to calculate the contribution of each mechanism in the frequency range considered previously. These results are shown in figure 3.16. In this figure it is possible to see that the principal mechanism of energy dissipation occurs in the bending of the members at most frequencies apart from around 500 Hz. This result is related to the prediction

of a large number of SWM discussed in the previous section. Some contribution to the energy dissipation also occurs due the longitudinal motion of the structural members. This mechanism becomes more predominant when a long wavelength mode occurs and this can be seen in some frequencies regions of this figure as for example around 70 Hz and 440 Hz. These results can be compared with the LW and SW natural frequencies in figure 3.6 which shows that longitudinal power dissipation is more dominant in the frequency gaps between the clusters of SWMs. Because of the way in which the system and members are excited, the contribution to the dissipation of energy due to the torsion of members can be neglected. The average value (summing the values in the frequency range for each dissipation mechanism and dividing by the total dissipated power) in this frequency range for these mechanisms are

- Bending motion - 80.71 %
- Longitudinal motion - 18.64 %
- Torsional motion - 0.65 %

The power dissipated by these mechanisms is also shown in figure 3.17 where the absolute values have been used to fit the dB scale. These results complement the previous discussion. The contribution of each member to the frequency-averaged total power dissipated in the structure is shown in figure 3.18 where the level in dB for each member is represented by its colour. It is clear in this figure that members near the disturbance forces contribute more to the dissipation of energy in the system. Some batten members in the middle of the structure do not contribute much because they are poorly exited by the disturbance force as shown in this figure. Figure 3.19 shows a similar result to that of figure 3.18, but in this case, only the bending contribution for the energy dissipation has been considered while figure 3.20 shows the longitudinal motion contribution for the dissipation of energy for each member. There are smaller differences between the levels of contribution for this mechanism of energy dissipation. A relatively small amount of power is dissipated by torsional motion and the members that contribute more are the ones in the end of the structure as shown in figure 3.21.

3.7.1 The influence of SWM in the energy dissipation mechanism

Figure 3.22 shows the sum of the input power for a harmonic force of 1 N applied at joint 4, in the y direction over the frequency range 20 Hz - 1 kHz (using frequency resolution of 1Hz), is shown as a function of the ratio $(I/l_B^2 S)$. These results are similar to figure 3.13. For the values of this ratio going from 1 to 25 times the nominal ratio $(I/l_B^2 S)_{\text{nominal}}$, the input power rises and falls, but has a general trend of decreasing its value as the ratio increases. The input power varies in a range of approximately 1.2 dB. This variation may be explained due to the interaction of short/long wavelength modes are also for changes of the nodal points for a certain mode shape. (If a force is applied close to a nodal point, the product between force and velocity is small, and consequently the power input at that position). The conclusion is that the input power does not change much when this ratio changes. The results of figure 3.23, however, do show that the mechanisms of power dissipation are influenced by $(I/l_B^2 S)$. In this figure, power dissipated by bending, longitudinal and torsional motion of the members are shown as fraction of the total power dissipated in the system as a function of $(I/l_B^2 S)$.

3.7.2 Power flow in the structure

In this section the power flow in the structural members of the lattice structure is considered. In a mechanical system, when power is input at a certain position, it flows from regions with higher energy to regions with lower energy. This behaviour can be seen in figure 3.24. In this figure, the power flow in the structural members is represented by the arrows at the end of each member. Power is input into joint 4, in the y direction as shown in the figure. The arrows are calculated by summing the values of power at a the end of each member in the frequency range 20 Hz - 1 kHz. It is clear that power flows from the left to the right hand side of the structure (this is easier to be seen in the longitudinal members). By summing the power flowing for all the members of each bay in the structure, the directions of power flow are given in figure 3.25 showing the side view of the lattice structure and the arrows pointing the direction of power flow in the structure for the third to tenth bay. The values of

power input into each of these bays are shown in the table 3.5 where the values are normalized with respect to the total input power applied at joint 4 in the y direction. The mechanisms of power flow are in contrast with the power dissipation, where most part of the power flows by longitudinal motion in the structure, the percentage of each mechanism are

- Bending - 18.63 %
- Longitudinal - 80.99 %
- Torsion - 0.38 %

3.8 Concluding remarks

In this chapter a description of the dynamic behaviour of the lattice structure has been presented regarding the interaction of short and long wavelength modes and their influence on the mechanisms of energy dissipation and power flow of the lattice structure. Simple expressions relating the geometric parameters of the lattice structure have been developed and can be used to predict when short and long wavelength modes occur and their respective frequency values. Some important conclusions of this chapter are listed below

- The lattice structure considered in this thesis has several SWM in the frequency range considered which are responsible for dissipating most of the energy in the system occurring by bending of the structural members.
- Because of the interaction between short and long wavelength modes, it is often difficult to identify LWMs. With the ratio β_i and the slenderness ratio l_B/Δ, developed in this chapter, it is possible to predict if a frequency range has SWMs.
- The ratio β_i also indicates which parameters of the structure control the presence of SW and LW modes. Some of them can be used for tailoring the frequency response of the system. These parameters are the cross section geometry (I/S), the length of the members and the number of bays.

- Although the frequency response of the cost function can be quite different when the ratio $(I/l_B^2 S)$ is changed, the overall levels, when the cost function is summed in the frequency range 20 Hz - 1 kHz, varies by only about 3 dB. Similar behaviour occurs with the input power, which varies by only about 1 dB.

- The mechanisms of power dissipation in the structure are, however, modified when the second moment of area changes. When the ratio $(I/l_B^2 S)$ increases, dissipation by longitudinal motion of the structural members become more important.

	pinned-pinned		clamped-clamped	
i - mode number	$\omega_{i,D}/2\pi$	$\omega_{i,L,B}/2\pi$	$\omega_{i,D}/2\pi$	$\omega_{i,L,B}/2\pi$
1	31.2	62.4	70.7	141.5
2	124.8	249.7	195.0	390.0
3	280.9	561.8	382.3	764.7
4	499.4	998.75	632.0	1264.1
5	780.3	1560.6	944.2	1888.3

Table 3.1: pinned-pinned and clamped-clamped natural frequencies for the members in the structure given in Hz.

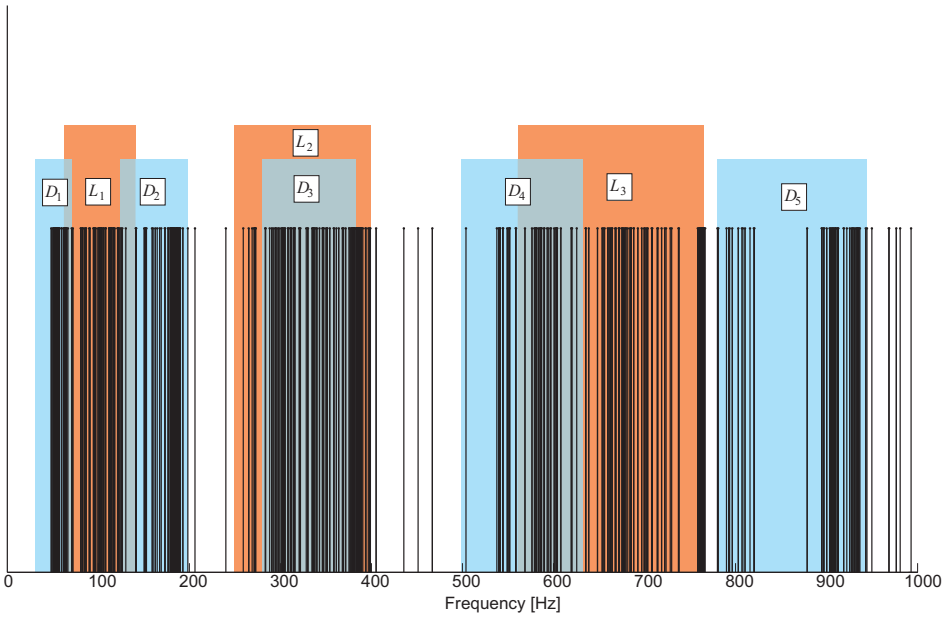

Figure 3.1: Natural Frequencies of the lattice structure. The vertical lines indicate each natural frequency. The left and right hand side of the boxes D and L indicate groups for the natural frequencies when considered the pinned-pinned and clamped-clamped boundary conditions for the structural members. D is for the diagonal members and L for longitudinal and batten members.

Mode number (i)	$\frac{l_B}{\Delta}$
1	$0.41m(m^2+C_s)^{1/2}$
2	$0.15m(m^2+C_s)^{1/2}$
3	$0.08m(m^2+C_s)^{1/2}$
4	$0.05m(m^2+C_s)^{1/2}$

Table 3.2: The values for the slenderness ratio for which the first four long wavelength bending modes to occur before the first SWM as a function of the number of bays

Mode number	$\frac{l_B}{\Delta}$
1	$4.18m$
2	$2.09m$
3	$1.39m$
4	$1.05m$

Table 3.3: The values for the slenderness ratio as a function of the number of bays for the first four long wavelength torsional modes

Mode number	$\frac{l_B}{\Delta}$
1	$1.18m$
2	$0.59m$
3	$0.39m$
4	$0.30m$

Table 3.4: The values for the slenderness ratio as a function of the number of bays for the first four long wavelength longitudinal modes to occur before the first SWM

Bay number	Power input in the bay / Total power input in the structure
3	0.8305
4	0.6845
5	0.5794
6	0.4879
7	0.3983
8	0.3204
9	0.2421
10	0.1628

Table 3.5: The sum of power input into the bays in a frequency range 20 Hz - 1kHz for a force of 1 N applied at joint 4, in the y direction. The structural damping in the system is given by $\eta = .005$

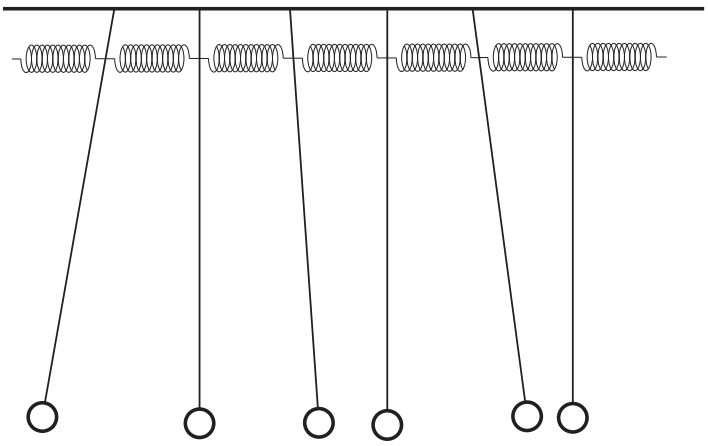

Figure 3.2: A schematic figure showing the coupled pendula system which exhibits mode localization

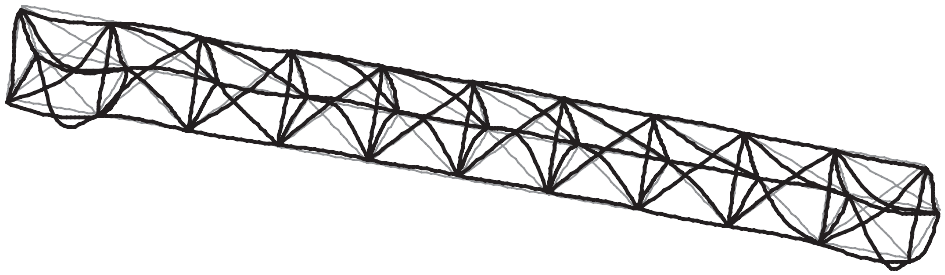

Figure 3.3: A Short wavelength mode where the larger displacements are confined at the two ends of the structure. For the structure considered in this thesis this occurs at 44.7 Hz.

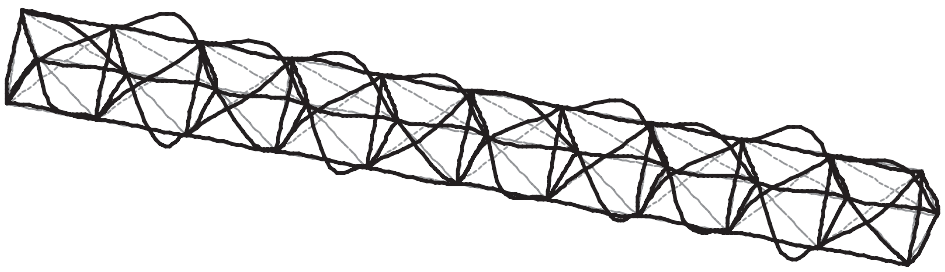

Figure 3.4: A short wavelength mode taking place in many diagonal members of the structure. For the structure considered in this thesis, this occurs at 65.8 Hz

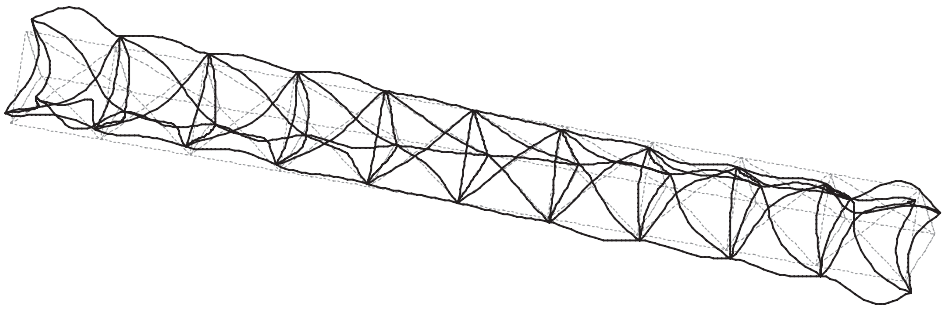

Figure 3.5: A hybrid mode of a long wavelength torsion and bending of some structural members. For the structure considered in this thesis this occurs at 72.3 Hz.

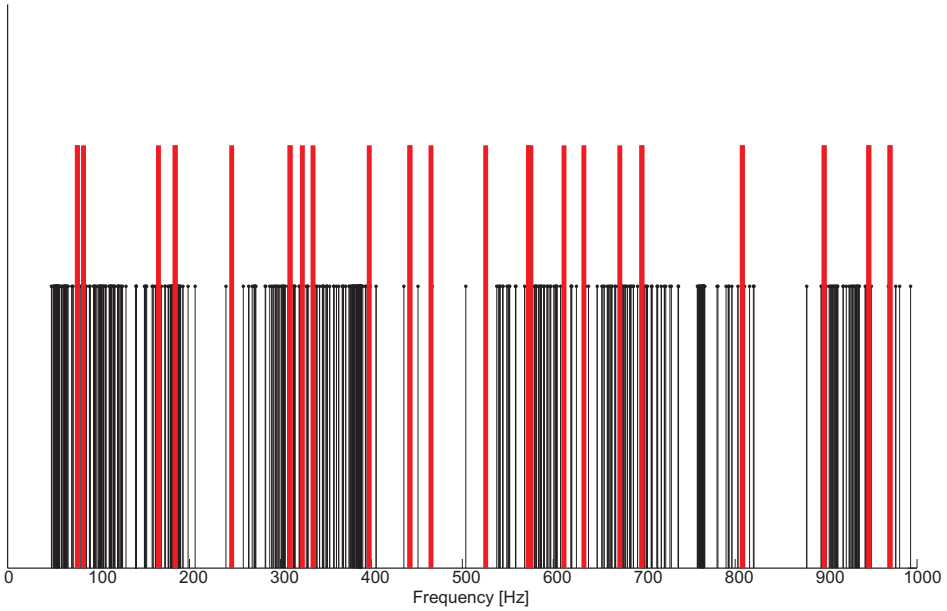

Figure 3.6: Natural frequencies of the lattice structure. The thin vertical lines indicate the natural frequencies of the structure obtained by finite element method using the beam element. The thicker and higher lines indicate the long wavelength natural frequencies obtained from an equivalent continuum model.

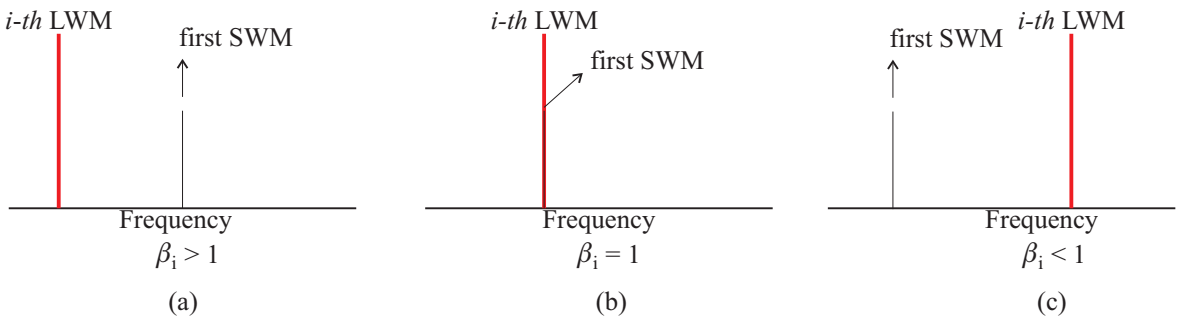

Figure 3.7: A diagram illustrating the ratio β_i. (a) first SWM occurs after the *i-th* LWM, (b) first SWM occurs at the same frequency of the *i-th* LWM and (c) first SWM occurs before the *i-th* LWM.

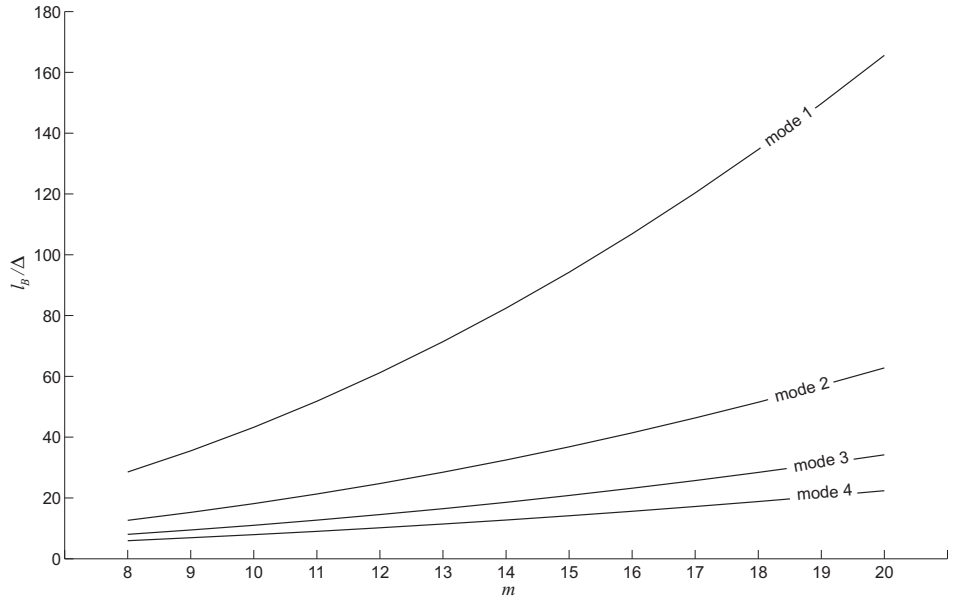

Figure 3.8: The slenderness ratio l_B/Δ as a function of the number of bays in the structure, m, plotted for the first four long wavelength bending modes of the lattice structure.

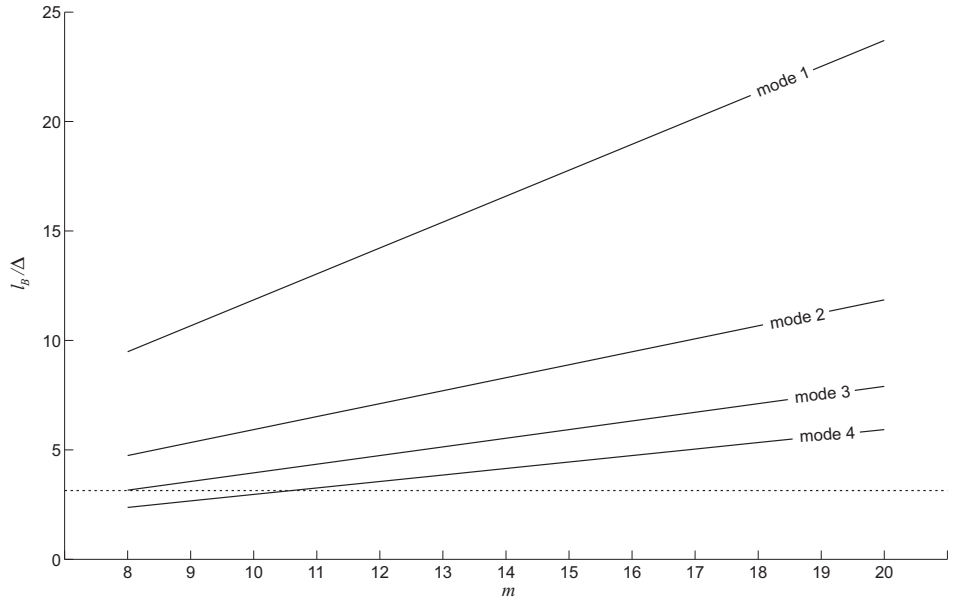

Figure 3.9: The slenderness ratio l_B/Δ as a function of the number of bays in the structure, m, plotted for the first four long wavelength longitudinal modes of the lattice structure. The dashed line indicated the Euler-Bernoulli limit for the first bending mode of the diagonal member.

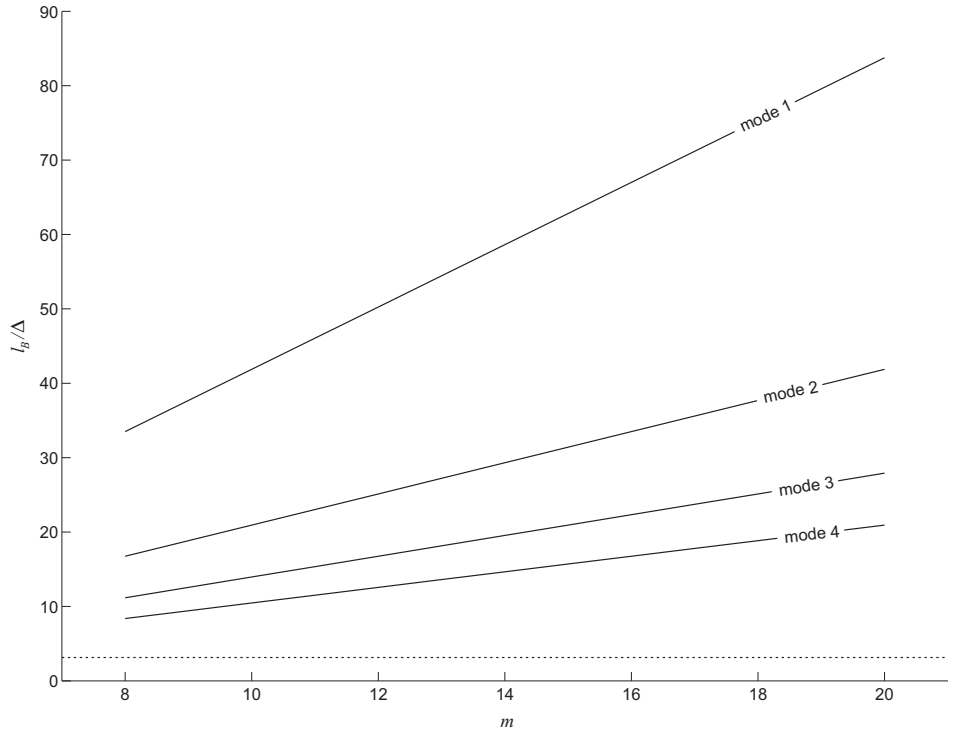

Figure 3.10: Slenderness ratio l_B/Δ as a function of the number of bays in the structure, m, plotted for the first four long wavelength torsinal modes of the lattice structure. The dashed line indicated the Euler-Bernoulli limit for the first bending mode of the diagonal member.

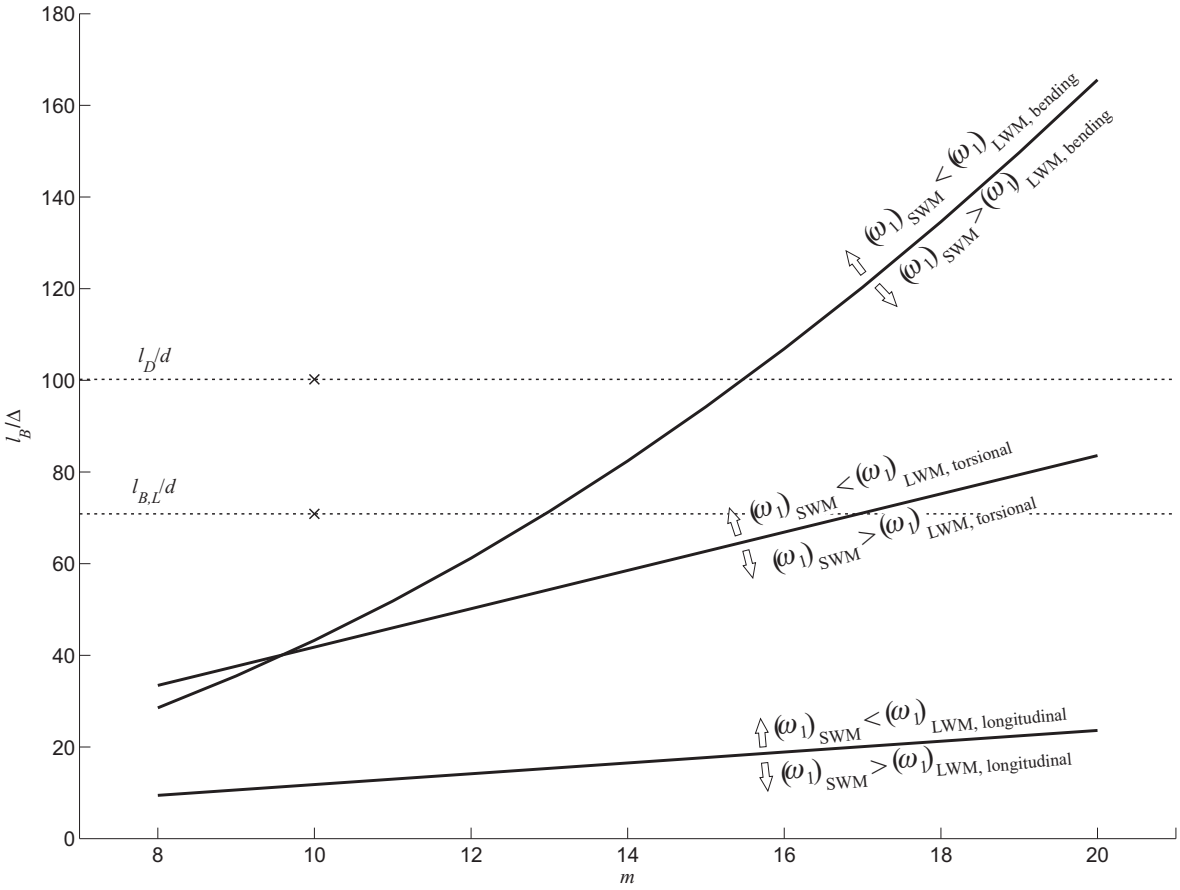

Figure 3.11: The slenderness ratio l_B/Δ as a function of the number of bays in the structure, m, plotted for the first long wavelength mode for bending, torsion and longitudinal motion of the lattice structure. The nominal ratio is identified for the diagonal members l_D/Δ and for the longitudinal/batten members l_B/Δ.

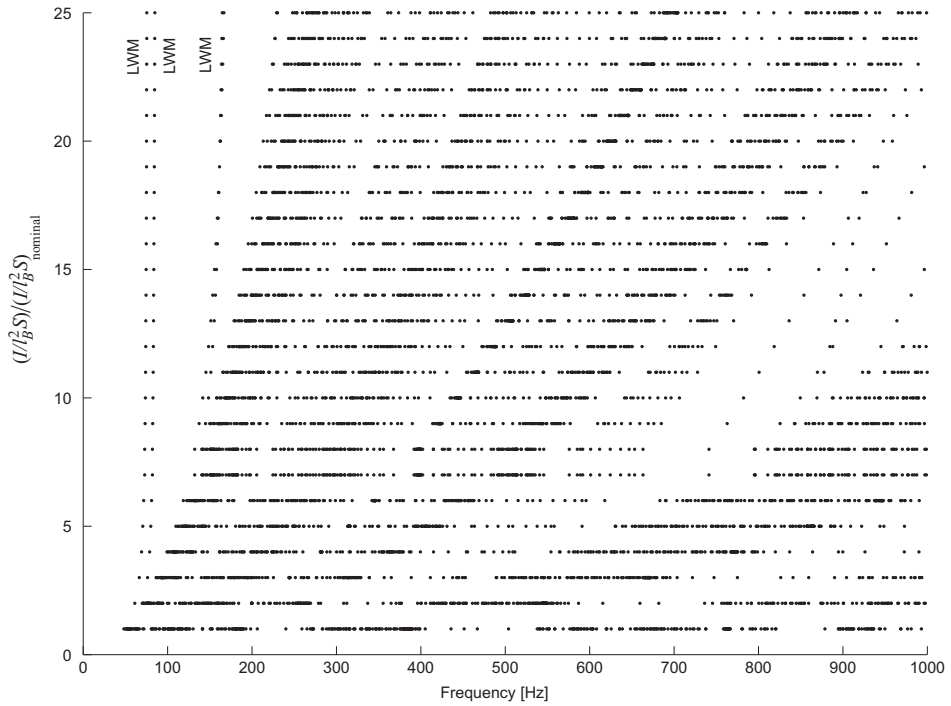

Figure 3.12: The natural frequencies of the lattice structure for various values of the ratio (I/l_B^2S) represented by the dots. The values in the vertical axis are normalized by the nominal ratio $(I/l_B^2S)_{\text{nominal}}$. Some long wavelength natural frequencies are identified.

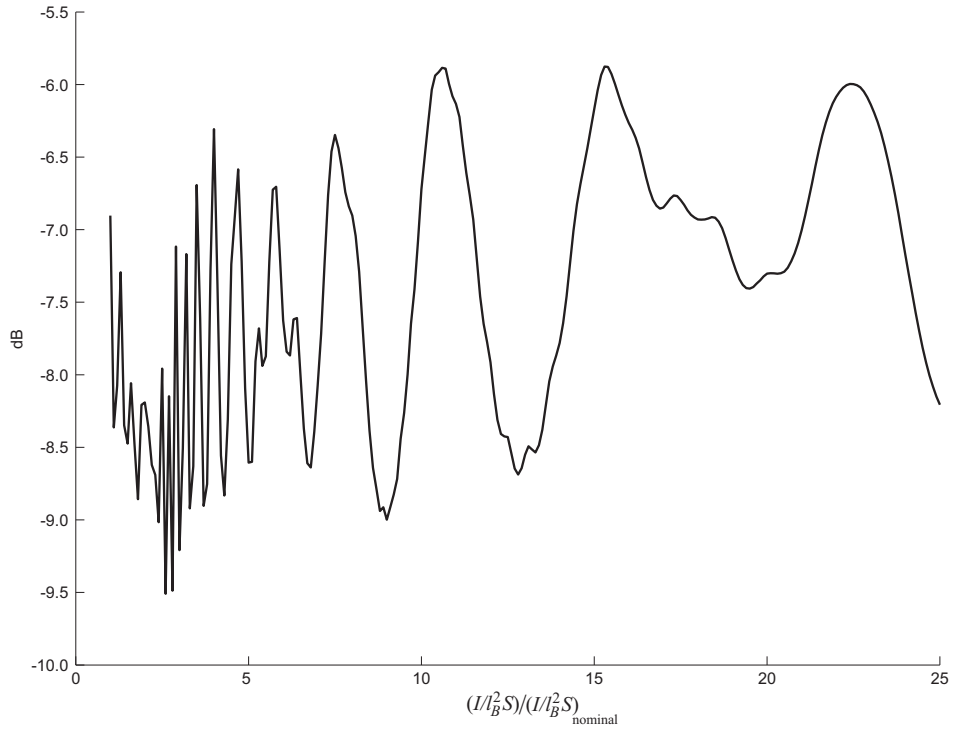

Figure 3.13: The sum of the cost function over the frequency range 20-1kHz (resolution 1 Hz) for different values of second moment of area of the structural members. dB ref. 1 m^2/Ns^2.

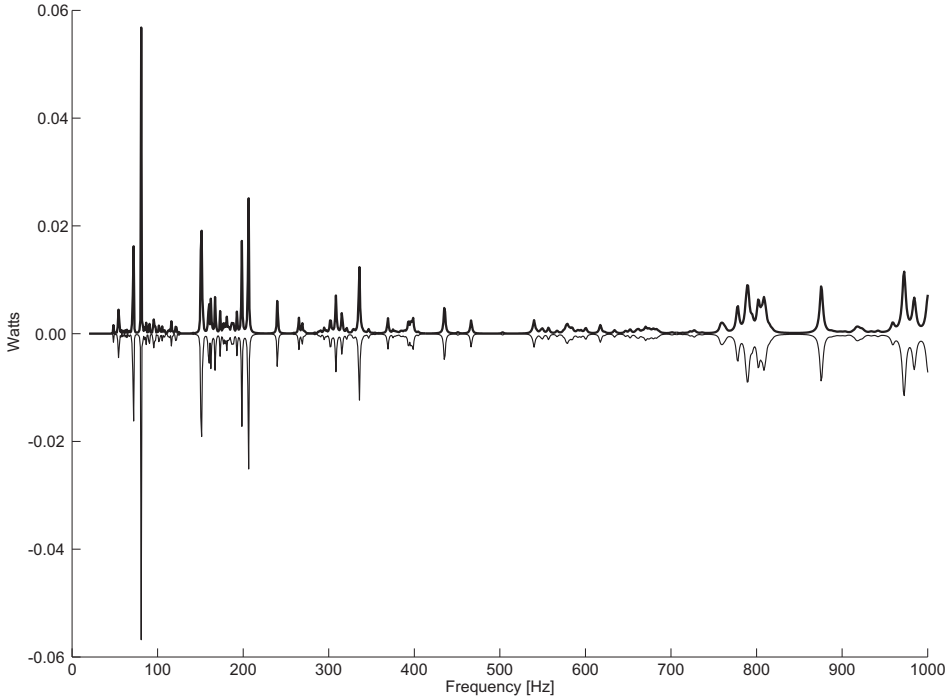

Figure 3.14: The total power input and power dissipated in the structure calculated by the dynamic stiffness method. The thick line is the power input and the thin line is the power dissipated. Values are relative to a force of 1 N applied at joint 4 in the y direction.

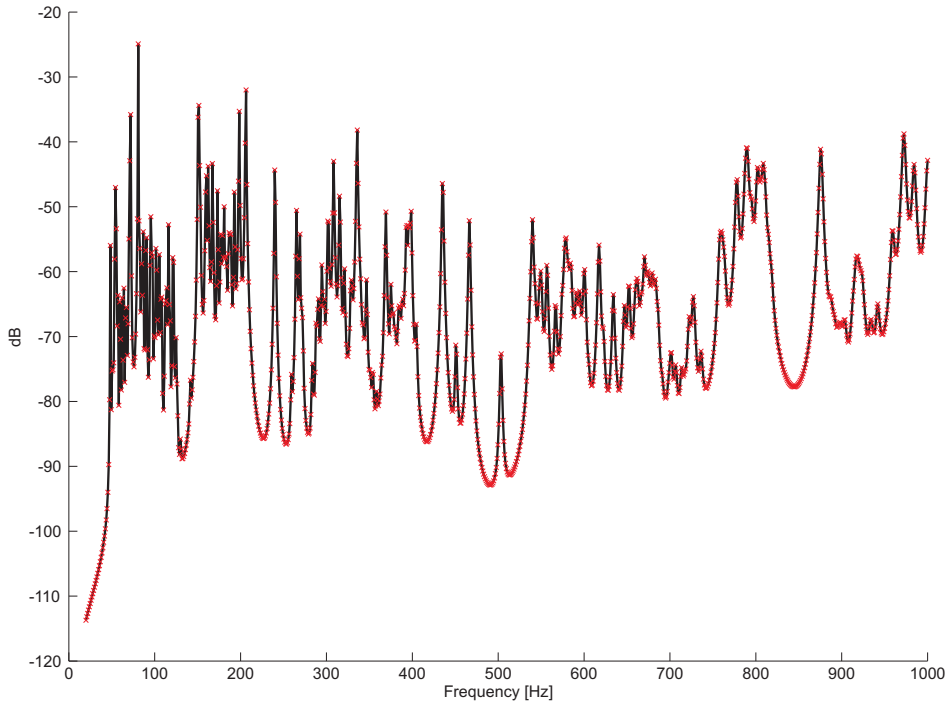

Figure 3.15: The total power input and power dissipated in the structure calculated by the dynamic stiffness method. The thick line is the power input and the thin line with $\times$ marks is the power dissipated (where the absolute value of these results have been used to fit the dB scale). Harmonic force has been applied at joint 4 in the y direction - dB ref. 1 W/N^2

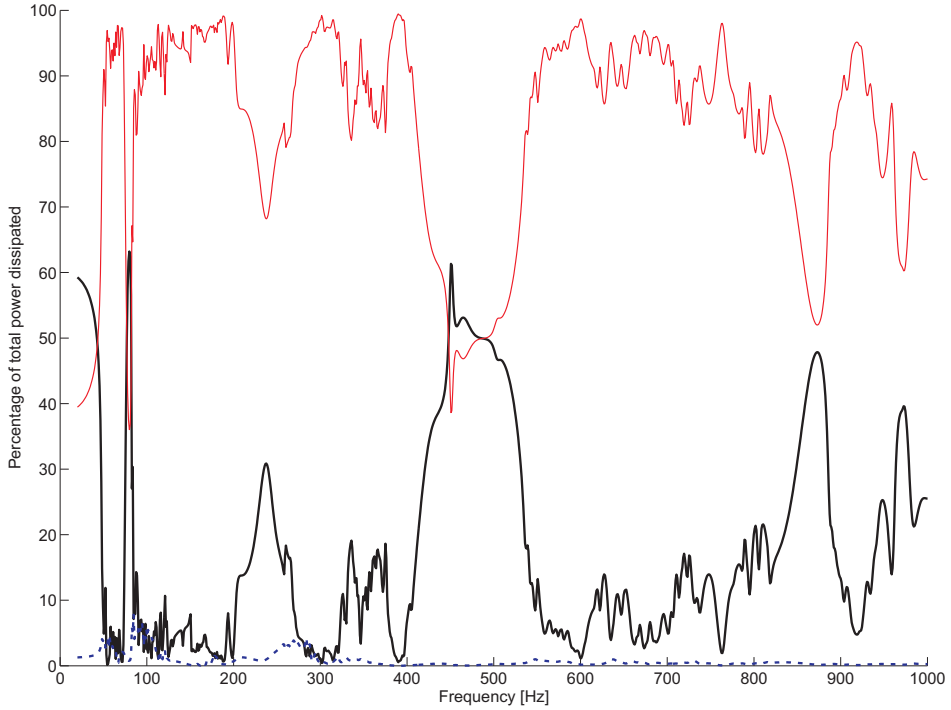

Figure 3.16: The proportion of power dissipated by longitudinal (thick line), torsional (dashed line) and bending (thin line) normalized by the total power dissipate in the structure. The results given are as a percentage of the total dissipated power and have been calculated by the dynamic stiffness method with a force applied at joint 4 in the y direction.

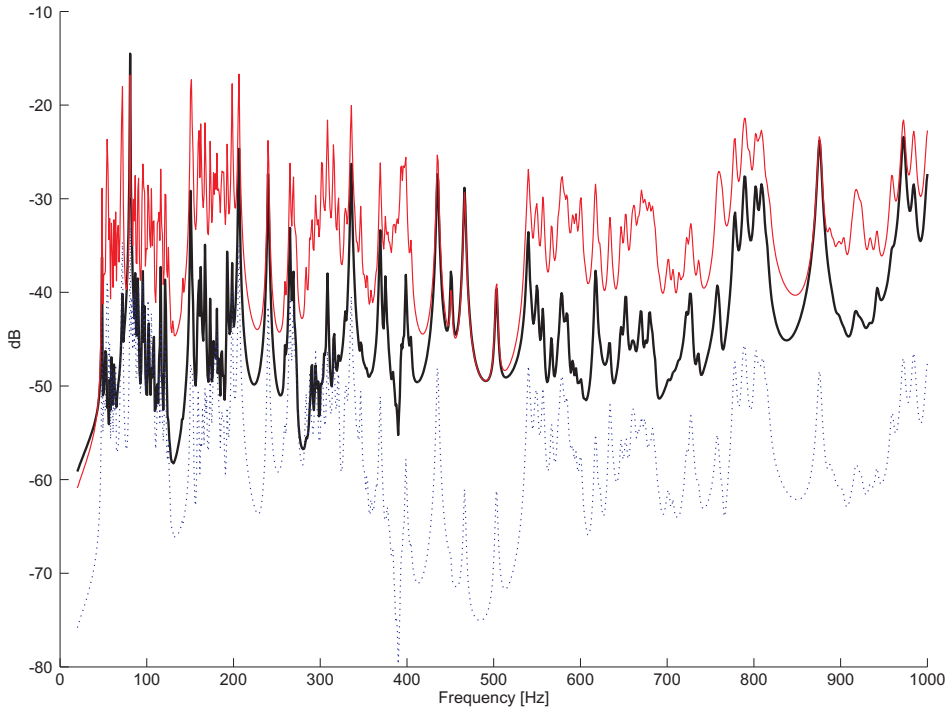

Figure 3.17: The power dissipated individually by longitudinal (thick line), torsional (dashed line) and bending (thin line). The results have been calculated by the dynamic stiffness method with a force applied at joint 4 in the y direction. - dB ref. 1 W/N^2

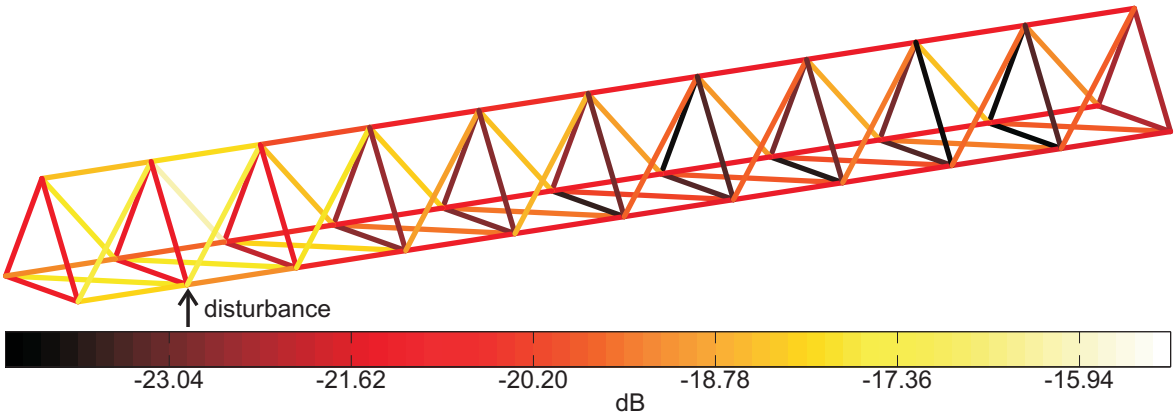

Figure 3.18: The total power dissipated by the structural members. Colours indicate power levels in dB for each structural members (light colours for higher values and darker colours lower values). Results are relative to the sum of the values in the frequency range 20 Hz - 1 kHz. - dB ref. 1 W/N^2

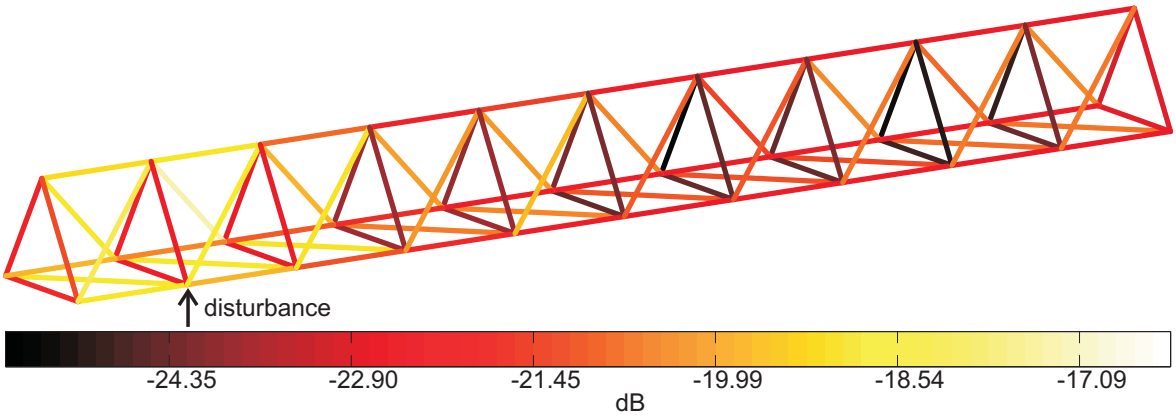

Figure 3.19: The power dissipated for each structural members by bending mechanism. Colours indicate levels of power in dB for each structural members (light colours for higher values and darker colours lower values.) - dB ref. 1 W/N^2

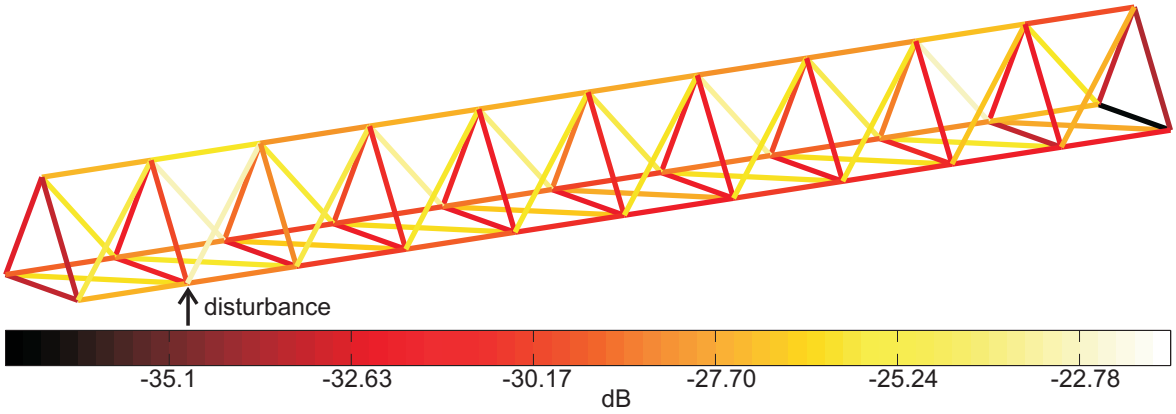

Figure 3.20: The power dissipated for each structural members by longitudinal motion. Colours indicate levels of power in dB for each structural members (light colours for higher values and darker colours lower values.) - dB ref. 1 W/N^2

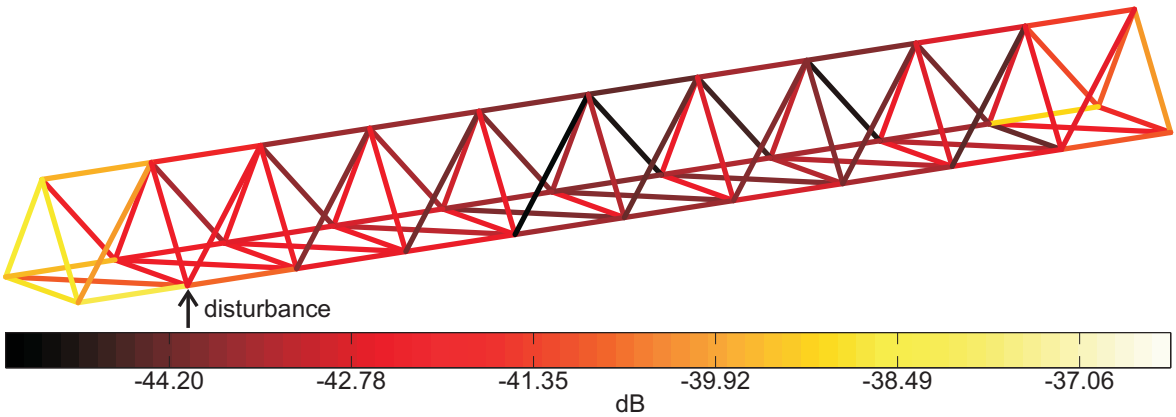

Figure 3.21: The power dissipated for each structural members by torsional motion. Colours indicate levels of power in dB for each structural members (light colours for higher values and darker colours lower values.) - dB ref. 1 W/N^2

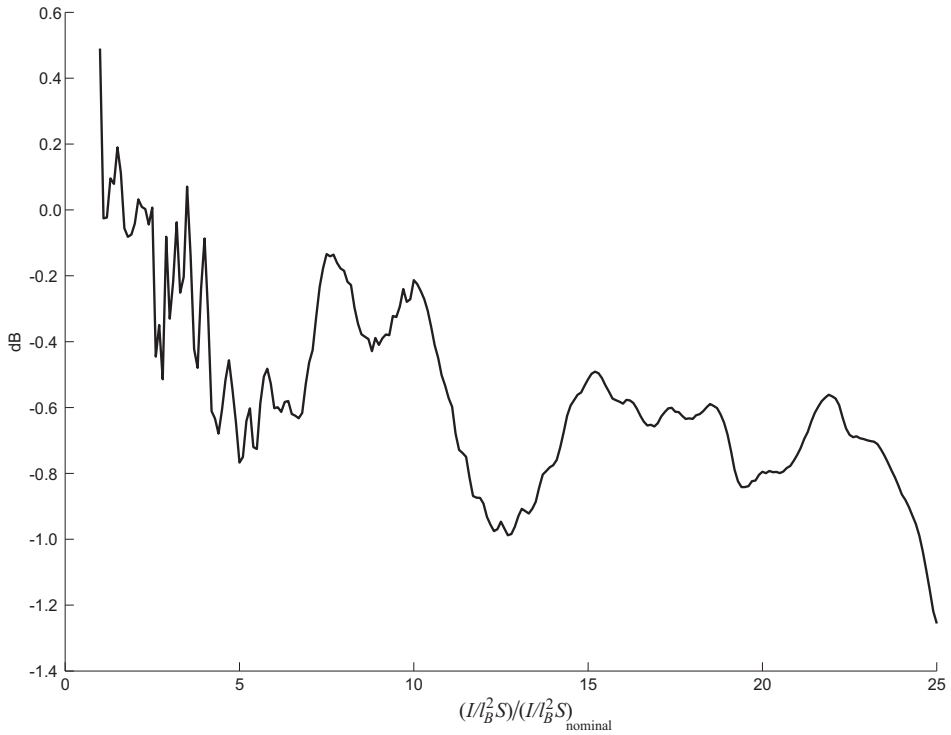

Figure 3.22: The sum of input power in the frequency range 20 Hz - 1 kHz (using frequency resolution of 1 Hz) for different values of (I/l_B^2S) for a disturbance force applied at joint 4 in the y direction. dB ref. 1 W/N^2

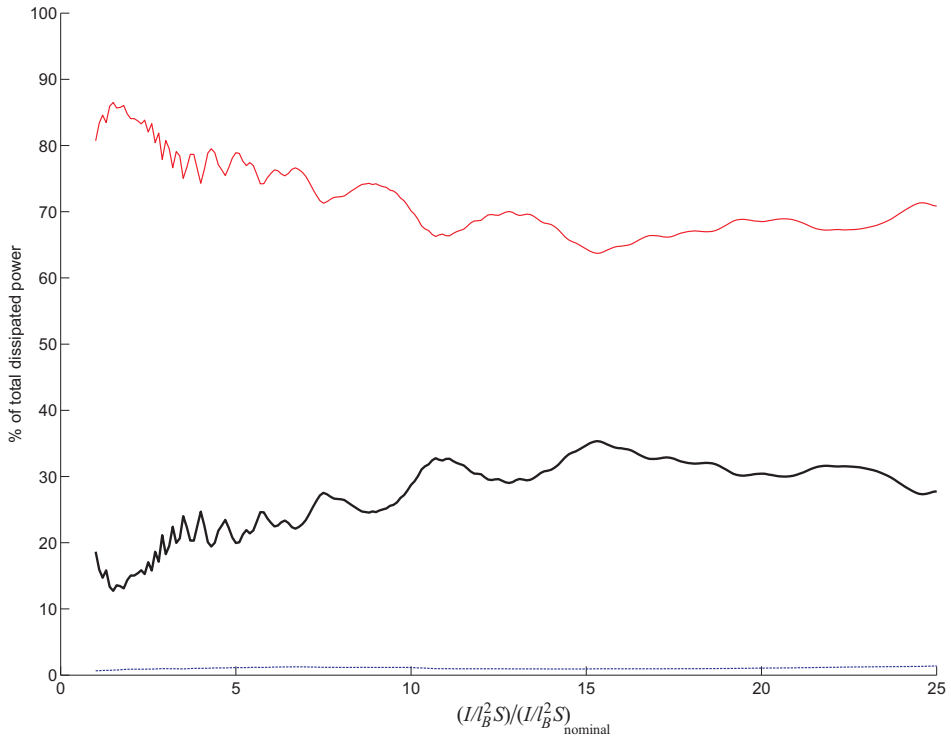

Figure 3.23: The average power dissipated in the frequency range 20-1kHz by longitudinal motion (thick line), torsional motion (dashed line) and bending motion (thin line) for various values of the second moment of area for a disturbance force of 1 N applied at joint 4 in the y direction.

Figure 3.24: Diagram showing the direction of power flow in the structure. Results are for the sum of power flow over the frequency range 20 Hz - 1kHz.

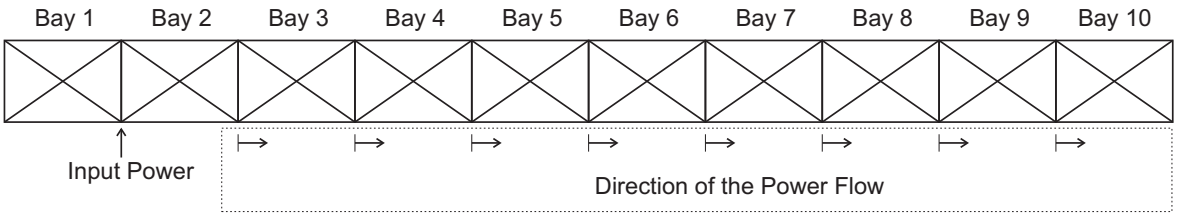

Figure 3.25: Side view of the lattice structure and the direction of power flow for the bays in the lattice structure. The disturbance force is applied at joint 4, in the y direction.

Chapter Four

The feedforward control of vibration

4.1 Introduction to feedforward control

In this chapter, active feedforward control of vibration is considered for the lattice structure shown in the introduction. The concept of feedforward control is based on the principle of superposition for linear systems, where the waves generated by a control actuator cause destructive interference in the waves generated by disturbance sources. In 1943 Paul Lueg filed a patent, certified in 1936 [98], describing the principle of controlling sound waves by means of a secondary source, which is recognized as one of the first applications of feedforward control. There is comprehensive literature on the applications of feedforward control applied to problems of vibration and noise. The principles of feedforward control applied to the reduction of noise are discussed in reference [54] and in the control of vibration of mechanical systems in references [55] and [99]. In the field of civil engineering, feedforward control has been applied in the control of seismic disturbances [100] and also in the control of vibration in offshore structures [101]. In the field of aerospace engineering, noise radiated from the payload faring has been controlled through feedforward control in reference [102] and the vibration of a lattice structure is controlled using feedforward control in reference [24]. In this thesis, active control is applied in the lattice structure described in chapter 1, with the objective of minimizing the cost function previously discussed in chapters 1, 2 and 3 (sum of the squared linear velocities at joints 31, 32 and 33). In this analysis, the disturbance force is applied at joint 4, in the y direction. All the discussion in this chapter assumes the existence of a tonal *reference signal*, where the magnitude and phase of the disturbance force are known. It is also assumed that the detection of the reference signal is unaffected by the action of the controlling forces. Although only one disturbance force is considered later, the analysis is initially presented for the case of multiple disturbances and multiple control sources. The theory discussed in this chapter is the multichannel feedforward control described by Nelson and Elliott [54] for the case of harmonic disturbances. As disturbances are assumed to be harmonic,

each frequency is considered as an individual problem and solved separately. Later in this chapter the application of feedforward control using one, two and three control sources are discussed. The optimum placement of actuators for theses cases is also considered. The next part of this chapter is an analysis of the power flow and dissipation mechanisms when feedforward control is applied in the lattice structure. The final section of this chapter examines the behaviour and performance of the feedforward control strategies taking into account the different regimes of short and long wavelength modes.

4.1.1 The feedforward control principles

Consider the block diagram shown in figure 4.1 describing the feedforward control strategy, where $\mathbf{H}_{ff}$ is the feedforward controller, the velocity vector $\mathbf{v}_m$ denotes the measured velocities in the cost function and is calculated from the mobility $\mathbf{Y}_{md}$ which is related to the vector of disturbance forces $\mathbf{f}_d$, and from the mobility $\mathbf{Y}_{mc}$ which related to the vector of control forces $\mathbf{f}_c$ in the frequency domain as

$$\mathbf{v}_m(\omega) = \mathbf{Y}_{md}(\omega)\mathbf{f}_d(\omega) + \mathbf{Y}_{mc}(\omega)\mathbf{f}_c(\omega) \tag{4.1}$$

where, ω is the angular frequency. This explicit dependence on ω has been dropped in the following formulation for simplicity. The vector $\mathbf{v}_m$ has dimension $n_m \times 1$, where n_m is the number of degrees of freedom to be controlled. The vector $\mathbf{f}_d$ has dimension $n_d \times 1$, where n_d is the number of disturbance forces; the vector $\mathbf{f}_c$ has dimension $n_c \times 1$, where n_c is the number of control forces. The mobility $\mathbf{Y}_{md}$ has dimension $n_m \times n_d$ and the mobility $\mathbf{Y}_{mc}$ has dimension $n_m \times n_c$. Equation 4.1 can be written in the form

$$\mathbf{v}_m = \mathbf{v}_{md} + \mathbf{Y}_{mc}\mathbf{f}_c \tag{4.2}$$

where, $\mathbf{v}_{md}$ is the contribution to the vector of velocities $\mathbf{v}_m$ due to the disturbance forces. This vector can be calculated as

$$\mathbf{v}_{md} = \sum_{k=1}^{n_d} \mathbf{y}_{md}(k) f_d(k) \tag{4.3}$$

where, $k = 1, \ldots, n_d$ is the number of disturbance forces, $\mathbf{y}_{md}(k)$ is a vector of mobilities relating each element of the vector $\mathbf{v}_{md}$ to the disturbance force $f_d(k)$. The vector $\mathbf{y}_{md}(k)$ has dimension $n_m \times 1$ and each column of the matrix $\mathbf{Y}_{md}$ if formed from the vectors $\mathbf{y}_{md}(k)$ which is calculated from

$$\mathbf{y}_{md}(k) = j\omega \left(\mathbf{B}_m \mathbf{D}^{-1} \mathbf{d}(k)\right) \quad \text{for } k = 1, \ldots, n_d \tag{4.4}$$

where, $\mathbf{D}$ is the dynamic stiffness matrix of the whole system that can be calculated from the methods described in chapter 2. $\mathbf{d}(k)$ is a distribution vector, where all elements are equal to zero, except the element corresponding to the degree of freedom where the disturbance force (or moment) is applied in the system. The non-zero element of $\mathbf{d}(k)$ has value 1. This lead to a normalization of the vector $\mathbf{y}_{md}(k)$ expressed in metres per second per unit force (m/Ns). $\mathbf{B}_m$ is a Boolean matrix that maps the degrees of freedom m corresponding to each element of the vector $\mathbf{v}_m$ with all degrees of freedom in the structure. $\mathbf{B}_m$ has dimension $n_m \times ndof$, where $nodf$ is the number of degrees of freedom in the system. Considering the lattice structure with 33 joints where 6 degrees of freedom are used to describe the motion at each joint, the structure has a total of $6 \times 33 = 198$ *dofs* and the dof number of the the linear velocities at joints 31, 32 and 33 are given in table 4.5, where, the dof number for the linear coordinate x, y and z for a joint is given by $(\mathrm{j}_n \times 6) - 5$, $(\mathrm{j}_n \times 6) - 4$ and $(\mathrm{j}_n \times 6) - 3$, respectively, where j_n in the joint number. The matrix $\mathbf{B}_m$ is given by

$$\begin{array}{c} dof \\ v_m(1) \\ v_m(2) \\ v_m(3) \\ v_m(4) \\ v_m(5) \\ v_m(6) \\ v_m(7) \\ v_m(8) \\ v_m(9) \end{array} \begin{array}{c} \begin{array}{ccccccccccccc} 1 & \cdots & 181 & 182 & 183 & \cdots & 187 & 188 & 189 & \cdots & 193 & 194 & 195 \end{array} \\ \left[\begin{array}{ccccccccccccc} 0 & \cdots & 1 & 0 & 0 & \cdots & 0 & 0 & 0 & \cdots & 0 & 0 & 0 \\ 0 & \cdots & 0 & 1 & 0 & \cdots & 0 & 0 & 0 & \cdots & 0 & 0 & 0 \\ 0 & \cdots & 0 & 0 & 1 & \cdots & 0 & 0 & 0 & \cdots & 0 & 0 & 0 \\ 0 & \cdots & 0 & 0 & 0 & \cdots & 1 & 0 & 0 & \cdots & 0 & 0 & 0 \\ 0 & \cdots & 0 & 0 & 0 & \cdots & 0 & 1 & 0 & \cdots & 0 & 0 & 0 \\ 0 & \cdots & 0 & 0 & 0 & \cdots & 0 & 0 & 1 & \cdots & 0 & 0 & 0 \\ 0 & \cdots & 0 & 0 & 0 & \cdots & 0 & 0 & 0 & \cdots & 1 & 0 & 0 \\ 0 & \cdots & 0 & 0 & 0 & \cdots & 0 & 0 & 0 & \cdots & 0 & 1 & 0 \\ 0 & \cdots & 0 & 0 & 0 & \cdots & 0 & 0 & 0 & \cdots & 0 & 0 & 1 \end{array}\right] \end{array} \tag{4.5}$$

On the right hand side of equation 4.2, $\mathbf{Y}_{mc}$ can be written in expanded form as

$$\mathbf{Y}_{mc} = \left[\begin{array}{c:c:c:c:c} \mathbf{y}_{mc}(1) & \dots & \mathbf{y}_{mc}(k) & \dots & \mathbf{y}_{mc}(n_c) \end{array} \right] \tag{4.6}$$

where the vectors $\mathbf{y}_{mc}(k)$, for $k = 1, \dots, n_c$, forming each column of $\mathbf{Y}_{mc}$ are determinated individually for each one of the control forces $f_c(k)$ as

$$\mathbf{y}_{mc}(k) = j\omega \left(\mathbf{B}_m \mathbf{D}^{-1} \left[\mathbf{B}_c^T(k) \mathbf{T}^T(k) \mathbf{b}^T \right] \right) \tag{4.7}$$

where, the term $\left[\mathbf{B}_c^T(k) \mathbf{T}^T(k) \mathbf{b}^T \right]$ is used in order to take into account the way the actuator applies forces in the structure. An example of an actuator in the lattice structures is shown in figure 4.2. The applications of feedforward control in lattice structures usually make use of piezoactuators which replace the structural members (or part of them). The structural members which before were passive elements are replaced by active members. The passive modifications introduced into the system dynamics can be considered in the system model by adding the dynamic stiffness matrices of the *active members* to the dynamic stiffness matrix of the whole system $\mathbf{D}$ (according to the principles of compatibility and force equilibrium), and removing the contribution of the replaced members. These actuators act by reaction in the structure which are represented by two point forces applied at the ends of the actuator in the longitudinal directions. For low frequencies these two forces can be considered equal in magnitude, however, they are applied in opposite directions as shown in figure 4.2. Therefore the use of the vector $\mathbf{b}$ given by

$$\mathbf{b} = \left[\begin{array}{cccccccccccc} -1 & 0 & 0 & 0 & 0 & 0 & 1 & 0 & 0 & 0 & 0 & 0 \end{array} \right] \tag{4.8}$$

where the non-zero elements of the vector $\mathbf{b}$ correspond to the longitudinal coordinates at the ends of a actuator. The matrix $\mathbf{T}(k)$ is the coordinate transformation matrix for the actuator k and $\mathbf{B}_c(k)$ is a Boolean matrix to map the ends of the actuator according to the joint numbering scheme of the structure (which has been discussed in chapter 2). $\mathbf{B}_m$ is the same matrix of equation 4.5.

4.1.2 The optimum control forces

In feedforward control theory, the optimum control forces can be calculated to minimize some quantity. Considering the vector of control forces related to the vector of disturbances forces by

$$\mathbf{f}_c = \mathbf{H}_{ff}\mathbf{f}_d \tag{4.9}$$

where, $\mathbf{H}_{ff}$ is the matrix of complex feedforward gains with dimension $n_c \times n_d$ in figure 4.1. Combining equations 4.9 and 4.1 leads to

$$\mathbf{v}_m = \left(\mathbf{Y}_{md} + \mathbf{Y}_{mc}\mathbf{H}_{ff}\right)\mathbf{f}_d \tag{4.10}$$

Often in applications of active vibration control it is common to use cost functions based on the square of a quantity such as acceleration or velocity. The formulation of sensible cost functions for similar applications has been discussed in references [24] and [59]. In this thesis, the objective function is defined as the sum of the linear squared velocities at the joints 31, 32 and 33 of the lattice structure showed in figure 1.4. This objective function, or cost function J, is proportional to the kinetic energy at these joints and it is calculated from

$$J = \mathbf{v}_m^H \mathbf{v}_m \tag{4.11}$$

where $\mathbf{v}_m$ comprises the linear velocities at these joints. Combining equations 4.2 and 4.11, the cost function is given by

$$\begin{aligned} J &= \left(\mathbf{v}_{md} + \mathbf{Y}_{mc}\mathbf{f}_c\right)^H \left(\mathbf{v}_{md} + \mathbf{Y}_{mc}\mathbf{f}_c\right) \\ &= \mathbf{v}_{md}^H\mathbf{v}_{md} + \mathbf{v}_{md}^H\mathbf{Y}_{mc}\mathbf{f}_c + \mathbf{f}_c^H\mathbf{Y}_{mc}^H\mathbf{v}_{md} + \mathbf{f}_c^H\mathbf{Y}_{mc}^H\mathbf{Y}_{mc}\mathbf{f}_c \end{aligned} \tag{4.12}$$

Equation 4.12 is known as *Hermitian quadratic form* and can be written in the form

$$J = \mathbf{f}_c^H\mathbf{A}\mathbf{f}_c + \mathbf{f}_c^H\mathbf{y} + \mathbf{y}^H\mathbf{f}_c + c \tag{4.13}$$

where, $\mathbf{A} = \mathbf{Y}_{mc}^H \mathbf{Y}_{mc}$ is a Hermitian matrix, $\mathbf{f}_c$ is a vector of complex control forces, so that $\mathbf{f}_c^H \mathbf{A} \mathbf{f}_c$ is a real scalar, $\mathbf{y} = \mathbf{v}_m^H \mathbf{Y}_{mc}$ is vector of complex constants, and as $\mathbf{f}_c^H \mathbf{y} + \mathbf{y}^H \mathbf{f}_c = \mathbf{f}_c^H \mathbf{y} + \left[\mathbf{f}_c^H \mathbf{y}\right]^*$ (where $()^*$ is the complex conjugate), the two terms also give a real scalar. The term $c = \mathbf{v}_{md}^H \mathbf{v}_{md}$ is a real scalar constant. The cost function J is then scalar as it is the sum of three real scalar terms. As the product $\mathbf{A} = \mathbf{Y}_{mc}^H \mathbf{Y}_{mc}$ is a positive definite matrix $\mathbf{A}$, the quadratic form of equation 4.12 describes a paraboloid which has a frequency dependent minimum. This means that the optimum control force should change with frequency. It is also import to point that in this analysis, the number of control forces is considered to be less than the number of error sensors. The mathematical details for finding the minimum are given in the reference [54]. The expression for the control forces that gives the minimum value of J is given by

$$\begin{aligned} \mathbf{f}_c^{\text{optimum}} &= -\left(\mathbf{Y}_{mc}^H \mathbf{Y}_{mc}\right)^{-1} \mathbf{Y}_{mc}^H \mathbf{v}_{md} \\ &= -\left(\mathbf{Y}_{mc}^H \mathbf{Y}_{mc}\right)^{-1} \mathbf{Y}_{mc}^H \mathbf{Y}_{md} \mathbf{f}_d \end{aligned} \tag{4.14}$$

From equations 4.9 and 4.14 the optimum feedforward controller is given by

$$\mathbf{H}_{ff}^{\text{optimum}} = -\left(\mathbf{Y}_{mc}^H \mathbf{Y}_{mc}\right)^{-1} \mathbf{Y}_{mc} \mathbf{Y}_{md} \tag{4.15}$$

The minimum value for the cost function is given by

$$J^{\text{optimum}} = \mathbf{v}_{md} \left[\mathbf{I} - \mathbf{Y}_{mc} \left(\mathbf{Y}_{mc}^H \mathbf{Y}_{mc}\right)^{-1} \mathbf{Y}_{mc}^H\right] \mathbf{v}_{md} \tag{4.16}$$

It is possible to measure the performance of the feedforward control by calculating the attenuation in the cost function. This attenuation can be expressed in decibels as

$$a\,[\text{dB}] = 10 \log_{10} \frac{J_0}{J_{ff}} \tag{4.17}$$

where, J_0 is the cost function without control and J_{ff} is the cost function when feedforward control is applied to the system. For optimum feedforward control, these values in dB are always greater than or equal to zero. This expression should be evaluated for each frequency of interest. In this thesis the frequency range of analysis is 20 Hz - 1 kHz. The low frequency limit (20 Hz) was chosen to remove the influence of the

rigid body in the analysis of the system, where the controller has no influence. For simplicity, 4.17 is reformulated as

$$a_k = 10 \log_{10} \frac{\sum_{\omega=20\text{Hz}}^{1000\text{Hz}} J(\omega)}{\sum_{\omega=20\text{Hz}}^{1000\text{Hz}} J_k(\omega)} \tag{4.18}$$

where a_k is the attenuation in decibels of the cost function due to the influence of the feedforward controller applied at member k and ω in this equation is a discrete variable evaluated in this case every 1 Hz. Although the details of the frequency dependency are not considered in equation 4.18, this expression can capture the overall performance of the controller in this frequency range, which makes it easier to compare the overall performance between different actuators positions on the structure.

4.1.3 Control effort

The control forces have a magnitude and a phase in relation to the disturbance forces. Different positions in the structure may require control forces with different magnitude. This is due to the control authority of the actuator for that position. Positions with larger control authority usually requires less control effort to attenuate the vibration. The effort of the *k-th* controlling force can be calculated as

$$e_k = \mathbf{f}_{c,k}^H \mathbf{f}_{c,k} \tag{4.19}$$

where, $\mathbf{f}_{c,k}$ is the vector of control forces for the *k-th* actuator. This result can be normalized in relation to the disturbance effort as

$$e_k\,[\text{dB}] = 10 \log_{10} \frac{e_k}{e_d} \tag{4.20}$$

where e_d is the effort associated by the disturbance force, which is equal to the squared disturbance force.

4.2 Numerical simulations

In this section, feedforward control simulations are presented using the model obtained by the dynamic stiffness method, described in chapter 2. The control forces are assumed to be applied using piezoelectric actuators which replace structural passive members. In practical situations, actuators will have different passive properties to the structural members, which will introduce passive modifications in the system. These modifications are not considered in the simulations used in this thesis. The result of this assumption is usually a small degradation in the performance of the active control which is verified by comparison of numerical results with simulations using experimental data and discussed in the section 4.2.2 of this chapter. In all the numerical simulations, only one disturbance force has been considered but the cases of one, two and three control actuators are considered. The disturbance force of 1 N is applied at joint 4, in the y direction in a frequency range of 20 Hz to 1 kHz using frequency resolution of 1 Hz.

4.2.1 One control force

Exhaustive simulations were performed using the model obtained by the dynamic stiffness method for each position where a single actuator could be placed in the lattice structure. (93 possible positions for the placement of a single actuator). To predict the best position of one actuator it is usually necessary to perform these simulations in all the candidate members to calculate the minimum cost function for each, as given by equation 4.18. These values are shown in table 4.2 when active control is applied for each member position. These positions are identified by the joint number of the members. The results of this table have also been plotted in the figure 4.3 in the form of a diagram, where attenuation values are represented by colour gradients. Most of the positions producing higher attenuation in the cost function are found around the position where the disturbance force is applied. Moreover, placing actuators in the members on the bottom of the structure give low values of attenuation. This is because they have low authority in controlling the disturbance force which is applied in the y direction. Members on the bottom have large authority in the x and z directions.

The best position for placing a single actuator is at the member between by the joints [04-05], giving an attenuation in the cost function of 9.08 dB. The worst position for placing one actuator is at the member between the joints [31-33] giving a attenuation of 3.34 dB. Frequency responses for the cost function with feedforward control with the first two best position to place a single actuator are shown in figures 4.4(a) and 4.4(b). The cost function for the two worst positions to place a single actuator are shown in figures 4.5(a) and 4.5(b). In these results the thin lines are the cost function without control and the thick line are the cost function with control. It can be seen that when feedforward control is applied there is higher attenuation in some frequency ranges than others. The frequency range with higher attenuation vary with the position of the actuator. This means that even though two positions for placing a single actuator can have similar attenuation values (using the expression of equation 4.18) their frequency response can be quite different. Also, for any frequency, the cost function with feedforward control is always equal to or smaller than the cost function without control. This is because each frequency is treated as separated problem and in some cases, the optimum control requires a small or null controller force.

4.2.2 Simulation using experimental data

In order to validate the simulations of feedforward control, frequency response functions were measured and feedforward control was simulated in an *off-line* mode using experimental data. The experimental data was obtained by an experiment consisting of two parts. The first part was the measurement of frequency response functions relating the disturbance force applied at joint 4 in the y direction to the linear velocities at joints 31, 32 and 33. This is similar to the experiment described in the chapter two. The only difference is that a piezoelectric actuator (see appendix F for details of the actuator) was included in the members described by the joints [04-08] as shown in figure 4.6. During these measurements no voltage was applied to the piezoelectric actuator, therefore, the set of frequency response functions contained only the passive influence of the actuator. The second part of the experiment consisted of the measurement of frequency response functions, using the actuator placed in the member [04-08] was used to excite the system. A random signal generated by the frequency analyser

passed through an amplifier (details are given in the appendix F) in order to provide the appropriate voltage to the piezoelectric actuator. The measured frequency response functions are given in m/Vs. During this test, the primary disturbance shaker was detached from the system. All the experiment set up, frequency parameters and sensors used in this test were the same used in the experiment described in chapter 2. The cost function calculated from the experimental data, with and without feedforward control are shown in the figure 4.7 and the simulated results obtained by the dynamic stiffness method are shown in the figure 4.8. The attenuation obtained from the experimental data in the frequency range 20 Hz - 1 kHz is 5.98 dB while the attenuation obtained by the numerical simulation for an actuator in this position is 7.83 dB. One of the reasons for this difference in the performance may be because the passive actuator properties were neglected in the numerical model. Despite this difference, both results show similarities in the frequencies ranges where feedforward control is capable of producing higher attenuation.

4.2.3 Two and three controlling forces

The analysis of feedforward control for the case of two and three control actuators is considered in this section. As discussed in a previous section, for a structure with n_m members, there are n_m candidate positions for placing one control actuator of the type shown in figure 4.6. If more than a single actuator is to be used, the number of candidate positions increases rapidly. The number of possible combinations u to place r actuators in the structure is given by

$$u_r = \frac{n_m!}{r!(n_m - r)!} \tag{4.21}$$

For two and three actuators $u_2 = 4278$ and $u_3 = 129766$. This shows that, high computational cost is expected to search all combinations of actuator position as the number of used actuators increases. In some cases, combinatorial search algorithms may be necessary as discussed in reference [24]. In this thesis, the optimum positions for two and three actuators are found by exhaustive search. The optimal positions are chosen based on the attenuation in the cost function in the frequency range 20 Hz - 1

kHz where frequency steps of 1 Hz were used in the analysis. Implementation of the exhaustive searching procedure can be simplified if all the transfer functions relating the forces from the actuator candidate positions are calculated *a priori* and stored. (In this case 93 sets of transfer functions). Using the principle of superposition, it is then possible to calculate the attenuation for configurations of two or more control actuators. Using this procedure, the search for optimum position for three actuators took approximately 30 hours to complete while the search for two actuators took less the two hours. For two actuators, the colourmap given in figure 4.9 shows the attenuation in the cost function represented by the colours. The two axes of the diagram represent members numbered from 1 to 93. These members are identified according to their joint number in appendix G. The bottom left part of the diagram is the regions where the two actuators are close to the disturbance force, which is applied at joint 4. The diagonal line going from the bottom left to the top right corners of the diagram showing lower levels of attenuation (darker colours) correspond to the use of only one control actuator. Higher levels of attenuation are obtained when at least one of the actuators is placed near to the disturbance source. The ten best configurations for placing two actuators and their respective attenuation are shown in table 4.3. Similarly, table 4.4 contains these results for three actuators. The range of performance for the worst and best positions for 1, 2 and 3 actuators are shown in the table 4.5. The maximum theoretical attenuation that can be achieved with 3 actuators applying feedforward control is 26.20 dB. This value can be used as a baseline to compare the performance of other forms of active control.

The cost functions without control and for the cases of one, two and three actuators for optimum feedforward control are compared in figure 4.10. The positions where chosen in such a way that the position of one actuator is included in one of the positions for two actuators and the positions for two actuators are also included in the actuator configuration for three actuators. The configuration for the three cases and their respective attenuation values are listed below

- 1 Actuator - Member [04-08] - 7.83 dB Attenuation
- 2 Actuators - Members [04-05] and [04-08] - 16.73 dB Attenuation

- 3 Actuators - Members [04-05], [04-08] and [11-15] - 25.63 dB Attenuation

4.3 Power analysis with feedforward control

In this section, analysis of power in the lattice structure is considered when feedforward control is applied to minimize the cost function. For a passive structure, the total power input in the system is dissipated internally by motion of the structural members. When a secondary source is applied to the system to reduce the vibration in certain positions of the structure, the energy behaviour should change. For a given frequency, the forces from a control actuator either supply or absorb energy from the system. Usually any form of active control can be seen as a change in the system impedance. For this reason, when control forces are applied to the system, the input power from the primary disturbance is affected. This means that, if power from the feedforward control is positive, then three possibilities can occur; the total power input into the system after control forces are applied remains the same before active control is turned on. Another possibility is that the sum of power from the primary disturbance and the power from the controller is smaller than the power from the primary disturbance before control is applied, this can be written as

$$(p_{d,\text{with control}} + p_c) < p_{d,\text{without control}} \tag{4.22}$$

where the frequency dependence has been dropped for simplicity. $p_{d,\text{with control}}$ is the power from the disturbance source when active control is applied to the system, p_c is the power from the control forces and $p_{d,\text{without control}}$ is the power from the disturbance forces before feedforward control was applied. The second possibility is that the total input power after control is applied is greater than the input power in the system before control, which can be written as

$$(p_{d,\text{with control}} + p_c) > p_{d,\text{without control}} \tag{4.23}$$

In this situation, even though the cost function may be reduced some other positions in the structure will have their levels of vibration increased to dissipate the extra energy supplied to the system. Two examples to illustrate the discussion in this section are

shown in figures 4.11 and 4.12. These figures show the system and the structural member where the feedforward control forces are applied to minimize the cost function with a single actuator. The arrows indicate the direction of power flow in the structure and the member where active control is applied. The results are relative to the sum of the frequency response points in the range 20 Hz - 1 kHz, using frequency steps of 1 Hz. In both cases, the input power from the primary source before control was 1 Watt. Without control both members act passively and dissipate a small amount of energy (0.008 and 0.009 Watts, respectively). The flow of energy in member [04-05] is higher because this member is at a position closed to the disturbance force. When active control is applied to the system, the flow of energy in the active members change. To minimize the cost function, the control forces both provide energy to the system as indicated by the direction of the arrows. The power from the primary source also changes, from 1 Watt to 0.421 Watts for control with member [04-05] and to 0.688 Watts for control with member [17-20]. The power input from the control sources as function of frequency for these two cases are shown in figures 4.13 and 4.14, respectively. In these figures, power is given in dB and negative values have been plotted in thicker lines. It can be seen that member [04-05], which is near the disturbance force, inputs more energy into the system than the actuator placed at member [17-20] (in the middle of the structure). Exhaustive simulations where performed for all positions of a single actuator in the lattice structure. These results are shown in figure 4.15 where the sum of the power over all frequencies is represented by the horizontal bars for each member. Figure 4.15(a) shows the power input by the disturbance source with control normalized by the power input by the disturbance source without control $[p_d(\text{in})_{\text{with control}}/p_d(\text{in})_{\text{without control}}]$. Figure 4.15(b) shows the total power input in the system with control normalized by the power input by the disturbance source without control $[(p_d(\text{in})_{\text{with control}} + p_c)/p_d(\text{in})_{\text{without control}}]$. For some positions the total power input into the system is greater than the total power input into the system before control. Figure 4.15(c) shows the power from the control sources normalized by the power from the disturbance source without control $[p_c/p_d(\text{in})_{\text{without control}}]$. These results shows that the power produced by the feedforward controllers is usually small compared to the power from the disturbance source, but in general is positive. In the members

at the end of the structure (near to the *dofs* to be controlled) the power from the actuators is slightly negative. It also should be clear that these results are relative to the sum of the points in a frequency range.

4.4 The influence of the short/long wavelength regime in the feedforward control

To investigate the influence of short wavelength modes in the performance of feedforward control, numerical simulations where performed in three regions of the lattice structure; close to the position where disturbance force is applied (joint 4), close to the joints 31, 32 and 33 and in the middle of the lattice structure. A number of structural members are chosen in these regions as actuator positions and the attenuation values have been obtained for two values of the ratio $(I/l_B^2 S)$ as described below in terms of the parameter β_i

- $(I/l_B^2 S) = (I/l_B^2 S)_{\text{nominal}}$, $\beta_{1,\text{bending}} = 0.61$ and $\beta_{1,\text{torsion}} = 0.59$
- $(I/l_B^2 S) = 10 \times (I/l_B^2 S)_{\text{nominal}}$, $\beta_{1,\text{bending}} = 1.92$ and $\beta_{1,\text{torsion}} = 1.87$

This means that for vales of $(I/l_B^2 S) = 10 \times (I/l_B^2 S)_{\text{nominal}}$, the first SW natural frequency is greater than the first LW bending natural frequency and the first LW torsional natural frequency. For nominal values of $(I/l_B^2 S)$, the first SW natural frequency is smaller than both LW bending and torsional natural frequencies. Figures 4.16, 4.18 and 4.20 illustrate the positions where feedforward control was implemented, for a region close to the disturbance source, close to the joints 31, 32 and 33 and at the middle of the lattice structure, respectively. The comparison for the attenuation in the overall cost function in the frequency range 20 Hz - 1 kHz (calculated using equation 4.18) are shown in figures 4.17, 4.19 and 4.21 for a region close to the disturbance source, close to the joints 31, 32 and 33 and at the middle of the lattice structure, respectively. In these figures, the attenuation in the cost function only varies slightly for some of the members. The maximum variation (for the member [29-33]) is smaller than 2.3 dB, which is considered to be small. The conclusion is that the performance of feedforward control is not affected much by different regime of SW/LW modes.

4.5 Concluding Remarks

In this chapter, the feedforward control of vibration in the lattice structure has been considered. The conclusions of this chapter are given below.

- The position of the control actuator is important in terms of the performance of the active control system. The optimal position depends on frequency and also the position of the disturbance force.
- The maximum theoretical attenuations achieved for one, two and three actuators are 9.08, 16.73 and 26.21 dB, respectively, for the conditions described in this chapter.
- Most of the good positions for placement of the actuator are in regions around the position where the disturbance source is applied. The control forces in these members, however, are required to input more energy into the system than at other places.
- Numerical results show that in most cases, the power produced by the controlling forces is positive, what brings to the conclusion that the physical mechanism of feedforward control are different from forms of active control denominated active damping.
- Short wavelength modes do not influence much the performance of feedforward control.

Joint number	31			32			33		
Coordinates	x	y	z	x	y	z	x	y	z
dof number	181	182	183	187	188	189	193	194	195

Table 4.1: The dof numbering of the coordinates x, y and z of the joints 31, 32 and 33.

Member	a[dB]	Member	a[dB]	Member	a[dB]
$[01-02]$	6.68	$[01-03]$	4.56	$[02-03]$	7.09
$[01-04]$	7.65	$[01-05]$	9.07	$[02-05]$	7.17
$[02-06]$	6.73	$[03-04]$	3.88	$[03-06]$	3.94
$[04-05]$	9.08	$[04-06]$	4.27	$[05-06]$	5.30
$[04-07]$	4.73	$[04-08]$	7.83	$[05-08]$	6.89
$[05-09]$	6.06	$[06-07]$	3.80	$[06-09]$	3.88
$[07-08]$	7.79	$[07-09]$	4.49	$[08-09]$	5.20
$[07-10]$	4.23	$[07-11]$	7.19	$[08-11]$	6.75
$[08-12]$	6.22	$[09-10]$	3.98	$[09-12]$	4.13
$[10-11]$	6.27	$[10-12]$	4.42	$[11-12]$	5.97
$[10-13]$	4.21	$[10-14]$	6.43	$[11-14]$	6.39
$[11-15]$	7.17	$[12-13]$	4.06	$[12-15]$	4.09
$[13-14]$	6.01	$[13-15]$	4.25	$[14-15]$	6.18
$[13-16]$	3.91	$[13-17]$	5.87	$[14-17]$	6.35
$[14-18]$	6.62	$[15-16]$	4.11	$[15-18]$	4.20
$[16-17]$	4.83	$[16-18]$	3.36	$[17-18]$	5.03
$[16-19]$	4.13	$[16-20]$	6.10	$[17-20]$	7.27
$[17-21]$	6.62	$[18-19]$	4.11	$[18-21]$	4.09
$[19-20]$	6.42	$[19-21]$	4.27	$[20-21]$	5.66
$[19-22]$	4.07	$[19-23]$	6.12	$[20-23]$	6.85
$[20-24]$	6.70	$[21-22]$	4.09	$[21-24]$	4.39
$[22-23]$	5.59	$[22-24]$	4.36	$[23-24]$	5.97
$[22-25]$	3.90	$[22-26]$	5.30	$[23-26]$	7.23
$[23-27]$	6.45	$[24-25]$	4.18	$[24-27]$	4.58
$[25-26]$	4.84	$[25-27]$	4.62	$[26-27]$	6.50
$[25-28]$	3.47	$[25-29]$	5.15	$[26-29]$	6.72
$[26-30]$	7.02	$[27-28]$	4.09	$[27-30]$	4.84
$[28-29]$	4.97	$[28-30]$	4.41	$[29-30]$	7.00
$[28-31]$	3.52	$[28-32]$	5.41	$[29-32]$	5.11
$[29-33]$	7.01	$[30-31]$	3.92	$[30-33]$	5.79
$[31-32]$	4.64	$[31-33]$	3.34	$[32-33]$	4.44

Table 4.2: The attenuation obtained by feedforward control in the frequency range 20 Hz - 1 kHz, using 1 Hz frequency resolution, when a single actuator is used. The values of attenuation have been calculated using equation 4.18.

Actuator 1	Actuator 2	Attenuation [dB]
$[04-05]$	$[04-08]$	16.73
$[02-05]$	$[04-05]$	15.74
$[01-05]$	$[07-09]$	15.69
$[02-03]$	$[04-05]$	15.64
$[20-24]$	$[04-05]$	15.37
$[02-06]$	$[01-05]$	15.34
$[05-09]$	$[04-05]$	15.27
$[01-03]$	$[01-05]$	15.26
$[07-11]$	$[11-15]$	15.25
$[07-08]$	$[04-05]$	15.21

Table 4.3: The ten best configuration for two actuators using feedforward control. The values are relative to the frequency range 20 Hz - 1 kHz, using 1 Hz of frequency resolution. The values of attenuation have been calculated using equation 4.18.

Actuator 1	Actuator 2	Actuator 3	Attenuation [dB]
$[02-03]$	$[04-05]$	$[04-08]$	26.21
$[04-05]$	$[02-06]$	$[04-08]$	26.21
$[10-11]$	$[01-05]$	$[05-09]$	26.17
$[04-05]$	$[01-05]$	$[04-08]$	25.69
$[04-05]$	$[04-08]$	$[05-09]$	25.82
$[04-05]$	$[04-08]$	$[11-15]$	25.63
$[10-11]$	$[11-12]$	$[01-05]$	25.59
$[05-06]$	$[01-05]$	$[09-10]$	25.48
$[01-05]$	$[05-09]$	$[06-07]$	25.46
$[03-06]$	$[02-03]$	$[01-05]$	25.16

Table 4.4: The ten best configuration for three actuators using feedforward control. The values are relative to the frequency range 20 Hz - 1 kHz, using 1 Hz of frequency resolution. The values of attenuation have been calculated using equation 4.18.

Number of Actuators	Minimum Attenuation [dB]	Maximum Attenuation [dB]
1	3.34	9.08
2	3.53	16.73
3	6.00	26.21

Table 4.5: The maximum and minimum attenuation obtained by using one, two and three actuators.

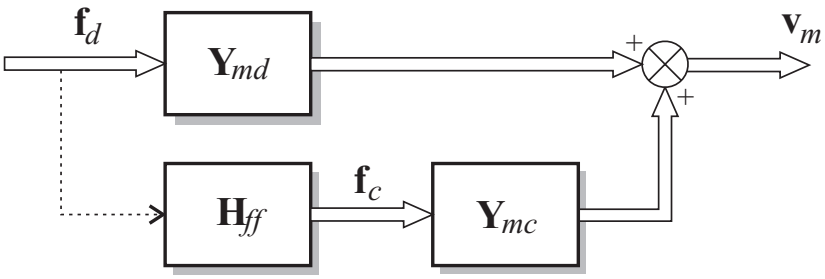

Figure 4.1: A block diagram describing the elements of feedforward control strategy. The dashed line indicate the detected signal correlated to the disturbance sources.

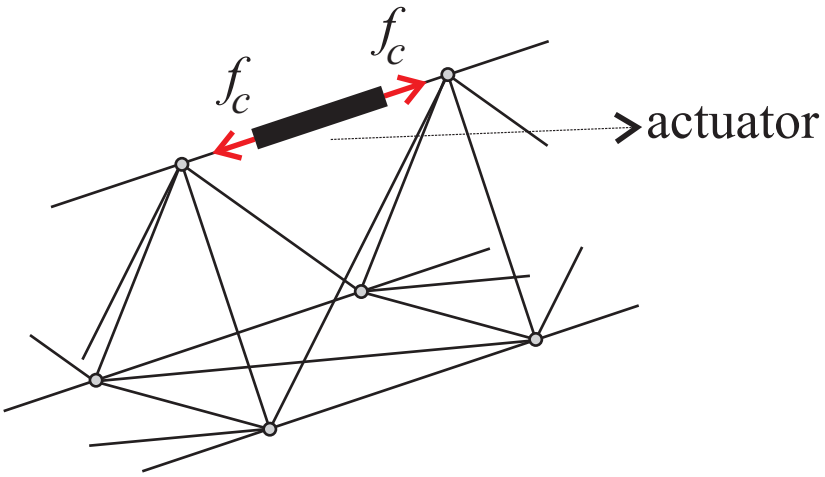

Figure 4.2: A diagram showing how the actuator applies forces in the lattice structure.

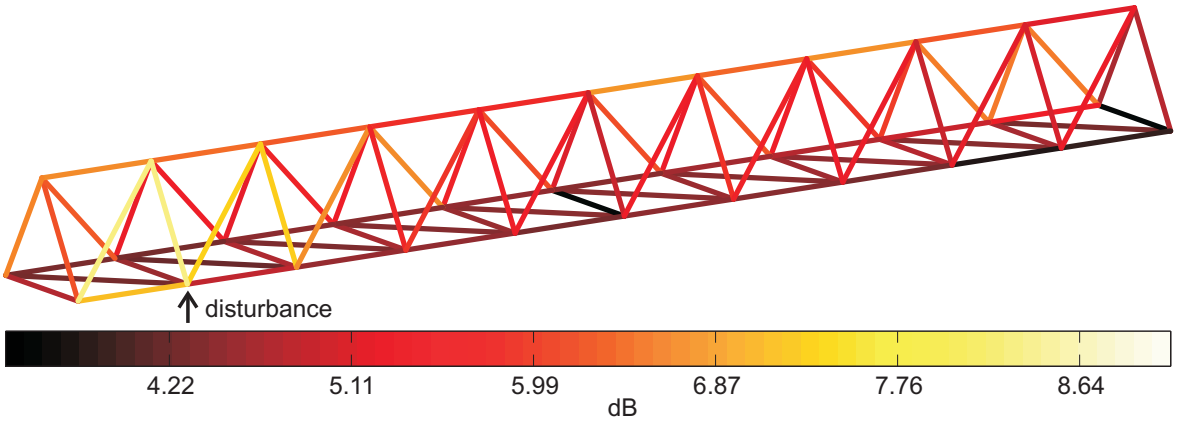

Figure 4.3: A diagram showing the attenuation values obtained when a single actuator is used to minimize the vibration at joints 31, 32 and 33 for each position in the lattice structure. The values in dB are represented by the colours, where lighter colours indicate higher attenuation and darker colours indicate lower attenuation. dB ref. 1 m^2/Ns^2.

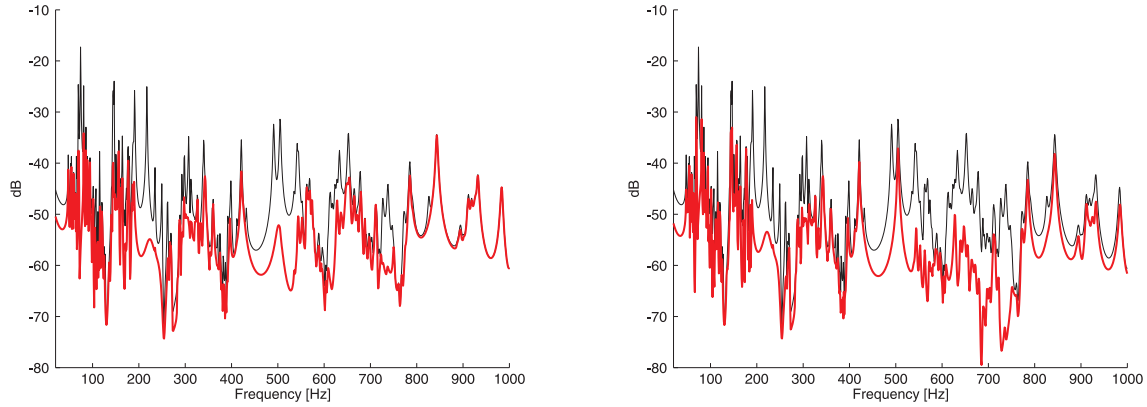

(a) (b)

Figure 4.4: The cost function without control (thin line) and with control (thick line). (a) actuator placed at member [4-5] and (b) actuator place at member [1-5]. The disturbance force is applied at joint 4, in the y direction - dB ref. 1 m^2/Ns^2.

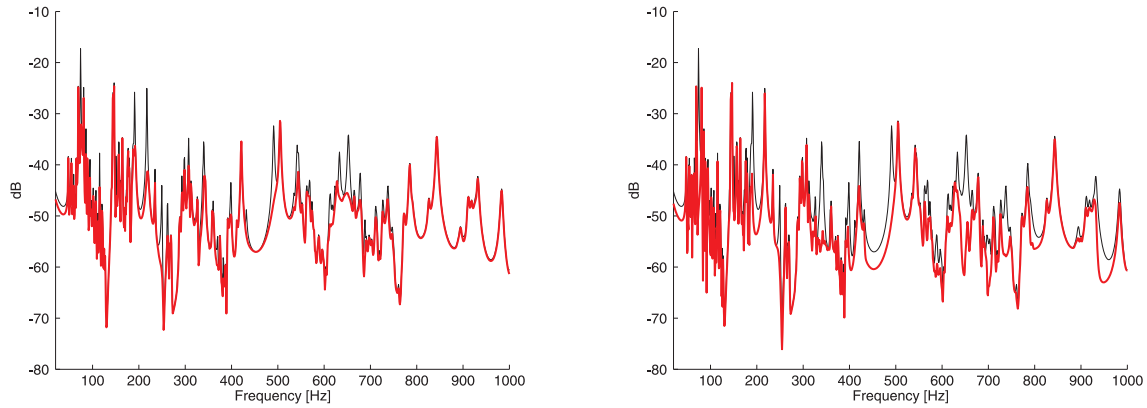

(a) (b)

Figure 4.5: The cost function without control (thin line) and with control (thick line). (a) actuator placed at member [31-33] and (b) actuator place at member [16-18]. The disturbance force is applied at joint 4, in the y direction - dB ref. 1 m^2/Ns^2.

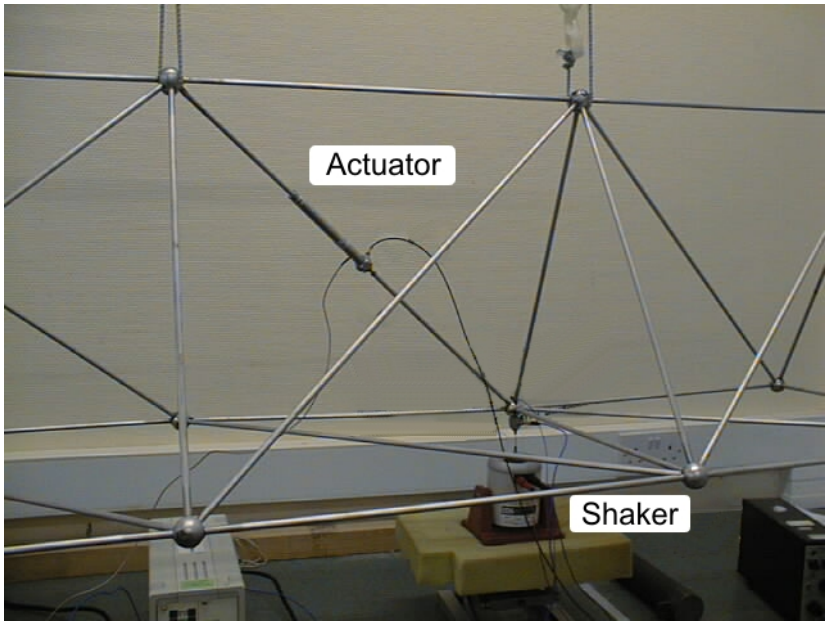

Figure 4.6: A photograph showing the piezoelectric actuator in the lattice structure placed at member [04-08].

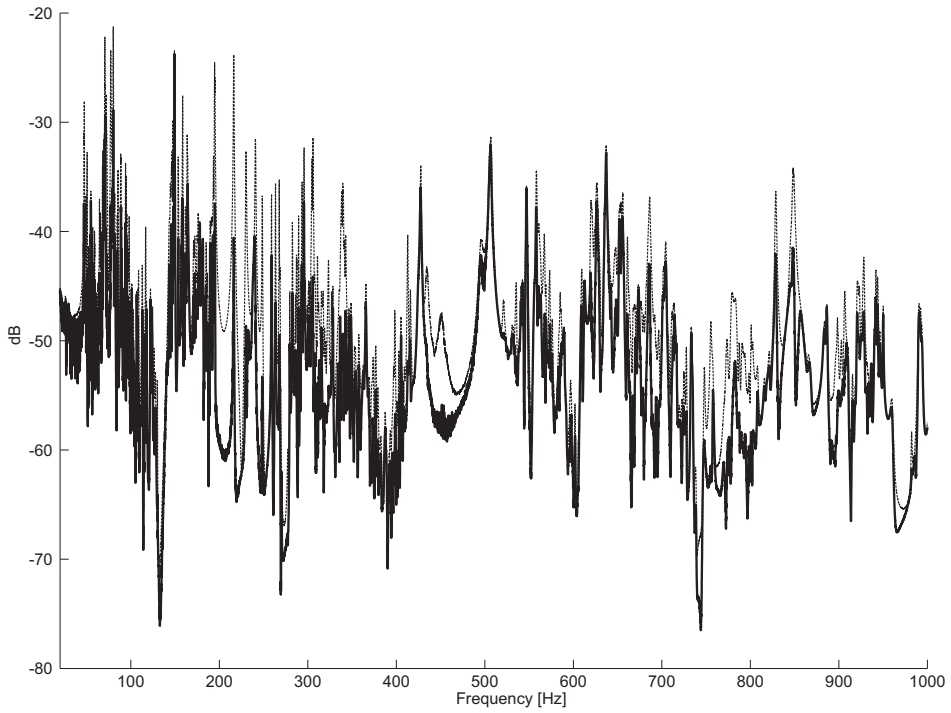

Figure 4.7: The experimental cost function without control (thin dashed line) and with control (thick line) for a actuator in member [04-08]. Disturbance applied at joint 4 in the y direction - dB ref. 1 m^2/Ns^2

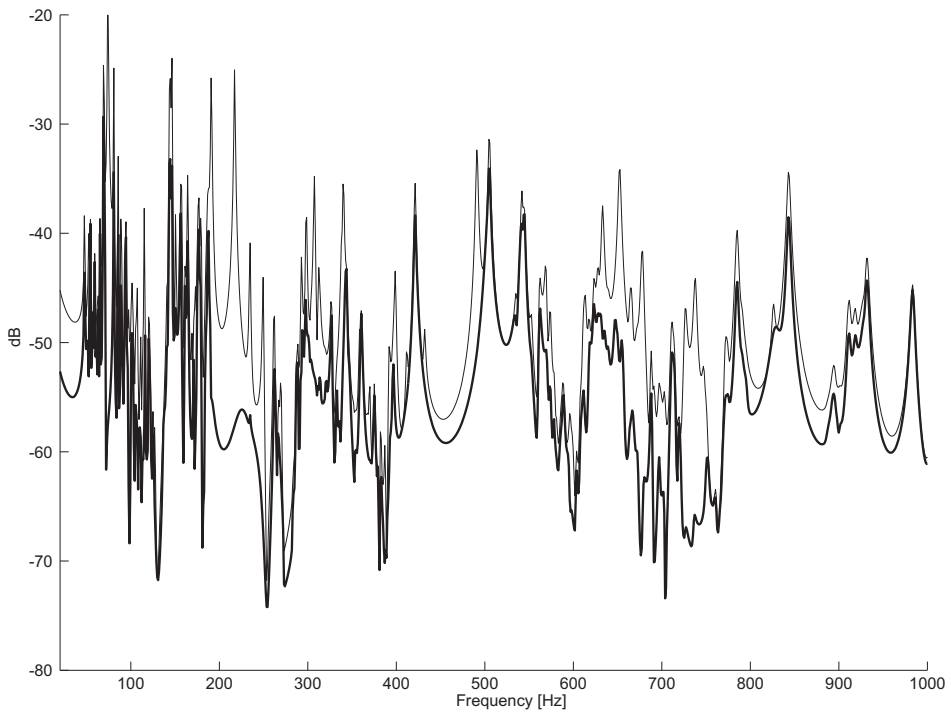

Figure 4.8: The theoretical cost function without control (thin dashed line) and with control (thick line) for a actuator in member [04-08]. Disturbance applied at joint 4 in the y direction - dB ref. 1 m^2/Ns^2.

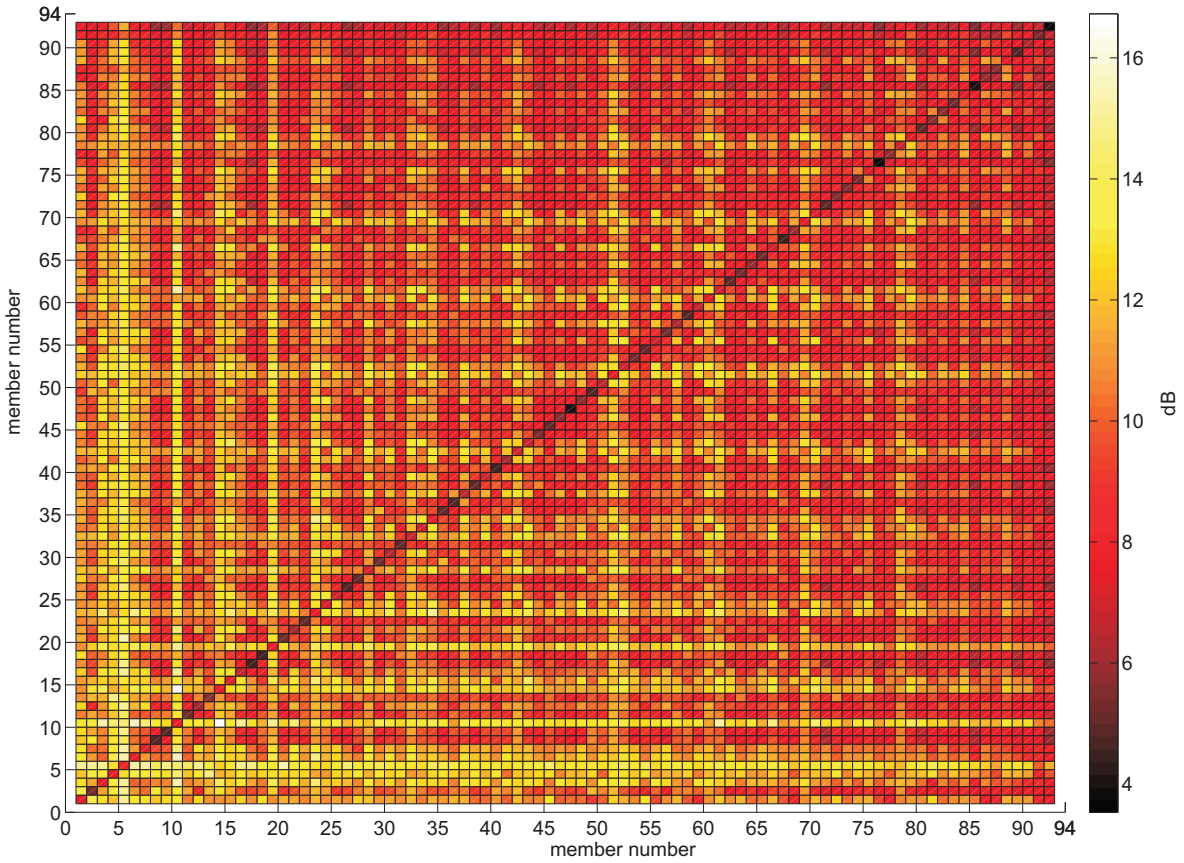

Figure 4.9: The attenuation in the cost function when two actuators are used. The colour gradients indicate the levels in dB where lighter colours refer to higher levels of attenuation and darker colours refer to lower levels of attenuation. The respective joint numbers for each member are given in appendix G. dB ref. 1 m^2/Ns^2.

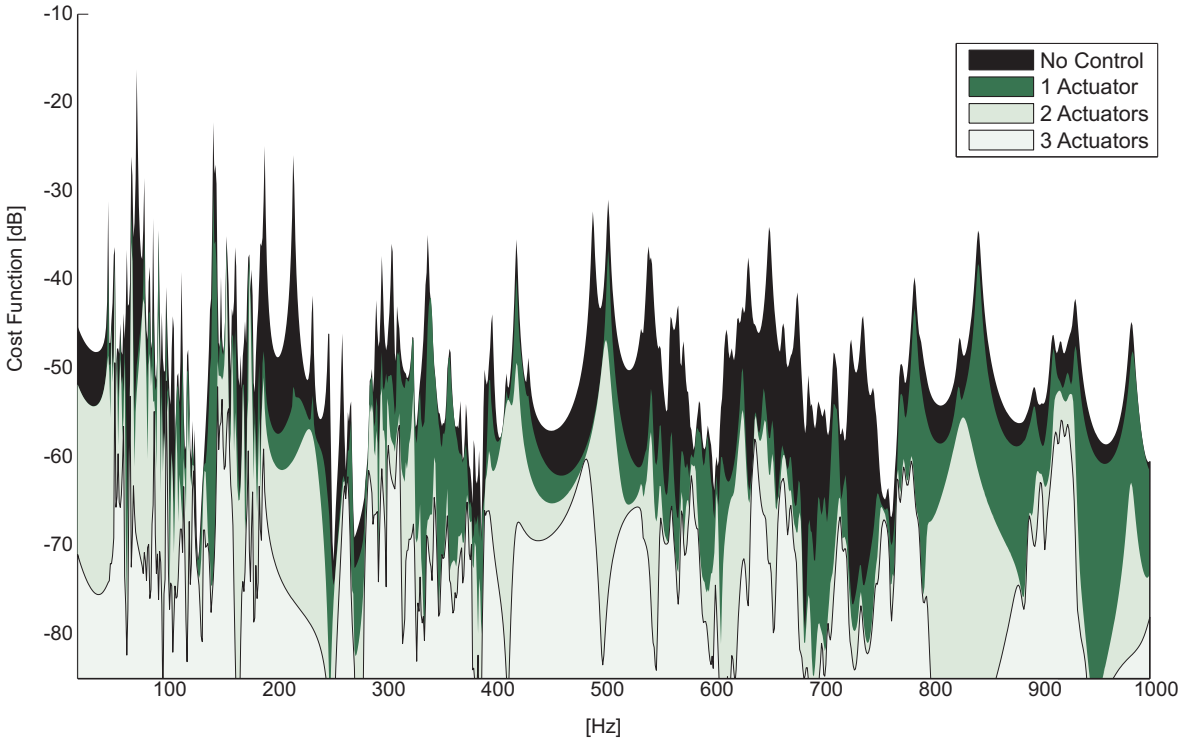

Figure 4.10: A comparison of the cost function without control and for the cases of 1, 2 and 3 control actuators. The positions for the actuators are: member [04-08] for one actuator, members [04-05] and [04-08] for two actuators and members [04-05], [04-08] and [11-15] for three actuators. dB ref. 1 m^2/Ns^2.

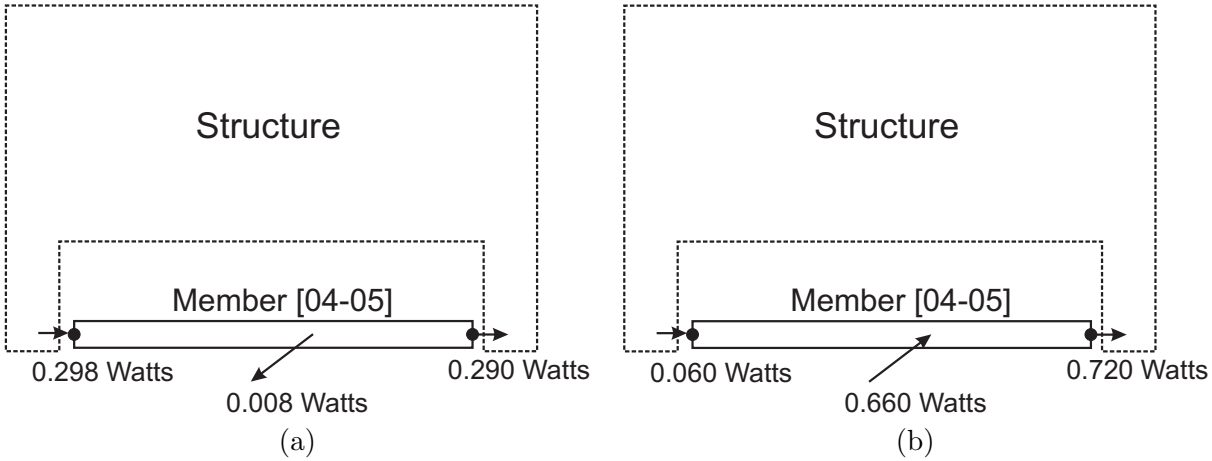

Figure 4.11: The flow of energy in the member used for feedforward control (member [04-05]) where arrows indicate the direction of the power flow. (a) without control, (b) with active control.

Figure 4.12: The flow of energy in the member used for feedforward control (member [17-20]) where arrows indicate the direction of the power flow. (a) without control, (b) with active control.

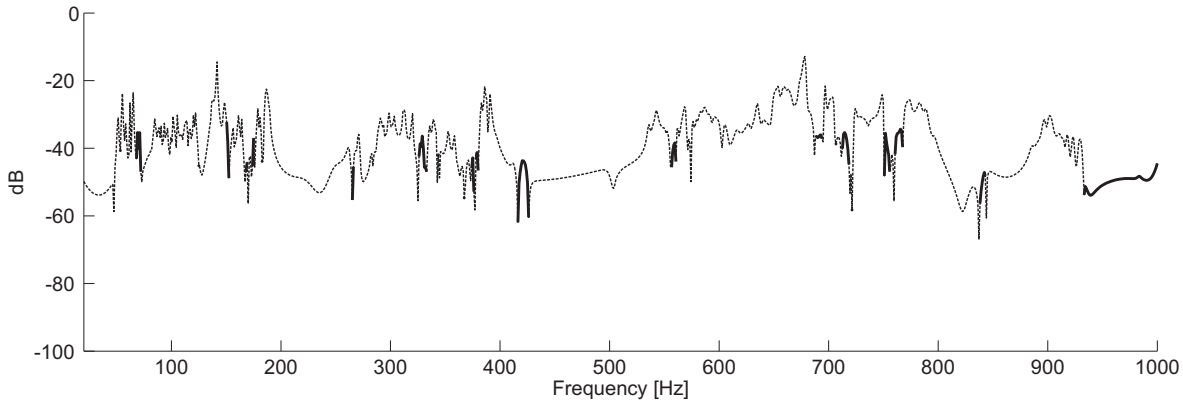

Figure 4.13: The power input/dissipated as function of the frequency by the actuator placed at member [04-05]. Thin lines indicate that power is positive and thick lines indicate that power is negative (dissipated). dB ref. 1 W/N^2

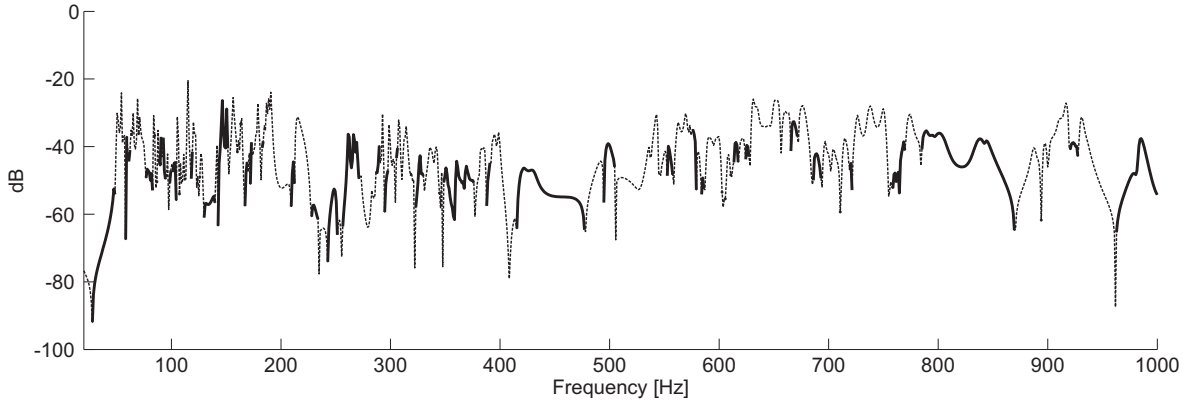

Figure 4.14: The power input/dissipated as function of the frequency by the actuator placed at member [17-20]. Thin lines indicate that power is positive and thick lines indicate that power is negative (dissipated). dB ref. 1 W/N^2

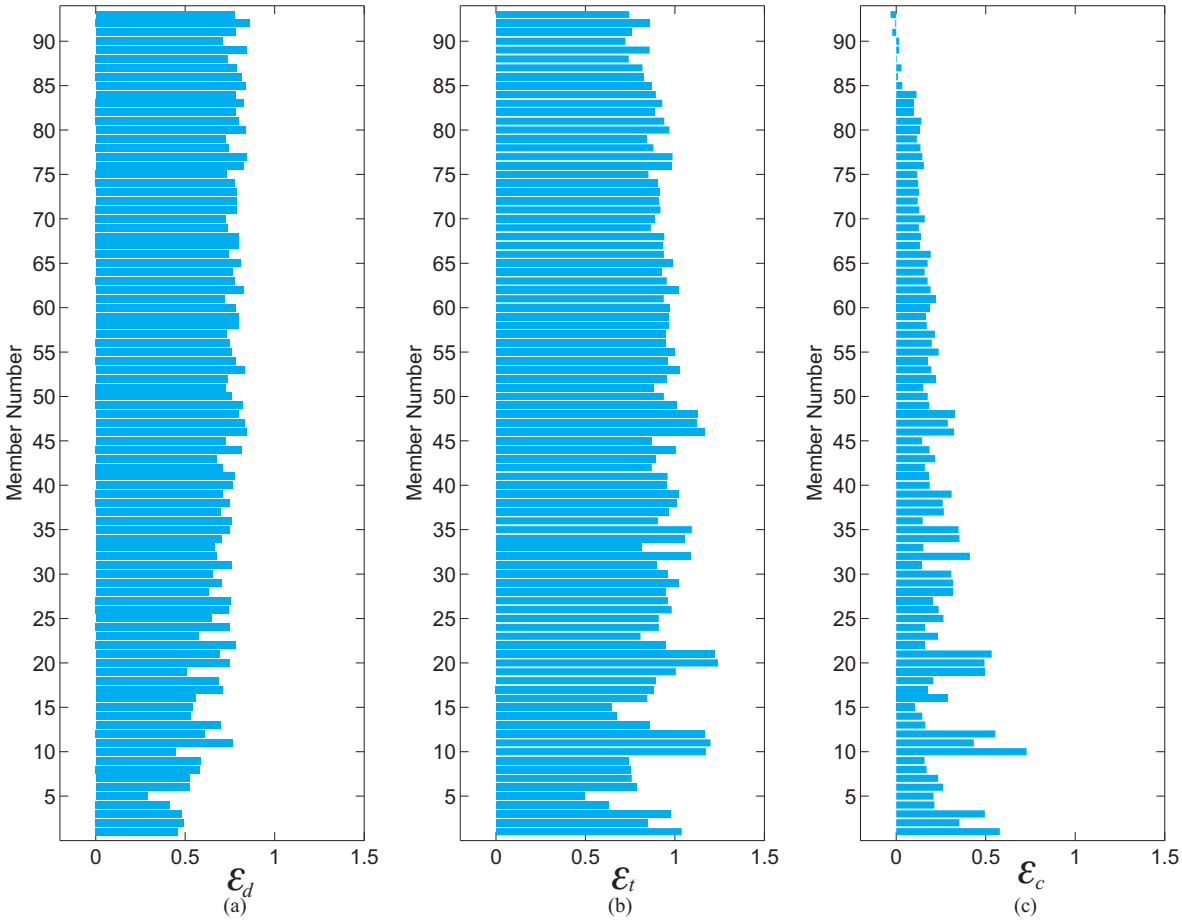

Figure 4.15: The sum of the frequency response of power in the range 20 Hz - 1 kHz (using 1 Hz of frequency resolution). (a) The bars indicate $\varepsilon_d = p_d(\text{in})_{\text{with control}}/p_d(\text{in})_{\text{without control}}$ when feedforward control is applied for each member position in the lattice structure. (b) The bars indicate $\varepsilon_t = p_d(\text{in})_{\text{with control}} + p_c/p_d(\text{in})_{\text{without control}}$ when feedforward control is applied for each member position in the lattice structure. (c) The bars indicate $\varepsilon_c = p_c/p_d(\text{in})_{\text{without control}}$. Members are identified according to their joint numbers in the appendix G.

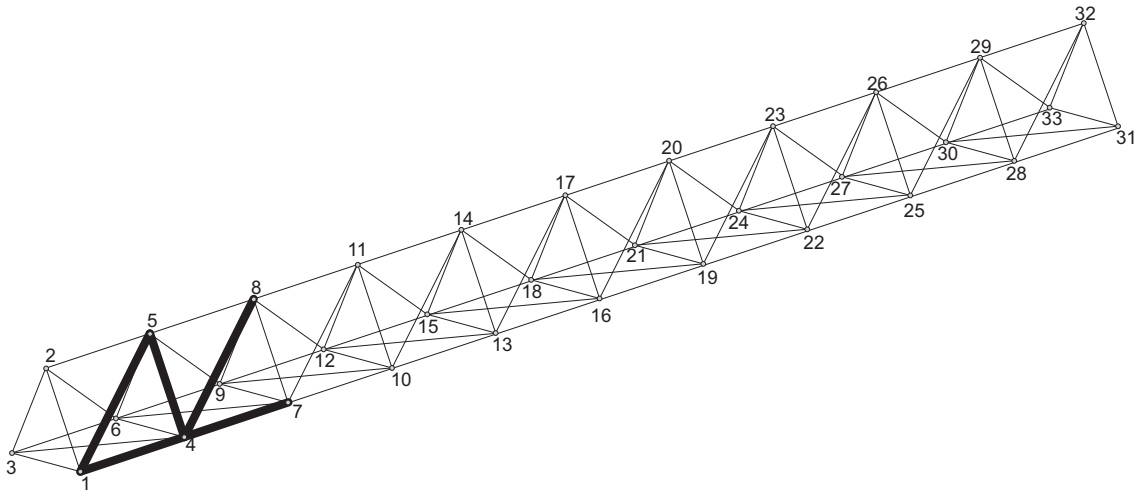

Figure 4.16: The lattice structure and the joint numbering scheme. Members plotted with thicker lines indicate the region close to the disturbance where feedforward control has been applied.

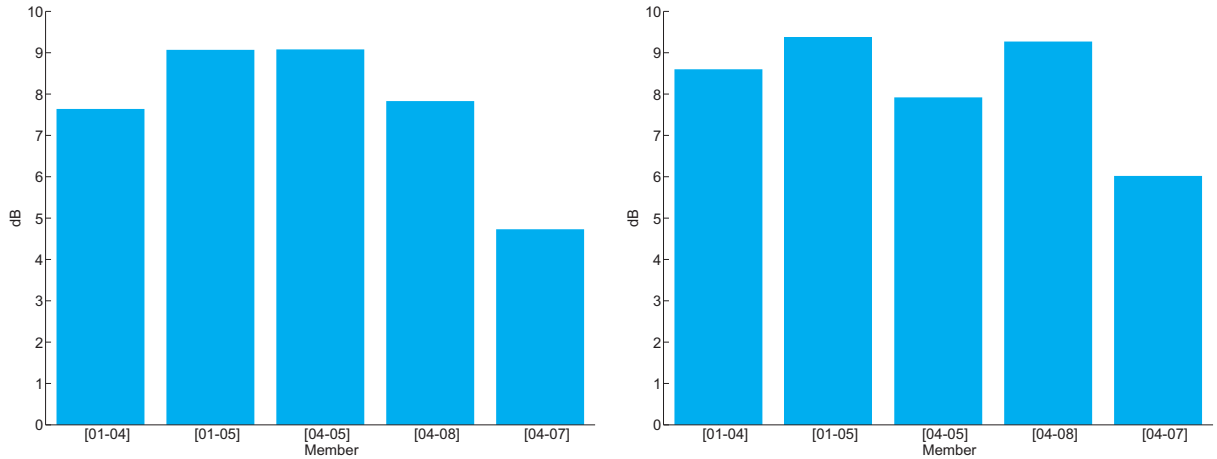

Figure 4.17: The attenuation obtained by feedforward control in the frequency range 20 Hz - 1 kHz using frequency resolution of 1 Hz when active control is applied close to the disturbance source. (a) for nominal values of the ratio $(I/l_B^2 S)_{\text{nominal}}$, (b) for values of the ratio $(I/l_B^2 S) = 10(I/l_B^2 S)_{\text{nominal}}$.

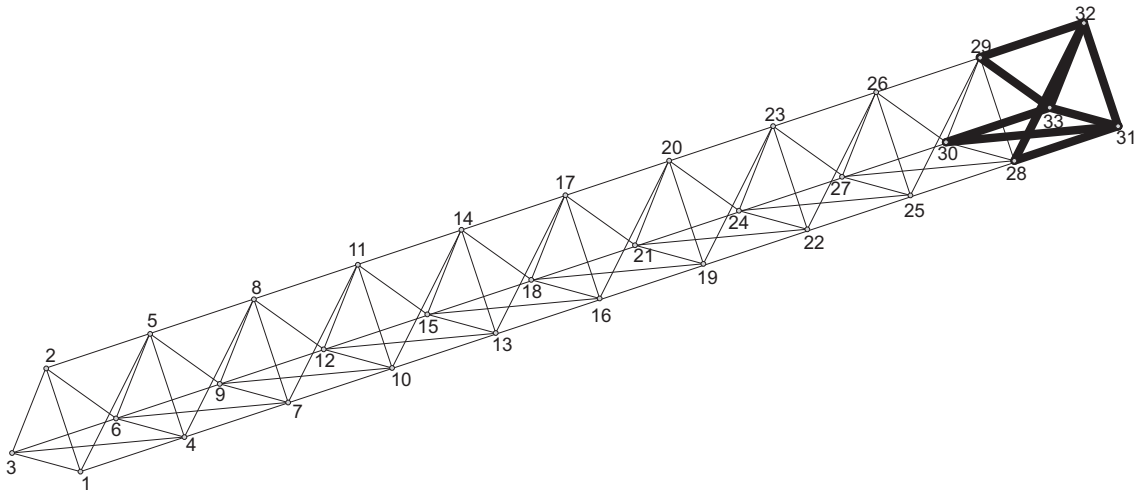

Figure 4.18: The lattice structure and the joint numbering scheme. Members plotted with thicker lines indicate the position close to the joints 31, 32 and 33 where feedforward control has been applied.

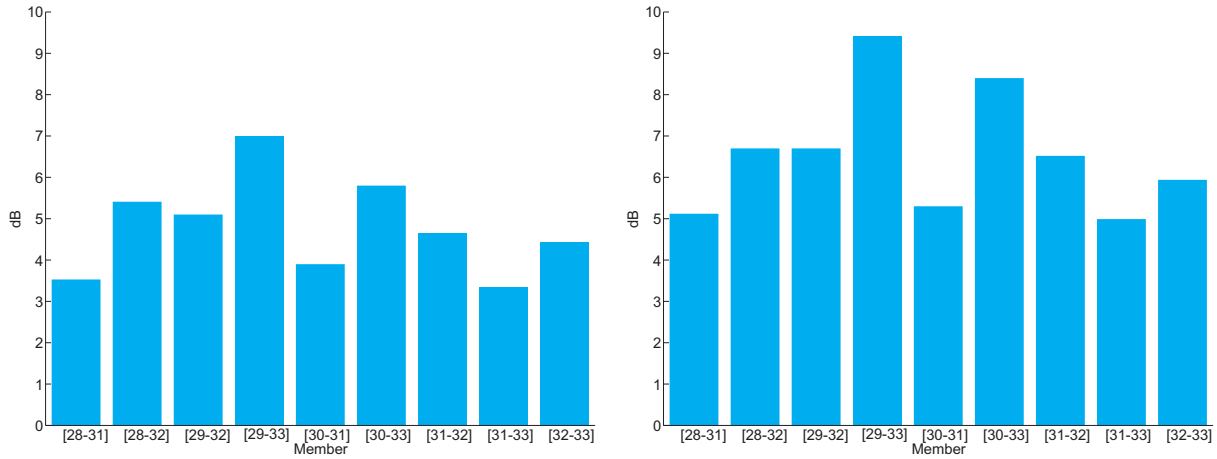

(a) (b)

Figure 4.19: The attenuation obtained by feedforward control in the frequency range 20 Hz - 1 kHz using frequency resolution of 1 Hz when active control is applied close to the joints 31, 32 and 33. (a) for nominal values of the ratio $(I/l_B^2 S)_{\text{nominal}}$, (b) for values of the ratio $(I/l_B^2 S) = 10(I/l_B^2 S)_{\text{nominal}}$.

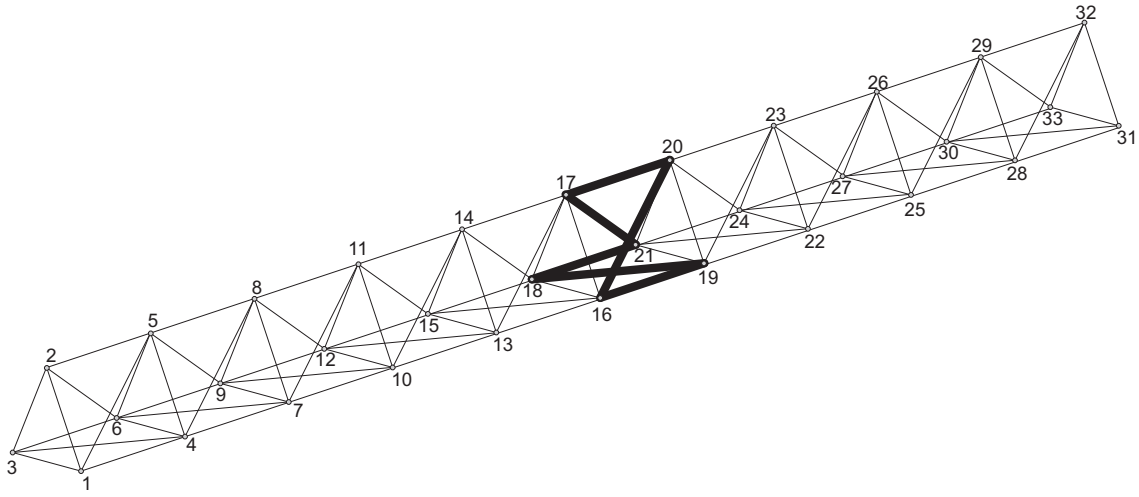

Figure 4.20: The lattice structure and the joint numbering scheme. Members plotted with thicker lines indicate the position in the middle of the lattice structure where feedforward control has been applied.

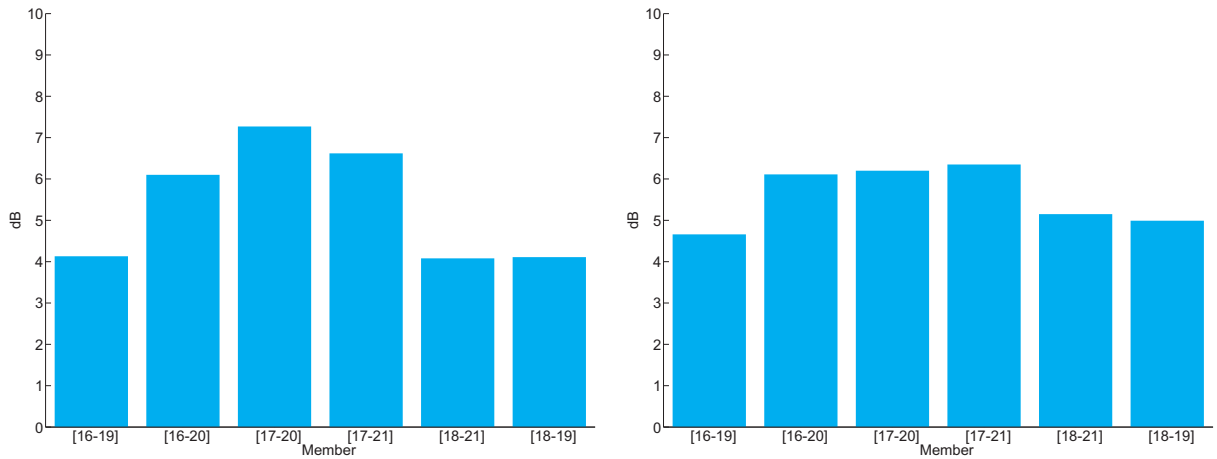

Figure 4.21: The attenuation obtained by feedforward control in the frequency range 20 Hz - 1 kHz using frequency resolution of 1 Hz when active control is applied in the middle of the lattice structure. (a) for nominal values of the ratio $(I/l_B^2 S)_{\text{nominal}}$, (b) for values of the ratio $(I/l_B^2 S) = 10 \times (I/l_B^2 S)_{\text{nominal}}$.

Chapter Five

The feedback control of vibration

5.1 Introduction

In this chapter, feedback control is considered as a strategy for reducing vibration in the lattice structure. The main aim of the chapter is to investigate a strategy of feedback control called integral force feedback (IFF) and determine which factors influence the performance when it is applied to control vibration in the lattice structure considered in this thesis. The influence of SWMs in the performance of feedback control is analysed, as well as the energy within the structure using power analysis. The numerical results of this chapter are based on the models obtained using the methods described in chapters 2 and 3. Some of the results are compared to the results of feedforward control from chapter 4.

The main difference between feedback and feedforward control is that no external reference signal is used, and the sensed output signal is used to drive the controller, including random and transient, but the performance is not generally as great as when external information drive the disturbance is incorporated in feedforward control.

5.2 Introduction to feedback control of vibration

Feedback control is an engineering discipline that is applied to various areas of science. In the field of vibration control, a feedback control system can reduce vibration by automatic modification of the structural response of the system. According to reference [55], a feedback active control system can assume many forms, but there are three important and common components; a sensor (to detect the vibration), an electronic controller (to manipulate the signal from the detector) and an actuator (to modify the mechanical response of the system). There is an enormous number of applications of feedback in the control of vibration in mechanical systems, so the review in this section discusses only about the applications in the field of space structures.

5.2.1 The feedback control applied to space structures

According to reference [103], the first major United States Government program in this area was the Active Control of Space Structures (ACOSS) started in 1978 which produced many of the first experiments related to the control of Large Space Structures [104, 105]. Various types of actuators have been considered in the feedback control of vibration of space structures. Laboratory experiments using magnet-coil force motors mounted on diagonal truss members, attached to the grounded base, are considered in references [106], [107], [108] and [109]. Grounded torque motors have been also considered in references [110] and [111]. Magnet-coil motors have limitations when used as primary load-carrying structural members because; 1) without electric power, they have zero stiffness; and 2) even with power, they are much more flexible than other similar structural members. (However such motors may be practical if applied in parallel with another structural member). Inertial actuators also known as reaction-mass or proof-mass actuators have been considered in references [112] and [113]. These types of actuators, however, have limitations in controlling vibration in frequencies below the natural frequency of the actuator. The use of tendons in the control of a flexible beam-like appendage attached to a large spacecraft is considered in references [114] and [115]. The use of piezoelectric active members to control vibration in space structures has also been considered by many researchers, for example, Wada [116] presents a general description of the research area of adaptive structures. Use of piezoelectric actuators in the semi-active control of space truss structures is considered in references [117] and [118]. The general theory of feedback control applied to the control of vibration in mechanical systems can be found in references such as [10, 55, 58, 119, 120, 121]. Applications of the IFF control strategy can be found in references such as [49, 57, 122, 123, 124, 125, 126, 127]. A recent reference on feedback control of a space lattice structures is given by [128].

5.3 Feedback control principles

Consider the block diagram describing the feedback control showed in chapter one and repeated in figure 5.1 for convenience, where $\mathbf{f}_d$ and $\mathbf{f}_c$ are the vectors of disturbance and

control forces. The terms $\mathbf{Y}_{sd}$ and $\mathbf{Y}_{sc}$ are mobility matrices relating the disturbance forces and control forces, respectively, to the vector of controlled velocities $\mathbf{v}_s$ and $\mathbf{H}_{fb}$ is a matrix of feedback control gains. The vector of controlled velocities can be written as

$$\mathbf{v}_s = \mathbf{Y}_{sd}\mathbf{f}_d + \mathbf{Y}_{sc}\mathbf{f}_c \tag{5.1}$$

As the controlled forces depend upon the control velocities $\mathbf{v}_s$, equation 5.1 can be written as

$$\mathbf{v}_s = \mathbf{Y}_{sd}\mathbf{f}_d + \mathbf{Y}_{sc}\mathbf{H}_{fb}\mathbf{v}_s \tag{5.2}$$

Equation 5.2 can be rearranged to give

$$\mathbf{v}_s = \left(\mathbf{I} - \mathbf{Y}_{sc}\mathbf{H}_{fb}\right)^{-1}\mathbf{Y}_{sd}\mathbf{f}_d \tag{5.3}$$

where, $\mathbf{I}$ is the identity matrix of the size of the product of $(\mathbf{Y}_{sc}\mathbf{H}_{fb})$. The cases considered in this thesis assume only collocated control. This means that the control input is applied at the same position and direction as the sensor output. Often in feedback control, the variables of interest, the velocities $(\mathbf{v}_m)$ are not in the same position where the control forces are applied. The general block diagram of such a feedback controller is represented in figure 5.2 in which the sensed velocities $\mathbf{v}_s$, which are feed back to the controller are distinguished from the measured velocities $\mathbf{v}_m$, used to evaluate the performance in the cost function. The closed loop response of the velocity vector $\mathbf{v}_m$ in this case is given by reference [58] as

$$\mathbf{v}_m = \left(\mathbf{Y}_{md} + \mathbf{Y}_{mc}\mathbf{H}_{fb}\left(\mathbf{I} - \mathbf{Y}_{sc}\mathbf{H}_{fb}\right)^{-1}\mathbf{Y}_{sd}\right)\mathbf{f}_d \tag{5.4}$$

There are many ways of designing the feedback controller to control the measured velocities $\mathbf{v}_m$. Optimal control, for example, can be used to specify the feedback controller that minimises a quadratic cost function involving $\mathbf{v}_m$, but requires a complete and accurate model of all the other responses in equation 5.4, usually in state-space form. The very high order of the dynamics of the structure considered here, as dis-

cussed in chapter 2 with about 700 modes in the bandwidth of interest would mean that such an optimal design would be computationally demanding. The optimal design also assumes that the system responses are fixed, whereas in reality there will be considerable changes, particularly in the responses of the higher order modes, with small temperature changes, external loads, etc. It was thus felt that such an optimal controller is impractical in this case.

Other feedback control approaches, using collocated actuators and sensors, are inherently stable, despite any changes in the response of the structure [10]. They have the additional advantage of using only single channel feedback loops, and are thus decentralized and inherently modular [129]. One such method, which is particularly applicable to lattice structures, is integral force feedback, in which a displacement actuator is driven by the integrated amplitude of a force sensor at one end. Preumont [10] shows that such an arrangement can only dissipate power, and must thus be inherently stable.

5.3.1 Stability of a single channel feedback control system

In the case of single channel feedback control, equation 5.4 can be written as

$$\mathbf{v}_m = \left(\mathbf{Y}_{md} + \mathbf{y}_{mc} H_{fb} \left(1 - Y_{sc} H_{fb}\right)^{-1} \mathbf{Y}_{sd}\right) \mathbf{f}_d \tag{5.5}$$

where Y_{sc} and H_{fb} are now complex numbers. According to reference [55] the stability of the system can be determinated by inspection of the position of the closed loop poles. The poles of the system can be determinated by finding the roots of the characteristic equation in the Laplace domain for a SISO (single input single output) system given by

$$\left(1 - Y_{sc}(s) H_{fb}(s)\right) = 0 \tag{5.6}$$

In many practical cases, especially when Y_{sc} must be measured experimentally, the polynomial form showed in equation 5.6 is not available. The stability of the system then needs to be determinated from input-output measurements, made on the system before control. The Nyquist stability criterion provides such a method, using the

open loop response ($Y_{sc}(j\omega)H_{fb}(j\omega)$). The theoretical bases for the Nyquist stability criterion is described, for example, in references [54], [57] and [130]. The outcome is that the closed loop system is stable only if the Nyquist plot of the open loop frequency response ($Y_{sc}(j\omega)H_{fb}(j\omega)$) does not enclose the point (-1,0) as ω varies from $-\infty$ to ∞.

5.4 Integral force feedback

Consider the diagram of force feedback control shown in figure 5.3, where the structure is subject to two forces f_c in opposite directions driven by the piezoelectric actuator. The integral force feedback controller is driven by the sensed force f_s in the member where the actuator is inserted (which is measured by a force sensor indicated in the figure). The feedback controller applies a voltage to the actuator proportional to this force that is converted to an extension or compression of the piezoelectric actuator. According to the diagram describing the elements of force feedback control shown in figure 5.4, the closed loop measured force f_s can be expressed as

$$\mathbf{f}_s = \mathbf{G}_{sd}\mathbf{f}_d + \mathbf{D}_{sc}\mathbf{H}_{\text{iff}}\mathbf{f}_s \tag{5.7}$$

where, $\mathbf{G}_{sd}$ is a transmission matrix which relates the disturbance forces $\mathbf{f}_d$ with the sensed forces $\mathbf{f}_s$. $\mathbf{D}_{sc}$ is the dynamic stiffness matrix that relates the unconstrained actuator displacements to the sensed forces. $\mathbf{H}_{\text{iff}}$ is a matrix of feedback gains and $\mathbf{f}_s$ is the closed loop measured forces. The integral feedback matrix $\mathbf{H}_{\text{iff}}$ can, for example, be written as

$$\mathbf{H}_{\text{iff}} = \frac{1}{j\omega}\begin{bmatrix} H_1 & 0 & \dots & 0 \\ 0 & H_2 & \dots & 0 \\ \vdots & \vdots & \ddots & \vdots \\ 0 & 0 & \dots & H_{n_c} \end{bmatrix} \tag{5.8}$$

where, H_1, H_2, $\dots H_{n_c}$ are the feedback gains for the actuators 1, 2, $\dots n_c$, where n_c is the number of control actuators to be used. Note that this matrix is diagonal, which implies decentralized control. The elements of the transmission matrix $\mathbf{G}_{sd}$ are

calculated one by one, The force in the *a-th* sensor $f_s(a,k)$ due to the *k-th* disturbance force $\mathbf{f}_d(k)$, is given by

$$f_s(a,k) = \mathbf{b}\mathbf{T}_a\mathbf{B}_a\mathbf{D}^{-1}\mathbf{f}_d(k) \tag{5.9}$$

where, $\mathbf{T}_a$ is the coordinate transformation matrix for the member where the sensor a is placed with dimension 12×12, $\mathbf{B}_a$ is the Boolean matrix that maps the joint coordinates of the member where the sensor is placed with the local coordinates of the member (as discussed in chapter 2 and 4) with dimension $12 \times 6n_{\mathrm{j}}$ (where n_{j} is the number of joints in the structure). The matrix $\mathbf{D}$ is the dynamics stiffness the whole structure, with dimension $6n_{rmj} \times 6n_{\mathrm{j}}$, $\mathbf{f}_d(k)$ is the vector of *k-th* disturbance force, with dimension $6n_{\mathrm{j}} \times 1$ and $\mathbf{b}$ is used in order to consider the longitudinal reactions on the structural member, given by

$$\mathbf{b} = \begin{bmatrix} -1 & 0 & 0 & 0 & 0 & 0 & 1 & 0 & 0 & 0 & 0 & 0 \end{bmatrix} \tag{5.10}$$

The closed loop sensed force can be calculated as

$$\mathbf{f}_s = \left(\mathbf{I} - \mathbf{D}_{sc}\mathbf{H}_{\mathrm{iff}}\right)^{-1}\mathbf{G}_{sd}\mathbf{f}_d \tag{5.11}$$

The velocity vector $\mathbf{v}_m$ can then be calculated as

$$\mathbf{v}_m = \mathbf{Y}_{md}\mathbf{f}_d + \mathbf{Y}_{md}\mathbf{D}_{sc}\delta_c \tag{5.12}$$

The relationship between the voltage applied and the unconstrained deformation in the piezoelectric actuator is given by [10]

$$\delta = n_s d_{33} V \tag{5.13}$$

where, n_s is the number of piezoelectric stack disks, d_{33} is the piezoelectric constant and V is the voltage applied to the actuator, which is proportional to f_s. The unconstrained control deformation δ_c of the piezoelectric actuator is given by

$$\delta_c = \mathbf{H}_{\text{iff}} \mathbf{f}_s \tag{5.14}$$

The elements of the dynamic stiffness matrix $\mathbf{D}_{sc}$ are also calculated one by one for each of the control displacements, according to the longitudinal displacements of the piezoelectric actuators. The closed loop velocities $\mathbf{v}_m$ are found by combining equations 5.11, 5.12 and 5.14 to give

$$\mathbf{v}_m = \left(\mathbf{Y}_{md} + \mathbf{Y}_c \mathbf{D}_{sc} \mathbf{H}_{\text{iff}} \left(\mathbf{I} - \mathbf{D}_{sc} \mathbf{H}_{\text{iff}} \right)^{-1} \mathbf{G}_{sc} \right) \mathbf{f}_d \tag{5.15}$$

which is the analogue of equation 5.5 in terms of the structural response.

5.5 Numerical simulations of IFF control

In this section simulations of IFF control are presented. The system responses are obtained by the dynamic stiffness method described in chapter 2. In a way similar to the procedure described in chapter 4, the actuator properties are not considered in the model for simplicity of the simulations. The disturbance force is applied at joint 4 in the y direction for the frequency range 20 Hz - 1 kHz. Exhaustive simulations were performed for all possible positions to place a single actuator in the structure, the behaviour of the cost function for different values of feedback gain, the placement of the actuator and the stability and performance of the controller regarding the influence of SWM considered in the following sections. The use of two actuators is considered in section 5.7.1, including the stability analysis of multiple actuators.

5.5.1 One control actuator

For one control actuator implementing IFF, the feedback control $\mathbf{H}_{\text{iff}}$ can be written as

$$\mathbf{H}_{\text{iff}} = \frac{H}{j\omega} \tag{5.16}$$

where, H is a constant gain given in m/N. The results in figure 5.5 show the behaviour of the sensed force in the closed loop with the actuator in position [17-20]. As the

feedback gain h increases, the force f_s decreases, and in the limit of $H \to \infty$, $f_s \to 0$. The interest, however, is to minimize the cost function J which comprises the sum of the squared velocities of the vector $\mathbf{v}_m$. It is then necessary to choose H in such a way that $\mathbf{J}_m$ is minimum. Figure 5.6 shows the sum of frequency points in the bandwidth 20 Hz - 1 kHz using 1 Hz of frequency resolution for the effort measured in sensor, while 5.7 shows the behaviour of the cost function for the same values of feedback gain. As an example, the attenuation in the cost function J as a function of the IFF gains is shown in figure 5.8 for some of the positions for a single actuator in the lattice structure. It can be seen that, although the attenuation in the cost function is small, there is a maximum for each position for placing a single actuator. Higher values of feedback can cause enhancement in the cost function

Because of the SWMs it is not possible to identify a good position for placing actuators using, for instance, the approach discussed in the work of Preumont (the fraction of modal strain) [122], which is discussed in section 5.6 of this chapter. For this reason, exhaustive simulations were performed on the lattice structure to find optimal positions for placing a single actuator. The results of the maximum attenuation in the cost function (for the frequency range 20 Hz - 1 kHz) obtained for each position in the structure are shown in figure 5.9 while the results of figure 5.10 shows the respective values of feedback gain that give these maximum attenuation. In both figures the joint number of the members can be identified in the appendix G. The conclusion from these results is that the maximum attenuation obtained is smaller than 3 dB, which can be considered small compared to the 9.08 dB achieved by feedforward control.

5.5.2 Stability analysis

In this section the Nyquist stability criterion is used to check the stability of IFF control described in the previous sections for a single control actuator. This analysis is based on the complex open loop frequency response of the controller $D_{sc}H_{\text{iff}}$, which is stable in the open loop, whose polar plot should not enclose the point (-1,0) in the complex plane if the system is to be stable [57]. The stability analysis has been performed for all the positions considered in the previous section. A typical Nyquist diagram is shown in figure 5.11, for an actuator placed at member [17-20]. If the actuator was massless, the

system would be unconditionally stable, since the controller could only dissipate power [10]. The actuator mass influences the longitudinal natural frequency of the actuator at which the phase is greater than 90°, as can be seen in figure 5.12. The longitudinal natural frequency of the actuator, however, is much higher than the frequency range of interest in this case. The Nyquist plot in figure 5.11 has been plotted for the frequency range 20 Hz - 1 kHz, while the result in figure 5.12 has been plotted in the frequency range 20 Hz - 5.9 kHz, and the longitudinal natural frequency of the actuator in this case is 5650 Hz.

5.6 The control of long wavelength modes

In this section, the case of controlling only LWM of the lattice structure is considered. For structures that have only long wavelength modes in the frequency range of interest, the selection of actuator position for feedback control has been described by Preumont, [10]. The modelled the structure using the finite element method, where structural members were modelled as truss elements (considering only longitudinal motion). The equation of motion for such undamped systems, in the frequency domain is given by

$$\left(-\omega^2\mathbf{M} + \mathbf{K} + \mathbf{K}_a\right)\mathbf{q} = \mathbf{f} \tag{5.17}$$

where, $\mathbf{M}$ is the mass matrix, $\mathbf{K}$ is the stiffness matrix of the system without the stiffness of the actuator and $\mathbf{K}_a$ is the stiffness matrix of the actuator given in global coordinates; $\mathbf{q}$ and $\mathbf{f}$ are the displacement and force vectors, respectively. The natural frequencies and mode shapes of the system are found by solving the following eigenvalue problem

$$\left(-\omega_i^2\mathbf{M} + (\mathbf{K} + \mathbf{K}_a)\right)\phi_i = 0 \tag{5.18}$$

where ϕ_i is the eigenvector (mode shapes) and ω_i is the eigenvalue (natural frequency). According to reference [10], the positions for placing actuators can be found using the *fraction of modal strain energy* given by

$$v_i = \frac{\phi_i^T \mathbf{B}_a^T \mathbf{T}_a^T \mathbf{K}_a \mathbf{T}_a \mathbf{B}_a \phi_i}{\phi_i^T (\mathbf{K} + \mathbf{K}_a) \phi_i} \tag{5.19}$$

where, v_i is the fraction of modal strain which can be seen as a ratio between the potential energy in the a member and the total potential energy in the system for the mode shape i. In practice, the value of v_i works as a controllability and observability index, where large values of v indicates regions in the structure where actuators should be placed for high control authority for a certain mode. To illustrate this, the fraction of modal strain energy v_i is calculated for the first six LWM of the structure using the finite element method and considering only the longitudinal motion of the members. These results are shown in figures 5.13-5.18 where the structural members plotted with thicker lines indicate the places with larger modal strain energy for that mode. Feedback control of each of these modes independently is described in [120, 121]. in which at least one actuator is used to control each of mode of the structure.

5.7 The influence of SWM in the performance of IFF control

To verify the influence of SWM in the performance of feedback control, numerical simulations where performed and the results are discussed in this section. The member [17-20] has again been chosen as the actuator position since this location has the largest value of the fraction of modal strain for the first bending mode (bending in the z direction). The analysis was carried out for values of the ratio

$$\mu = \frac{(I/l_B^2 S)}{(I/l_B^2 S)_{\text{nominal}}} \tag{5.20}$$

with μ varying from 1 to 25. The SW natural frequencies varies of the square root of the ratio $(I/l_B^2 S)$ and in this case it is possible to shift the SW natural frequencies to higher frequencies in such a way that $\beta_i > 1$. This means that the first SWM will occur at frequencies greater than those of the *i-th* LWM.

For each of the values of μ, the maximum attenuation in the cost function (in the frequency range 20 Hz - 1 kHz) was found by exhaustive search of the feedback gains. The results of this simulation are shown in figure 5.19, that compares the attenuation due to IFF control with that obtained with feedforward control using the same actuator.

It is clear that for low values of μ, the low frequency response of the structure is dominated by SWMs and the performance of the feedback controller is small. For values of $\mu > 5$, the low frequency response of the structure is dominated by LWMs as can be seen in figure 5.20 where the cost function has been plotted for $\mu = 10$, for example. The low frequency peaks in the cost function are identified according to the modes shown in figure 5.21. The IFF control can then control the peak of the cost function associated with the first bending mode and have also some control authority of the peak associated with the first torsional LWM as shown in figure 5.22. This result shows also that the attenuation at high frequencies is small.

The detail of the low frequency range is shown in figure 5.23 where these results have also been compared with the results of feedforward control. In figure 5.24, a similar result is given for the system with nominal properties. The results of figure 5.25 can be used to help explain these differences in the performance, where the attenuation in this frequency range (20 Hz - 100 Hz) has been plotted as a function of the IFF gain. It can be seen that for the case without SWM, the attenuation of in the cost function is greater than that for the case with SWM. The values of feedback gain are also slightly different.

To complement this analysis, simulations were performed for three other regions of the lattice structure; (close to the positions where disturbance force is applied (joint 4), close to the joints 31, 32 and 33 and in the middle of the lattice structure). A number of structural members have been chosen in these regions as a position to place a single actuator positions and the attenuation values have been obtained for two values of the ratio μ as described bellow in terms of the SW and LW natural frequencies for bending and torsion of the structure

- $\mu = 1$, $(\omega_1)_{SWM} < (\omega_1)_{LWM,\text{ bending}}$, $(\omega_1)_{SWM} < (\omega_1)_{LWM,\text{ torsional}}$
- $\mu = 10$, $(\omega_1)_{LWM} > (\omega_1)_{LWM,\text{ bending}}$, $(\omega_1)_{LWM} > (\omega_1)_{LWM,\text{ torsional}}$

This means that for vales of $\mu = 10$, the first SW natural frequency is greater than the first LW bending natural frequency and the first LW torsional natural frequency. For nominal values of $(I/l_B^2 S)$ $(\mu = 1)$, the first SW natural frequency is smaller than both LW bending and torsional natural frequencies. Figures 5.26, 5.28 and 5.30 illustrate

the positions where IFF control was implemented. The comparison for the attenuation in the cost function in the frequency range 20 Hz - 1 kHz (calculated using equation 4.18) are shown in figures 5.27, 5.29 and 5.31. These figures shows that there is a increase in the performance of the IFF control when the SWM modes are shifted to higher frequencies for the members that are placed at a position with large fraction of modal strain. This can be seen in figure 5.31, where those positions have large control authority to control the first bending and torsional LWM and at position [04-08] of figure 5.27, where this member have large control authority to control the second bending LWM.

5.7.1 Two control actuators

In this section the effect of decentralized integral force feedback control is investigated using two actuators. As the influence of SWM reduces the performance of the IFF control, the implementation of IFF with two control actuators is simulated for a system with ratio $\mu = 10$. The values of the two feedback gain were found by exhaustive search in a range of values based in the attenuation of the cost function for the frequency range 20 Hz - 100 Hz. The first actuator is placed in the position of member [16-20] and the second actuator is placed in the position of member [17-20] as shown in figure 5.32. Figure 5.33 shows the attenuation in the cost function for a range of values of the feedback gains in both controllers. The values of the feedback gains that produce the optimum attenuation in the cost function used in the simulations were $H_1 = 5.83 \times 10^{-5}$ m/N and $H_2 = 1.25 \times 10^{-5}$ m/N. The cost function without control is compared with the results of IFF and feedforward control in figure 5.34, and the detail in low frequency is shown in figure 5.35. The attenuation in the frequency range 20 Hz - 100 Hz obtained by the IFF control is 7.4 dB while for feedforward control, the attenuation is 12.6 dB.

5.7.2 Stability analysis for multiple actuators

The analysis of stability of multiple control actuators can be assessed by the graphical techniques similar to the Nyquist criterion described in a previous section of this chapter [130]. This can be done by considering the roots of the controller characteristic

equation. According to the Nyquist stability criteria, a multi-channel control systems is stable if it is open loop stable and the plot of det $[\mathbf{I} - \mathbf{D}_{sc}\mathbf{H}_{\text{iff}}] = 0$ does not encircle the point (-1,0) in the complex plane as the frequency goes from $-\infty$ to $+\infty$. This can also be evaluated by examining the individual eigenvalues $[\mathbf{D}_{sc}\mathbf{H}_{\text{iff}}]$ 1which must then be correctly ordered, [131]. According to [130], the generalized (MIMO) Nyquist theorem is given as: Let P_{ol} denote the number of open-loop unstable poles in a transfer function L(s). The closed-loop system with loop transfer function L(s) and negative feedback is stable if and only if the Nyquist plot of $det(I + L(s))$

1. makes P_{ol} anti-clockwise encirclements of the origin, and
2. does not pass through the origin.

where, "Nyquist plot of $det(I + L(s))$" means the image of $det(I + L(s))$ as s goes clockwise around the Nyquist D-contour. The prof of the theorem is given in the same reference [130]. The polar plots of the eigenvalues for the two controllers placed at members [16-20] and [17-20] are shown in figure 5.36. It can be seen that for the feedback gains used, the circles do not enclose the instability point.

5.8 The analysis of power in IFF control

In this section, the behaviour of energy in the lattice structure when IFF control is applied to reduce the cost function is considered using the analysis of power described in chapters 2 and 3. Exhaustive simulations where performed for all positions to place a single actuator in the lattice structure. The optimal values of gain for IFF control have been used considering the attenuation in the cost function for the frequency range 20 Hz - 1 kHz. As discussed by Preumont [49], this type of active control strategy can only dissipate power (for frequencies different from that of the longitudinal natural frequency of the actuator). This can be seen in the results shown in figure 5.37. This figure is similar to the results shown in the figure 4.15 of chapter 4, where

- $p_d(\text{in})_{\text{without control}}$ is the power from the disturbance source before IFF control is applied

- $p_d(\text{in})_{\text{with control}}$ is the power from the primary disturbance after IFF control is applied
- p_c is the power provided/dissipated from the control sources

All the results in figure 5.37 are normalized to $p_d(\text{in})_{\text{without control}}$. Figure 5.37(a) shows the power from the disturbance sources after IFF control is applied to the system, 5.37(b) shows the total power ($[p_d(\text{in})_{\text{with control}} + p_c]$) when IFF control is applied to the system and 5.37(c) shows the power from the control forces p_c, which are all negative. It can be seen that the behaviour of IFF control is purely dissipative. The power from the disturbance source is not affected much by action of the feedback control. The results of figure 5.38 shows the typical power dissipated by the IFF controller as a function of the frequency when control is applied at member [17-20] for a structure with ratio $\mu = 10$ ($(I/l_B^2 S) = 10(I/l_B^2 S)_{\text{nominal}}$). The total power input in the system ($p_d(\text{in})_{\text{with control}} + p_c$) after control is applied is compared with the power input in the system before control is applied in figure 5.39 showing also the low frequency detail. It can be seen, there is a reduction in the peaks associated to the first bending LWM as the actuator is placed at member [17-20].

5.9 Concluding Remarks

In this chapter, integral force feedback has been considered as a strategy for control of vibration in the lattice structure. It has been shown that the performance of this strategy of active control can be limited if a frequency band has SWMs. The optimal placement for actuators using the fraction of modal strain can only be used to control LWMs and it is necessary at least one control actuator per each mode to be controlled. It has been shown that the performance of the active control is improved when SWM are shifted to higher frequencies changing the ratio $(I/l_B^2 S)$ and placing the actuator according to the index of fraction of modal strain. It has been also shown that the behaviour of the IFF control is purely dissipative, where the power from the disturbance sources are not affected much the action of the controller, but the total power is reduce due to the enhancement of the dissipation of energy in the active member.

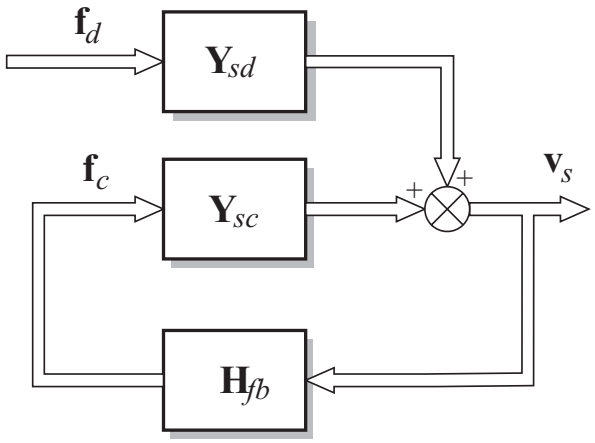

Figure 5.1: A block diagram describing the basic elements of feedback control.

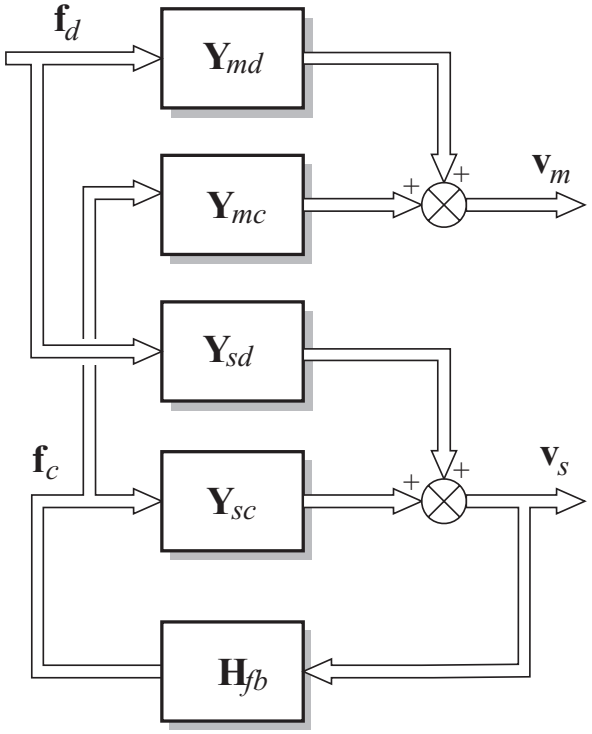

Figure 5.2: A block diagram describing the elements of feedback control including the measured velocities $\mathbf{v}_s$ and the objective velocities $\mathbf{v}_m$.

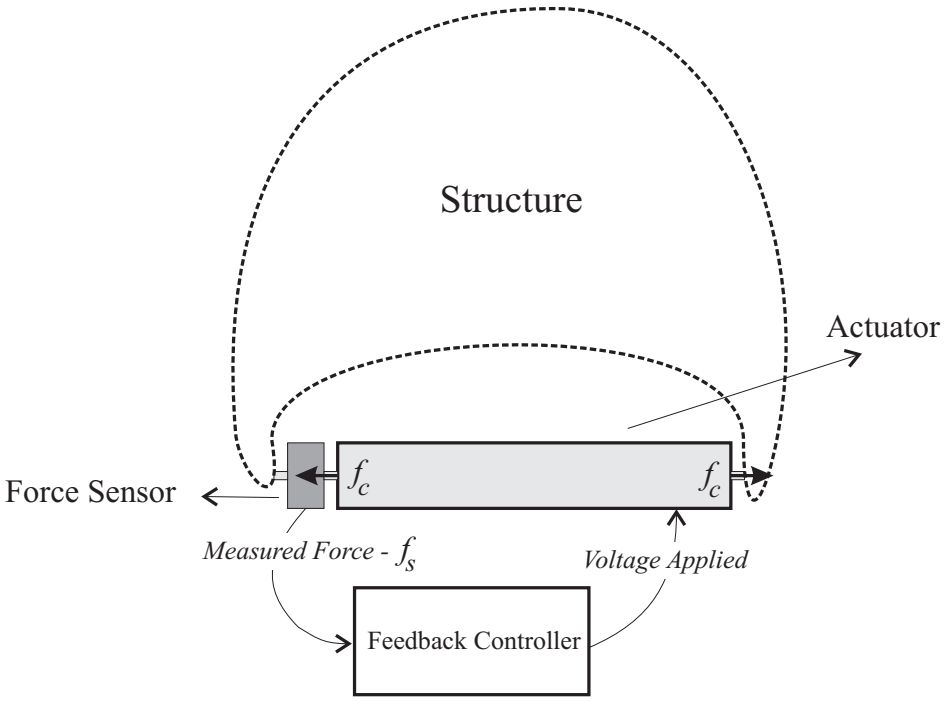

Figure 5.3: A diagram describing force feedback control in a structure with a piezoelectric actuator attached.

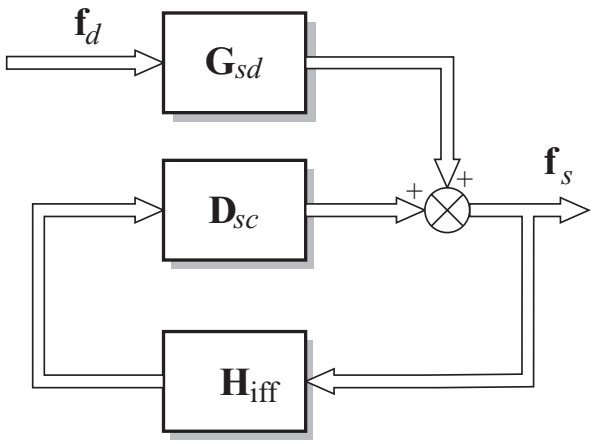

Figure 5.4: A block diagram describing the elements of force feedback control.

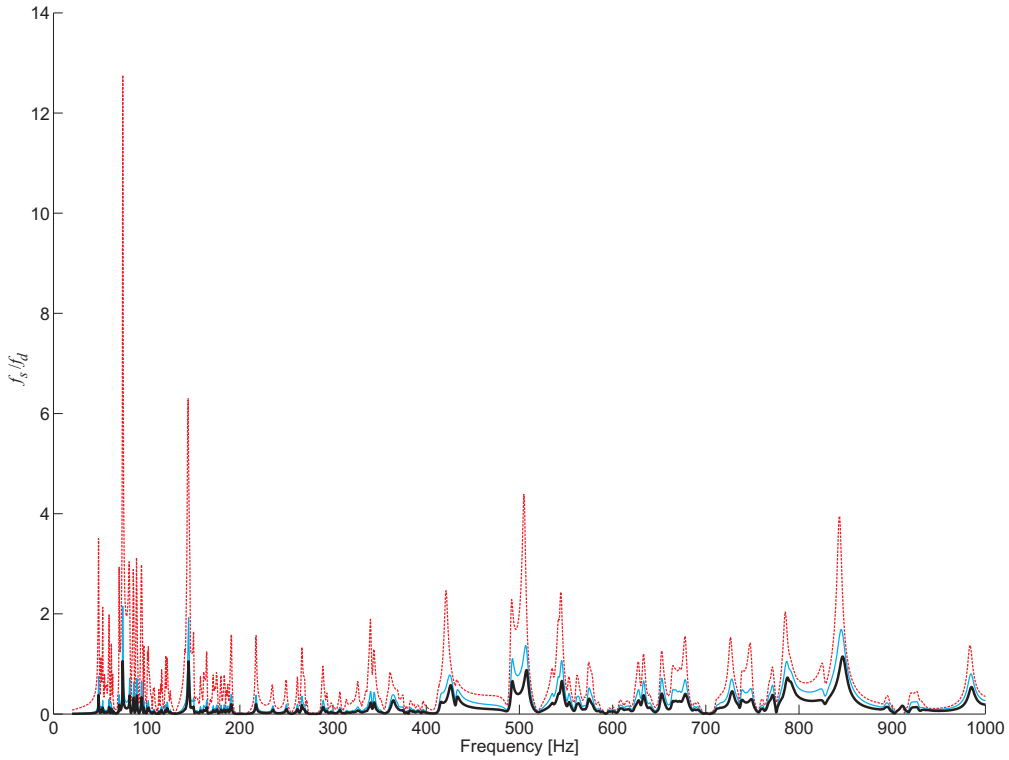

Figure 5.5: The measured force f_s normalized by the disturbance force f_d for different values of gain. The dashed line is for $h = 4.17 \times 10^{-5}$ m/N, the thin line is for $h = 3.75 \times 10^{-4}$ m/N and the thick line is for $h = 7.92 \times 10^{-4}$ m/N.

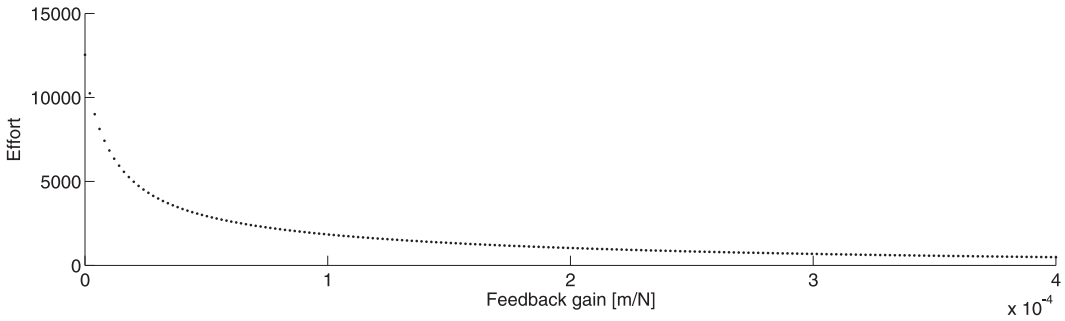

Figure 5.6: The sum of the sensed force effort in the frequency range 20 Hz - 1 kHz (using 1 Hz of frequency resolution) as a function of the IFF gain. Actuator is placed at member [17-20].

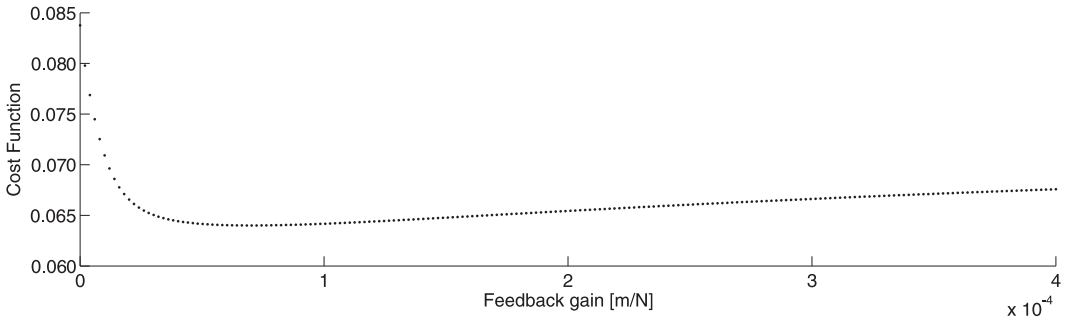

Figure 5.7: The sum of the cost function in the frequency range 20 Hz - 1 kHz (using 1 Hz of frequency resolution) as a function of the IFF gain. Control is applied at member [17-20].

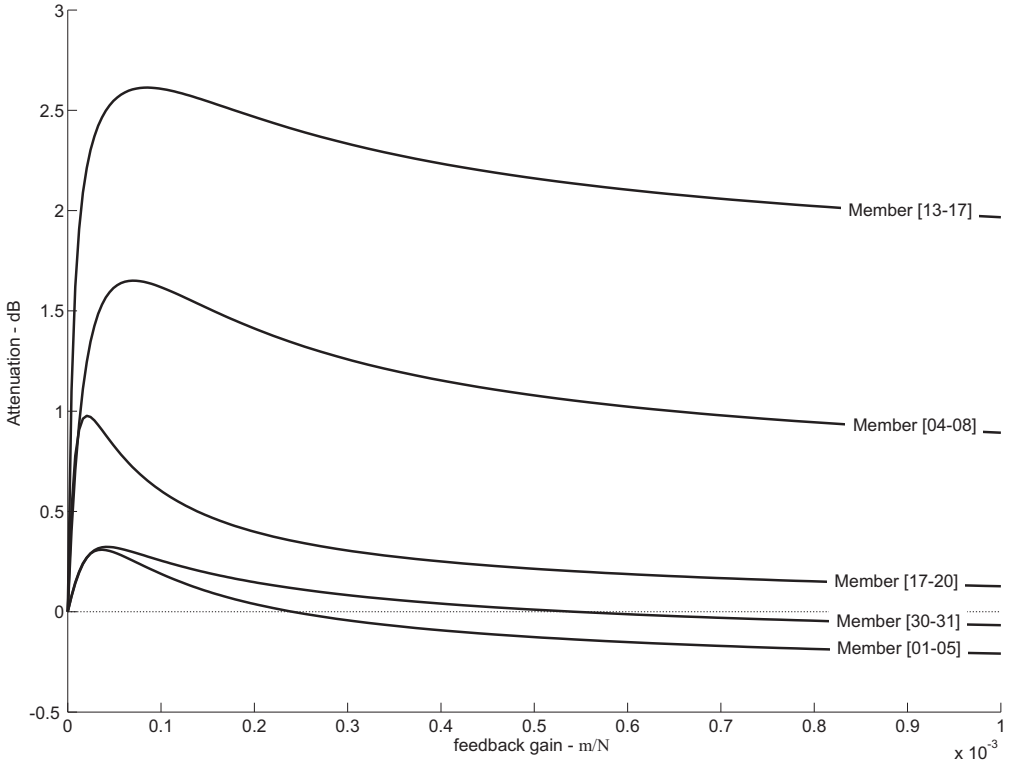

Figure 5.8: The attenuation in the cost function J as a function of the integral force feedback gain given in m/N for some of the position for placing one actuator.

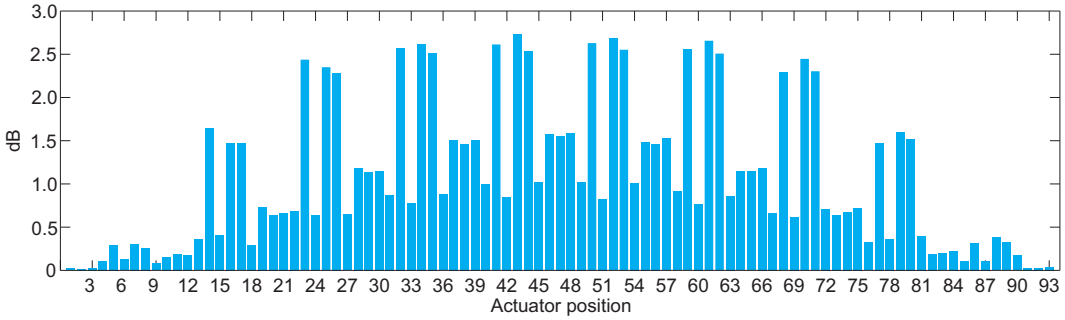

Figure 5.9: The maximum attenuation in the cost function for each position for placing a single actuator in the structure for the frequency 20 Hz - 1 kHz using 1 Hz of frequency resolution. dB ref. 1 m^2/Ns^2. The actuator position are represented by numbers which are identified in the appendix G.

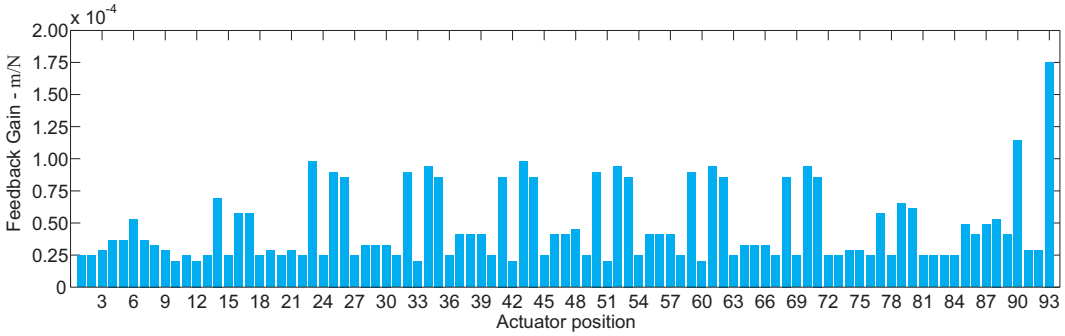

Figure 5.10: The values of feedback gain that produces the maximum attenuation in the cost function shown in figure 5.9. The members are represented by numbers which are identified in the appendix G.

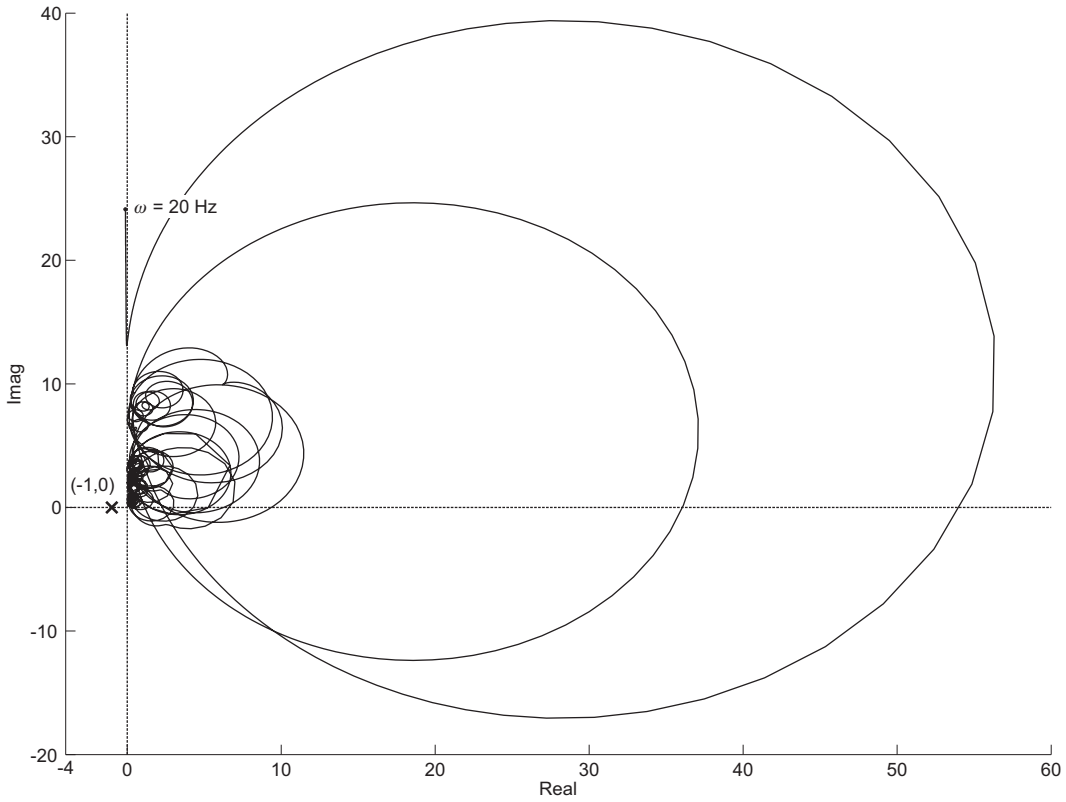

Figure 5.11: The real and imaginary part of the of loop transfer function $D_{sc}H_{\text{iff}}$ when control is applied at member [17-20].

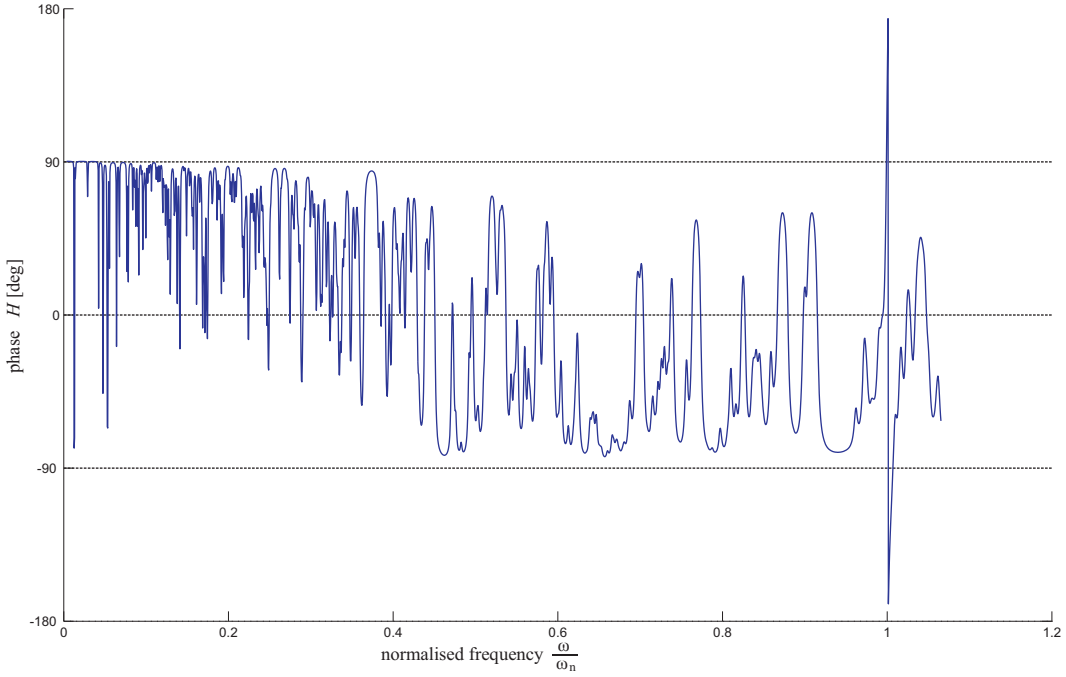

Figure 5.12: Typical phase diagram of a integral force feedback controller with normalised frequency ω/ω_n, where ω_n is the first longitudinal natural frequency of the actuator.

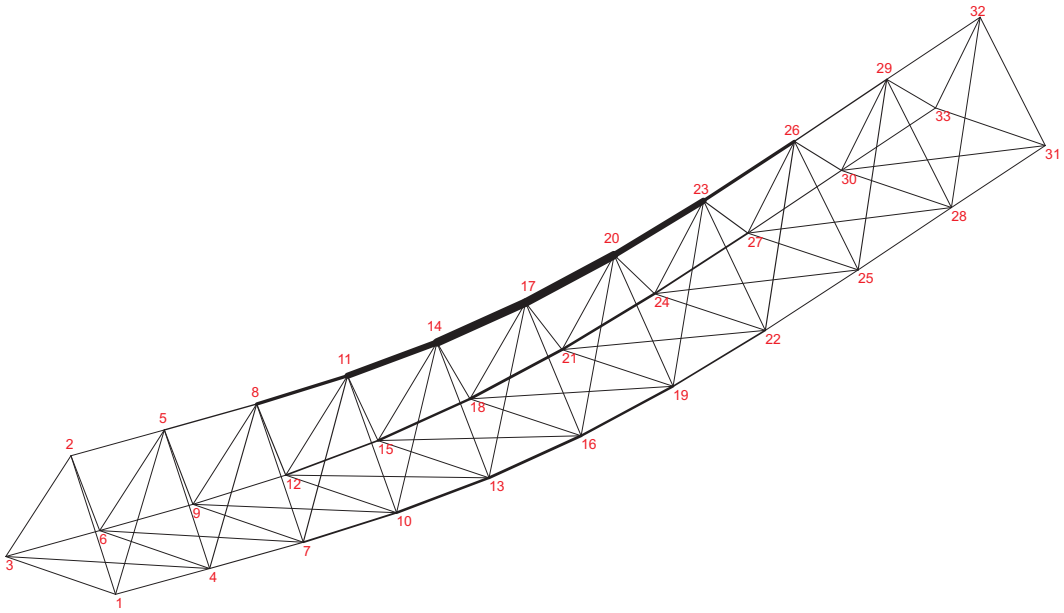

Figure 5.13: The first mode of the lattice structure obtained by the finite element method considering only longitudinal motion of the structural members. The structural members plotted with thicker lines correspond to the positions with higher indexes of fractional strain energy for that mode.

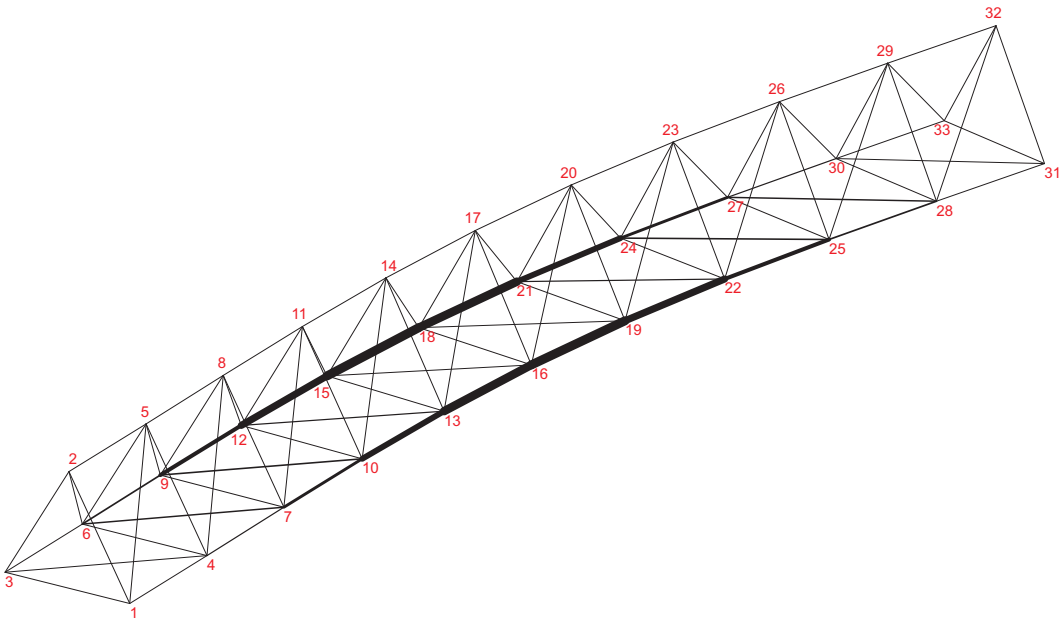

Figure 5.14: The second mode of the lattice structure obtained by finite element method considering only longitudinal motion of the structural members. The structural members plotted with thicker lines correspond to the positions with higher indexes of fractional strain energy for that mode.

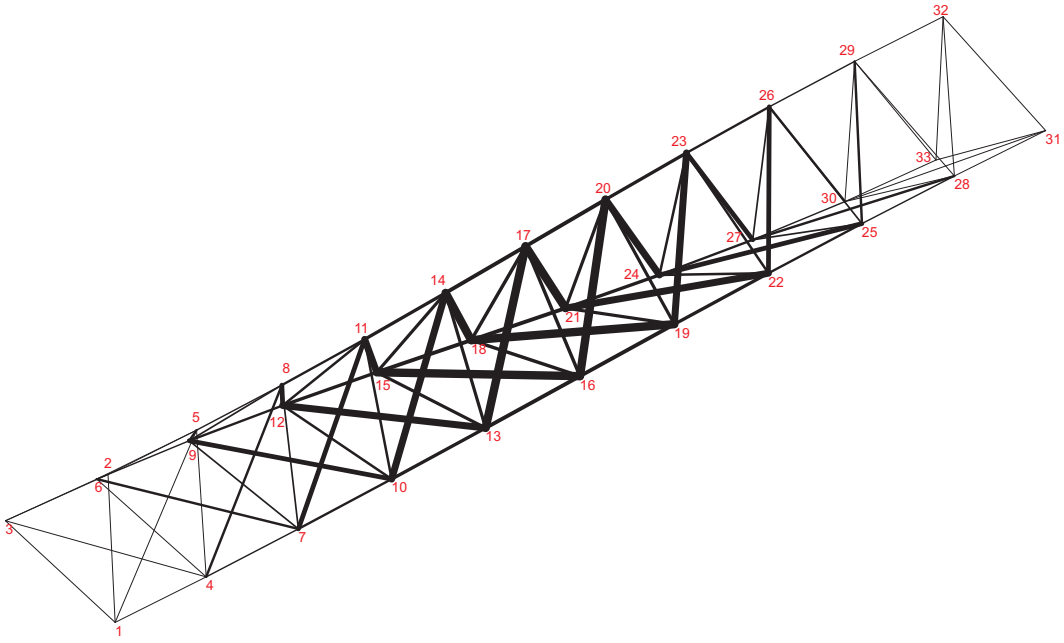

Figure 5.15: The third mode of the lattice structure obtained by finite element method considering only longitudinal motion of the structural members. The structural members plotted with thicker lines correspond to the positions with higher indexes of fractional strain energy for that mode.

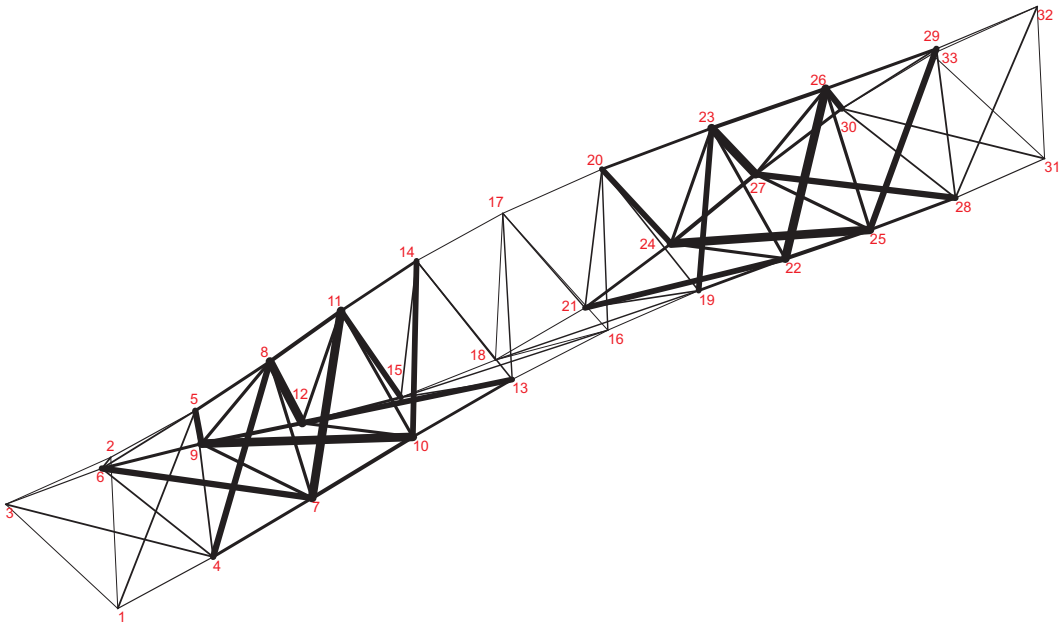

Figure 5.16: The fourth mode of the lattice structure obtained by finite element method considering only longitudinal motion of the structural members. The structural members plotted with thicker lines correspond to the positions with higher indexes of fractional strain energy for that mode.

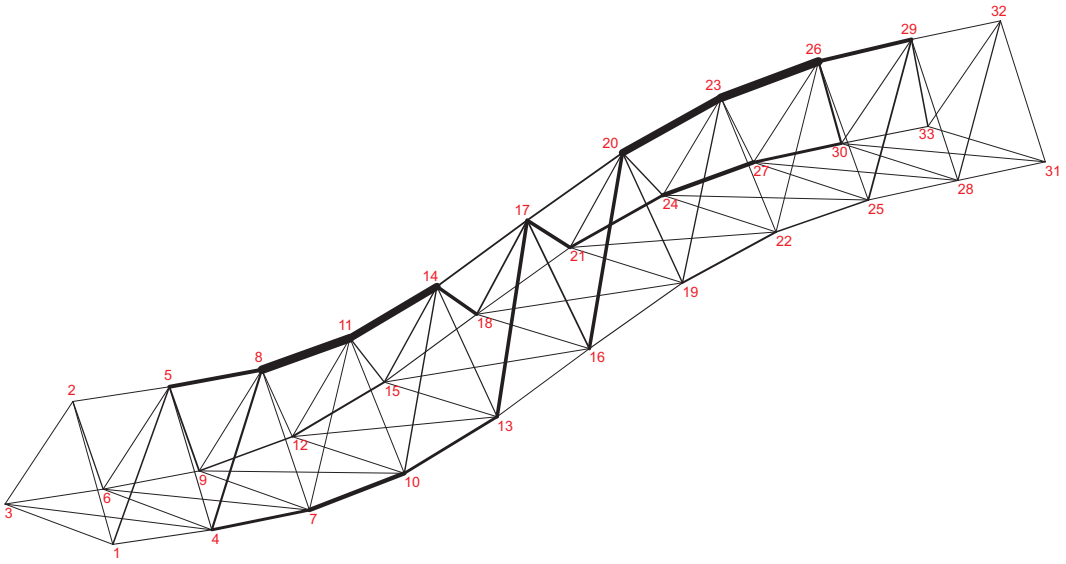

Figure 5.17: The fifth mode of the lattice structure obtained by finite element method considering only longitudinal motion of the structural members. The structural members plotted with thicker lines correspond to the positions with higher indexes of fractional strain energy for that mode.

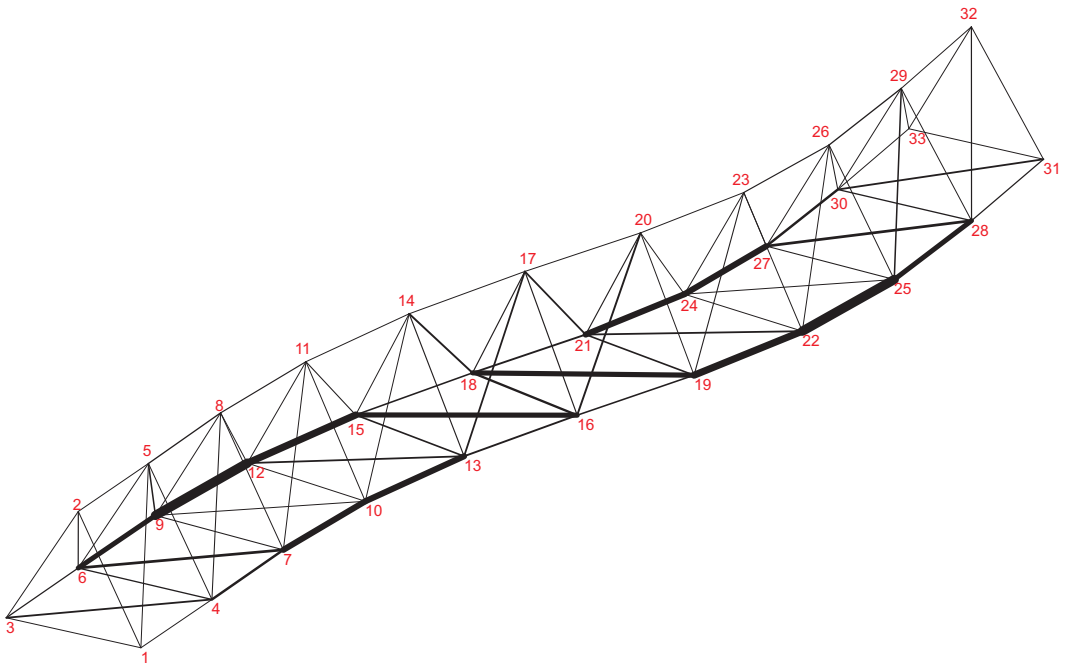

Figure 5.18: The sixth mode of the lattice structure obtained by finite element method considering only longitudinal motion of the structural members. The structural members plotted with thicker lines correspond to the positions with higher indexes of fractional strain energy for that mode.

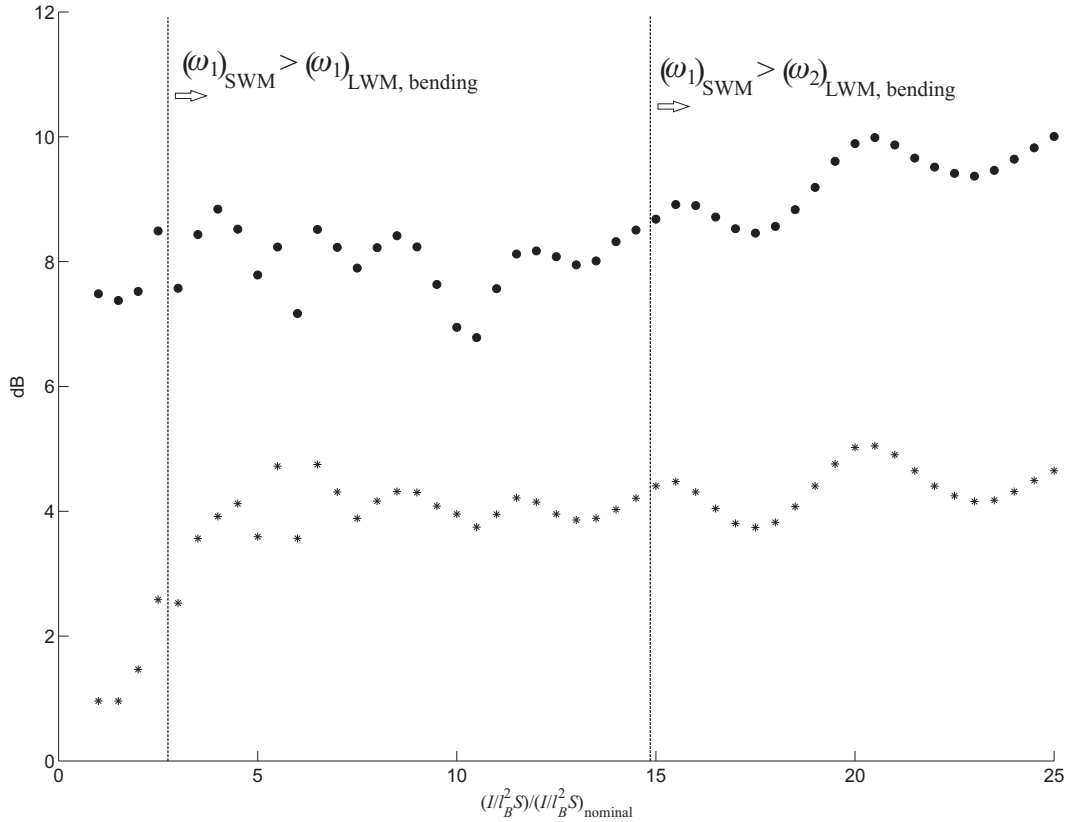

Figure 5.19: The attenuation in the cost function as function of the ratio $\mu = (I/l_B^2 S)/(I/l_B^2 S)_{\text{nominal}}$ when control is applied at member [17-20]. The dots correspond to feedforward control and the stars correspond to the integral force feedback control. As for values of $\mu > 2.6$ the first SWM occurs at frequencies higher than that of the first bending LWM. For values of $\mu > 15$, the first SWM occurs at frequencies higher than that of the second bending LWM.

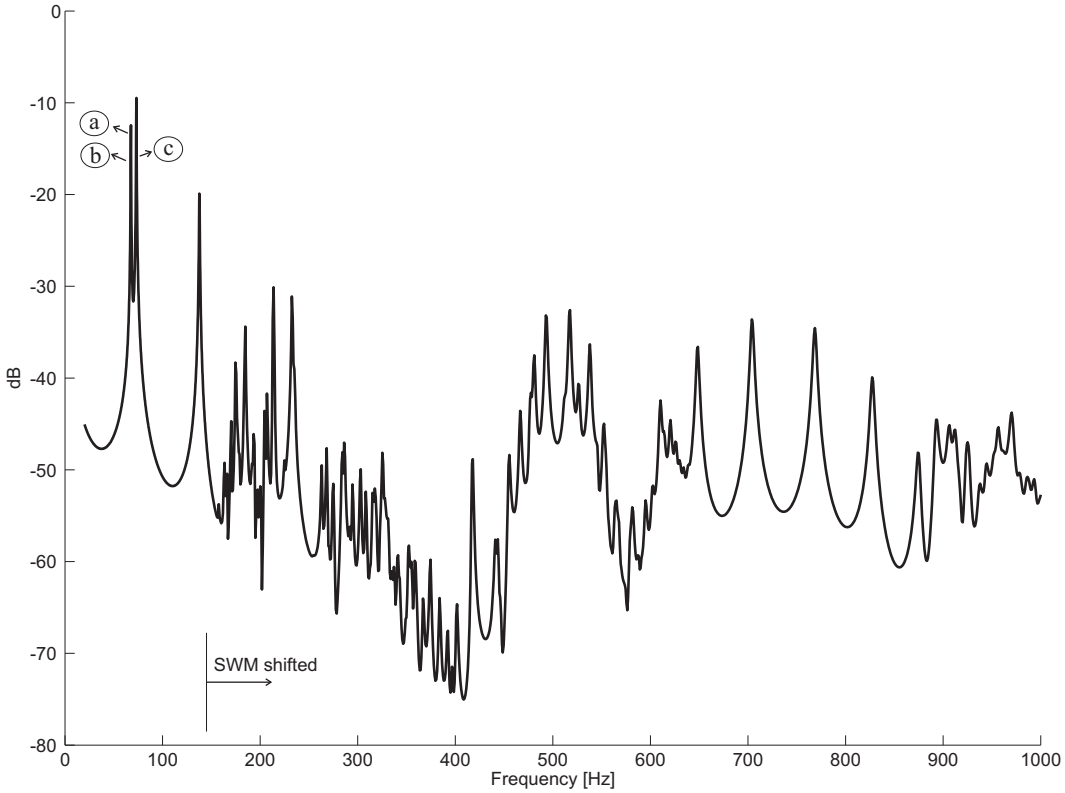

Figure 5.20: The cost function calculated using the dynamic stiffness method for the ratio $\mu = 10$. The long wavelength modes (a), (b) and (c) are illustrated in figure 5.21. dB ref. 1 m^2/Ns^2

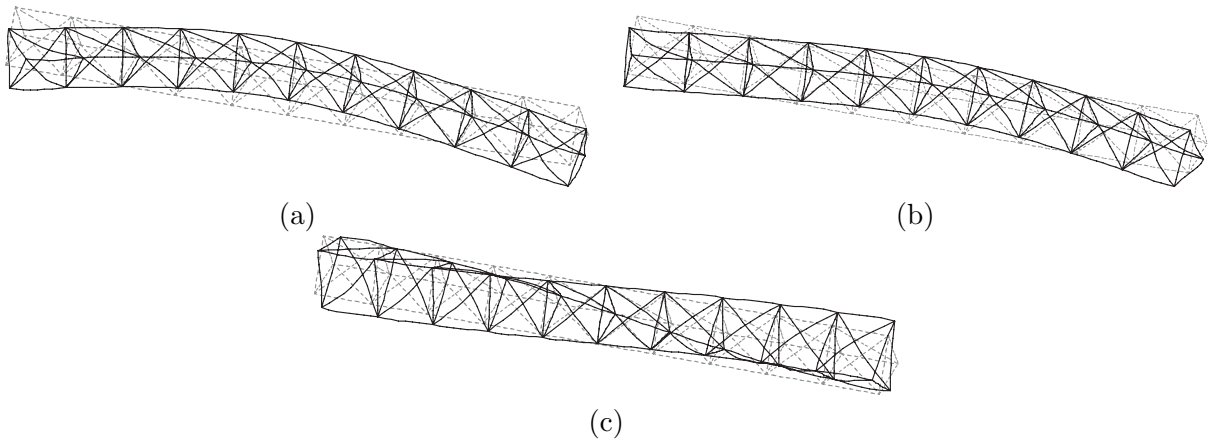

Figure 5.21: The first three mode mode shapes of the lattice structure with ratio $\mu = 10$ calculated by finite element method.

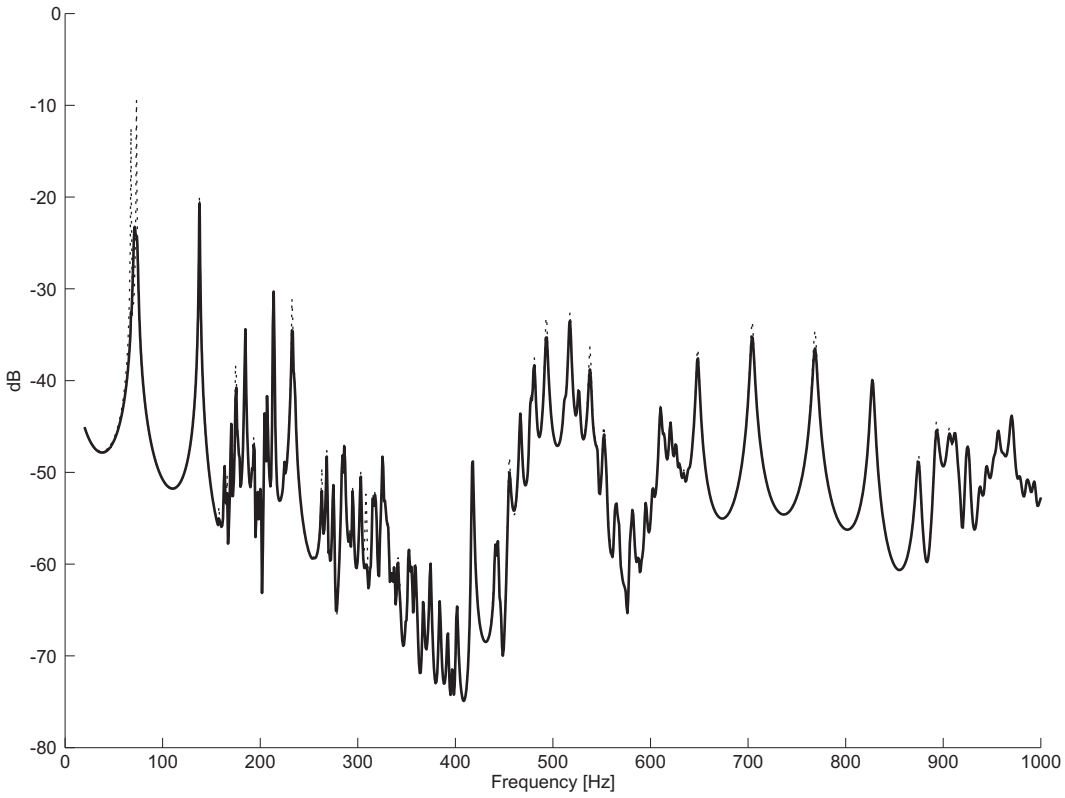

Figure 5.22: The cost function plotted in the frequency range 20 Hz - 1 kHz for $\mu = 10$, where the dashed line is the without control and the thin line is with IFF control applied at member [17-20]. dB ref. 1 m^2/Ns^2

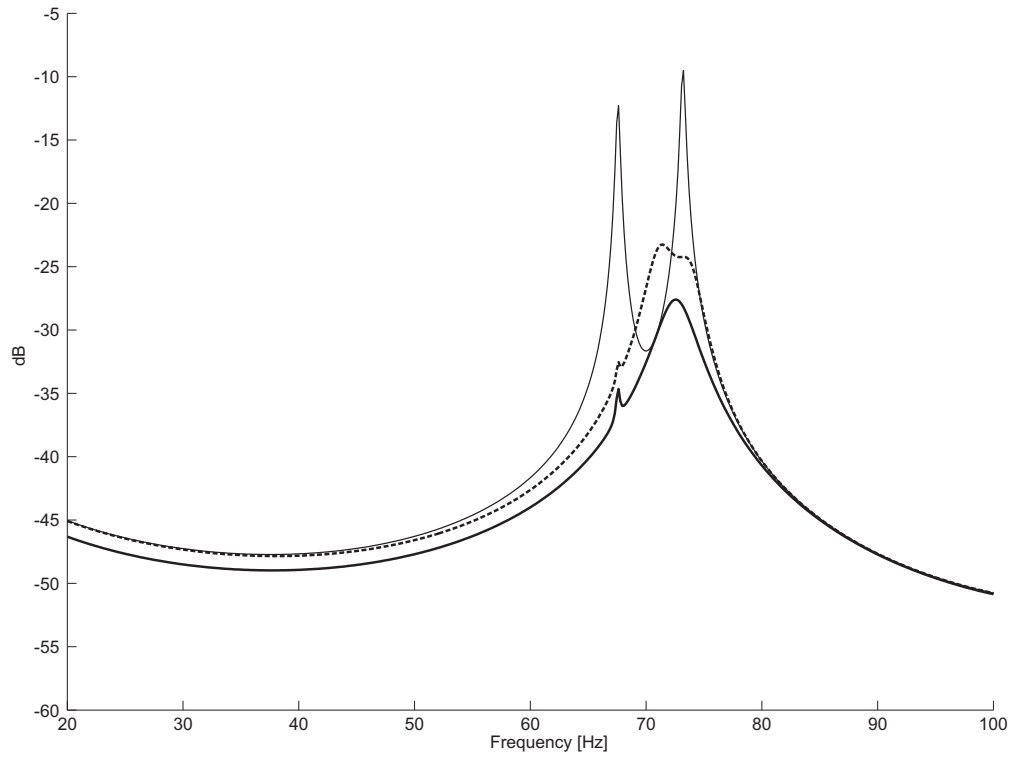

Figure 5.23: The cost function plotted in the frequency range 20 - 100 Hz for the ratio $\mu = 10$, where the thin line is without control, dashed line is with IFF control and the thick line is with feedforward control. dB ref. 1 m^2/Ns^2

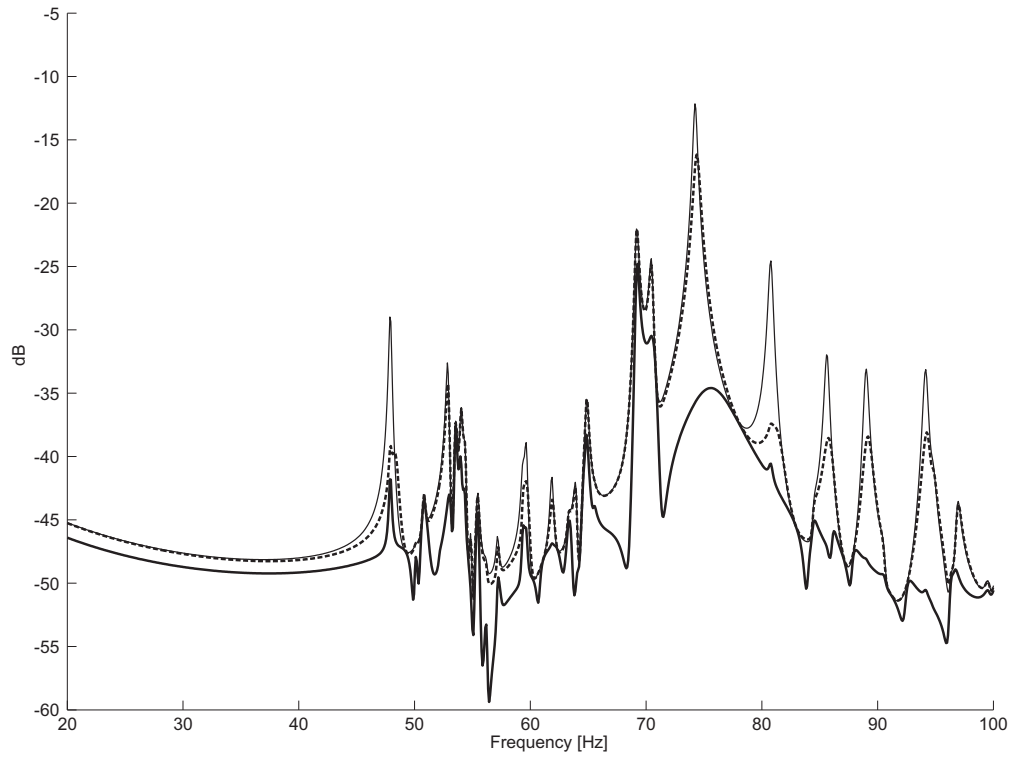

Figure 5.24: The cost function plotted in the frequency range 20 Hz - 100 Hz for the nominal ratio $(I/l_B^2 S)$, where the thin line is without control, dashed line is with IFF control and the thick line is with feedforward control. dB ref. 1 m^2/Ns^2

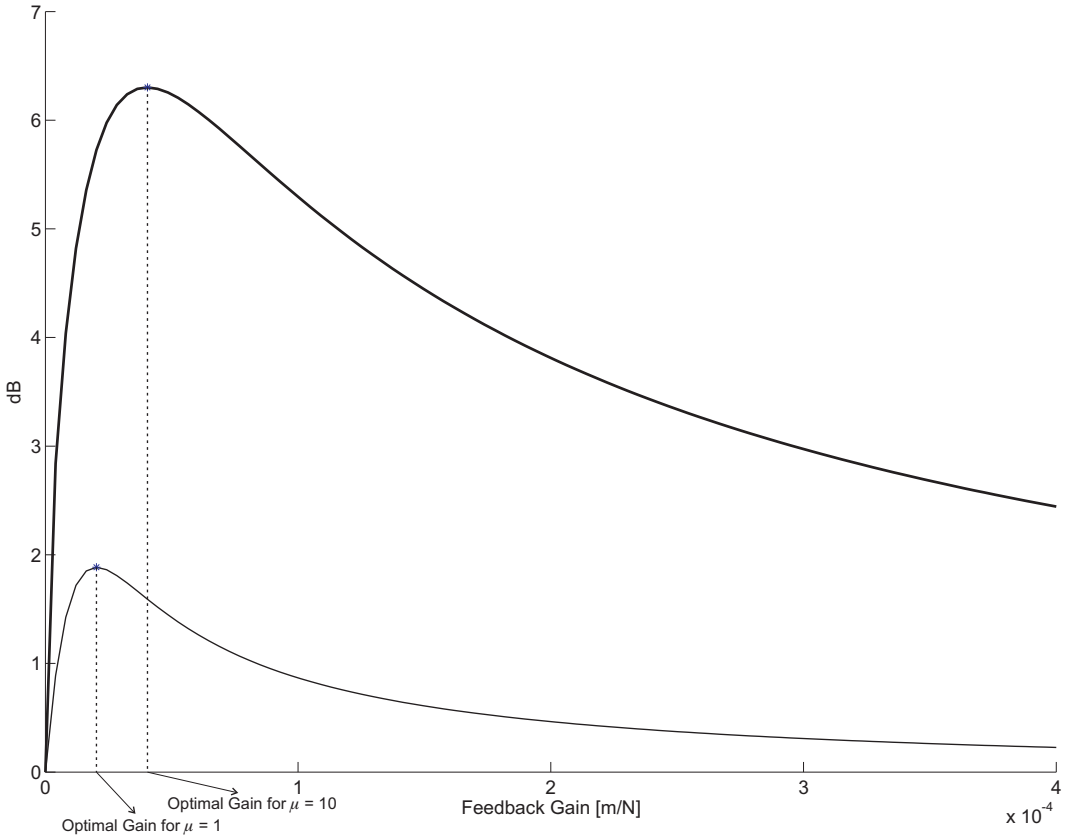

Figure 5.25: The attenuation in the cost function for different values of IFF control gains. The thin line is for the system with nominal properties and the thick line is for the system with $(I/l^B S) = 10(I/l^B S)_{\text{nominal}}$.

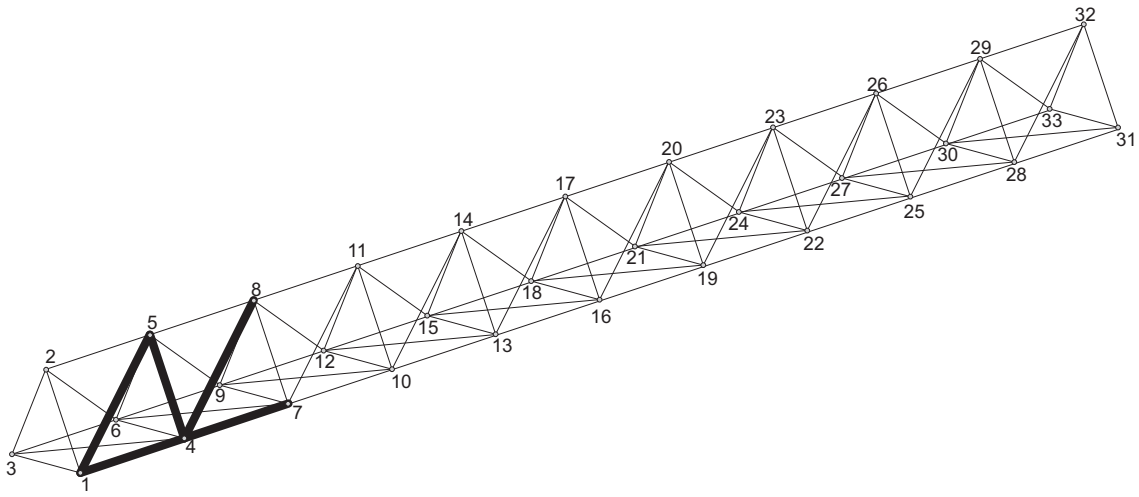

Figure 5.26: The lattice structure and the joint numbering scheme. Members with thicker lines indicate the region close to the disturbance where integral force feedback control is applied for figure 5.27.

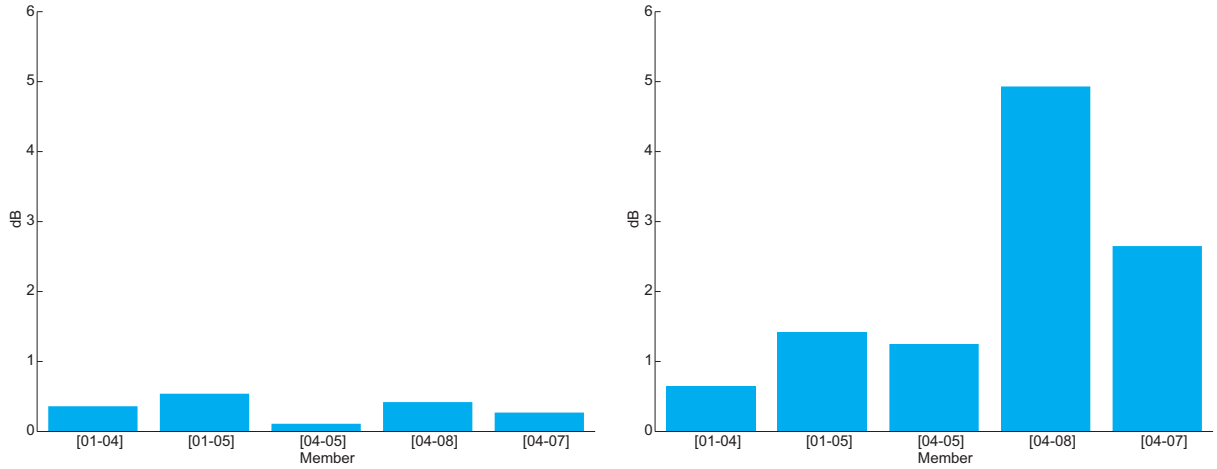

Figure 5.27: The overall attenuation obtained with the integral force feedback control in the frequency range 20 Hz - 1 kHz calculated when active control is applied close to the disturbance source. (a) for the nominal properties of the structure, (b) for values of $\mu = 10$ $((I/l^B S) = 10(I/l^B S)_{\text{nominal}})$.

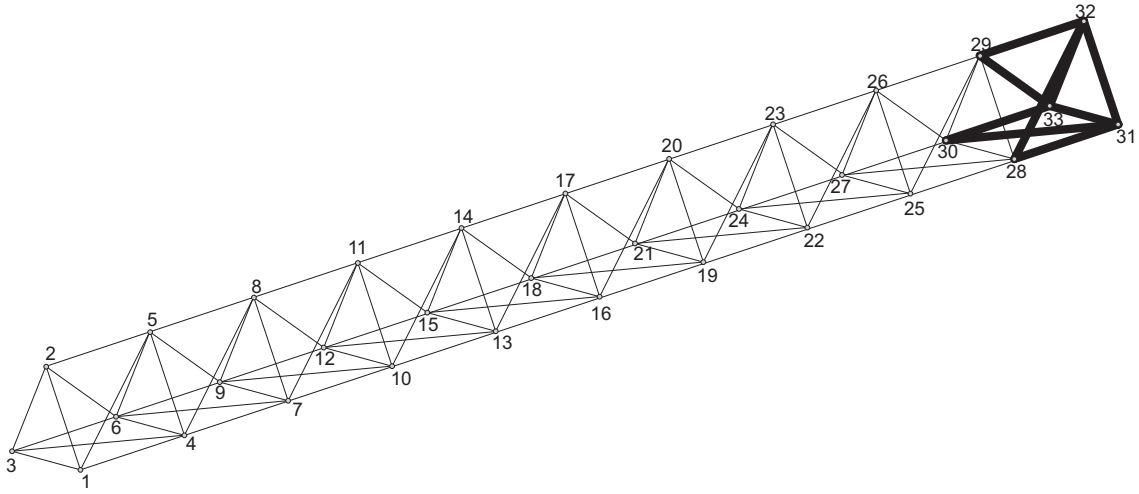

Figure 5.28: The lattice structure and the joint numbering scheme. Members with thicker lines indicate the region far from the disturbance where integral force feedback control is applied for figure 5.29.

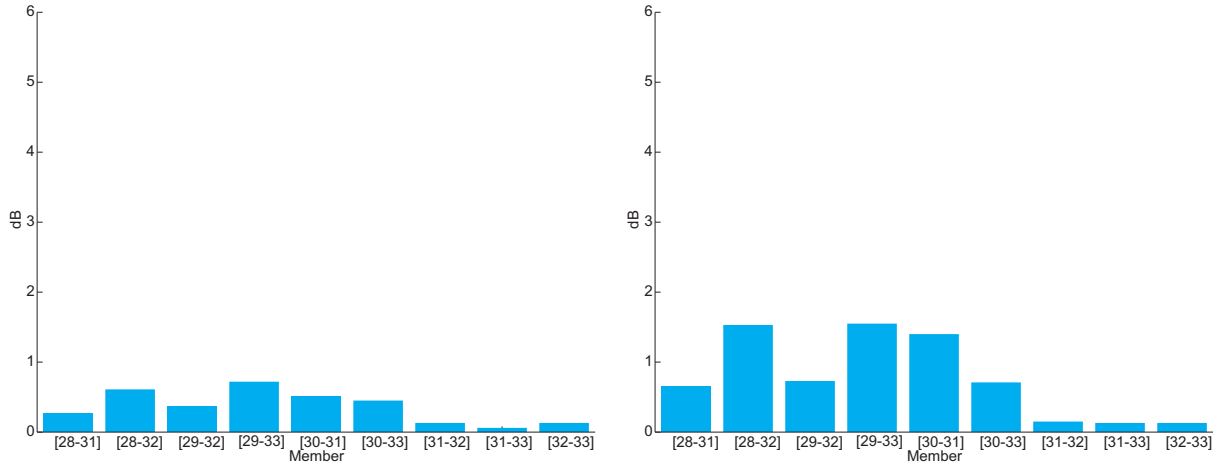

Figure 5.29: The overall attenuation obtained with the integral force feedback control in the frequency range 20 Hz - 1 kHz calculated when active control is applied at actuator positions far from the disturbance source. (a) for the nominal properties of the structure, (b) for values of $\mu = 10$ $((I/l^B S) = 10(I/l^B S)_{\text{nominal}})$.

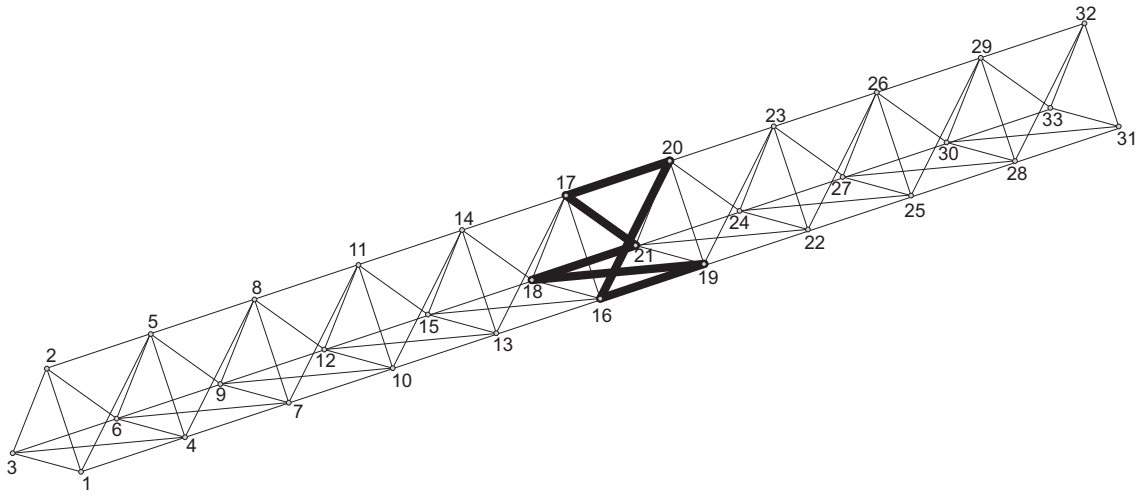

Figure 5.30: The lattice structure and the joint numbering scheme. Members with thicker lines indicate the region in the middle of the lattice where integral force feedback control is applied for figure 5.31.

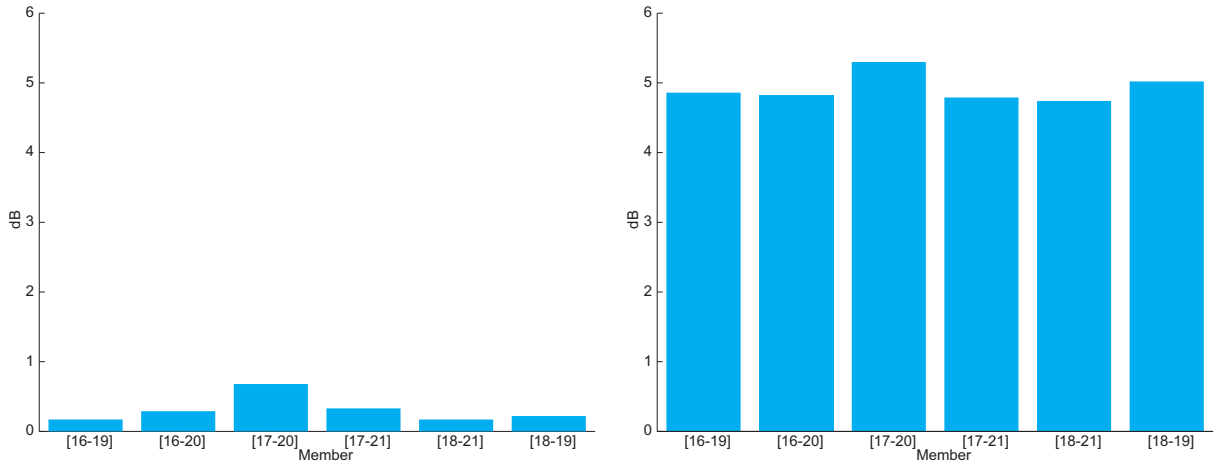

Figure 5.31: The overall attenuation obtained with the integral force feedback control in the frequency range 20 Hz - 1 kHz calculated when active control is applied at actuator positions in the middle of the lattice structure. (a) for the nominal properties of the structure, (b) for values of $\mu = 10$ ($(I/l^B S) = 10(I/l^B S)_{\text{nominal}}$)

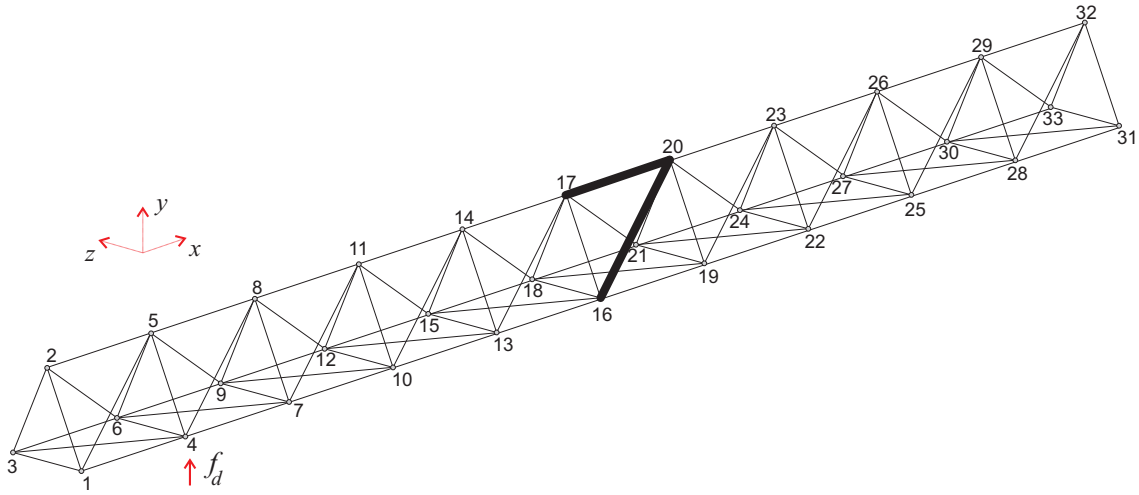

Figure 5.32: The lattice structure and the position of the two actuators which are highlighted with thicker lines.

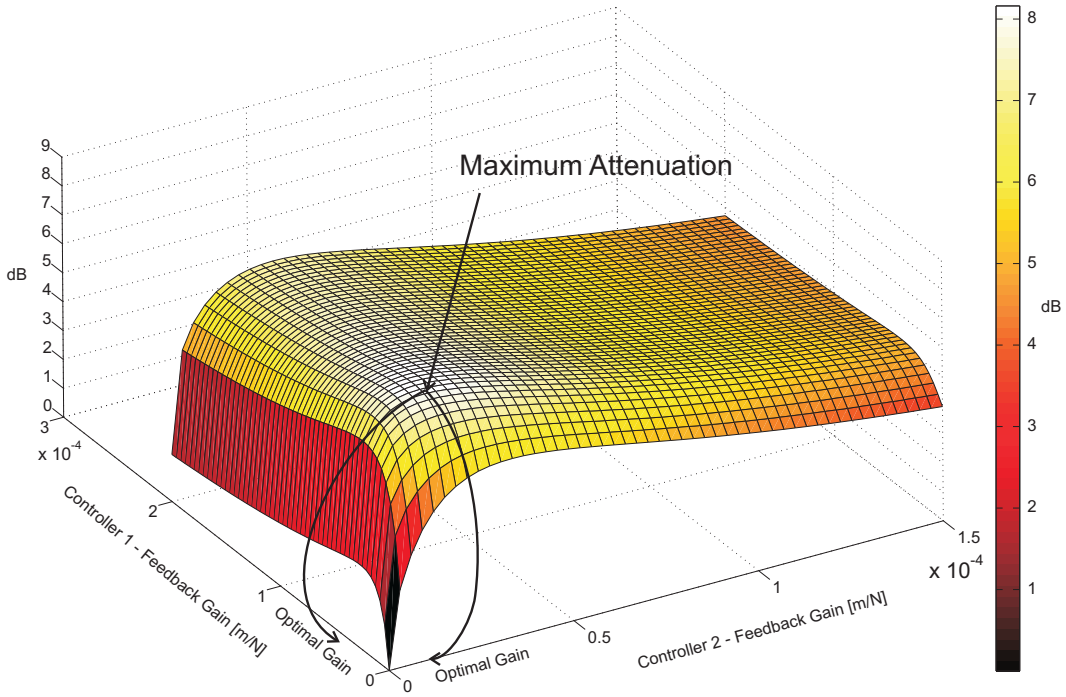

Figure 5.33: The attenuation in the cost function in the frequency range 20-100 Hz as function of the IFF gain for two control actuators placed at member [16-20] (actuator 1) and at member [17-20] (actuator). Results correspond to a system with $\mu = 10$.

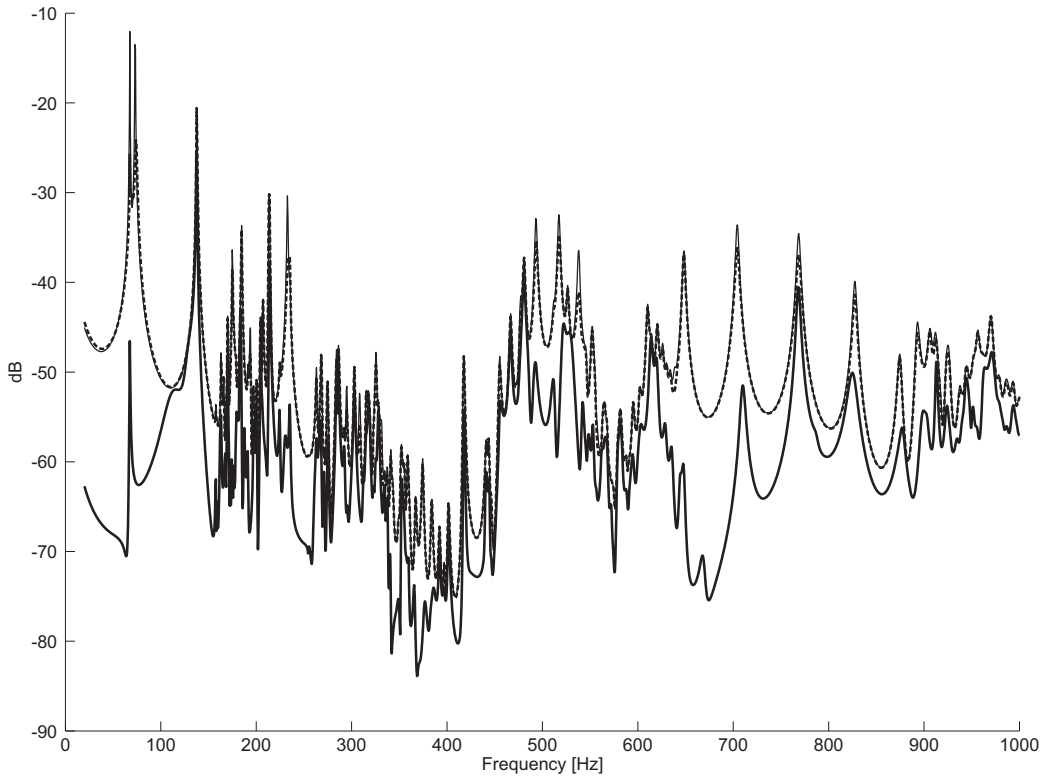

Figure 5.34: The cost function without control (thin line), and with control applied at members [16-20] and [17-20] for a structure with the ratio $\mu = 10$, where IFF control is the dashed line and feedforward control is the thick line. dB ref. 1 m^2/Ns^2

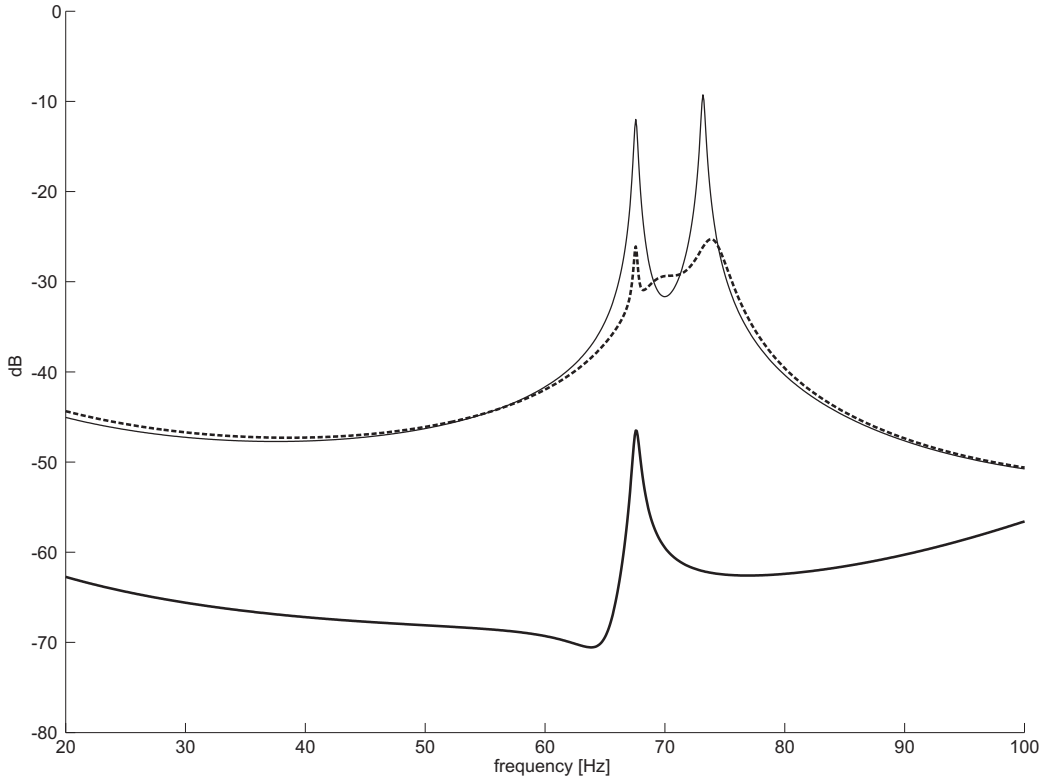

Figure 5.35: The low frequency detail of the results shown in figure 5.34, for cost function without control (thin line), and with control applied at members [16-20] and [17-20] for a structure with the ratio $\mu = 10$, where IFF control is the dashed line and feedforward control is the thick line. dB ref. 1 m^2/Ns^2

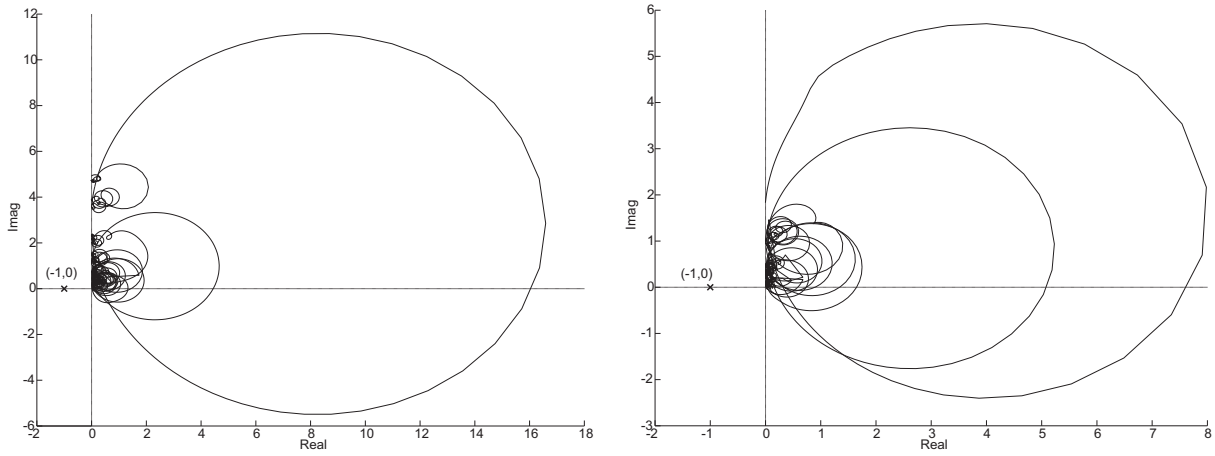

(a) (b)

Figure 5.36: The real and imaginary parts of the eigenvalues of $\mathbf{D}_{sc}\mathbf{H}_{\text{iff}}$ for the frequency range 20 Hz - 1 kHz. The actuators were placed at members [16-20] and [17-20] for a structure with the ratio $\mu = 10$.

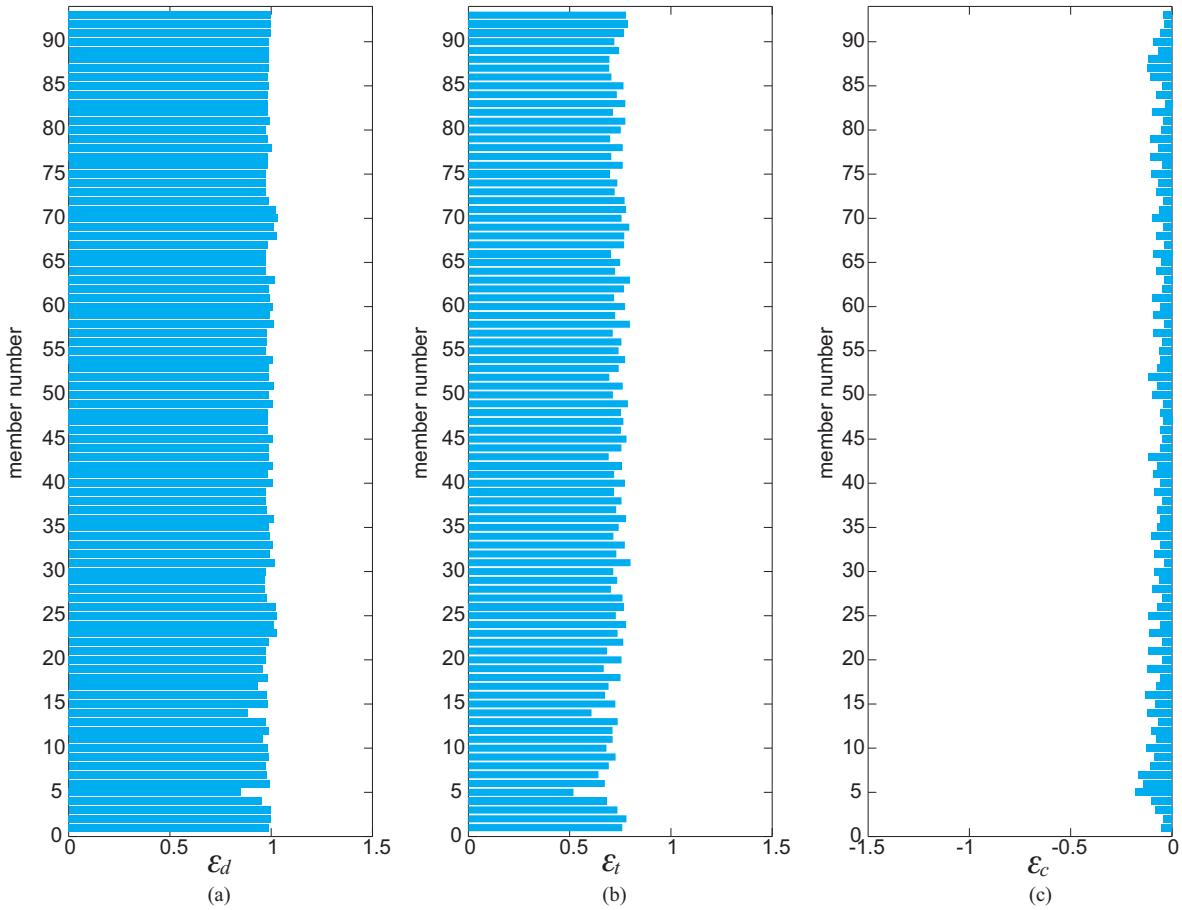

Figure 5.37: The sum of power in the frequency range 20 Hz - 1 kHz (using 1 Hz of frequency resolution). (a) The bars indicate $\varepsilon_d = [p_d(\text{in})_{\text{with control}}/p_d(\text{in})_{\text{without control}}]$ when feedforward control is applied for each member position in the lattice structure. (b) The bars indicate $\varepsilon_t = [(p_d(\text{in})_{\text{with control}} + p_c)/p_d(\text{in})_{\text{without control}}]$ when feedforward control is applied for each member position in the lattice structure. (c) The bars indicate $\varepsilon_c = [p_c/p_d(\text{in})_{\text{without control}}]$. Members are identified according to their joint numbers in the appendix G.

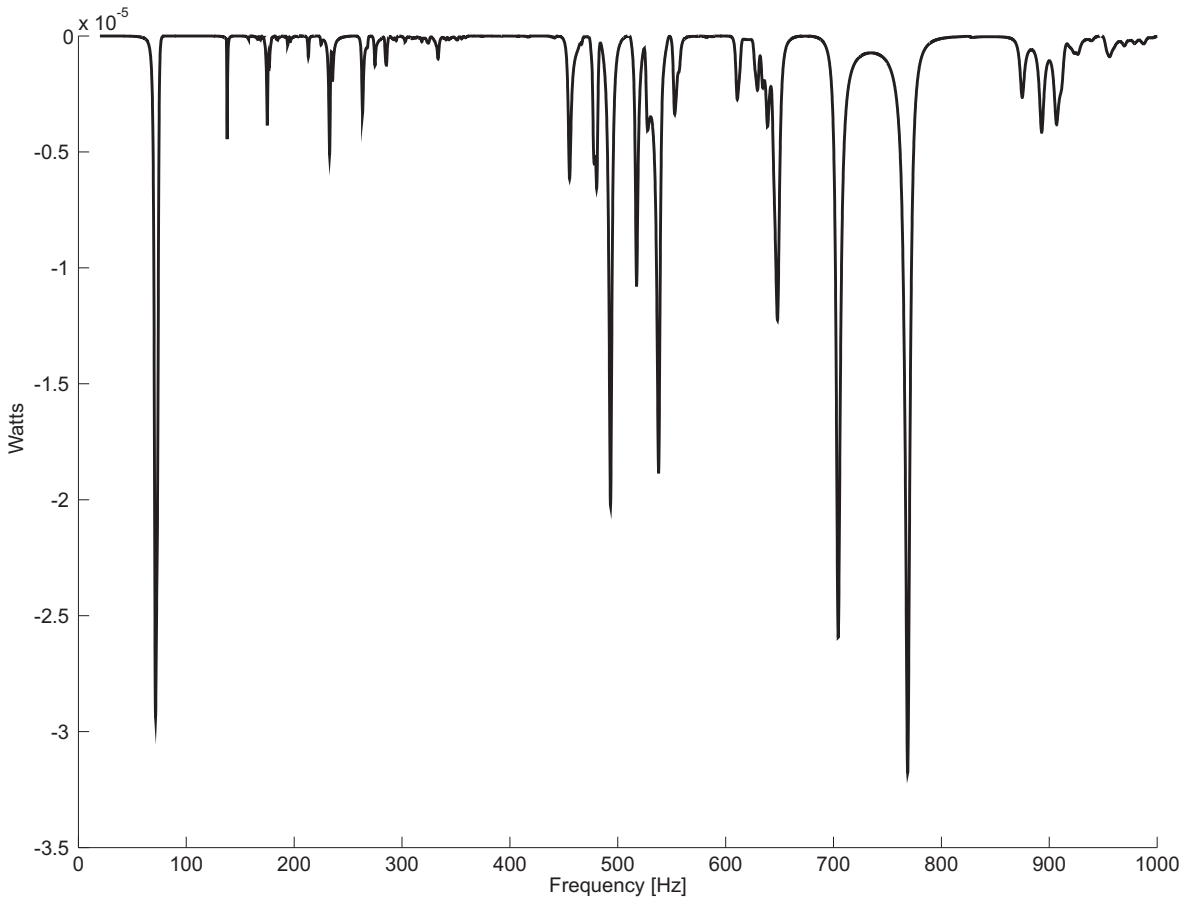

Figure 5.38: The power dissipated by the IFF controller as a function of the frequency. Actuator placed at position [17-20] for the structure with ratio $\mu = 10$. The figure also shows the low frequency detail.

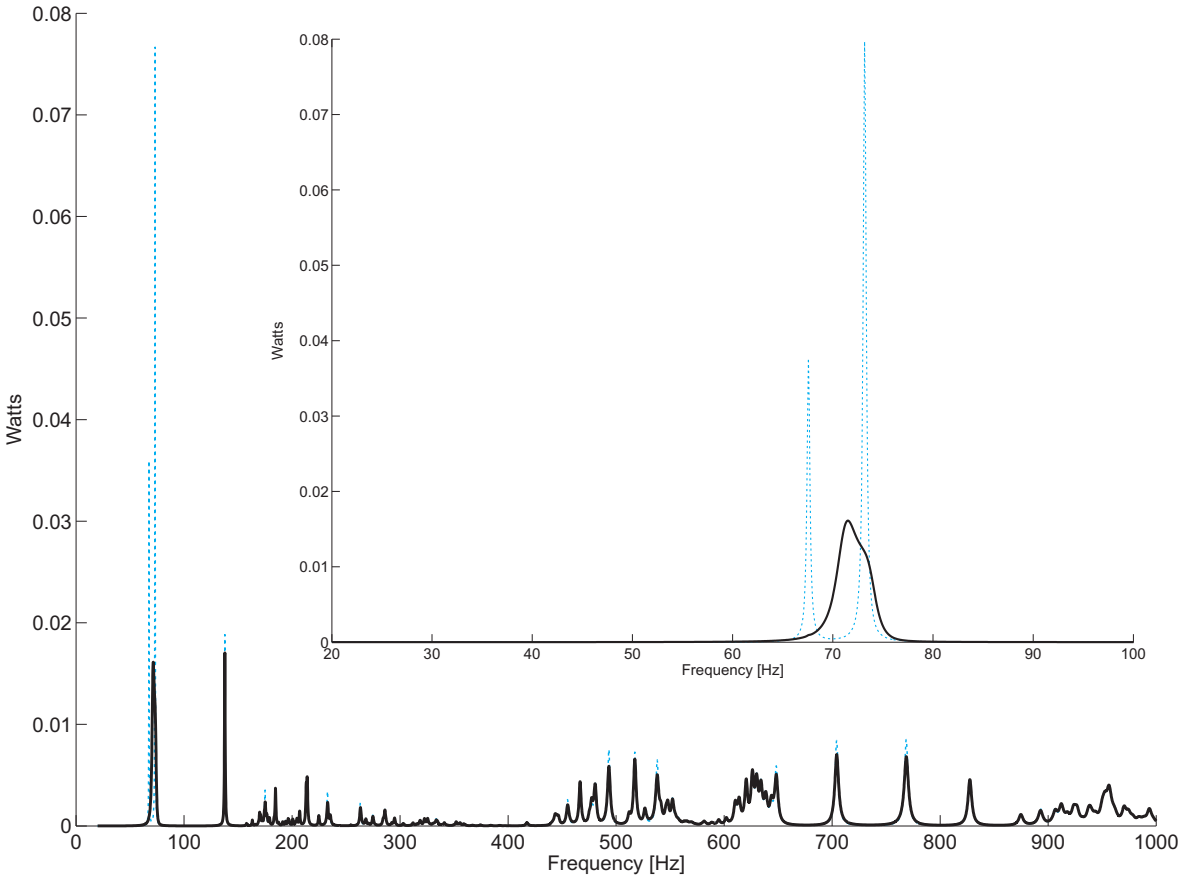

Figure 5.39: The total power input into the system by the disturbance source as a function of the frequency for the structure with ratio $\mu = 10$. The dashed line is without control and the thick line is with IFF control applied at member [17-20].

Chapter Six

Conclusions and recommendations for further work

6.1 Conclusions

The aim of the work presented in this thesis was to describe the factors controlling the performance of two strategies of active vibration control for a lattice structure similar to those used in space applications. Previous analysis tended to emphasise the long wavelength modes of such structures, in which the whole structure bends or twists. The structure considered here has also many short wavelength modes ($\sim$ 700 modes), in the frequency range considered 20 Hz - 1 kHz. These SW modes occur when the length of the members is a multiple of half wavelength of a bending wave.

Comparison with experimental data shows that the structural dynamic response can be predicted with some accuracy with the dynamics stiffness method, by considering that structural members are subject to longitudinal, torsional and bending motion. When modelling the individual structural elements, the use of exact solutions of wave equations has shown to be preferable in comparison to the modal summation method. Numerical analysis shows that SW modes occur in groups over small frequency ranges (clusters). The upper and lower limits of these frequency ranges can be estimated by calculating the bending natural frequencies of a beam with equivalent properties for the boundary conditions pinned-pinned and clamped-clamped, respectively.

Some of the parameters that control the frequency range where LW and SW modes occur are different and they are identified through an analysis that compares the first SW natural frequency with a certain LW natural frequency. The results of this analysis shows that are three parameters influencing the structural response concerning SW and LW modes. They are the number of bays in the structure, the length of the structural members and the ratio between the second moment of area and the cross sectional area of the members (I/S). The non-dimensional parameter ($I/l_B^2 S$) can then be altered to adjust the natural frequencies of SWM since it has lower influence on the LW modes.

The structural response of the system is represented in this thesis as the sum of linear velocities of three joints at one end of the structure, while the disturbance forces are

considered to be applied at an opposite end. By changing the non-dimensional ratio $(I/l_B^2 S)$, it is possible to shift the SW natural frequencies. This can be achieved by changing the shape of the cross sectional area of the members from solid to a hollow circular cross section, for instance. Although the frequency response of the structure can be quite different as the ratio $(I/l_B^2 S)$ changes, the average level of the frequency response does not vary significantly.

The analysis of the energy showed that the principal mechanism of energy dissipation occurs by bending of the structural members. This becomes less predominant in the gaps between the clusters of SW modes where dissipation by longitudinal motion of the members is equivalent or higher than the dissipation by bending. Because of the way the members are excited, only a small percentage of the energy is dissipated by torsion of the structural members. The mechanisms of energy dissipation can vary as the SW modes are shifted to higher frequencies. The dissipation of energy by longitudinal motion of the structural members becomes more predominant in this situation.

In this thesis, two strategies of active control have been analysed. Feedforward control is used for applications where external reference signal exists for the disturbance sources. This is particularly suitable for controlling disturbances originated from rotating equipment, such as reaction wheels, frequently found in space applications.

The results of the simulations have shown that good positions for placing actuators in this case are concentrated around the members close to the position where the disturbance source is applied. The analysis of power shows that, on average, the feedforward control forces input energy into the system, but it also reduces the energy input by the disturbance source by actively modifying the system input impedance. The frequency averaged attenuation in the frequency range 20 Hz - 1 kHz achieved with one, two and three actuators were 7.8, 16.7 and 25.6 dB, respectively, for the structure considered in this thesis. The numerical simulations where also used to demonstrate that the overall attenuation obtained by feedforward control does not depend much on whether SW modes are present or not, as this strategy of active control is based on the minimization of wave amplitudes at certain positions of the structure by the principle of superposition.

In contrast to feedforward control, the feedback control strategy does not require any

external reference signal, which makes it suitable for applications involving random or transient disturbances. The type of feedback control considered in the thesis is the Integral force feedback. This form of active control has previously been considered in the control of LW modes of lattice structures. This thesis extends the analysis to the cases where SWM are present in the frequency range of interest, considering the performance and stability of the control system. Numerical simulations showed that the performance of IFF is affected if a frequency range has SWMs. In this case, the performance of the feedback control in the system response is localized.

The general conclusion of the thesis is that the design of lattice structures should take into account the effects of SWM in the dynamics of the structure, specifically when a control strategy is required to control vibration in the system. Vibration levels associated with SWMs can be reduced by feedforward control. Feedback control, however, would have low performance for the situations described in this thesis.

6.2 Recommendations for further work

The work developed in this thesis has been based on numerical simulations using a mathematical model obtained by dynamic stiffness method and supported by comparison with experimental tests. The simulations of feedforward control assume a perfect plant model. As the design of optimum feedforward control involves inversion of mobility matrices, errors in the measurement of these mobilities can lead to numerical problems in the calculation of optimum feedforward control. In practice for high order uncertain systems such as this, the system response will not be known perfectly. Investigation of the effects, stability and performance when such a system is implemented be a good direction for further work. Experimental work involving feedforward and feedback control or a combination of both is also a recommended direction for future work. The design of the lattice structure would, however, need to take into account whether SWMs occur or not in the frequency range of interest for the performance of feedback control strategies.

Appendix A

The dynamic stiffness matrix for a free-free beam in space

In this Appendix, the dynamic stiffness matrix for a beam under free-free boundary conditions is derived from the solution to equation of motion for the beam. The starting point is the solution for longitudinal and torsional motion given in equation 2.4, which is repeated here for convenience, it is

$$Q(x) = A_r e^{-jkx} + A_l e^{jkx} \tag{A.1}$$

equation A.1 can also be written in terms of trigonometric functions as

$$Q(x) = A \sin kx + B \cos kx \tag{A.2}$$

A.1 The dynamic stiffness for the longitudinal vibration

Considering the beam in figure A.1 subject to the harmonic force per unit length applied at the joint **0** where the force F is a harmonic force of the type $Fe^{j\omega t}$ and the wavenumber for the longitudinal motion of the beam is $k_l = \omega(\rho/E)^{1/2}$. The boundary conditions for the longitudinal motion of the beam under the free-free boundary condition with a force applied at one end can be written as

$$Q'(0) = -\frac{F}{ES} \tag{A.3}$$

and

$$Q'(L) = 0 \tag{A.4}$$

where $()'$ denotes $\partial()/\partial x$. By applying equation A.3 to A.2, the value of the constant A is given by

$$A = -\frac{F}{k_l ES} \tag{A.5}$$

Similarly, the value of B can be found by applying equation A.4 to A.2

$$B = -\frac{F}{kES}\frac{\cos k_l l}{\sin k_l l} \tag{A.6}$$

If equations A.5 and A.6 are now applied to equation A.2, the motion at ends **0** and **1** can be expressed as

$$\frac{Q(\mathbf{0})}{F(\mathbf{0})} = \frac{\cot k_l l}{kES} \tag{A.7}$$

and

$$\frac{Q(\mathbf{1})}{F(\mathbf{0})} = \frac{\csc k_l l}{kES} \tag{A.8}$$

The results of equation A.7 and A.8 are known as the point receptance and the transfer receptance, respectively. Using the reciprocity principle, the forces and displacements at both ends of the beam can be written in matrix form as

$$\begin{bmatrix} Q(\mathbf{0}) \\ Q(\mathbf{1}) \end{bmatrix} = \begin{bmatrix} -\frac{\cot k_l l}{k_l ES} & -\frac{\csc k_l l}{k_l ES} \\ -\frac{\csc k_l l}{k_l ES} & -\frac{\cot k_l l}{k_l ES} \end{bmatrix} \begin{bmatrix} F(\mathbf{0}) \\ F(\mathbf{1}) \end{bmatrix} \tag{A.9}$$

The receptance matrix can be inverted to give the dynamic stiffness matrix for the longitudinal motion of the beam as

$$\begin{bmatrix} F(\mathbf{0}) \\ F(\mathbf{1}) \end{bmatrix} = \begin{bmatrix} -k_l ES \cot k_l l & k_l ES \csc k_l l \\ k_l ES \csc k_l l & -k_l ES \cot k_l l \end{bmatrix} \begin{bmatrix} Q(\mathbf{0}) \\ Q(\mathbf{1}) \end{bmatrix} \tag{A.10}$$

A.2 The dynamic stiffness for the torsional vibration

The dynamic stiffness matrix for torsional vibration can be found in a similar manner to that described by the longitudinal vibration in the beam. The excitation at one end is, however, assumed to be a moment per unit length of M/GJ (where M is a hamonic moment of the type $Me^{j\omega t}$) and the displacement Q is now an angular displacement. The wavenumber for torsional vibration in this case is given by $k_t = \omega(\rho/G)^{1/2}$ (considering members with circular cross sectional area). The receptance matrix for torsional vibration is given by

$$\begin{bmatrix} Q(\mathbf{0}) \\ Q(\mathbf{1}) \end{bmatrix} = \begin{bmatrix} -\frac{\cot k_t l}{k_t GJ} & -\frac{\csc k_t l}{k_t GJ} \\ -\frac{\csc k_l l}{k_t GJ} & -\frac{\cot k_t l}{k_l GJ} \end{bmatrix} \begin{bmatrix} M(\mathbf{0}) \\ M(\mathbf{1}) \end{bmatrix} \tag{A.11}$$

and by inversion of this matrix, the dynamic stiffness matrix for torsional vibration is given by

$$\begin{bmatrix} M(\mathbf{0}) \\ M(\mathbf{1}) \end{bmatrix} = \begin{bmatrix} -k_t GJ \cot k_t l & k_t GJ \csc k_l l \\ k_t GJ \csc k_l l & -k_t GJ \cot k_l l \end{bmatrix} \begin{bmatrix} Q(\mathbf{0}) \\ Q(\mathbf{1}) \end{bmatrix} \tag{A.12}$$

A.3 The dynamic stiffness for bending vibration

The solution to the equation of motion for the bending vibration of an Euler-Bernoulli beam can be written as

$$Q(x) = B_r e^{-kx} + A_r e^{-jkx} + B_l e^{kx} + A_l e^{jkx} \tag{A.13}$$

Equation A.13 can also be written in terms of trigonometric and hyperbolic functions as

$$Q(x) = A \sin k_b l + B \cos k_b l + C \sinh k_b l + D \cosh k_b l \tag{A.14}$$

where $k_b = \omega^{1/2} (\rho S/EI)^{1/4}$ is the bending wavenumber. Considering the beam shown in figure A.2 with free-free boundary conditions, the receptances for the beam are calculated first for a force per unit length applied at end **0**, where F has the form $Fe^{j\omega t}$ and second for a moment per unit length at end **0**, where M has the form $Me^{j\omega t}$. The procedures for finding the terms of the receptance matrix are similar to that of the longitudinal vibration of the beam, discussed in the previous section. The receptance matrix for bending vibration is given by [[66, 72, 71]

$$\begin{bmatrix} Q(\mathbf{0}) \\ Q'(\mathbf{0}) \\ Q(\mathbf{1}) \\ Q'(\mathbf{1}) \end{bmatrix} = \begin{bmatrix} -Q_{11} & -P & Q_{12} & V \\ -P & K_{11} & -V & K_{12} \\ Q_{12} & -V & -Q_{11} & P \\ V & K_{12} & P & K_{11} \end{bmatrix} \begin{bmatrix} F(\mathbf{0}) \\ M(\mathbf{0}) \\ F(\mathbf{1}) \\ M(\mathbf{1}) \end{bmatrix} \tag{A.15}$$

where

$$K_{11} = N\left(\cos\left(k_b l\right)\sinh\left(k_b l\right) + \sin\left(k_b l\right)\cosh\left(k_b l\right)\right) \tag{A.16a}$$

$$K_{12} = N\left(\sin\left(k_b l\right) + \sinh\left(k_b l\right)\right) \tag{A.16b}$$

$$P = N\frac{\sin\left(k_b l\right) + \sinh\left(k_b l\right)}{k_b} \tag{A.16c}$$

$$V = N\frac{\cos\left(k_b l\right) - \cosh\left(k_b l\right)}{k_b} \tag{A.16d}$$

$$Q_{11} = N\frac{\cos\left(k_b l\right)\sinh\left(k_b\right) - \sin\left(k_b l\right)\cosh\left(k_b l\right)}{k_b^2} \tag{A.16e}$$

$$Q_{12} = N\frac{\sin\left(k_b l\right) - \sinh\left(k_b l\right)}{k_b^2} \tag{A.16f}$$

$$N = \frac{EIk_b^3}{\left(\cos\left(k_b l\right)\cosh\left(k_b l\right) - 1\right)} \tag{A.16g}$$

The mathematical details for the calculation of the receptance matrix for bending vibration in the beam can be found in the reference [66]. The matrix representing the bending dynamic stiffness for a free-free beam is found by inversion of the matrix in equation A.15 to give

$$\begin{bmatrix} F(\mathbf{0}) \\ M(\mathbf{0}) \\ F(\mathbf{1}) \\ M(\mathbf{1}) \end{bmatrix} = \begin{bmatrix} -K_{11} & -P & K_{12} & V \\ -P & Q_{11} & -V & Q_{12} \\ K_{12} & -V & -K_{11} & P \\ V & Q_{12} & P & Q_{11} \end{bmatrix} \begin{bmatrix} Q(\mathbf{0}) \\ Q'(\mathbf{0}) \\ Q(\mathbf{1}) \\ Q'(\mathbf{1}) \end{bmatrix} \tag{A.17}$$

A.4 The dynamics stiffness for the free-free beam in space

Considering figure A.3 showing the numbering scheme for the degrees of freedom and the forces/moments applied at the ends of a free-free beam

The displacement $\mathbf{q}$ and force $\mathbf{f}$ vectors of this beam are related by the dynamic stiffness matrix $\mathbf{D}$ as

$$\mathbf{qD} = \mathbf{f} \tag{A.18}$$

The dynamic stiffness matrix is given by

$$
\mathbf{D} = \begin{bmatrix}
\psi_1 & 0 & 0 & 0 & 0 & 0 & \psi_2 & 0 & 0 & 0 & 0 & 0 & 0 \\
 & -K_{11}(z) & 0 & 0 & 0 & -P(z) & 0 & K_{12}(z) & 0 & 0 & 0 & 0 & V(z) \\
 & & -K_{11}(y) & 0 & P(y) & 0 & 0 & 0 & K_{12}(y) & 0 & -V(y) & 0 & \\
 & & & \sigma_1 & 0 & 0 & 0 & 0 & 0 & \sigma_2 & 0 & 0 & \\
 & & & & Q_{11}(y) & 0 & 0 & 0 & V(y) & 0 & Q_{12}(y) & 0 & \\
 & & & & & Q_{11}(z) & 0 & -V(z) & 0 & 0 & 0 & Q_{12}(z) & \\
 & & & & & & \psi_1 & 0 & 0 & 0 & 0 & 0 & \\
 & & & & & & & -K_{11}(z) & 0 & 0 & 0 & P(z) & \\
 & & & & & & & & -K_{11}(y) & 0 & P_y & 0 & \\
 & & & & & & & & & \sigma_2 & 0 & 0 & \\
 & & & & & & & & & & Q_{11}(y) & 0 & \\
 & & & & & & & & & & & Q_{11}(z) &
\end{bmatrix} \tag{A.19}
$$

The elements of the dynamics stiffness are given by

$$\psi_1 = \omega S\sqrt{E\rho}\cot k_l l \tag{A.20a}$$

$$\psi_2 = -\omega S\sqrt{E\rho}\csc k_l l \tag{A.20b}$$

$$\sigma_1 = \omega\sqrt{GJI_o\rho}\cot k_s l \tag{A.21a}$$

$$\sigma_2 = -\omega\sqrt{GJI_o\rho}\csc k_s l \tag{A.21b}$$

$$K_{11} = N\left(\cos\left(k_b l\right)\sinh\left(k_b l\right) + \sin\left(k_b l\right)\cosh\left(k_b l\right)\right) \tag{A.22a}$$

$$K_{12} = N\left(\sin\left(k_b l\right) + \sinh\left(k_b l\right)\right) \tag{A.22b}$$

$$P = N\frac{\sin\left(k_b l\right) + \sinh\left(k_b l\right)}{k_b} \tag{A.22c}$$

$$V = N\frac{\cos\left(k_b l\right) - \cosh\left(k_b l\right)}{k_b} \tag{A.22d}$$

$$Q_{11} = N\frac{\cos\left(k_b l\right)\sinh\left(k_b\right) - \sin\left(k_b l\right)\cosh\left(k_b l\right)}{k_b^2} \tag{A.22e}$$

$$Q_{12} = N\frac{\sin\left(k_b l\right) - \sinh\left(k_b l\right)}{k_b^2} \tag{A.22f}$$

$$N = \frac{EIk_b^3}{\left(\cos\left(k_b l\right)\cosh\left(k_b l\right) - 1\right)} \tag{A.22g}$$

Figure A.1: A free-free beam subject to longitudinal excitation in the end **0**

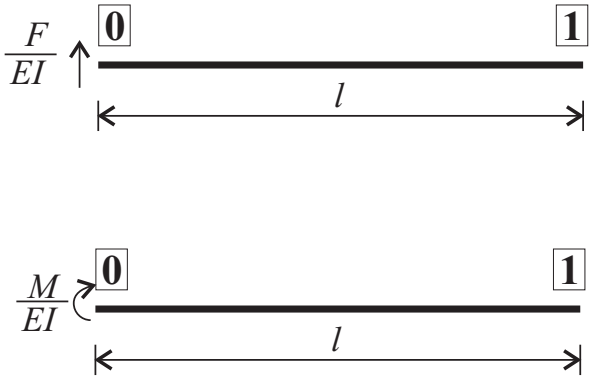

Figure A.2: A free-free beam subject to transversal excitation in the end **0**

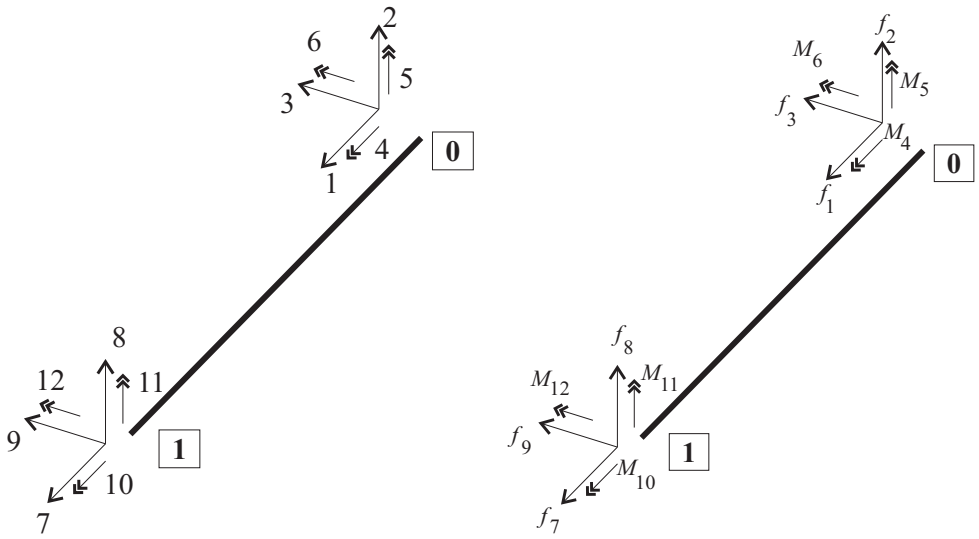

Figure A.3: The local coordinates of degrees of freedom numbering scheme and the forces numbering scheme for a beam in space

Appendix B

Coordinate Transformation Matrix

In this Appendix, the coordinate transformation matrix is considered, where this matrix is used in chapter 2 for the modelling of lattice structure. A beam in space and its local coordinate system can be defined by the location of the ends **0** and **1** in the global coordinate system XYZ shown in figure B.1. The length L of the *i-th* beam is then defined by

$$L_i = \left(\left(p_X^1 - p_X^0\right)^2 + \left(p_Y^1 - p_Y^0\right)^2 + \left(p_Z^1 - p_Z^0\right)^2 \right)^{1/2} \tag{B.1}$$

where p_X^1 is, for instance, the coordinate in the X axis for the end **1**. The coordinate transformation matrix can be calculated from the direction cosines C (the direction cosines are the cosines of the Euler angles of a vector), defined as

$$C_X = \frac{(p_X^1 - p_X^0)}{L_i},\ C_Y = \frac{(p_Y^1 - p_Y^0)}{L_i},\ C_Z = \frac{(p_Z^1 - p_Z^0)}{L_i} \tag{B.2}$$

The coordinate transformation matrix $\mathbf{T}$ of the *i-th* beam, is given by [81, 132]

$$\mathbf{T}_i = \begin{bmatrix} C_X & C_Y & C_Z \\ -\frac{C_X C_Y \cos\alpha + C_Z \sin\alpha}{C_{XZ}} & C_{XZ}\cos\alpha & -\frac{C_Y C_Z \cos\alpha + C_X \sin\alpha}{C_{XZ}} \\ -\frac{C_X C_Y \sin\alpha + C_Z \cos\alpha}{C_{XZ}} & -C_{XZ}\sin\alpha & \frac{C_Y C_Z \sin\alpha + C_X \cos\alpha}{C_{XZ}} \end{bmatrix} \tag{B.3}$$

where, $C_{XZ} = (C_X^2 + C_Z^2)^{1/2}$. α is the angle of rotation about the x axis. This relation is valid for all situations except when $C_X = C_Z = 0$ (beam oriented vertically). For this situation, the following matrix can be used,

$$\mathbf{T}_i = \begin{bmatrix} 0 & C_Y & 0 \\ -C_Y\cos\alpha & 0 & \sin\alpha \\ C_Y\sin\alpha & 0 & \cos\alpha \end{bmatrix} \tag{B.4}$$

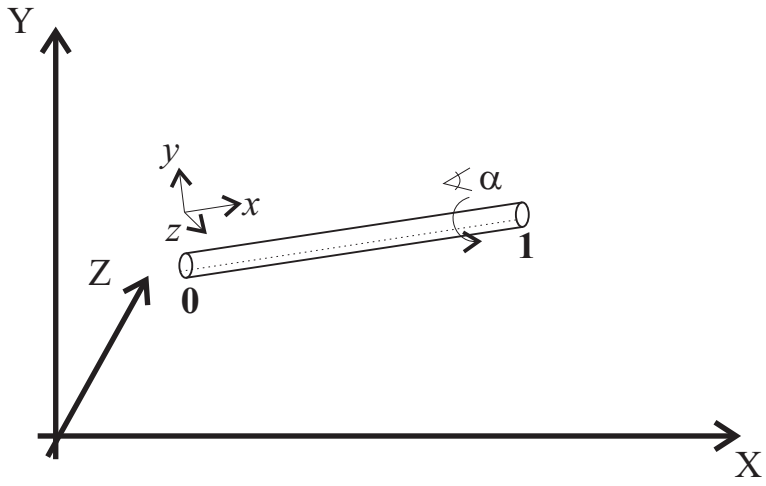

Figure B.1: Global and Local Coordinate Systems

Appendix C

The finite element matrices

In this appendix, the finite element mass and stiffness matrices are given for two different types of finite element. These matrices are available in many finite element text books, such as , and are presented here for easy reference.

The finite element matrices for a *Truss* element (considering only the longitudinal motion of the members are given

$$\mathbf{K} = \frac{ES}{L}\begin{bmatrix} 1 & 0 & 0 & -1 & 0 & 0 \\ 0 & 0 & 0 & 0 & 0 & 0 \\ 0 & 0 & 0 & 0 & 0 & 0 \\ -1 & 0 & 0 & 1 & 0 & 0 \\ 0 & 0 & 0 & 0 & 0 & 0 \\ 0 & 0 & 0 & 0 & 0 & 0 \end{bmatrix}, \quad \mathbf{M} = \frac{\rho SL}{6}\begin{bmatrix} 2 & 0 & 0 & 1 & 0 & 0 \\ 0 & 2 & 0 & 0 & 1 & 0 \\ 0 & 0 & 2 & 0 & 0 & 1 \\ 1 & 0 & 0 & 2 & 0 & 0 \\ 0 & 1 & 0 & 0 & 2 & 0 \\ 0 & 0 & 1 & 0 & 0 & 2 \end{bmatrix} \tag{C.1}$$

where, $\mathbf{K}$ is the stiffness matrix, $\mathbf{M}$ is the mass matrix, E is the Young's modulus, ρ is the density, l is the element length and S is the cross sectional area. For a complete finite element, considering longitudinal and torsional motion and bending in two orthogonal planes (y and z) the stiffness matrix is given by equation C.2 where, G is the shear modulus, I is the second moment of area and J is the polar second moment of area. The mass matrix for the respective complete element is shown in equation C.3.

$$\mathbf{K} = \begin{bmatrix}
SE/l & 0 & 0 & 0 & 0 & 0 & -SE/l & 0 & 0 & 0 & 0 & 0 \\
 & 12EI_z/l^3 & 0 & 0 & 0 & 6EI_z/l^2 & 0 & -12EI_z/l^3 & 0 & 0 & 0 & 6EI_z/l^2 \\
 & & 12EI_y/l^3 & 0 & -6EI_y/l^2 & 0 & 0 & 0 & -12EI_y/l^3 & 0 & -6EI_y/l^2 & 0 \\
 & & & GJ/l & 0 & 0 & 0 & 0 & 0 & -GJ/l & 0 & 0 \\
 & & & & 4EI_y/l & 0 & 0 & 0 & 6EI_y/l^2 & 0 & 2EI_y/l & 0 \\
 & & & & & 4EI_z/l & 0 & -6EI_z/l^2 & 0 & 0 & 0 & 2EI_z/l \\
 & & & & & & SE/l & 0 & 0 & 0 & 0 & 0 \\
 & & & & & & & 12EI_z/l^3 & 0 & 0 & 0 & -6EI_z/l^2 \\
 & & & & & & & & 12EI_y/l^3 & 0 & 6EI_y/l^2 & 0 \\
 & & & & symmetric & & & & & GJ/l & 0 & 0 \\
 & & & & & & & & & & 4EI_y/l & 0 \\
 & & & & & & & & & & & 4EI_z/l
\end{bmatrix} \tag{C.2}$$

$$\mathbf{M} = \begin{bmatrix}
\frac{\rho Sl}{3} & 0 & 0 & 0 & 0 & 0 & \frac{\rho Sl}{6} & 0 & 0 & 0 & 0 & 0 \\
 & \frac{156}{420}\rho Sl & 0 & 0 & 0 & \frac{22}{420}\rho Sl^2 & 0 & \frac{54}{420}\rho Sl & 0 & 0 & 0 & -\frac{13}{420}\rho Sl^2 \\
 & & \frac{156}{420}\rho Sl & 0 & -\frac{22}{420}\rho Sl^2 & 0 & 0 & 0 & \frac{54}{420}\rho Sl & 0 & \frac{13}{420}\rho Sl^2 & 0 \\
 & & & \frac{J}{3S} & 0 & 0 & 0 & 0 & 0 & \frac{J}{6S} & 0 & 0 \\
 & & & & \frac{4}{420}\rho Sl^3 & 0 & 0 & 0 & -\frac{13}{420}\rho Sl & 0 & \frac{3}{420}\rho Sl^3 & 0 \\
 & & & & & \frac{4}{420}\rho Sl^3 & 0 & \frac{13}{420}\rho Sl & 0 & 0 & 0 & \frac{3}{420}\rho Sl^3 \\
 & & & & & & \frac{\rho Sl}{3} & 0 & 0 & 0 & 0 & 0 \\
 & & & & & & & \frac{156}{420}\rho Sl & 0 & 0 & 0 & \frac{22}{420}\rho Sl^2 \\
 & & & & & & & & \frac{156}{420}\rho Sl & 0 & -\frac{22}{420}\rho Sl^2 & 0 \\
 & & & & \textit{symmetric} & & & & & \frac{J}{3S} & 0 & 0 \\
 & & & & & & & & & & \frac{4}{420}\rho Sl^3 & 0 \\
 & & & & & & & & & & & \frac{4}{420}\rho Sl^3
\end{bmatrix} \tag{C.3}$$

Appendix D

Introduction to power analysis

In this Appendix, a introduction to the analysis of power in mechanical systems is considered. Power is the rate at which a work is performed. The SI unit of power is the Watt [W]. Power is usually seen as an energy flow, which is equivalent to the rate of change of energy in a system, or in other words, it is the rate at which a a work is done. It is defined

$$P = \frac{dW}{dt} = \frac{dE}{dt} \tag{D.1}$$

where, W is work and E is energy. The average power is the average amount of work done or energy transfered per unit time. Instantaneous power is then the limiting value of the average power as the time interval Δt approaches zero

$$P = \lim_{\Delta t \to 0} \frac{\Delta W}{\Delta t} \tag{D.2}$$

Power is a quantity usually used in the electrical engineering field, but its concepts have been used for some time to describe vibrational energy in mechanical systems. For mechanical systems, work is defined by

$$W = \int f \cdot dq \tag{D.3}$$

where f is the force and q is the displacement. When the motion is in the same direction of the force, work is positive. Note that work only exists in the direction that the force is applied. By differentiating both sides in respect to time, it gives

$$P(t) = f(t) \cdot v(t) \tag{D.4}$$

where, v is the velocity. Power is a measure of the in-phase components between force and velocity. It should be noted, that when dealing in the frequency domain, with complex values, it is important to consider the phase between the two quantities.

Assuming harmonic motion,

$$f(t) = F\sin(\omega t + \theta_f) \tag{D.5}$$

$$v(t) = V\sin(\omega t + \theta_v) \tag{D.6}$$

equation D.4 can be re-written as

$$p(t) = FV\sin(\omega t + \theta_f)\sin(\omega t + \theta_v) \tag{D.7}$$

Using the trigonometric identity

$$\sin(A)\sin(B) = \frac{\cos(A-B) + \cos(A+B)}{2} \tag{D.8}$$

equation D.7 becomes

$$p(t) = \frac{FV}{2}\overbrace{\cos(\theta_f - \theta_v)}^{\text{fixed value}} - \frac{FV}{2}\overbrace{\cos(2\omega t + \theta_f + \theta_v)}^{\text{time varying}} \tag{D.9}$$

From equation D.9, the time average power can be calculated for a number of periods T as

$$\begin{aligned}\langle p(t)\rangle_T &= \frac{1}{T}\int_0^T f(t)v(t)dt \\ &= \frac{FV}{2T}\cos(\theta_f - \theta_v)\int_T^0 dt - \frac{FV}{2T}\overbrace{\int_0^T \cos(2\omega t + \theta_f + \theta_v)dt}^{0} \\ &= \frac{FV}{2}\cos(\theta_f - \theta_v)\end{aligned} \tag{D.10}$$

Thus the time average power can be written as

$$P(\omega) = \frac{1}{2}\{F\cdot V\} + \frac{1}{2}\{F\cdot V^*\} \tag{D.11}$$

where, F and V are respectively the force and velocity, V^* is the complex conjugate of V . Equation D.11 can also be written in the form

$$P(\omega) = \frac{1}{2}\mathrm{Re}\{F \cdot V^*\} \tag{D.12}$$

Because V is the velocity at the position where the force is applied, it can be written in terms of the point mobility of the system as

$$P_{in} = \frac{|F|^2}{2}\mathrm{Re}\{Y\} \tag{D.13}$$

Where Y is the point mobility where the force F is applied. Similarly D.13 can also be defined in terms of the system point impedance as

$$P_{in} = \frac{|V|^2}{2}\mathrm{Re}\{Z\} \tag{D.14}$$

D.1 Power Analysis in a SDOF system

Consider the SDOF (*single degree of freedom*) system shown in figure D.1. The equation of motion of the system in figure D.1 is given by

$$m\ddot{q}(t) + c\dot{q}(t) + kq(t) = f(t) \tag{D.15}$$

where, m, c and k are respectively the mass, viscous damping coefficient and stiffness of the system, q and f are, respectively, the displacements and forces acting on the system. Assuming harmonic motion ($f = Fe^{j\omega t}$), equation D.15 can be transformed to the frequency domain to give

$$Q(\omega) = \frac{F}{(-\omega^2 m + j\omega c + k)} \tag{D.16}$$

where the term $(-\omega^2 m + j\omega c + k)^{-1}$ is known as the system receptance. The system mobility $Y = Q/F$ is found by differentiating the receptance in the frequency domain to give

$$Y = \frac{j\omega}{(-\omega^2 m + j\omega c + k)} = \frac{1}{j\omega m + c + k/j\omega} \tag{D.17}$$

And the impedance $Z = Y^{-1}$ is defined by $(j\omega m + c + k/j\omega)$. Using equation D.13, and the system mobility, it is possible to find that the input power in the single degree

of freedom is

$$P_{in} = \frac{|F|^2}{2} \frac{c}{c^2 + (\omega m + k/\omega)^2} \tag{D.18}$$

The dissipation force that the damper produces is proportional to the velocity of the system. The dissipation force is defined by

$$F_{diss} = -cV \tag{D.19}$$

The power dissipated P_{diss} by the damping present in the system is then defined by the in-phase component between the dissipation force and velocity in the system damper.

$$P_{diss} = \frac{1}{2}\mathrm{Re}\left\{-cV \cdot V^*\right\} = -\frac{|F|^2}{2} \frac{c}{c^2 + (\omega m + k/\omega)^2} \tag{D.20}$$

The results of equations D.18 and D.20 lead to the conclusion that the total power input in a system is equal to the power dissipated. This is reasonable since the damper is the unique dissipative element in the SDOF system. The second conclusion is that, in theory, power only exists if there are dissipative element in the system.

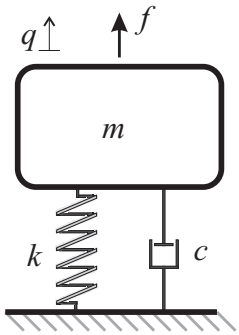

Figure D.1: Single Degree of Freedom System

Appendix E

Experimental results

In this section, the detailed results of the experimental test discussed in chapter 2 are presented. Table E.1 shows the summary of the figures given in this appendix.

Joint Number, Direction	Figure Number
4, y	E.1
31, x	E.2
31, y	E.3
31, z	E.4
32, x	E.5
32, y	E.6
32, z	E.7
33, x	E.8
33, y	E.9
33, z	E.10

Table E.1: Experimental test results sumary

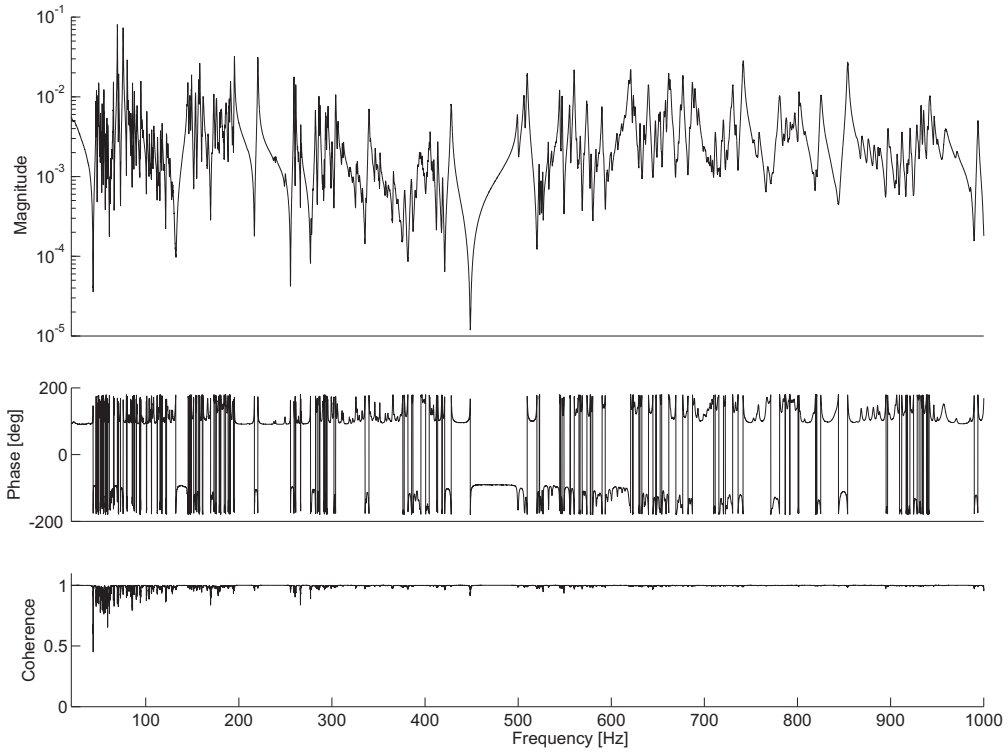

Figure E.1: Magnitude and phase of velocity in joint 4, y direction, measurement coherence

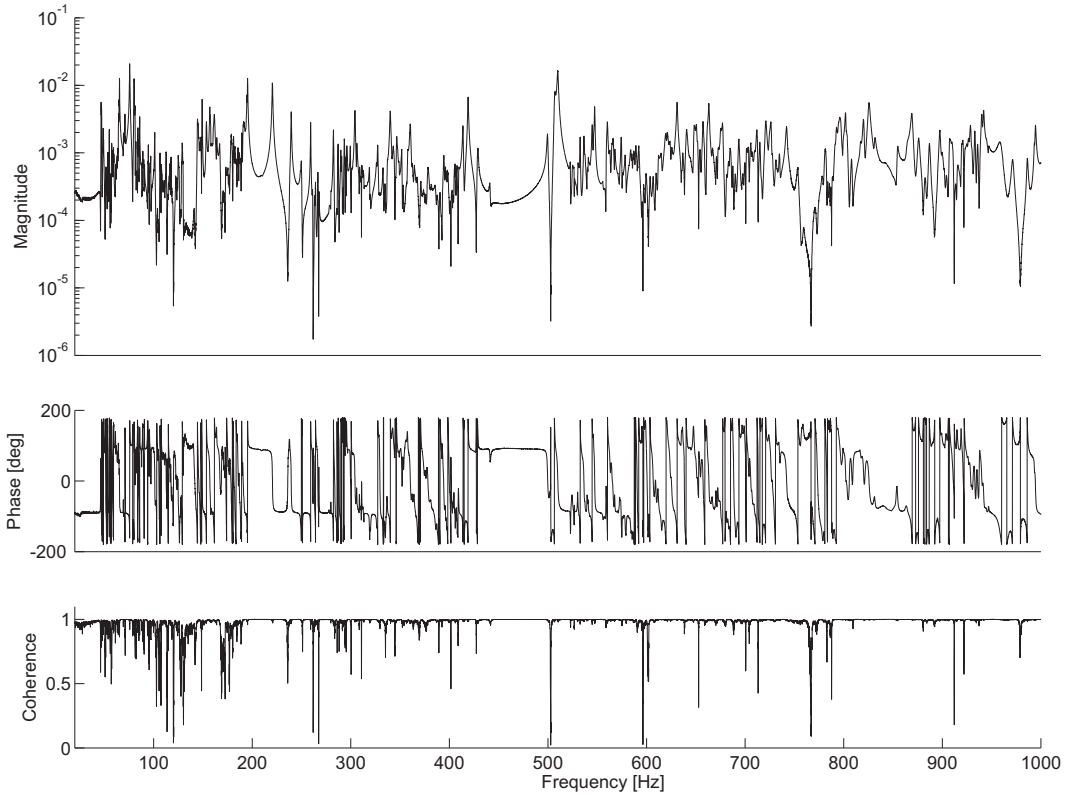

Figure E.2: Magnitude and phase of velocity in joint 31, x direction, measurement coherence

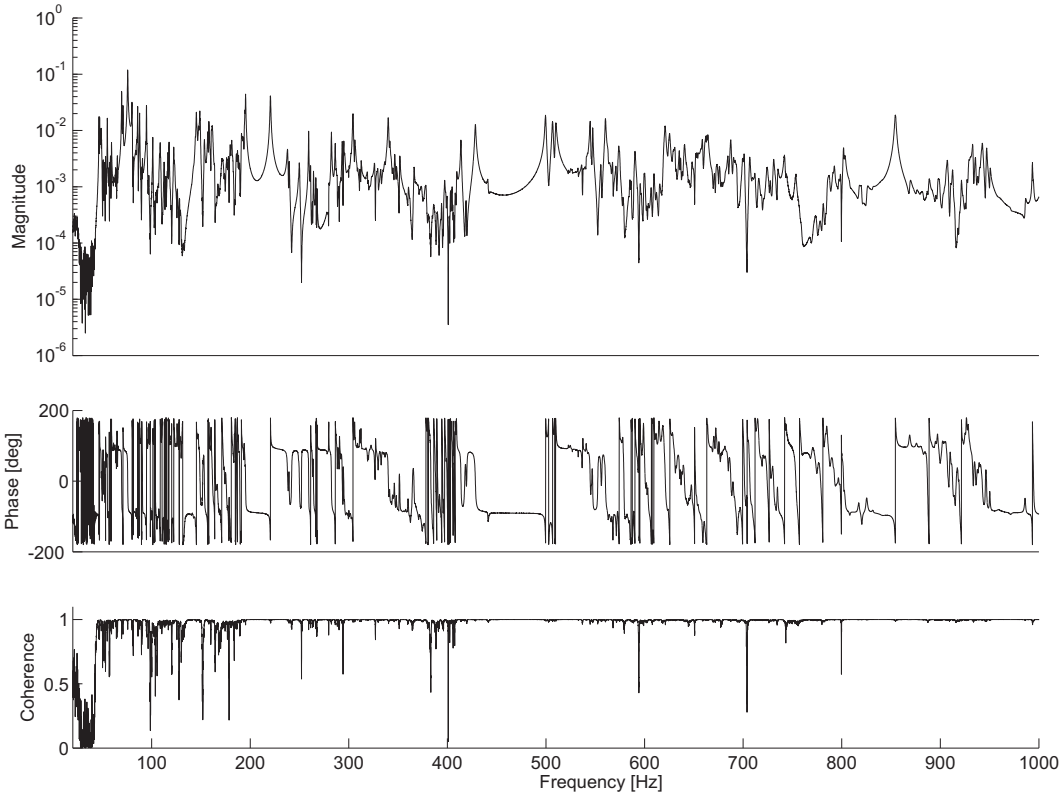

Figure E.3: Magnitude and phase of velocity in joint 31, y direction, measurement coherence

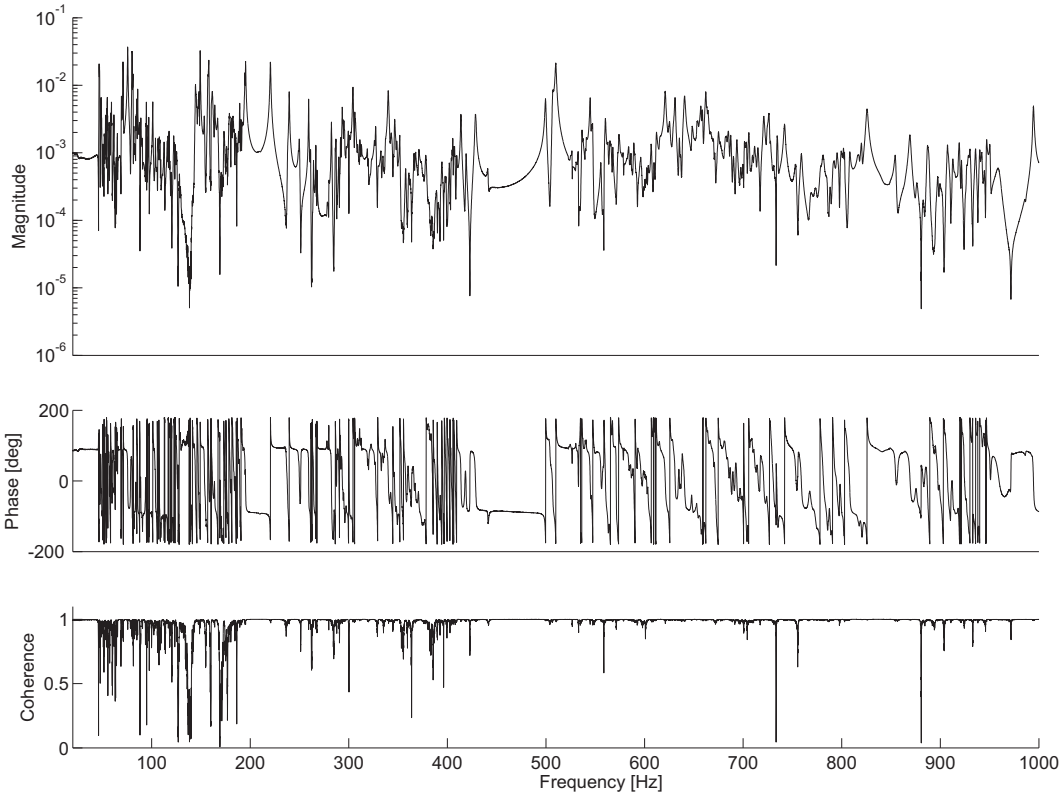

Figure E.4: Magnitude and phase of velocity in joint 31, z direction, measurement coherence

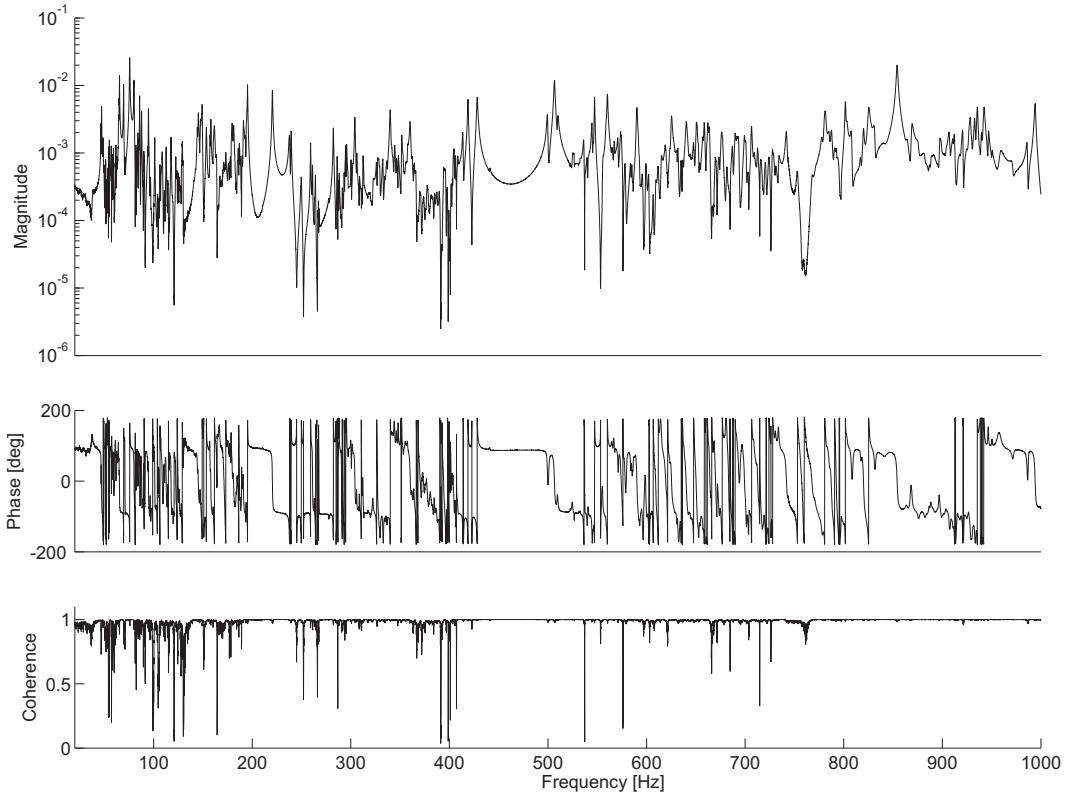

Figure E.5: Magnitude and phase of velocity in joint 32, x direction, measurement coherence

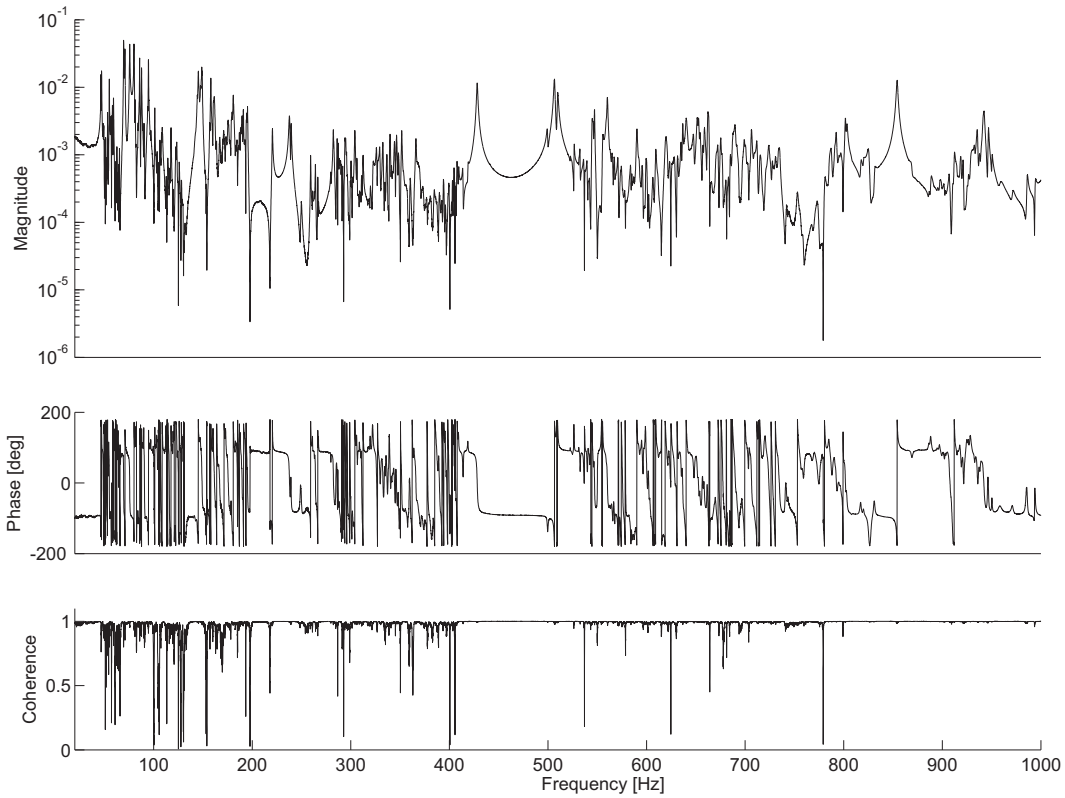

Figure E.6: Magnitude and phase of velocity in joint 32, y direction, measurement coherence

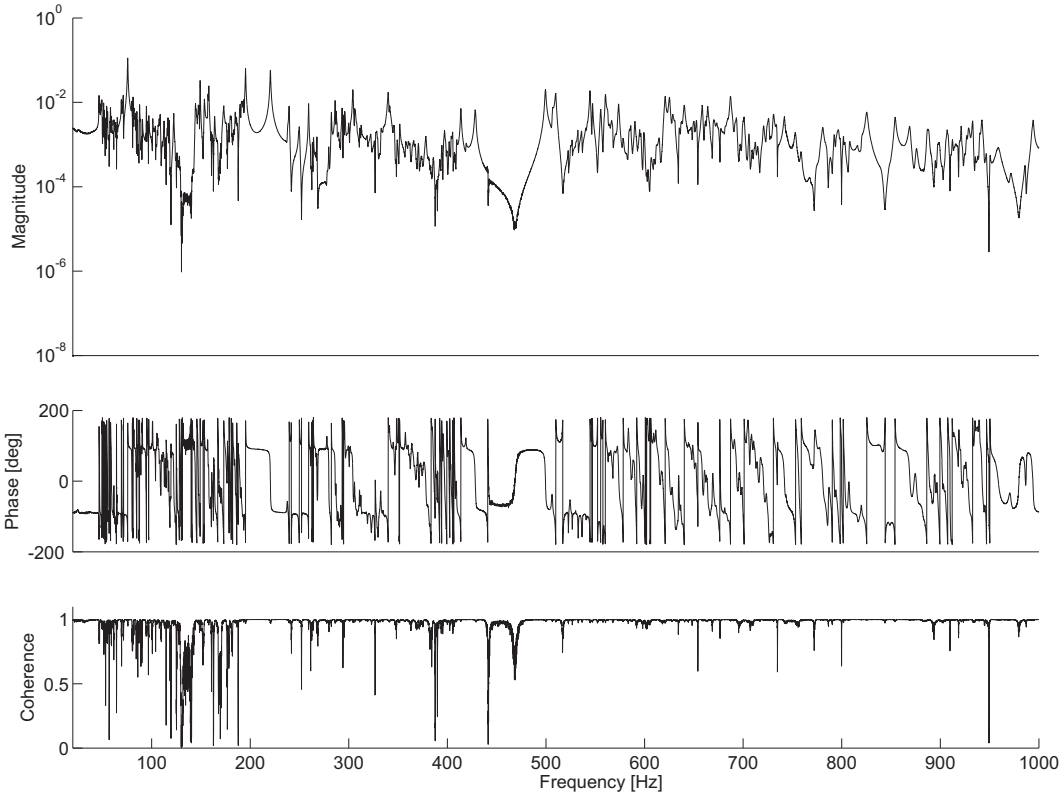

Figure E.7: Magnitude and phase of velocity in joint 32, z direction, measurement coherence

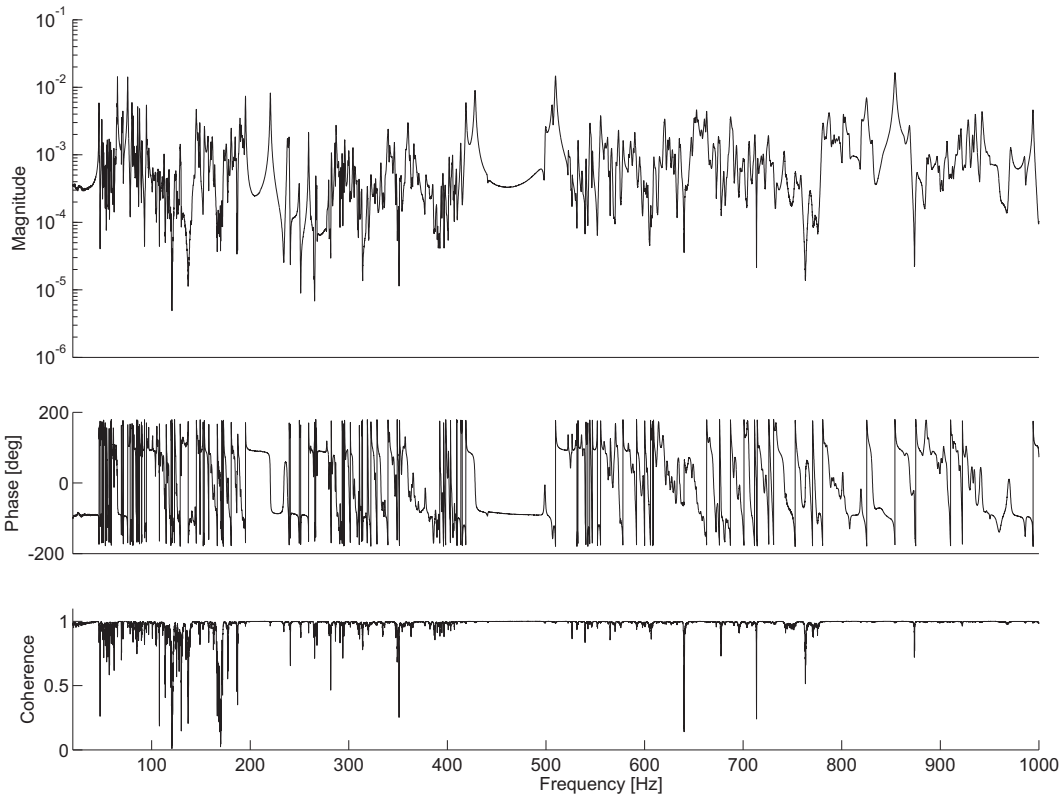

Figure E.8: Magnitude and phase of velocity in joint 33, x direction, measurement coherence

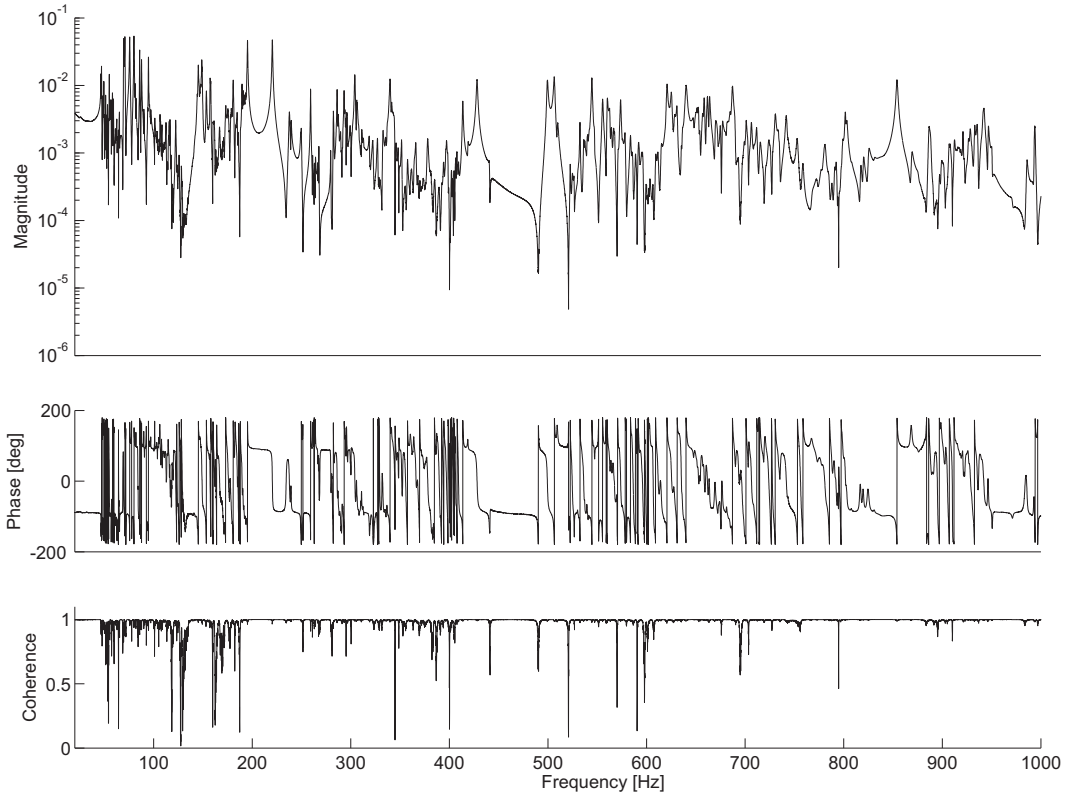

Figure E.9: Magnitude and phase of velocity in joint 33, y direction, measurement coherence

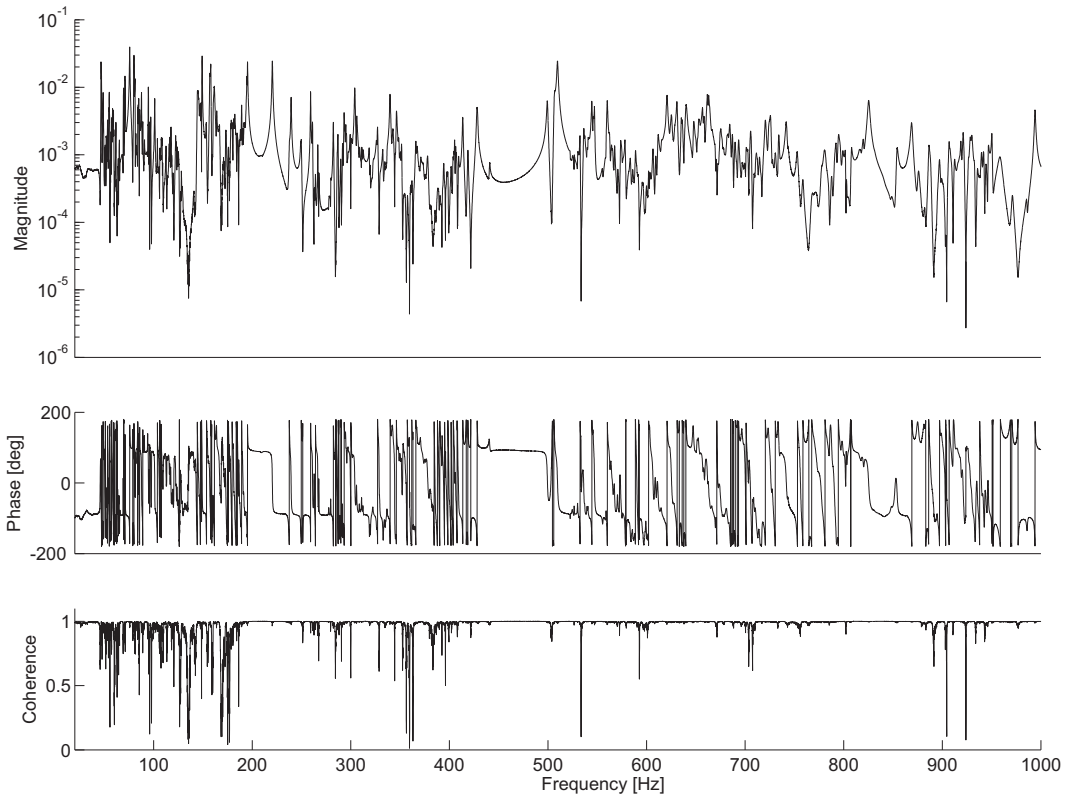

Figure E.10: Magnitude and phase of velocity in joint 33, z direction, measurement coherence

Appendix F

Actuator Properties

In this appendix the properties of the piezoelectric actuator and the power amplifier are presented. Table F.1 shows the properties of the actuator used in the experimental tests and shown in figure F.1

Property	Value	Units
Open-loop travel at 0 to 100 V	90	μm ±20 %
Push/pull force capacity	1000/50	N
Torque limit (at tip)	0.35	Nm
Electrical capacitance	9	μF ±20 %
Dynamic operating current coefficient (DOCC)	12.5	μA/ (Hz × μm)
Unloaded resonant frequency (f_0)	6	kHz ±20 %
Standard operating temperature range	-20 to +80	°C
Weight without cables	62	g ±5 %
Length L	122	mm ±0.3

Table F.1: Properties of the piezoelectric actuator model P.I. (Physics Instrument) P-841.60.

The properties of the power amplifier used to drive the appropriate voltage to the piezoelectric actuator are shown in table F.2

Properties	Values
Channels	1
Maximum output power ...	200 W
Average output power	30 W
Peak output current	<5 ms 2000 mA
Average output current ...	>5 ms 300 mA
Current limitation	Short-circuit proof
Voltage gain	10 ±0.1
Polarity	Positive
Control input voltage	-2 to +12 V
Output voltage	-20 to +120 V
DC-offset setting	0 to 100 V at output with 10-turn pot.
Input impedance	1 MW / 1 nF
Control input sockets	BNC
PZT voltage output socket	LEMO ERA.00.250.CTL
Dimensions	One 14T slot wide, 3H high
Weight	0.9 kg
Operating voltage Requires	E-530/E-531 power supply (E-500/E-501 system)

Table F.2: Function power amplifier properties. Model E-505.00 from Physic Instruments.

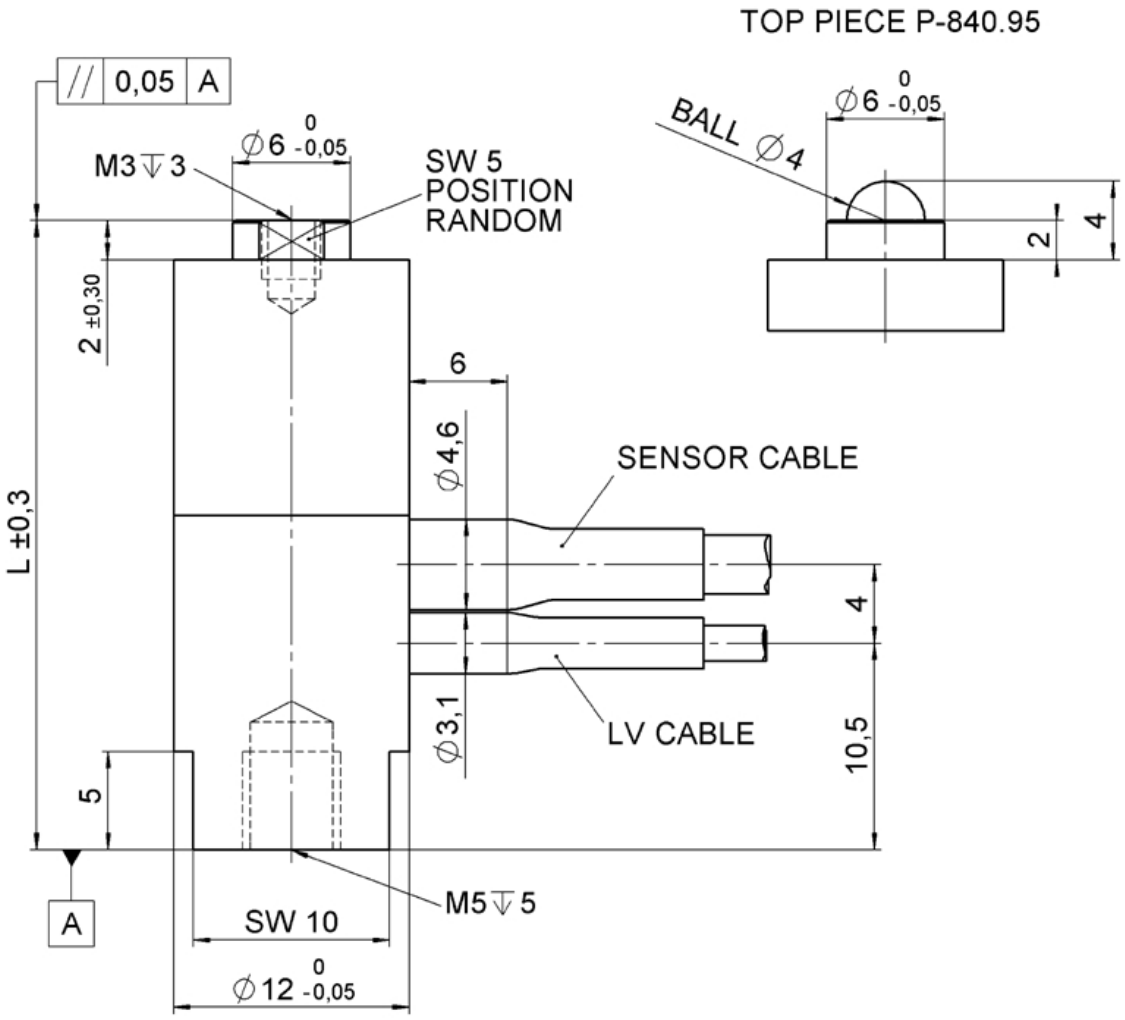

Figure F.1: Geometric details of the actuator used in the experimental tests.

Appendix G

Numbering Scheme for the Members in the Structure

This appendix present the members numbering scheme used in some picture and tables of the thesis identified by their joints number given in the table bellow. The members are identified in figures G-G according to their categories (longitudinal, batten or diagonal).

Joints	Member	Joints	Member	Joints	Member
[01 – 02]	1	[01 – 03]	2	[02 – 03]	3
[01 – 04]	4	[01 – 05]	5	[02 – 05]	6
[02 – 06]	7	[03 – 04]	8	[03 – 06]	9
[04 – 05]	10	[04 – 06]	11	[05 – 06]	12
[04 – 07]	13	[04 – 08]	14	[05 – 08]	15
[05 – 09]	16	[06 – 07]	17	[06 – 09]	18
[07 – 08]	19	[07 – 09]	20	[08 – 09]	21
[07 – 10]	22	[07 – 11]	23	[08 – 11]	24
[08 – 12]	25	[09 – 10]	26	[09 – 12]	27
[10 – 11]	28	[10 – 12]	29	[11 – 12]	30
[10 – 13]	31	[10 – 14]	32	[11 – 14]	33
[11 – 15]	34	[12 – 13]	35	[12 – 15]	36
[13 – 14]	37	[13 – 15]	38	[14 – 15]	39
[13 – 16]	40	[13 – 17]	41	[14 – 17]	42
[14 – 18]	43	[15 – 16]	44	[15 – 18]	45
[16 – 17]	46	[16 – 18]	47	[17 – 18]	48
[16 – 19]	49	[16 – 20]	50	[17 – 20]	51
[17 – 21]	52	[18 – 19]	53	[18 – 21]	54
[19 – 20]	55	[19 – 21]	56	[20 – 21]	57
[19 – 22]	58	[19 – 23]	59	[20 – 23]	60
[20 – 24]	61	[21 – 22]	62	[21 – 24]	63
[22 – 23]	64	[22 – 24]	65	[23 – 24]	66
[22 – 25]	67	[22 – 26]	68	[23 – 26]	69
[23 – 27]	70	[24 – 25]	71	[24 – 27]	72
[25 – 26]	73	[25 – 27]	74	[26 – 27]	75
[25 – 28]	76	[25 – 29]	77	[26 – 29]	78
[26 – 30]	79	[27 – 28]	80	[27 – 30]	81
[28 – 29]	82	[28 – 30]	83	[29 – 30]	84
[28 – 31]	85	[28 – 32]	86	[29 – 32]	87
[29 – 33]	88	[30 – 31]	89	[30 – 33]	90
[31 – 32]	91	[31 – 33]	92	[32 – 33]	93

Table G.1: The respective joints for each of the structural members of the lattice structure

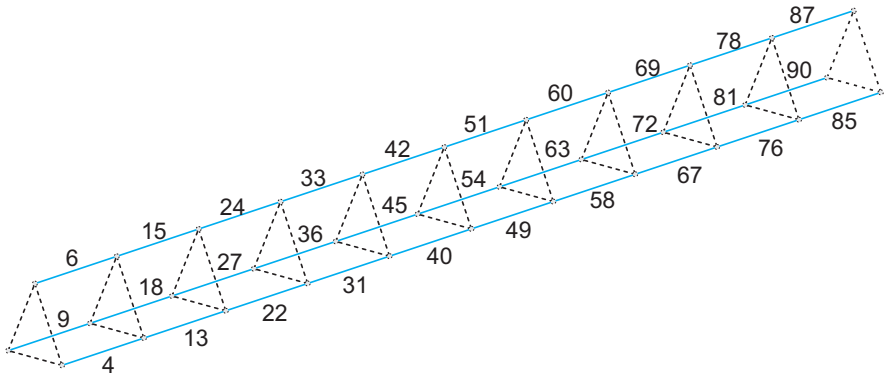

Figure G.1: The numbering scheme for the longitudinal members

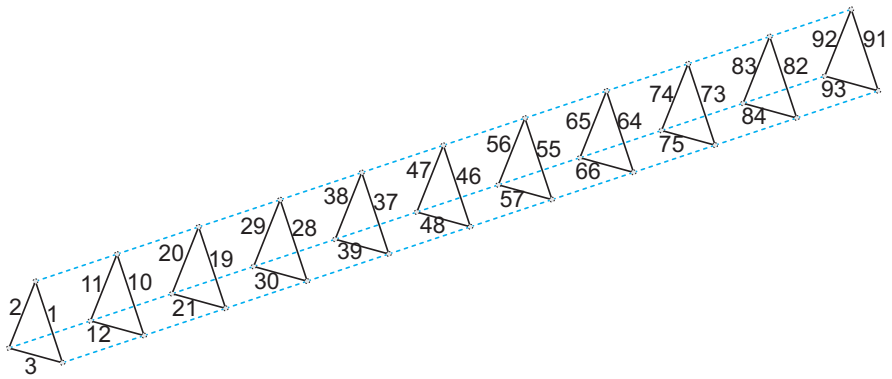

Figure G.2: The numbering scheme for the batten members

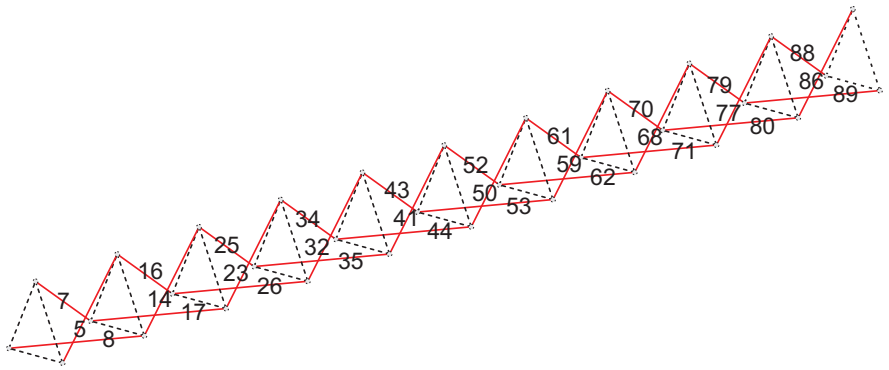

Figure G.3: The numbering scheme for the diagonal members

Appendix H

The influence of periodicity in the dynamics of lattice structures

A structure is said to be periodic when it has the form of spatially repeated units. These units are joined together in an identical manner (end-to-end or side-by-side) to form the whole system. It is well-known that such periodic systems act as wave filters, having propagation and attenuation zones (PZs and PAs) in the frequency-wavenumber-domain [34]. Mead [133, 134] has made an important contribution to this area in the understanding of PZs and PAs. According to Mead, the limits of the PZs, (also known as bound frequencies) contain the system natural frequencies. Certain periodic systems (like, supported beams) have the further property that the bounding frequencies are identical to the system natural frequencies of a single element of the whole system, with it ends either fully-fixed or free. Signorelli and von Flotow [41] have considered this problem applied to space lattice structures. Consider one of the repeating units of the lattice structure used in this thesis, shown in figure H.1, where the left and right hand sides have three joints. At these joints, other members are connected in tandem forming the whole structure.

$$\mathbf{q} = \mathbf{D}_{\text{bay}}\mathbf{f} \tag{H.1}$$

where the displacement $\mathbf{q}$ and force $\mathbf{f}$ vectors have dimension 36×1,which correspond to 6 degrees of freedom for each joint (3 on the left and 3 on the right hand side). The dynamic stiffness matrix for the bay $\mathbf{D}_{\text{bay}}$ has dimension 36×36. The displacement vector $\mathbf{q}$ can be sub-divided in two vectors $\mathbf{q}^T = \begin{bmatrix} \mathbf{q}_{\text{l}} & \mathbf{q}_{\text{r}} \end{bmatrix}$ and the force vector can also be written as $\mathbf{f}^T = \begin{bmatrix} \mathbf{f}_{\text{l}} & \mathbf{f}_{\text{r}} \end{bmatrix}$, where $\mathbf{q}_{\text{l}}$ and $\mathbf{f}_{\text{l}}$ contain the displacements and forces at the bay left hand side, respectively. $\mathbf{q}_{\text{r}}$ and $\mathbf{f}_{\text{r}}$ contain the displacement and forces at the bay right hand side, respectively. The dynamic stiffness can be written as

$$\mathbf{D}_{\text{bay}} = \begin{bmatrix} \mathbf{D}_{\text{ll}} & \mathbf{D}_{\text{lr}} \\ \mathbf{D}_{\text{rl}} & \mathbf{D}_{\text{rr}} \end{bmatrix} \tag{H.2}$$

where, the sub-matrix $\mathbf{D}_{\mathrm{rl}}$ relates the vectors of forces $\mathbf{f}_{\mathrm{l}}$ at left hand side of the bay to the vector of displacements $\mathbf{q}_{\mathrm{r}}$ at right hand side of the bay, for instance. Using the procedure described in [78], equation H.1 can be written in transfer matrix form as

$$\begin{bmatrix} \mathbf{f}_{\mathrm{r}} \\ \mathbf{q}_{\mathrm{r}} \end{bmatrix} = \begin{bmatrix} \boldsymbol{\Psi}_a & \boldsymbol{\Psi}_b \\ \boldsymbol{\Psi}_c & \boldsymbol{\Psi}_d \end{bmatrix} \begin{bmatrix} \mathbf{f}_{\mathrm{l}} \\ \mathbf{q}_{\mathrm{l}} \end{bmatrix} \tag{H.3}$$

where,

$$\left.\begin{aligned} \boldsymbol{\Psi}_a &= \mathbf{D}_{\mathrm{lr}}^{-1}\mathbf{D}_{\mathrm{ll}} \\ \boldsymbol{\Psi}_b &= -\mathbf{D}_{\mathrm{lr}}^{-1} \\ \boldsymbol{\Psi}_c &= -\mathbf{D}_{\mathrm{rr}}\mathbf{D}_{\mathrm{lr}}^{-1}\mathbf{D}_{\mathrm{ll}} + \mathbf{D}_{\mathrm{rl}} \\ \boldsymbol{\Psi}_d &= \mathbf{D}_{\mathrm{rr}}\mathbf{D}_{\mathrm{lr}}^{-1} \end{aligned}\right\} \tag{H.4}$$

and the relationship in equation H.3 can be written in compact form as

$$\boldsymbol{\psi}_r = \boldsymbol{\Psi}\boldsymbol{\psi}_l \tag{H.5}$$

where, $\boldsymbol{\psi}_r^T = \begin{bmatrix} \mathbf{f}_{\mathrm{r}} & \mathbf{q}_{\mathrm{r}} \end{bmatrix}$ and $\boldsymbol{\psi}_l^T = \begin{bmatrix} \mathbf{f}_{\mathrm{l}} & \mathbf{q}_{\mathrm{l}} \end{bmatrix}$.

H.1 Wave mode properties for the transfer matrix

A wave mode propagating along a periodic structure can be characterized by

$$\boldsymbol{\psi}_{b+1} = \lambda\boldsymbol{\psi}_b \tag{H.6}$$

which indicates that the cross-sectional state vector at station $b+1$ and b (where $b+1$ is a bay adjacent to the bay b) are related by a multiplication factor λ. This together with the transfer matrix relationship of equation H.5 forms an eigenvalue problem for λ. According to [41], the eigenvalues are generally complex and occur in λ and $1/\lambda$ pairs. This means, that for each wave mode there are frequency regions where the wave propagates without attenuation $|\lambda| = 1$ (PZs) and regions in which the wave is attenuated $|\lambda| < 1$ or $|\lambda| > 1$ (AZs). From the eigenvalues λ, it is possible to write

$$\lambda_r = \mathrm{e}^{-jk_r l} \tag{H.7}$$

The relationship given in equation H.7 is demonstrated in reference [77]. From equation H.7 it is possible to find the wavenumber as

$$k_r = \frac{\ln \lambda_r}{-jl} \tag{H.8}$$

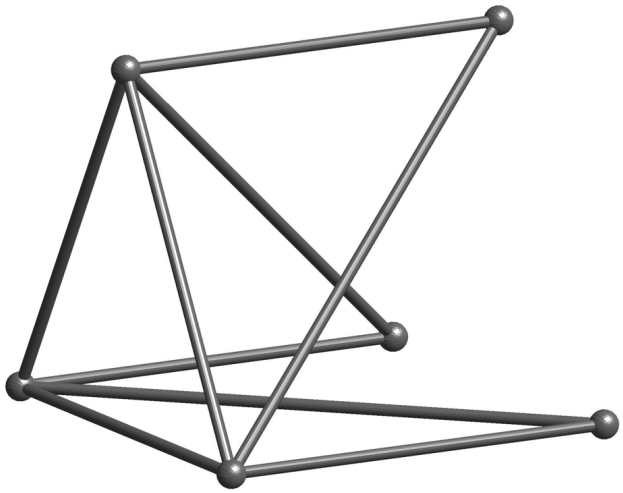

Figure H.1: The repeating unit of the lattice structure (One bay)

Publications

The following works have been published during the development of this thesis.

1. Gonçalves, P.J.P., Brennan, M.J. and Elliott, S. *The effects of short and wavelength modes on the active control of vibration in lattice structures.* Proceedings of COBEM 2007 - 19th International Congress on Mechanical Engineering - Brasilia - Brazil, 2007.

2. Gonçalves, P.J.P., Brennan, M.J. and Elliott, *Numerical evaluation of high-order modes of vibration in uniform Euler-Bernoulli beams. Journal of Sound and Vibration*, 301, (3-5), 1035-1039, 2007.

3. Gonçalves, P.J.P., Brennan, M.J. and Elliott, S. *Active Vibration Control of Space Truss Structures: Power Analysis and Energy Distribution.* Proceedings of ISMA - International Conference on Noise and Vibration, 2006, Leuven, Belgium. 2006.

4. Gonçalves, P.J.P., Brennan, M.J. and Elliott, S. *Power Analysis in Vibration Control of Truss Structures.* Proceedings of the IX International Conference on Recent Advances in Structural Dynamics, 2006, Southampton, UK. 2006.

References

[1] K. Miura. Adaptive structures research at ISAS, 1984-1990. *Journal of Intelligent Material Systems and Structures*, 3:54–74, 1992.

[2] H. H. Bush, M. M. Mikulas-Jr., and W. L. Heard-Jr. Some design considerations for large space structures. *AIAA Journal*, 16(4):352–359, 1978.

[3] L.Vaillon, B. Petitjean, B. Frapard, and D. Lebihan. Active isolation in space truss structures: From concept to implementation. *Smart Materials and Structures*, 8:781–790, 1999.

[4] G. Bodineau, S. Boulade, B. Frappard, W. Chen, S. Salehi, and F. Ankersen. Robust control of large flexible appendages for future space missions. *In Proc. 14th IFAC World Congress, Beijing, China*, pages 1034–1037, 2004.

[5] R. L. James Jr. Large space systems technology overview. *Large Space Systems - NASA CP 2168*, Volume 1:1–8, 1980.

[6] F. M. Ham, S. W. Greeley, and B. L. Henniges. Active vibration suppression for the mast fligth system. *IEEE Control System Magazine*, pages 85–90, 1989.

[7] J. N. James and R. R. McDonald. Outlook for space. *Rep. to NASA Administrator. NASA*, 1976.

[8] D. I. Jones. Vibration control in space. *Computing and Control Engineering Journal*, 2:89–95, 1994.

[9] J. A. Garba, B. K. Wada, and J. L. Fanson. Adaptive structures for precision controlled large space systems. *Journal of Intelligent Material Systems and Structures*, 3:348–366, 1992.

[10] A. Preumont. *Vibration Control of Active Structures: An Introduction*. Springer, 2nd edition, 1999.

[11] L. Vaillon and C. Philippe. Passive and active microvibration control for very high pointing accuracy space systems. *Smart Materials and Structures*, 8:719–728, 1999.

[12] G. S. Aglietti, S. B. Gabriel, R. S. Langley, and E. Rogers. A modeling technique for active control design studies with application to spacecraft microvibrations. *Journal of the Acoustic Society of America*, 102 (4):2158–2166, 1997.

[13] S. Fay, S. Gates, T. Herderson, L. Sackett, K. Kirchwey, I. Stooddardand, and J. Storch. Control of flexible structures - II (Fligth control, structure, and gimbal system interaction study. *NASA - CR 172095*, 1988.

[14] M. J. Balas. Trends in large space structure control theory: Fondest hopes, wildest dreams. *IEEE transactions in automatic control*, 27(3):522–535, 1982.

[15] L. Foster, M.L. Tinker, G.S. Nurre, and W.A. Till. The solar array-induced disturbance of the hubble space telescope pointing system. *NASA Technical Paper 3556*, 1995.

[16] A. Thornton, J. Mahaney, and P. Dechaumphai. Finite element thermal-structural modelling of orbiting truss structures. *NASA CP-2215 - Large Space Systems Technology*, pages 93–108, 1981.

[17] G. W. Neat, J. W. Melody, Member, and B. J. Lurie. Vibration attenuation approach for spaceborne optical interferometers. *IEEE Transactions on control systems technology*, 6(6):689–700, 1998.

[18] T. R. Graves Smith. *Linear Analysis of Frameworks*. Ellis Horwood Limited, 1983.

[19] A. Palladio. *The Four Books of Architecture*. Dover Publications, 1965.

[20] The American Society of Civil Enginnering. Bibliography on latticed structures. *Journal of the Structural Division, ASCE*, 98(ST7):1545–1566, July 1972.

[21] The American Society of Civil Engineering. Lattice structures: State-of-the-art report. *Journal of the Structural Division, ASCE*, 102(ST11):2197–2230, 1976.

[22] I. Beckey and J. E. Naugle. Just over the horizon in space. *Astronautics and Aeronautics*, 18:64–76, 1980.

[23] J. F. Rogers and R. D. Tutterow. ACCESS flight hardware design and development. *NASA Conference Publication*, CP 2490:31–53, 1986.

[24] M. Moshrefi-Torbati, A.J. Keane, S.J. Elliott, M.J. Brennan, D.K. Anthony, and E. Rogers. Active vibration control (AVC) of a satellite boom structure using optimally positioned stacked piezoelectric actuators. *Journal of Sound and Vibration*, 292:203–220, 2006.

[25] M. Moshrefi-Torbati, A.J. Keane, S.J. Elliott, M.J. Brennan, and E. Rogers. The integration of advanced active and passive structural noise control methods. *International Journal of Solids and Structures*, 43(21):6472 – 6487, 2006.

[26] M. Moshrefi-Torbati, A. J. Keane, S. J. Elliott, M. J. Brennan, and E. Rogers. Passive vibration control of a satellite boom structure by geometric optimization using genetic algorithm. *Journal of Sound and Vibration*, 267(4):879–892, 2003.

[27] A. K. Noor, M. S. Anderson, and W. H. Greene. Continuum models for beam- and platelike lattice structures. *AIAA Journal*, 16(12):1219–1228, 1978.

[28] J. D. Renton. The beam-like behavior of space trusses. *AIAA Journal*, 22(2):273–280, 1984.

[29] A. H. von Flotow. Control-motivated dynamic tailoring of truss-work structures. In *AIAA Guidance, Naviagation and Control Conference, Williamsburg, Virginia*, pages 622–628, 1986.

[30] A. K. Noor and M. M. Mikulas Jr. Continuum modeling of large lattice structures - status and projections. *NASA Technical Paper*, 2767, 1988.

[31] P. W. Anderson. Absence of diffusion in certain random lattices. *Physical Review*, 109(5):1942–1505, 1958.

[32] S. D. Lust, P. P. Friedmann, and O. O. Bendiksen. Free and forced response of multi-span beams and multy-bay trusses withlocalized modes. *Journal of Sound and Vibration*, 180(2):313–332, 1995.

[33] C. Pierre and P. D. Cha. Strong mode localization in nearly periodic disordered structures. *AIAA Journal*, 27(2):227–241, 1989.

[34] E. Emaci, M. A. F. Azeez, and A. F. Vakakis. Dynamics of trusses: Numerical and experimental results. *Journal of Sound and Vibration*, 214(5):953–964, 1988.

[35] A. H. von Flotow. *The acoustic limit of control of structural dynamics*, chapter 10, pages 213–237. Springer-Verlag, 1988.

[36] L. Brillouin. *Wave propagation in periodic structures*. Dover, 1946.

[37] D. J. Mead. Free wave propagation in periodically supported, infinite beams. *Journal of Sound and Vibration*, 11:191–197, 1970.

[38] L. Cremer, M. Heckel, and E. Ungar. *Structure-Borne sound*. Springer-Verlag, 1973.

[39] M. Faulkner and D. Hong. Free vibrations of a mono-coupled periodic systems. *Journal of Sound and Vibration*, 99:29–42, 1985.

[40] D. J. Mead. Vibration response and wave propagation in periodic structures. *ASME J. Eng. Ind.*, 93:783–792, 1971.

[41] J. Signorelli and A. H. von Flotow. Wave propagation, power flow, and resonance in a truss beam. *Journal of Sound and Vibration*, 126(1):127–144, 1988.

[42] K. C. Park and J. M. Winget. The potential of nonperiodic truss structures for space applications. In *Large Space System Technology - CP 2215*. NASA, 1981.

[43] S. O. Reza Moheimani, D. Halim, and A. J. Fleming. *Spatial control of vibration - Theory and Experiments*. World Scientific, 2003.

[44] D. J. Leo and D. J. Inman. Modeling and control simulations of a slewing frame containing active members. *Smart Materials and Structures*, 2:82–95, 1993.

[45] J.L. Fanson and T.K. Caughey. Positive position feedback control for large space structures. *AIAA Journal*, 28(4):717 – 724, 1990.

[46] M. C. Brennan and A.-M. R. McGowan. Piezoelectric power requirements for active vibration control. volume 3039, pages 660–669. SPIE, 1997.

[47] M. I. Frecker. Recent advances in optimization of smart structures and actuators. *Journal of Intelligent Material Systems and Structures*, 14:207–216, 2003.

[48] B.J. Maclean, J.L. Draper, and M.S. Misra. Development of a shape memory material actuator for adaptive truss applications. *Journal of Intelligent Material Systems and Structures*, 2:261–280, 1991.

[49] A. Preumont and F. Bossens. Active tendon control of vibration of truss structures: Theory and experiments. *Journal of Intelligent Material Systems and Structures*, 11(2):91–99, 2000.

[50] Lothar Gaul, Stefan Hurlebaus, Hans Albrecht, and Jan Wirnitzer. Controlled friction damping by semi-active joints. *VDI Berichte*, (2003):131 – 146, 2007. Friction damping;Lightweight structures;Structural joints;Optimal placement;Semi-active control;.

[51] Ricardo Carvalhal, Vicente Lopes Jr., and Michael J. Brennan. An efficient modal control strategy for the active vibration control of a truss structure. *Shock and Vibration*, 14(6):393 – 406, 2007. Intelligent truss structures;Independent modal space control;Piezoelectric stack actuator;Feedback force;.

[52] Lorenzo Dozio. Deadbeat predictive control on a space truss structure. *Journal of Guidance, Control, and Dynamics*, 29(6):1444 – 1446, 2006. Pulse amplitude modulated (PAM) devices;Analog devices;Truss experiment for space structure (TESS);.

[53] Andreas Rittweger, Hans-Georg Beig, Peter Konstanzer, and Rafael Bureo Dacal. Active paylaod adaptor for ariane 5. volume 6, pages 3654 – 3665, Fukuoka, Japan, 2005. Paylaod adaptor;Passive payload adaptors;Mass impact;.

[54] P.A. Nelson and S.J. Elliott. *Active control of sound*. Academic Press, 1992.

[55] C. R. Fuller, S. J. Elliott, and P. A. Nelson. *Active Control of Vibration*. Academic Press Limited, 1996.

[56] K. Ogata. *Modern control engineering*. Prentice Hall, 1990.

[57] G. F Franklin, J. D Power, and A. Enami-Naeini. *Feedback control of dynamic systems*. Addison Wesley, 1994.

[58] R. L. Clark, W. R. Saunders, and G. P. Gibbs. *Adaptive structures : dynamics and control*. Wiley-Interscience, 1998.

[59] D. K. Anthony, S. J. Elliott, and A. J. Keane. Robustness of optimal desing solutions to reduce vibration transmission in a lightweight 2-d structure, part i: Geometric design. *Journal of Sound and Vibration*, 229(3):505–528, 2000.

[60] P.J.P. Gonçalves, M. J. Brennan, and S. Elliott. Active vibration control of space truss structures: Power analysis and energy distribution. In *Proceedings of ISMA - International Conference on Noise and Vibration, 2006, Leuven, Belgium*, 2006.

[61] P.J.P. Gonçalves, M.J. Brennan, and Elliott. The effects of short and wavelength modes on the active control of vibration in lattice structures. In *Proceedings of COBEM 2007 - 19th International Congress on Mechanical Engineering*, 2007.

[62] P.J.P. Gonçalves, M. J. Brennan, and S. Elliott. Power analysis in vibration control of truss structures. In *Proceedings of the IX International Conference on Recent Advances in Structural Dynamics, 2006, Southampton, UK*, 2006.

[63] P. J. P. Gonçalves, M. J. Brennan, and S. Elliott. Numerical evaluation of higher modes of vibration in Euler-Bernoulli beams. *Journal of Sound and Vibration*, 301:1035–1039, 2007.

[64] A. K. Noor. Assessment of current state of the art in modeling techniques and analysis methods for large space structures. *NASA CP 2258*, pages 5–32, 1982.

[65] F. Fahy. *Sound and Structural Vibration, Radiation, Transmission and Response.* Academic Press Inc., 1985.

[66] R.E.D Bishop and D. B. Johnson. *The Mechanics of Vibration*. Cambridge: Cambridge Press, 1960.

[67] F. Y. Cheng and W. H. Tseng. Dynamics matrix of Timoshenko beam columns. *Proceedings of the American Society of Civil Enginners*, 99 (ST3):527–549, 1973.

[68] S. P. Timoshenko. *Vibration Problems in Engineering*. Van Nostrand, 3rd ed. edition, 1978.

[69] T. M. Wang and T. A. Kinsman. Vibration of frame structures according to the timoshenko theory. *Journal of Sound and Vibration*, 14:215–227, 1971.

[70] R.S Langley. Analysis of power flown in beam and frameworks using the direct-dynamicstiffness method. *Journal of Sound and Vibration*, 136(3):439–452., 1990.

[71] T. H. Richards and Y.T. Leung. An accurate method in structural vibration analysis. *Journal of Sound and Vibration*, 55(3):363–376., 1977.

[72] P. Gardonio and M.J. Brennan. *Chapter 9 in Advanced applications in acoustics, noise and vibration*. Spon Press Publisher., 2004:.

[73] K.-J. Bathe. *Finite Element Procedures (Part 1-2), 2nd Edition*. Prentice Hall., 1995.

[74] O.C. Zienkiewicz. *The finite element method*. McGraw-Hill, 1988.

[75] N. H. Farag and J. Pan. Dynamic response and power flow in three-dimensional coupled beam structures.i. analytical modeling. *Journal of the Acoustical Society of America*, 102(1):315–25., 1997.

[76] K. Shankar and A. J. Keane. Energy flow predictions in a structure of rigidly joined beams using receptancetheory. *Journal of Sound and Vibration*, 185(5):867–890, 1995.

[77] V. H. Neubert. *Mechanical Impedance: Modelling/Analysis of Structures*. Jostens Printing and Pub. Co., 1987.

[78] S. Rubin. Mechanical immitance- and transmission-matrix concepts. *Journal of Acoustic Society of America*, 12.7:1171–1179, 1966.

[79] C. S. Manohar and S. Adhikari. Statistics of vibration energy flow in randomly parametered trusses. *Journal of Sound and Vibration*, 217(1):43–74, 1998.

[80] J. F. Doyle. *Wave propagation in structures : spectral analysis using fast discrete Fourier transforms*. Springer, 1997.

[81] A. F. M. Azevedo. *Método dos Elementos Finitos (in portuguese)*. Faculdade de Engenharia da Universidade do Porto, 2003.

[82] R. L. Boylestad. *Introductory circuit analysis*. Pretince Hall, 1997.

[83] R. D. Cook, D. S. Malkus, M. E. Plesha, and R. J. Witt. *Concepts and Applications of Finite Element Analysis*. John Wiley & Sons, Inc., 2002.

[84] R. W. Clough. The finite element in plane stress analysis. In *Proc. 2nd ASCE Conf. on Electronic Computation*, 1960.

[85] Y. W. Kwon and H. Bang. *The finite element method using matlab*. CRC Press, 1996.

[86] U. Lee. Dynamic continuum modeling of beamlike space structures using finite-element matrices. *AIAA Journal*, 28(4):725–731, 1990.

[87] N. H. Polakowski and E. J. Ripling. *Strength and Structure of Enginnering Materials*. Prentice-Hall, 1996.

[88] C.-F. Shih, J.C. Chen, and J. A. Garba. Verification of large beam-type space structures. *Journal of Spacecraft*, 1987.

[89] F. Bleich. *Buckling Strength of Metal Structures*. McGraw-Hill, 1952.

[90] N. F. Mott and P. W. Anderson. Nobel lectures in physics for 1977. *Rev. Mod. Physics*, 50:191–208, 1978.

[91] R. A. Ibrahim. Structural dynamics with parameter uncertainties. *Applied Mechanics Reviews*, 40(3):309–238, 1987.

[92] N. A. Valero and O. O. Bendiksen. Vibration characteristics of mistuned shrouded blade assemblies. *ASME Journal of Engineering for Gas Turbines and Power*, 108(2):293–299, 1986.

[93] S. T. Wei and C. Pierre. Localization phenomena in mistuned assemblies with cyclic symmetry. part i: free vibrations. In *Proceedings of the Eleventh Biennial Conference on Mechanical Vibration and Noise, Boston, MA; USA*, pages 61–79, 1987.

[94] O. O. Bendiksen. Mode localization phenomena in large space structures. *AIAA Journal*, 25(9):1241–1248, 1987.

[95] P. J. Cornwell and O. O. Bendiksen. Localization of vibrations in large space reflectors. *AIAA Journal*, 27(2):219–226, 1989.

[96] C. H. Hodges and J. Woodhouse. Vibration isolation from irregularity in a nearly periodic structure: Theory and measurements. *Journal of The acoustic Society of America*, 74(3):894–905, 1983.

[97] J. J. Ziman. *Principles of the theory of solids.* Cambridge U. P., 1964.

[98] P. Lueg. Process of silencing sound oscillations. *US Patent*, No. 2,043,416, 1936.

[99] S. D. Snyder and N. Tanaka. On feedforward active control of sound and vibration using vibration error signals. *Journal of the Acoustical Society of America*, 94(4):2181–2193, 1993.

[100] J. Suhardjo, B. F. Spencer, and M. K. Sain. Feedback feedforward control of structures under seismic excitation. *Structural Safety*, 8(1-4):69–89, 1990.

[101] H. Ma, G. Y. Tang, and Y. D. Zhao. Feedforward and feedback optimal control for offshore structures subjected to irregular wave forces. *Ocean Engineering*, 33(8-9):1105–1117, 2006.

[102] Steven A. Lane, Marty Johnson, Chris Fuller, and Arnaud Charpentier. Active control of payload fairing noise. *Journal of Sound and Vibration*, 290(3-5):794–819, 2006.

[103] W. L. Hallauer Jr. *Mechanics and Control of Large Flexible Structures*, volume 129, chapter 18, pages 465–489. American Institute of Aeronautics and Astronautics, 1990.

[104] D. C. Fraser. Large space structures control: Early experiments. *Journal of Guidance, Control and Dynamics*, 7(5):513, 1984.

[105] G. S. Nurre, R. S. Ryan, H. N. Scofield, and J. L. Sims. Dynamics and control of large space structures. *Journal of Guindance, Control and Dynamics*, 7(5):514–526, 1984.

[106] C. S. Major and E. B. Shain. Demonstration of vibration control of a flexible truss structure. *Dynamics and Control of Large Structures*, Edited by L. Meirovitch:183–190, 1958.

[107] R. L. Dailey and Lukich M. S. Recent results in identitication and control of a flexible truss structure. In *Proceedings of the 1988 American Control Conference*, volume 2, pages 1468–1473, 1988.

[108] G. J. Balas, M. Lukich, R. L. Dailey, and J. C. Doyle. Robust control of a truss experiment. *AIAA paper*, 88-4084, 1988.

[109] M. Lukich. System identication and control of the truss experiment: a restropective. *AIAA Paper*, 88:4142, 1988.

[110] P. T. Kotnik, S. Yurkovich, and U. Ozguner. Acceleration feedback for control of a flexible manipulator arm. *Journal of robotic systems*, 5(3):181–196, 1988.

[111] S. Yurkovich and F. E. Pacheco. On controller tuning for a flexible-link manipulator with varying payload. *Journal of robotic systems*, 6:233–254, 1989.

[112] D. W. Miller, E. F. Crawley, and B. A. Ward. Inertial actuators design for maximum passive and active energy dissipation in flexible space structures. *AIAA Paper*, 85-0777, 1985.

[113] D. W. Miller and E. F. Crawley. Theoretical and experimental investigation of space-realizable inertial actuation for passive and active structural control. *Journal of Guidance, Control and Dynamics*, 11(5):449–458, 1988.

[114] Y. Murotsu, H. Okubo, and Terui F. Low-autorith control of large space structures by using a tendon control system. *Journal of Guidance, Control and Dynamics*, 12(2):264–272, 1989.

[115] Y. Murostu, H. Okubo, F. Terui, K. Senda, and K. Shinoda. Dynamics and control of experimental tendon control sytem for flexible space structures. *AIAA Paper*, 87-2325, 1988.

[116] B. K. Wada. Adaptive structures. *AIAA paper*, 89-1160, 1989.

[117] N. W. Hagood and E. F. Crawley. Experimental investigaion into passive damping enhancement for space structures. *AIAA paper*, 89-3536, 1989.

[118] A. Preumont, B. de Marneffe, and A. Deraemaeker. Active and passive damping of piezoelectric structures. In *Forum Acusticum*, 2005.

[119] A. Preumont. *Mechatronics - Dynamics of Electromechanical and Piezoelectric Systems*. Springer, 2006.

[120] W. K. Gawronski. *Dynamics and control of structures: a modal approach*. Springer-Verlag, 1998.

[121] L. Meirovitch. *Dynamics and control of structures*. John Wiley and Sons, 1990.

[122] A. Preumont, J. P. Dufour, and C. Malekian. Active damping by a local force feedback with piezoelectric actuators. *AIAA Journal of Guidance*, 15(2):390–395, 1992.

[123] E. H. Anderson, D. M. Moore, J. L. Fanson, and M. A. Ealey. Development of an active member using piezoelectric and electrostrictive actuation for control of precision structures. In *SDM conference*, volume AIAA paper 90-1085-CP, 1990.

[124] G. S. Chen, B. J. Lurie, and B. K. Wada. Experimental studies of adaptive structures for precision and performance. In *SDM conference*, volume AIAA paper 89-1327-CP, 1989.

[125] J. L. Fanson, G. H. Blackwood, and C. C. Chen. Active member control of precision structures. In *SDM Conference*, volume AIAA paper 89-1329-CP, 1989.

[126] T. T. Hyde and E. H. Anderson. Actuator with built-in viscous damping for isolation and structural control. *AIAA Journal*, 1:129–135, 34.

[127] L. D. Peterson, J. J. Allen, J. P. Lauffer, and A. K. Miller. An experimental and analytical synthesis of controlled structure design. In *SDM Conference*, volume AIAA paper 89-1170-CP, 1989.

[128] Armaghan Salehian, Eugene M. Cliff, and Daniel J. Inman. Continuum modeling of an innovative space-based radar antenna truss. *Journal of Aerospace Engineering*, 19:227–240, 2006.

[129] S. J. Elliott, P. Gardonio, T. C. Sors, and M. J. Brennan. Active vibroacoustic control with multiple local feedback loops. *Journal of the Acoustical Society of America*, 111(2):908915, 2002.

[130] S. Skogestad and I. Postlethwaite. *Multivariable feedback control*. John Wiley & Sons, 1996.

[131] X. Huang, S.J. Elliott, and M.J. Brennan. Active isolation of a flexible structure from base vibration. *Journal of Sound and Vibration*, 263:357–376, 2003.

[132] E. Spacone, V. Ciampi, and F. C. Filippou. A beam element for seismic damage analysis. Technical Report UCB/EERC-92/07, Earthquake Enginnering Reserach Center - College of Engineering - University of California, Berkeley, 1992.

[133] D. J. Mead. Wave propagation and natural modes in periodic systems: I. monocoupled systems. *Journal of Sound and Vibration*, 40(1):1–18, 1975.

[134] D. J. Mead. Wave propagation and natural modes in periodic systems. II. multicoupled sytems, with and without damping. *Journal of Sound and Vibration*, 40(1):19–39, 1975.